

University of Wisconsin Milwaukee

UWM Digital Commons

Theses and Dissertations

May 2020

Investigation of Heat Transfer in Stationary and Rotating U-Duct Passage Representing Internal Cooling of Gas Turbine Blade Channel

Mandana Sheikhzad Saravani
University of Wisconsin-Milwaukee

Follow this and additional works at: <https://dc.uwm.edu/etd>



Part of the [Mechanical Engineering Commons](#)

Recommended Citation

Sheikhzad Saravani, Mandana, "Investigation of Heat Transfer in Stationary and Rotating U-Duct Passage Representing Internal Cooling of Gas Turbine Blade Channel" (2020). *Theses and Dissertations*. 2423.
<https://dc.uwm.edu/etd/2423>

This Dissertation is brought to you for free and open access by UWM Digital Commons. It has been accepted for inclusion in Theses and Dissertations by an authorized administrator of UWM Digital Commons. For more information, please contact open-access@uwm.edu.

INVESTIGATION OF HEAT TRANSFER IN STATIONARY AND ROTATING U-DUCT PASSAGE
REPRESENTING INTERNAL COOLING OF GAS TURBINE BLADE CHANNEL

by

Mandana Sheikhhzad Saravani

A Dissertation Submitted in
Partial Fulfillment of the
Requirements for the Degree of

Doctor of Philosophy

in Engineering

at

University of Wisconsin-Milwaukee

May 2020

ABSTRACT

INVESTIGATION OF HEAT TRANSFER IN STATIONARY AND ROTATING U-DUCT PASSAGE REPRESENTING INTERNAL COOLING OF GAS TURBINE BLADE CHANNEL

by

Mandana Sheikhzad Saravani

The University of Wisconsin-Milwaukee, 2020
Under the supervision of Professor Ryoichi S. Amano

Gas turbines are used in various systems, including in power plants, marine, and aircraft propulsion engines. The airflow in gas turbines can reach temperatures as high as 2000 K that exceeds the softening points for most high-performance blade materials, such as special steels, titanium alloys, and super-alloys. Preventing thermal failure in the turbine-blades has driven many technological advances in materials science and mechanical design. In this thesis, the main focus is on improving the performance of the internal cooling channel technology. In this study, the optimized thermal behavior of the coolant gas and surfaces in turbines by incorporating novel internal cooling channels is modeled. Various computational simulations for modeling the minute details of the fluid dynamics of the coolant in blade airfoil channels are performed. This computation is done by the Large Eddy simulation method and implementing a conjugate heat transfer model. Many computational parameters are included to capture the details of airflow and hot surface interactions. These parameters are materials surface properties, Coriolis and centrifugal buoyancy forces due to rotation, effects of separating/reattaching shear layers, and the secondary flows induced by the bending regions. The maximum blade temperature and its impact on the heat transfer coefficient (The Nusselt number) are determined.

In this thesis, the following major challenges that were not considered in earlier investigations were targeted

- 1- A heat transfer method to present the heat transfer distribution and flow behavior near realistic gas turbine operating conditions.
- 2- Turning region turbulator design that causes less pressure drop along the channel and enhances the total heat transfer coefficient.
- 3- The combined physical and geometrical effects on heat transfer efficiency.
- 4- Validating the numerical results with an experimental set up that can provide similar gas turbine operating conditions.
- 5- Heat transfer correlation for calculating local Nusselt number for a developing flow passing the channel.

This study deliberates the channel turning effect and revealed the importance of this phenomena on the cooling channel's overall heat transfer performance and pressure distribution. Turning guide vanes that enhance the heat transfer coefficient in the turning region of the channel are designed. This study found the optimum guide vane design and rib turbulator configuration that led to a 1.5 times increase in the heat transfer coefficient of the system. Also, it is found that the Nusselt number strongly depends on the Reynolds number. In order to explain the relationship between the Nusselt number and Reynolds number, the Nusselt number is characterized by smooth wall channels and developed a new correlation between the Nusselt number and the Reynolds number. The Nusselt number calculated based on this proposed relationship captures the developing flow and turning the region's effects on

the local Nusselt number. It also has a better agreement with the numerical and experimental results. This correlation can be a reference for similar studies.

For the experimental heat transfer investigation, the experimental setup was built, and it reached the maximum rotation speeds up of 1500 rpm. Achieving this rotational speed is mechanically challenging and is considered substantial to similar experimental setups. This experimental setup enabled the execution and evaluation of the numerical predictions. For the test section in this study, the same size geometry that modeled in the numerical study is designed and built. The corresponding boundary conditions used in the numerical study are implemented in the experiment. An innovational method to record temperature measurement in the rotational motion is used. A series of miniature portable wireless thermocouple connectors and data loggers, and a wireless receiver to measure and collect temperature values at various points along the channel were implemented. Different thermocouple at the different channel's cross-section location, taking the average temperature in each cross-section, are utilized. This method provided real-time data at high speed. Air bulk temperature is calculated at each cross-section by using the recorded experimental data. This method of calculating the Bulk temperature before investigating the heat transfer along the channel is one of the novelties of the experimental study. After measuring the heated wall temperature and bulk temperature along the channel, the heat transfer coefficient in both stationary and rotational motion is calculated. Results from this study are in good agreement with the numerical results that approved the accuracy of the test section.

© Copyright by Mandana Sheikhzad Saravani, 2020
All Rights Reserved

with love,
To my mom, Shahin, and my dearest uncle, Rez
and
to my brother my hero, Shahin

TABLE OF CONTENTS

List of Figures.....	xi
List of Tables.....	xvi
List of Nomenclature.....	xvii
Acknowledgments	xx
1 Introduction.....	1
1.1 Gas Turbine Efficiency	1
1.2 Objective	2
1.3 Methodology	3
2 Chapter 2: Turbine Blade Cooling: State of the Art and Technology	4
2.1 Turbine Cooling Requirement.....	4
2.2 Cooling Technology	6
2.2.1 External Cooling.....	8
2.2.2 Internal Cooling System.....	9
2.2.2.1 Internal cooling of turbine vanes	11
2.2.2.2 Internal Cooling of the Blade.....	14
2.3 Literature survey.....	18
3 Computational Fluid Dynamics of Cooling Channel	27
3.1 Fluid Motion and Heat Transfer.....	27
3.1.1 Continuity.....	27
3.1.2 Momentum	27
3.1.3 Energy	28
3.1.4 Rotational Modification.....	28
3.2 Flow Model.....	29
3.2.1 SST K-Omega Model	30
3.2.2 LES Model.....	31
3.3 CFD Set Up.....	32
3.3.1 Mesh Independent Study Methodology.....	33

4	Experimental apparatus and test procedures.....	41
4.1	Experimental Set up Introduction.....	41
4.2	Counterweight Stress Analysis.....	45
4.3	Data Reduction	48
4.4	Experimental Results	49
4.4.1	Smooth Wall Validation	50
4.4.2	Ribbed Wall Validation	53
4.4.2.1	90-degree Ribbed Wall Validation.....	54
4.4.2.2	45-degree Ribbed Wall Validation.....	55
4.4.2.3	60-degree ribbed wall Validation	58
4.4.2.4	High-Performance V-rib wall Validation	59
4.4.2.5	Guide Vane with Parallel 45-deg rib Validation	60
4.5	Conclusions.....	61
5	Heat Transfer Investigation for a Two-Passage Smooth Wall Channel.....	63
5.1	Effect of Reynolds number in Smooth Wall Channel	63
5.1.1	Numerical Results.....	64
5.1.1.1	Stationary Cases	64
5.1.1.2	Rotation Cases.....	70
5.1.1.3	Pressure Drop Comparison.....	75
5.2	Effect Wall Heating in constant Reynolds number.....	76
5.2.1	Numerical Results.....	77
5.2.1.1	Stationary Results.....	77
5.2.1.2	Rotational Results	82
5.3	Conclusion	87
6	Heat Transfer Investigation for a Two-Passage Ribbed Wall Channel	89
6.1	Heat Transfer Distribution Study for 90-deg Rib with Different P/e ratio.....	89
6.1.1	Stationary Cases	91
6.1.2	Rotational Cases	98
6.2	Heat Transfer Distribution Study for 45-deg Rib with Different P/e ratio.....	100
6.2.1	Stationary Cases	103
6.2.2	Rotational Cases	109

6.3	Heat Transfer Distribution Study for 60-deg Parallel Rib with Different P/e ratio	111
6.3.1	Stationary Cases	113
6.3.2	Rotational Cases	119
6.4	Heat Transfer Distribution Study for V-Shape Rib with Different P/e ratio.....	122
6.4.1	Stationary Cases	124
6.4.2	Rotational Cases	130
6.4.3	V-Rib different installation configuration	133
6.4.3.1	Stationary results comparison.....	133
6.4.3.2	Rotational results comparison.....	135
6.5	Summary of P/e Ratio and rib Geometry Comparison.....	137
6.5.1	stationary	138
6.5.2	Rotation.....	140
6.6	Conclusions.....	142
7	Turning Guide Vane Effect on Internal cooling of Two-Passage channel.....	144
7.1	Introduction.....	144
7.2	Effect of Turning Guide Vanes on the Smooth Wall Channel.....	145
7.2.1	Smooth Wall channel with Turning Guide Vanes-Stationary results	147
7.2.2	Rotational Results.....	150
7.3	The effect of turning guide vane on the channel with parallel 45-deg rib channel.....	153
7.3.1	Results for Stationary Cases	154
7.3.2	Heat transfer for rotational Cases	157
7.4	Conclusion	160
8	Conjugate Heat Transfer	162
8.1	Introduction.....	162
8.2	Numerical Set Up.....	162
8.3	Results	164
8.3.1	Smooth wall Results	164
8.3.2	Ribbed Wall Results.....	167
8.4	Conclusions.....	169
9	Overall Conclusions and Recommendations.....	171

10	References	174
	Curriculum Vitae.....	183

LIST OF FIGURES

Figure 1-1:(a) Schematic of an ideal Bryton cycle,(b) Thermodynamic states of Bryton Cycle[1].....	1
Figure 1-2: Specific Core Power with Turbine Rotor inlet temperature[2]	2
Figure 2-1: Design challenges in internal Cooling.....	4
Figure 2-2: Typical airfoil cooling system for the high-pressure turbine blade[5].....	7
Figure 2-3: Blade structure and different cooling system [5]	8
Figure 2-4: Film cooling mechanism [5].....	9
Figure 2-5: Development of cooling technology in gas turbine blade [8]	10
Figure 2-6: Example of a turbine blade internal cooling system [9]	11
Figure 2-7: Schematic of a Turbine Vane Cross-Section with Impingement and Trailing Edge Pin-Fin Cooling[10]....	11
Figure 2-8: A ribbed channel configuration [6].....	15
Figure 2-9: Flow separation and reattachment around ribs[27]	16
Figure 3-1: U-bend Configuration (a) Inlet/Outlet and rotation axis, (b) Dimensions of the duct	33
Figure 3-2: Contours of streamline on the normal planes for different mesh size (a) 1.8M (b) 2.6M (c) 4.8M (d)10.5M	35
Figure 3-3: Wall y^+ values for the U-Bend Channel.....	37
Figure 3-4: A closer look at the prism layer	37
Figure 3-5: Mesh construction in the bending region	38
Figure 4-1: The experimental test set up.....	42
Figure 4-2: (left) The entire experimental setup, and (right) a closer look at the test section, the heater, the thermocouples, and Slip ring.....	43
Figure 4-3: Experimental setup overview: (a) Connecting Shaft to the motor through the pulley (b) Motor	44
Figure 4-4: ANSYS 3-D Geometry for the Stress Analysis	45
Figure 4-5: Stress contour for the entire shaft and bearing system.....	46
Figure 4-6: Total deformation of the entire shaft and bearing system	47
Figure 4-7: Cage structure set up	48
Figure 4-8: The approximate locations of the thermocouples along the channels	50
Figure 4-9: Experimental Nusselt Number Distribution along the channel for Various Reynolds number and Rotation Speed (a) stationery, (b) Rotation.....	52
Figure 4-10: Experimental Nusselt number distribution along the channel for a U-Bend Channel (a) Stationary $Re=12000$ (b) Rotational cases $Re=12000$, and $\omega=600$ rpm	53
Figure 4-11: Experimental Rib Configuration (a) 45-deg rib,(b) 60-deg rib,(c) 90-deg rib, (d) V-shape rib	54

Figure 4-12: Experimental Nusselt Number Distribution comparison along the channel with 90 deg parallel ribs stationary and rotational cases	55
Figure 4-13: Experimental Nusselt Number Distribution along the channel with 45 deg parallel ribs for Various Reynolds number and Rotation Speed (a) stationery, (b) Rotation	56
Figure 4-14: Experimental Nusselt number distribution along the channel for a U-Bend Channel (a) Stationary Re=6000 (b) Rotational cases Re=6000, and $\omega=300$ rpm	57
Figure 4-15: Experimental Nusselt Number Distribution along the channel with 60 deg parallel ribs for Various Reynolds number and Rotation Speed (a) stationery, (b) Rotation	59
Figure 4-16: Experimental Nusselt Number Distribution along the channel with V-Shaped ribs for Various Reynolds number and Rotation Speed.....	59
Figure 4-17: Comparison of Nusselt number ratio results for the experimental and CFD for case V1 (a) Stationary Re=6000 (b)Stationary Re=35000, (c) Rotational RO=0.75.....	61
Figure 5-1: Velocity magnitude contours (U_{in}) at the horizontal mid-plane for stationary cases (a) Re=6000, (b) Re=9000, (c) Re=12000, (d) Re=18000, and (e) Re=35000	65
Figure 5-2: Velocity contours on the normal planes Re=6000	66
Figure 5-3: Velocity contours the normal planes, Re=9000	67
Figure 5-4: Velocity contours on the normal planes, Re=12000	67
Figure 5-5: Velocity contours on the normal planes, Re=18000	68
Figure 5-6: Velocity contours on the normal planes, Re=35000	68
Figure 5-7: Nusselt number augmentation along U-shape channel for different Reynolds number (a) First Passage, (b) U-bend Region, (c) Second Passage	69
Figure 5-8: Vector velocity contours comparison at horizontal mid-plane for (a) stationary case with $U_{in} = 4.15$ m/s and (b) rotating case with $U_{in} = 4.15$ m/s and $\omega = 300$ rpm	71
Figure 5-9: Effect of Reynolds number on the Nusselt number in the same rotational speed $\omega = 600$ rpm (a) First Passage, (b) U-Turn Region, (c) Second Passage	72
Figure 5-10: Effect of rotational speed on the Nusselt number with the same Reynolds number Re = 35000 (a) First Passage, (b) U-Turn Region, (c) Second Passage	73
Figure 5-11: Combined effects of rotational speed and Reynolds number on the Nusselt number (a) First Passage, (b) U-Turn Region, (c) Second Passage	74
Figure 5-12: Friction factor ratio comparison in stationery and rotation cases	76
Figure 5-13: Velocity vectors for (a) $q=2700$ W/m^2 (b) $q=12500$ W/m^2 (c) $q=16200$ W/m^2 (d) $q=25000$ W/m^2	79
Figure 5-14: Temperature distribution (a) $q=2700$ W/m^2 (b) $q=12500$ W/m^2 (c) $q=16200$ W/m^2 (d) $q=25000$ W/m^2	81
Figure 5-15: Heat transfer augmentation along a smooth wall U-shape channel in different heat flux- Stationary case.....	82
Figure 5-16: Heat transfer augmentation along a smooth wall U-shape channel in different rotation number and density Ratio	86

Figure 6-1: : inlet/outlet for Channel with 90-deg rib configuration (a)p/e=7, (b)p/e=10, (c) p/e=12.....	90
Figure 6-2: Isometric view for Channel with 90-deg rib configuration (a)p/e=7, (b)p/e=10, (c) p/e=12.....	91
Figure 6-3: Contours of velocity and streamline on the normal planes for 90-deg rib configuration, P/e=7 Uin=12.5m/s	94
Figure 6-4: Contours of velocity and streamline on the normal planes for 90-deg rib configuration, P/e=10 Uin=12.5m/s	95
Figure 6-5: Contours of velocity and streamline on the normal planes for 90-deg rib configuration, P/e=12 Uin=12.5m/s	96
Figure 6-6: Temperature distribution at the bottom wall of the channel for stationary case 90-deg rib configuration Uin= 12.5m/s (a) p/e=7, (b) p/e=10, (c) p/e=12	97
Figure 6-7: Nusselt distribution at the bottom wall of the channel for stationary case 90-deg rib configuration Uin= 12.5m/s (a) p/e=7, (b) p/e=10, (c) p/e=12.....	98
Figure 6-8: Temperature distribution at the bottom wall of the channel for rotational case 90-deg rib configuration Uin= 12.5m/s (a) p/e=7, (b) p/e=10, (c) p/e=12	99
Figure 6-9: Nusselt distribution at the bottom wall of the channel for rotational case 90-deg rib configuration Uin= 12.5m/s (a) p/e=7, (b) p/e=10, (c) p/e=12.....	100
Figure 6-10: inlet/outlet for Channel with 45-deg rib configuration (a)p/e=7, (b)p/e=10, (c) p/e=12.....	101
Figure 6-11: isometric view for Channel with 45-deg rib configuration (a)p/e=7, (b)p/e=10, (c) p/e=12.....	102
Figure 6-12: Contours of velocity and streamline on the normal planes 45-deg rib configuration, P/e=7 Uin=12.5m/s	104
Figure 6-13: Contours of velocity and streamline on the normal planes, 45-deg rib configuration P/e=10 Uin=12.5m/s	105
Figure 6-14: Contours of velocity and streamline on the normal planes, 45-deg rib configuration, P/e=12 Uin=12.5m/s	106
Figure 6-15: Temperature distribution at the bottom wall of the channel for stationary case Uin= 12.5m/s, 45-deg rib configuration (a) p/e=7, (b) p/e=10, (c) p/e=12	107
Figure 6-16: Nusselt distribution at the bottom wall of the channel for stationary case Uin= 12.5m/s, 45-deg rib configuration (a) p/e=7, (b) p/e=10, (c) p/e=12	108
Figure 6-17: Temperature distribution at the bottom wall of the channel for stationary case Uin= 12.5m/s, 45-deg rib configuration (a) p/e=7, (b) p/e=10, (c) p/e=12	110
Figure 6-18: Nusselt distribution at the bottom wall of the channel for stationary case Uin= 12.5m/s, 45-deg rib configuration (a) p/e=7, (b) p/e=10, (c) p/e=12	111
Figure 6-19: inlet/outlet for Channel with 60-deg rib configuration (a) p/e=7, (b)p/e=10, (c) p/e=12.....	112
Figure 6-20: Isometric view for Channel with 60-deg rib configuration (a) p/e=7, (b)p/e=10, (c) p/e=12.....	113
Figure 6-21: contours of velocity and streamline on the normal planes, 60-deg rib configuration, P/e=7 Uin=12.5m/s	115

Figure 6-22: contours of velocity and streamline on the normal planes, 60-deg rib configuration $P/e=10$ $U_{in}=12.5\text{m/s}$	116
Figure 6-23: contours of velocity and streamline on the normal planes, 60-deg rib configuration $P/e=12$ $U_{in}=12.5\text{m/s}$	117
Figure 6-24: Temperature distribution at the bottom wall of the channel for stationary case $U_{in}=12.5\text{m/s}$, 60-deg rib configuration (a) $p/e=7$, (b) $p/e=10$, (c) $p/e=12$	118
Figure 6-25: Nusselt distribution at the bottom wall of the channel for stationary case 60-deg rib $U_{in}=12.5\text{m/s}$ (a) $p/e=7$, (b) $p/e=10$, (c) $p/e=12$	119
Figure 6-26: Temperature distribution at the bottom wall of the channel for stationary case, 60-deg rib configuration $U_{in}=12.5\text{m/s}$ (a) $p/e=7$, (b) $p/e=10$, (c) $p/e=12$	120
Figure 6-27: Nusselt distribution at the bottom wall of the channel for rotational case 60-deg rib configuration $U_{in}=12.5\text{m/s}$ (a) $p/e=7$, (b) $p/e=10$, (c) $p/e=12$	121
Figure 6-28: inlet/outlet for Channel with V-shape rib configuration (a) $p/e=7$, (b) $p/e=10$, (c) $p/e=12$	122
Figure 6-29: Isometric view for Channel with V-Shape rib configuration (a) $p/e=7$, (b) $p/e=10$, (c) $p/e=12$	124
Figure 6-30: contours of velocity and streamline on the normal planes, V-Shape configuration $P/e=7$ $U_{in}=12.5\text{m/s}$	126
Figure 6-31: contours of velocity and streamline on the normal planes, V-Shape configuration $P/e=10$ $U_{in}=12.5\text{m/s}$	127
Figure 6-32: contours of velocity and streamline on the normal planes, V-Shape configuration $P/e=12$ $U_{in}=12.5\text{m/s}$	128
Figure 6-33: Temperature distribution at the bottom wall of the channel for stationary case – V-Shape rib $U_{in}=12.5\text{m/s}$ (a) $p/e=7$, (b) $p/e=10$, (c) $p/e=12$	129
Figure 6-34: Nusselt distribution at the bottom wall of the channel for stationary channel with V-Shape rib case $U_{in}=12.5\text{m/s}$ (a) $p/e=7$, (b) $p/e=10$, (c) $p/e=12$	130
Figure 6-35: Temperature distribution at the bottom wall of the channel with V-Shape rib for rotational case $U_{in}=12.5\text{m/s}$, V-Shape (a) $p/e=7$, (b) $p/e=10$, (c) $p/e=12$	132
Figure 6-36: Nusselt distribution at the bottom wall of the channel with V-Shape rib for Rotational case $U_{in}=12.5\text{m/s}$ (a) $p/e=7$, (b) $p/e=10$, (c) $p/e=12$	133
Figure 6-37: inlet/outlet for Channel with V-shape rib design two configuration $P/e=10$	133
Figure 6-38: Temperature distribution comparison for various V-rib configuration, Stationary case with $Re=35000$, (a) Initial Design, (b) V-Shape Design 2	134
Figure 6-39: Nusselt distribution comparison for various V-rib configuration, Stationary case with $Re=35000$, (a) Initial Design, (b) V-Shape Design 2	135
Figure 6-40: Temperature distribution comparison for various V-rib configuration, the rotational case with $Re=35000$, (a) Initial Design, (b) V-Shape Design 2	136
Figure 6-41: Nusselt distribution comparison for various V-rib configuration, the rotational case with $Re=35000$, (a) Initial Design, (b) V-Shape Design 2	137

Figure 6-42: Nusselt Comparison of Stationary Cases for various rib configurations and P/e ratios	138
Figure 6-43: Pressure Drop Comparison for various rib configuration and P/e ratios	139
Figure 6-44: Performance Comparison for various rib configurations and P/e ratios.....	140
Figure 6-45: Nusselt Comparison Rotational Cases for various rib configurations and P/e ratios	141
Figure 6-46: Pressure Drop Comparison for various rib configurations and P/e ratios.....	141
Figure 6-47: Performance Comparison for various rib configuration sand P/e ratios.....	142
Figure 7-1: Various guide vane designs: (a) V1 (one guide vane after the turn;(b) V2 (two guide vanes after the turn) (c)V3 (Semi circle guide vane),(d) V4(three guide vanes after the turn) (e) V5(three guide vanes before the bend, (f)V6 one guide vane before the bend(g) V7(two guide vanes before the bend, (h) V8 one guide vane with longer length before the turn	146
Figure 7-2: Nusselt number comparison in the stationary case for Re=6000 and Re=35000	148
Figure 7-3: Normalized friction factor comparison for stationary cases with Reynolds 6000 and 35000.....	149
Figure 7-4: Thermal performance comparison for stationary cases for Re=6000 and Re=35000.....	150
Figure 7-5:Nusselt Number comparison for various guide vane in stationary and rotational condition	151
Figure 7-6: Friction factor comparison for smooth wall channel and turning guide vane, stationary and rotational cases	151
Figure 7-7: Thermal performance comparison for the smooth wall channel and turning guide vane, stationary and rotational cases	152
Figure 7-8: Various guide vane designs: (a) VR1 (one guide vane after the turn;(b) VR2 (two guide vanes before the turn;(c) VR4 (three guide vanes after the turn)(d) VR8 (one guide vane with longer length before the turn)	154
Figure 7-9: Nusselt number distribution for the stationary cases for Re=6000 (a) VR1(b) VR2 (c) VR4 (d) VR8	155
Figure 7-10: Heat Transfer augmentation along the channel, with different guide vane designs for Re=6000	156
Figure 7-11: Channel Nusselt number for stationary case in various Reynolds number.....	157
Figure 7-12: Heat Transfer augmentation along the channel, with different guide vane designs for RO=0.75	158
Figure 7-13: Friction factor ratio comparison in stationary and rotation cases for different guide vane designs	159
Figure 7-14: Thermal Performance comparison in stationery and rotation cases for different guide vane designs	160
Figure 8-1: Fluid and solid interface schematic	162
Figure 8-2: Temperature distribution on the solid wall of a smooth wall Channel (a) Stationary with Re=35000, (b) Rotation with Re=35000 and 300 rpm	165
Figure 8-3: Bottom wall temperature distribution for the smooth wall channel (a) Stationary (b) Rotation	166
Figure 8-4: Temperature distribution on the solid wall of a 45-deg ribbed wall Channel (a) Stationary with Re=35000, (b) Rotation with Re=35000 and 300 rpm	168
Figure 8-5: Temperature distribution for top and the bottom wall of the 45-deg ribbed wall channel (a) Stationary (b) Rotation.....	169

LIST OF TABLES

Table 2-1: Main Failure Mechanism of the Blade Failure[3]	5
Table 4-1: stress and strain concentrations in the model	47
Table 4-2: Location of thermocouples on the bottom of the channel	51
Table 5-1 : Stationary Cases Parameter Used for Computation and Experiments	63
Table 5-2 : Rotational Cases Parameter Used for Computations and Experiments	63
Table 5-3: Summary of Stationary Cases with variable heat flux	77
Table 5-4: Summary of rotation cases	83
Table 7-1: Dimensions of the channel with 45-deg parallel rib	145
Table 7-2: Dimensions of the channel with 45-deg parallel rib	153

LIST OF NOMENCLATURE

A	= Heater Surface Area (m^2)
AR	= Channel Aspect ratio
Bo	= Buoyancy Number ($(\frac{\Delta\rho}{\rho}) \cdot Ro^{0.2} \cdot \frac{x_i}{D_h}$)
c_p	= Specific heat at constant pressure
D_h	= hydraulic Diameter (m)
f	= Friction Factor ($f = (\frac{D_h}{2L}) (\frac{\Delta p}{\rho U_m^2})$)
f_0	= Friction Factor for fully developed Flow
e	= Rib Height (m)
k	= Thermal conductivity [$W/m.K$]
H	= passage Height(m)
h	= heat transfer coefficient [W/m^2K]
I	= Current (Amp)
k	= Heat Conduction Coefficient of Working Fluid
\dot{m}	= Mass flow rate (kg/sec)
L	= Passage Length (m)
Nu	= Nusselt Number ($\frac{hD_h}{k}$)
Nu_0	= local Nusselt Number ($0.023 \cdot Re^{0.8} \cdot Pr^{0.4}$)
P	= Rib to Rib Pitch(m)
R	= Resistance (Ohms)
Re	= Reynolds Number ($\frac{\rho U D_h}{\mu}$)
Ro	= Rotation Number ($\frac{\Omega D_h}{U}$)
T_{ij}	= Surface Forces
T_s	= Surface temperature
T_o	= Air temperature at the inlet [K]
T_w	= Wall temperature [K]

Pr	= Prandtl Number (=0.71)
U	= inlet velocity [m/s]
u_{τ}	= Friction Velocity
q''	= Convective Heat Flux (W/m^2), ($\frac{RI^2}{A}$)
W	= passage Width(m)
x	= actual distance from axis of rotation [m]
y^+	= non-dimensional distance of the first layer of cells

Greek

ρ	= Density [kg/m^3]
μ	= Dynamic viscosity [Pa.s]
Ω	= Rotational Speed [rad/sec]
η'_{th}	= Thermal Performance
λ	= Taylor Micro Scale
η'	= Kolmogorov Length Scale

ACKNOWLEDGEMENTS

I would like to express my gratitude toward my advisor Professor Ryoichi Amano, for his support, guidance in my four years working in his group. He provided detailed help and supervision in all aspects of the research is presented here. He always encouraged me to actively be involved in academic and professional events to advance my scholarly research and build professional confidence. He gave me the platform to practice analytical thinking and develop leadership skills. I would like to sincerely thank my doctoral committee, Professor Deyang Qu, Professor John Reisel, Professor Robert Cuzner, Doctor Istvan Lauko, Professor David Yu, for their insights in my research.

I had the opportunity to work with brilliant undergraduate students during my graduate school years at UWM. Nicholas DiPasquale did a fantastic job of helping me building the experimental setup. Joseph Halmo worked with me to collect the experimental data. I wish them all the best in their studies and future career.

I should thank Doctor Randy Jackson, Doctor Saman Beyhaghi, and Doctor Ping Dong for their mentorship and invaluable insights and suggestions for my research. Finally, I thank all my friends and family, including my mom Shahin, my dearest uncle Rez, and my brother Shahin for their endless support and love.

1 Introduction

1.1 Gas Turbine Efficiency

Power generation and aeronautical industries are always subject to increase the power generation capacity. For a gas turbine cycle, the working principle is based on the Brayton thermodynamic cycle, presented in Figure 1-1. In an ideal cycle, compression of fresh air (a-b) and expansion of burnt hot gases (c-d) are assumed to be isentropic. In contrast, the combustion of the fuel-air mixture (b-c) and the gas exhaust to the atmosphere (d-a) are considered isobaric processes.

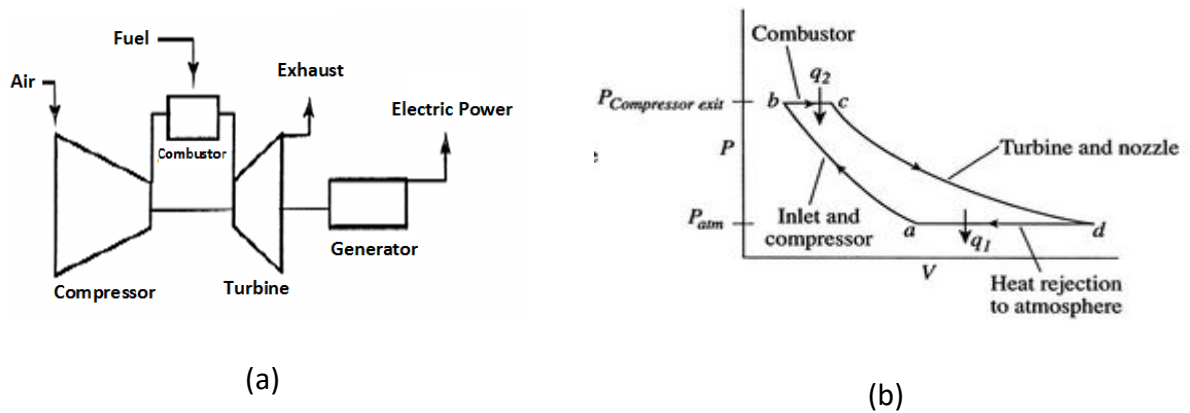


Figure 1-1:(a) Schematic of an ideal Bryton cycle,(b) Thermodynamic states of Bryton Cycle[1]

In the Bryton cycle, increasing the power generation means improving the thermal efficiency of the gas turbine. To satisfy these requirements, increasing the turbine's inlet temperature is one of the most effective ways. The ideal Brayton cycle efficiency equation can be shown in Equation 1-1.

$$\eta_{thermal} = 1 - \frac{T_a}{T_b} \quad \text{Equation 1-1}$$

Also, maximum power in the Brayton cycle can be calculated from Equation 1-2.

$$Power = \dot{m}c_p T_a \left[\frac{T_c}{T_a} - 2 \sqrt{\frac{T_c}{T_a}} + 1 \right] \quad \text{Equation 1-2}$$

Hence, in real applications such as a gas turbine engine, it is necessary to understand the effect of increasing temperature and thermal stresses on the turbine component.

1.2 Objective

Figure 1-2 illustrates the specific core power for various engines as a function of the inlet temperature of the inlet flow and increasing temperature presented by Koffi and Meese. As was shown, there is a direct relationship between increasing the specific core power and increasing the inlet temperature.

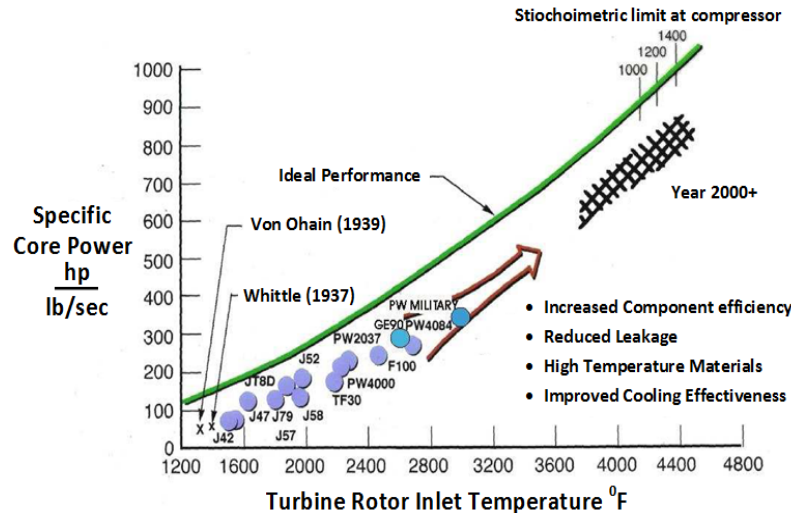


Figure 1-2: Specific Core Power with Turbine Rotor inlet temperature[2]

Increasing the inlet temperature applies a significant amount of thermal stresses on the blades. Blade failure can account for the severe effects of these thermal stresses. Therefore, various cooling technologies have been implemented on gas turbine blades to prevent any

thermal failures. Among these technologies, the internal cooling system is one of the most effective approaches to reduce blade temperature. In this technique, many internal channels drilled or molded into the vanes and blades. Utilizing these channels in the blade removes heat from more extensive areas of the blades.

1.3 Methodology

In the presented study, the focus was on implementing a heat transfer investigation for a flow passing the internal cooling channel. Both stationary and rotational motion were studied. For the rotational motion, the primary attention in this study would be on the effect of Reynolds number, density ratio, and high rotation number (up to 1.5) on the heat transfer coefficient. The methodology used in this thesis is defined as follows:

- Introducing various turbulence models used to solve the Navir-Stokes equations and near-wall treatment to resolve the near-wall viscous region
- Using commercial Computational Fluid Dynamics (CFD) software to solve the heat transfer phenomena in the channel under the study
- Study the effect of high rotation number and Reynolds number on the flow field in a square channel with a smooth channel and various rib configurations
- Introducing turning guide vane and their effect on increasing the turbulence and heat transfer
- Result verification using the same size experimental set up.

2 Chapter 2: Turbine Blade Cooling: State of the Art and Technology

2.1 Turbine Cooling Requirement

The need for achieving higher thermal efficiency in the gas turbine has promoted a great effort in advancing better and efficient techniques for cooling the turbine blades. Advanced gas turbines operating temperature can be as high as 3000K. This high temperature at the rotor blade can exceed the melting temperature of super alloyed used in turbines. Thus, to prevent any blade thermal failure, it is necessary to implement novel cooling systems that can remove a significant amount of heat from the gas turbine blades. Among all the blade cooling systems, optimizing the internal cooling of the gas turbine blade becomes very crucial to have high thermal performance. As the operating temperature in the gas turbine increases, the internal cooling channel, and its system becomes more complicated. Furthermore, due to the gas turbine working condition, designing an efficient cooling system involving many physical and geometrical aspects. defines some of the main challenges in developing an internal cooling system.

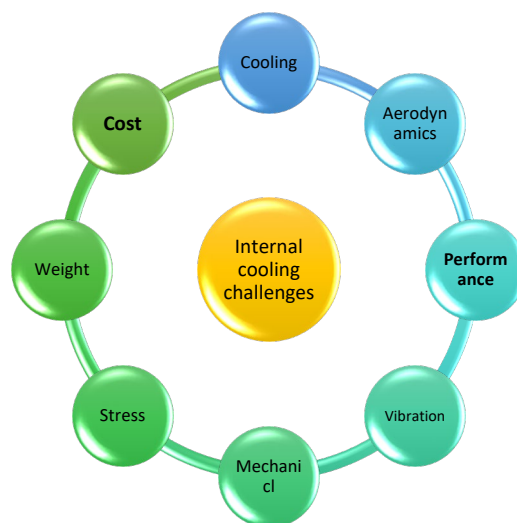


Figure 2-1: Design challenges in internal Cooling

A study done at the Von Karman Institute, describes different types of failure mechanism happen in the blade failure. Table 2-1 shows only the primary failure mechanism of blade failure. Here two common and vital factors that enhance the blade failure were discussed.

- High temperature

It is one of the major reasons for blade failure; a higher temperature gradient brings the damaging effect on service life. As is shown in Table 2-1, a large temperature gradient causes corrosion and creep on the blade.

- High Stress

Rotational motion induces centrifugal forces and fluid forces, which can cause the fracture, yielding, and sometimes creep failure. Gas turbine operation condition is involving a combination of vibration and high temperature. High vibration usually causes fatigue, which is one of the common types of failure.

Table 2-1: Main Failure Mechanism of the Blade Failure[3]

Mechanism	Temperature
Corrosion	15°C
Creep	15°C
Low Cycle Fatigue	30°C
High cycle Fatigue (Vibration)	Independent of temperature change

2.2 Cooling Technology

Gas turbine blades are cooled by using a combination of traditional cooling concepts and novel cooling technologies. The objective of the blade cooling is to maximize the heat removal from the blade surface and increase the thermal efficiency of the gas turbines.

Cooling technologies can be classified into many different groups. It can be impingement cooling, which mainly focuses on cooling the inner surface of the leading edge. The internal cooling removes heat from the internal blade surface through convective heat transfer. The other cooling group is film cooling or external cooling. In this cooling approach, the blade surface is protected from the hot gases using a film of cooling air. In this chapter, a brief description of these methods has been revealed.

Figure 2-2 describes the modern cooling technique, which contains three internal cooling zones in a turbine blade. It can be seen from the figure, the blade is hollow, which let the cooling air pass through in the channel. The main internal channel consists of serpentine cooling passages, which are ribbed roughened. The leading edge is cooled by an impinging coolant on its inner surface. Also, the trailing edge is provided with pin-shaped fins; the outcome of having this pin is the increase in the heat transfer. After passing the trailing edge and the tips, a portion of cooling air leaves the internal of the blade. This amount of airflow acts like a thin, coolant film on the van's external surface, known as film cooling. The thick film serves as a cold insulating blanket along the outer surface of the turbine blade. All these efforts make it possible to have a longer lifetime for the blade and to be able to operate in higher turbine operating temperatures [4].

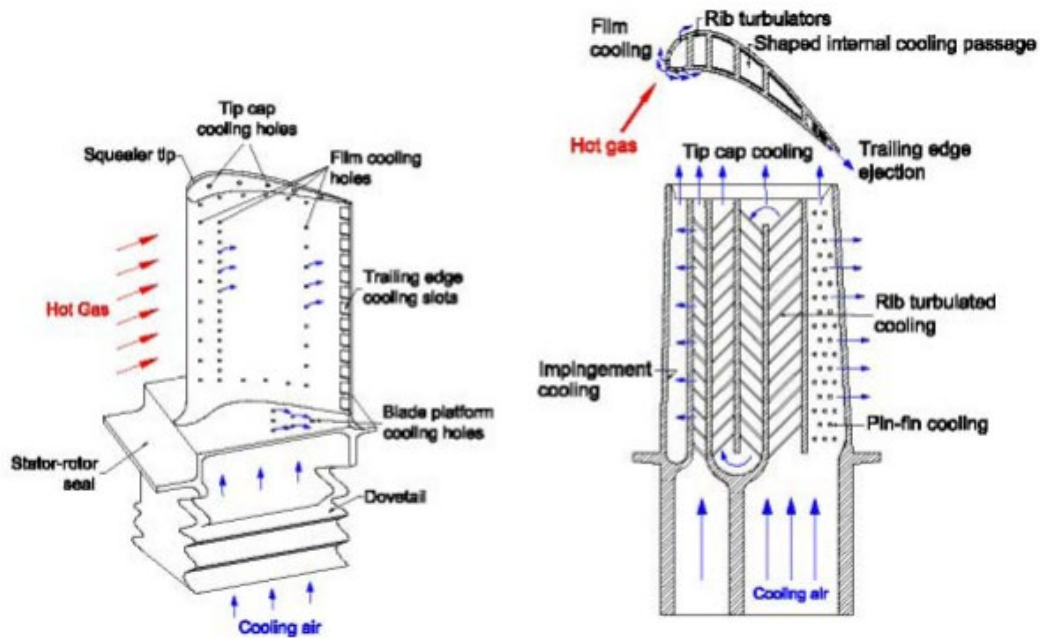


Figure 2-2: Typical airfoil cooling system for the high-pressure turbine blade[5]

The objective of these technologies is to obtain high overall cooling effectiveness with the lowest losses on the thermodynamic performance cycle.

For this thesis application, the model discussed here has the geometry shown in Figure 2-3. This type of construction is the most common one. The starting point is the root of the blade that attached to the body of the turbine; this part has an inlet channel that leads the cooling air to the blade. This cooling fluid is the extracted air from the compressor of the engine. The air goes through many channels in the blade and exhausts from the main turbine vein. Based on the cooling air that interacts with external or internal faces of the blade, there are two types of cooling systems.

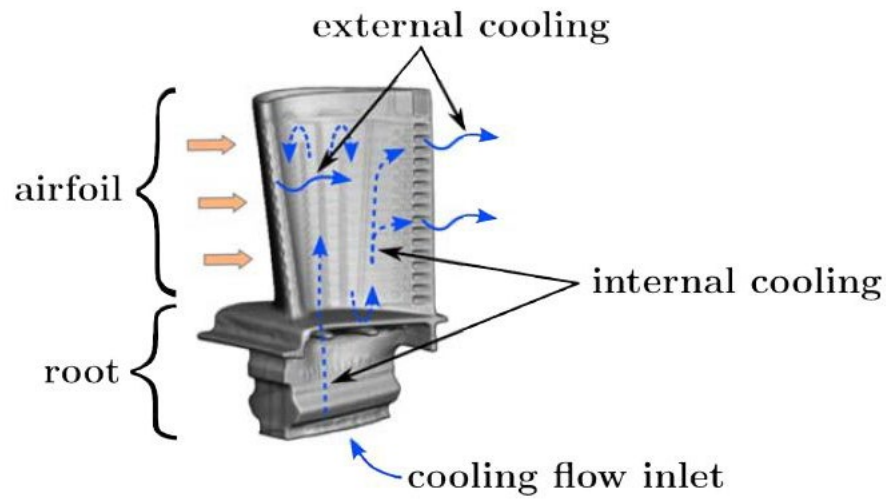


Figure 2-3: Blade structure and different cooling system [5]

2.2.1 External Cooling

The objective of external cooling to have better protection of the blade surface faces from high-temperature gases that come from the combustion[6]. In External cooling, two techniques could be used[7]. Film cooling happens in the secondary fluid, which can be the coolant or injected fluid at single or many discrete locations along the surface, which exposed to a high temperature. The reason is to protect the surface in both immediate regions of injection and the downstream region. In the film cooling technology, cold air injected from the internal cooling system through small holes, which are located on the airfoil part of the blade. The external cooling technique depends on many parameters such as flow properties, the injection geometry walls properties, and many other parameters. Han et al. [6] discussed the effects of these parameters in detail.

The film cooling reduces the external heat load to the airfoil by lowering the driving temperature from the local gas temperature. Figure 2-4 shows an overview of the film cooling

mechanism. The film cooling effectiveness is a function of injection geometry on the airfoil, including the hole diameter, hole spacing, effectiveness slot height parameter, density ratio, and the film coverage.

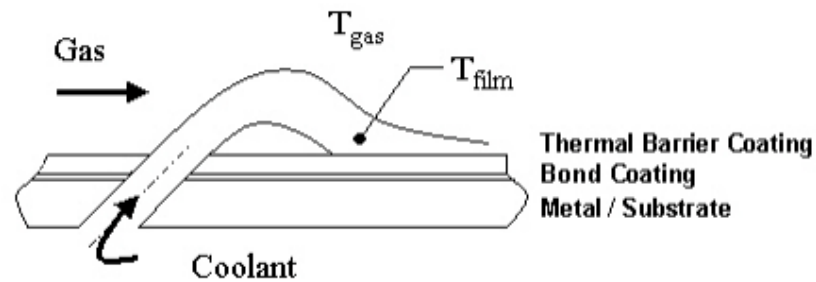


Figure 2-4: Film cooling mechanism [5]

2.2.2 Internal Cooling System

In the internal cooling of the gas turbine blade, the heat is removed by a variety of convection and impingement cooling configuration. The main mechanism of this type of internal cooling is that high-velocity air flows and hits the inner surface of the turbine vanes and blades. There have been many studies in internal cooling based on the traditional technologies in this field. Figure 2-5 describes the developments done in this field from 1950. Here the techniques for cooling both blades and vanes are going to be discussed.

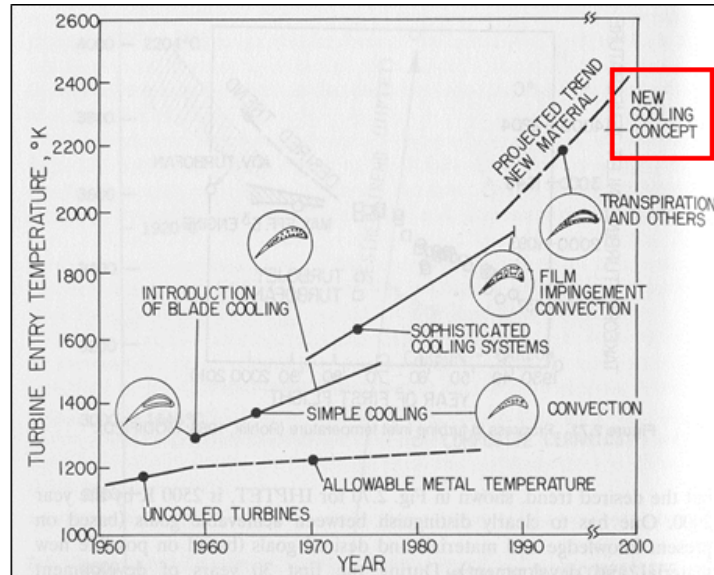


Figure 2-5: Development of cooling technology in gas turbine blade [8]

In the internal cooling technique, the objective is to decrease the blade surface temperature by increasing the heat transfer between the blade surface and the coolant. The coolant flow is the extracted air from the compressor of the engine. Since this extraction incurs a penalty on the thermal efficiency and power output of the engine, it is essential to understand and optimize the cooling technology for a given turbine blade geometry under engine operating conditions. Gas turbine cooling technology is sophisticated and varies between engine manufacturers. A schematic of a turbine blade cooling system is shown in Figure 2-6.

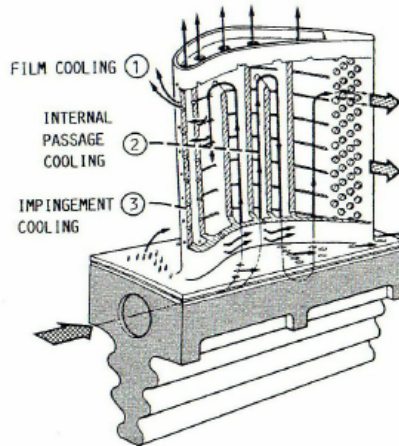


Figure 2-6: Example of a turbine blade internal cooling system [9]

The internal cooling technique is widely used for the main blade body and the vane section. In this chapter, a brief description of each cooling technology is going to be discussed.

2.2.2.1 Internal cooling of turbine vanes

Impingement and pin fin cooling are the technologies mostly used for internal cooling of the turbine vane. Figure 2-7 illustrates vane geometry. As can be seen, coolant air from the compressor enters the hollow parts of the vane and is distributed between internal jet impingement and pin fin cooling section on the vane.

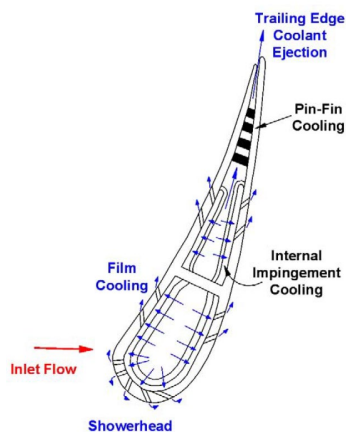


Figure 2-7: Schematic of a Turbine Vane Cross-Section with Impingement and Trailing Edge Pin-Fin Cooling[10]

2.2.2.1.1 Impingement Cooling

Jet impingement is one of the most effective cooling technologies which remove a significant portion of heat from the blade van wall. Thus, the jet impingement method is mostly used in the blade leading edge, where the thermal stresses are high.

The other reason that makes leading walls suitable for this type of cooling technology is that wall thickness in this area is relatively high, which impinging can remove more amount of heat. Many factors need to be considered in the impingement cooling techniques such as jet hole size, holes distribution, cooling channel cross-section, and target surface shape for cooling channel heat transfer.

- Jet Impingement from Multiple Jets

There have been many efforts to increase the heat transfer from the vane wall. Metzger et al.[11] shown that there is a considerable difference between the cooling performance of multiple jets from single jet striking for a target surface. They showed for various jets; the Nusselt number is strongly dependent on Reynolds number while there is no significant dependence on jet-to target plate spacing. Florschuetz et al.[12] and Koopman et al.[13] studied the impingement cooling technology. Their results show one jet can alter the performance of another jet. Based on the experimental study that Kercher et al.[14] and Florschuetz et al.[15] have done; they developed a correlation to calculate the heat transfer enhancement from an array of impinging jets.

- Jet Impingement on a Curved Surface

As shown in Figure 2-9, near the leading edge of the airfoil curvature, the target surface creates different cross-flow behavior. Chupp et al. [16] done a study on the leading edge; they

concluded Nusselt number ratio increases as the curvature of the target plate increases. Bunker et al. [17] researched the comparison of the Nusslet number in Sharper nose radius and smooth-nosed radius. Their result shows in sharper nose radius yielded more uniform Nusselt Number distribution. Furthermore, if the bleed from the pressure and suction are equal, there would be a drastic decrease in the Nusselt number.

2.2.2.1.2 Pin Fin Cooling

As has been shown due to the manufacturing constraint in the very narrow edge of the blade, pin fin cooling technology is used to enhance the heat transfer from the blade wall in this region. Many factors must be considered in studying the pin fin cooling. The pin-fin array, spacing, shape, and size affect the heat transfer distribution in the channel.

There have been many studies on the pin fin configuration. Generally, inline and staggered array arrangements of pin fin structure widely are used. Metzger et al.[18] studied the staggered array configuration for circular pins with 1.5 to 5 pin diameter spacing in a rectangular channel. They concluded a closer space array has higher heat transfer. Chyu et al.[19] found the heat transfer coefficient is higher for both array configurations. Metzger et al.[18] and VanFossen [20] implemented an experimental study on the Nusselt number prediction for different pin fin arrays.

2.2.2.1.3 Dimple Cooling

Dimple cooling usually considers as a back-up for Pin-Fin cooling systems. Many factors affect the performance of this cooling technique, such as dimple size, dimple depth, distribution shape. There has been a significant amount of studies on this cooling technology. Many of them agree that there is no dependence on Reynolds number and channel aspect ratio [21]–[25]

2.2.2.2 Internal Cooling of the Blade

Due to the increasing demand for more power generation in power in industrial and aeronautical sectors, gas turbine inlet temperature increased significantly. Thus a constant improvement in cooling technology is needed to avoid any blade thermal failure. As mentioned earlier, the internal cooling technique is one of the most effective approaches to reduce the blade temperature. The advantage of this cooling technology is that it can remove heat from a large blade surface area. The internal cooling development includes include the introduction of ribs in the mid-span of the blade, allowing cooling to impinge at the leading edge and placing the pin at the trailing edge. There have been many studies that focus on the effects of each of these factors in internal cooling. In the current work, the primary focus is on the impact of various rib turbulator configuration on heat transfer enhancement.

2.2.2.2.1 Rib Turbulator Cooling

Secondary flow usually increases the heat transfer rate. To improve the secondary flow, using the rib turbulator in blade design is necessary. Ribs induce secondary flow, which increases turbulence mixing. Rib turbulence promoters, which usually cast in the internal cooling passages. Rib installation often depends on the blade size, and gas turbine application. These ribs can be installed on the pressure and suction walls, or only one side of the wall in the internal cooling passage, to provide the same amount of pressure to match the external load.

Han et al.[6] devoted many studies stationary channels with and without rib turbulators. In their studies, various channel geometries and rib turbulator configurations were investigated. They found the heat transfer enhancement compare with the smooth walls channel was significant. In installing the ribs, many considerations need to be taken into account.

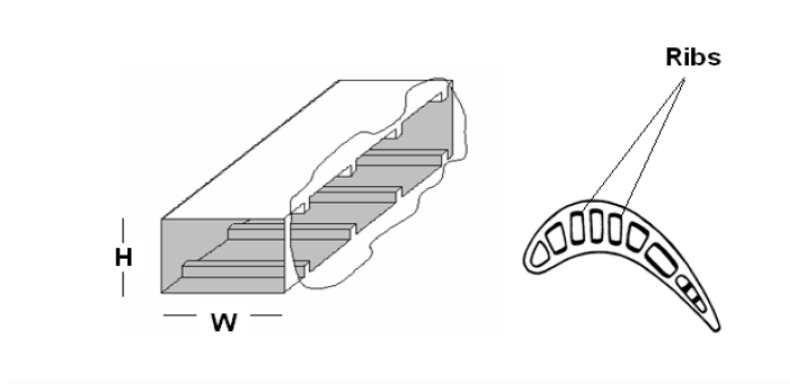


Figure 2-8: A ribbed channel configuration [6]

Figure 2-9 describes the flow separation and reattachment due to the presence of ribs. The boundary layer is distributed, and the turbulence of the flow increases due to flow separation and reattachment. These two phenomena result in a higher mixing ratio in the fluid elements near the wall with the cooler ones in the middle of the stream. When this happens, more heat will remove from the hot blade wall. However, to achieve the highest thermal performance, it is necessary to find an optimized rib design and spacing for different channels. Thus, the effect of rib pitch-to-rib height ratio (P/e), rib height-to-channel hydraulic diameter ratio (e/D_h), and rib arrangement along the channel on the heat transfer performance were mainly investigated in previous researches [22], [26].

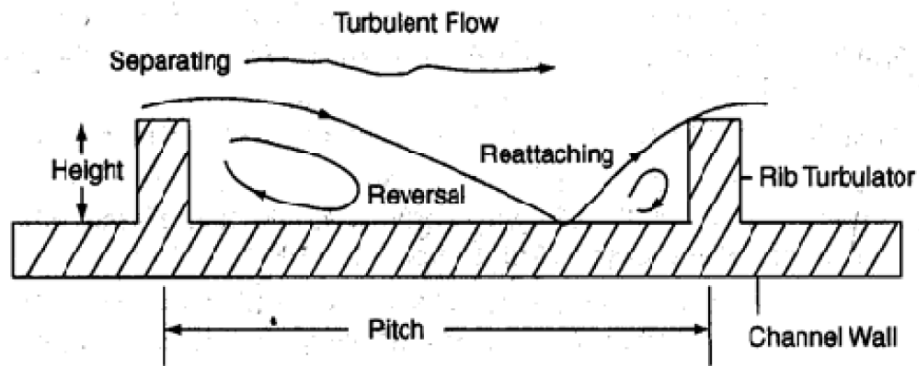


Figure 2-9: Flow separation and reattachment around ribs[27]

Rib spacing is one of the most critical aspects of installing ribs on the internal cooling. When the mainstream flow reaches a rib, flow separation from the surface occurs. After passing the rib, in the distance between the ribs, which is called rib pitch, flow reattaches. It is essential to optimize the distance between the ribs since placing them very close together possibly jeopardize this reattachment zone where high heat transfer is experienced due to mainstream flow impingement. Also, setting the ribs at a distance more than optimum distance causes in growing in a boundary layer, which reduces heat transfer.

Han et al. [6] dedicated many years to optimize the thermal performance of the internal cooling channel. They investigated the physical and geometrical rib parameter effects on the flow passing through these channels. Their early studies were mainly on the stationary channels and the comparison of the heat transfer ratio results between the smooth and ribbed wall channel with various size and geometry. Their results showed that the heat transfer ratio in the ribbed wall channel had a significant enhancement compared to the smooth wall channels. To find the optimum rib pitch-to-rib height ratio, Han et al. [26], [28], [29] investigated a wide range of rib pitch-to-rib height ratios on channels with different aspect ratios. His results for

square cross-section channels showed that the optimum rib pitch-to-rib height (p/e) ratio to obtain the highest heat transfer ratio was 10. Taslim and Wadsworth [30] studied a channel with an aspect ratio of 1:1, with a wider range of P/e . Furthermore, Liu et al.[31] surveyed a rotational ribbed wall channel with an aspect ratio of 1:2, and they found another optimum P/e ratio. They observed that as the P/e ratio decreased, there was a significant increase in the heat transfer ratio. They also investigated the pressure distribution and discussed it by tracking the friction factor changes for the ribbed wall channel. They found that by decreasing the P/e ratio, the friction factor also reduced. The other important parameter needed to be considered in studying the rib effects is the amount of the rib blockage that is usually discussed as the rib height-to-hydraulic diameter (e/D_h) effect. Han[32] studied effect of different e/D_h ratios on a square cross section channels. The results showed that in a constant Reynolds number as the e/D_h ratio increased, the Nusselt number increased. Taslim and Spring [33] also, investigated the relation between e/D_h and P/e ratios and their effect on the Nusselt number for a channel with 1:2 aspect ratio. They concluded that as the e/D_h ratio increased, changing the P/e ratio didn't have a significant influence on the Nusselt number.

The cooling passages are not limited to a real straight channel. A common type of these passages is the ones consist of the first pass with coolant flowing radially outward from the engine's hub to the center in the second pass. Another turn would connect the second pass to the third pass with radially outward flow. Coolant flow in these turns is very complicated, and the heat transfer is dependent on both the channel and turn geometry. Therefore, it is crucial to investigate the turning effect on the cooling channel performance.

Rotation is another factor which affects the flow behavior in the cooling channel. Rotation induced the secondary flow patterns, which results in an uneven heat transfer ratio at leading, and trailing walls. Coriolis forces generated by rotation motion can have opposite effects on the coolant heat transfer performance in an inward flow and channels with radially outward flow. Besides, there are many Geometrical factors which affect on the heat transfer in the cooling passages, such as channel geometry, channel aspect ratio, surface geometry. Thus, it is essential to consider the combined effects of rotation, turn, channel geometry, and flow condition on the heat transfer in the internal cooling passages. Many researchers have studied these factors' effects on the heat transfer coefficient and channel cooling performance. An overview of previous work is presented in section 2.3.

2.3 Literature survey

Studying the internal cooling blades, starting with the stationary and one pass models. In these studies, surface roughness effect and channel aspect ratio were the primary focus. Metzger and Sahm[34], were the first group who started studying heat transfer in the multi-pass flow channels. Their main focus was investigating the forced convection in a two-pass smooth rectangular channel by changing the divider location and the gap at the 180-deg turn. Later, Fan and Metzger[35] continue previous work[34], and this time they changed the channel width. Their results showed increasing the channel aspect ratio increases overall heat transfer. Han et al.[36], studied the local heat and mass transfer distribution for a stationary two-pass ribbed channel. Han and Zhang[37] investigated the effect of rib-angled orientation on the local heat and mass transfer distribution in a stationary three-pass rib-roughened channel. They found that rib angle, rib orientation, and the sharp 180-deg turn have a significant effect on the

local heat transfer distributions. In the other study, Park et al.[38] studied the effects of the rib angle on five different aspect ratios for a rectangular channel in a stationary case. They concluded that the heat transfer enhancement for small aspect ratio ducts $AR=1:1$, $1:2$, and $1:4$ happened in 60-deg, 45-deg, and 30-deg angled ribs, respectively. While in higher aspect ratio ducts, $AR=2:1$ and $AR=4:1$, the augmentation order is 90-deg or 60-deg, 45-deg, and 30-deg angled ribs.

Ekkad and Han[39], performed a study on heat transfer distribution in different rib arrangements in a stationary square channel with a 180-deg turn using liquid crystal technology. For this study, they used different rib geometries. Results from their survey showed the channel with a V-shaped rib has a higher heat transfer coefficient in the first passage. While in the turn and the second channel, the 60-deg parallel ribs produced higher heat transfer enhancement.

In all of the above studies for non-rotating channels, it has been observed angled ribs have better heat transfer enhancement than 90-deg ribs, and the V-shaped ribs have better heat transfer than angled ribs.

Wagner et al.[40], [41] conducted a detailed experimental study to determine the rotational effect on the local heat transfer for a multi-pass square channel with smooth walls. They showed in the first passage; rotation caused a thinner layer on the trailing surface and thicker boundary layer on the leading surface. These changes in the boundary layer thickness increase the heat transfer on the trailing wall and decreasing on the leading wall. In the second pass, the Nusselt number ratios in the leading wall were higher than the Nusselt number ratio on the trailing wall, which can be counted as the effect of the Coriolis force direction.

Taslim et al.[42], [43] investigated the heat transfer distribution on a square and rectangular one pass channel. The channel under the study was a ribbed roughened channel. Their result showed in the larger aspect ratio; the rotational effect is more significant than smaller aspect ratios.

One of the critical parameters that need to be considered in internal cooling is the heating boundary condition. Han et al.[44] studied on the uneven wall temperature effect on local heat transfer in a rotating two-pass square channel with a smooth wall. Their result showed that uneven wall temperature on leading and trailing walls changed the density ratio of the flow, which causes a change in the buoyancy forces. Zhang et al.[45], investigated on the heating condition effects in the two-pass square duct with angled rib turbulators. They showed the same impact as Han et al.[44] concluded. Johnson et al.[46] [47], done an experimental study on a four-pass square channel with rib roughened walls to investigate the effect of Coriolis and Buoyancy forces on the heat transfer. The experimental study was utilized for a rotational channel in both clockwise and counterclockwise to ensure both reward and forward flow condition can be investigated. Their result showed for both the rotation and channel orientation, change the leading and trailing wall heat transfer coefficients.

Parsons et al. [48][49] investigated the combined effect of channel orientation and wall heating conditions on the local heat transfer coefficients. The channel under their study was a two-pass square ribbed wall channel. They reported the effect of Coriolis forces and Cross-stream flow were reduced as the channel orientation changed from normal to $\beta=90$ -deg to an angled orientation of $\beta=135$ -deg. Also, Dutta and Han [50] did a study on the effect of channel orientation on the heat transfer coefficient for both smooth and ribbed two-pass channel.

Deng et al.[51] performed an experimental study on a smooth square U-duct and investigated the heat transfer at high rotation numbers. They showed the correlation between rotation number and dimensionless location on the heat transfer coefficient. Their results showed in the leading and trailing wall at high rotation numbers, the heat transfer coefficient on the trailing wall is more elevated than the leading wall. Wagner et al. [40] worked on heat transfer differences in a rotating four-pass smooth wall. They found rotation induces Coriolis forces, which have different effects on trailing and leading walls. In the trailing wall, it improves the heat transfer, while it has a negative impact on heat transfer on the leading wall in the first passage. In the second passage, this effect is reversed, and heat transfer enhancement is significant in the leading wall. Amano and Beyhaghi [52] showed a constant Reynolds number, increasing the rotation number, boosts the local and average Nusselt number.

There are also many experimental studies on the effect of rotation on the heat transfer ratio. Li et al. [53] have done a survey on the rotating smooth U-duct, with uneven wall temperature, they found a critical rotation number for the first passage and also, developed a correlation for minimum Nusselt number ratio as a function of rotation number. Burberi et al.[54] have done a numerical and experimental study on the rotational effects on the heat transfer coefficient. Their results showed rotation has effects on the bending region and causes very non-uniform temperature patterns.

The effect of density ratio cannot be ignored since it has a significant impact on the heat transfer on different rotation number. Johnson et al.[46] studied the heat transfer in a four-duct system. Their result showed in a constant rotation number, increasing the density ratio increases the heat transfer rate in the inlet of the first passage. In the second passage, on the

trailing wall, the heat transfer increases due to the low pressure. Wagner et al. [40] also showed by increasing the density ratio; the Nusselt number ratio increased at the pressure and suction sides of the walls.

The relationship between the Nusselt number and Reynolds number, in a duct with constant temperatures boundaries, can be found by the Dittus-Boelter equation [55]. This relationship is usually recommended to be used when there is a small temperature difference between the wall and coolant. Sieder and Tate [56] introduced another correlation which is valid for Reynolds numbers more than 10,000 and a wide range of Prandtl number. In their correlation, viscosity variation has been considered. Thus, a more extensive range of temperature differences between the wall and coolant fluid can be used. The other relationship for the Nusselt number and Reynolds Number is introduced by Colburn[57]. This correlation is close to the Dittus-Boelter equation; however, it considers all the properties at the arithmetic mean of Bulk and wall surface temperature. Furthermore, the relationship between Reynolds number and Nusselt number for a fully developed flow of air in a square duct with smooth walls and constant wall temperature can be defined by $Nu_{\infty} = 0.0176Re^{0.8}$ [46]. Yang and Fuchs [58] performed a numerical study for incompressible flow in a rotating duct. They observed in the low Reynolds number, a pair of secondary flow vortices were developing regardless of the rotation number.

The body forces due to rotation are Coriolis and Centrifuge forces. Sewall et al.[59] carried out a numerical study on developing flow region in a rotating gas turbine blade, by considering the Coriolis and Centrifuge forces. They showed that in the same rotation number, heat transfer on the trailing wall increases by increasing the buoyancy number; however, on the leading wall, a drop in heat transfer in a Buoyancy range of 0-0.25 has been observed. Li et al. [60] did an

experimental study on the buoyancy effect on heat transfer in a rotating two-pass square channel. They found in the same rotational number, higher wall temperature ratio, which corresponds to higher buoyancy number increases heat transfer on both passages. They also showed higher buoyancy number in higher rotation number enhance the heat transfer. Huh et al. [61] found that regional averaged Nusselt number increases with buoyancy number on the leading wall and decreases with buoyancy number on the trailing wall. Also, in another study, for a heated condition, Huh et al.[62] concluded the same results for increasing and decreasing Nusselt number on leading and trailing walls, respectively.

Dutta et al.[63] done an experimental study on the effect of the channel orientation on the heat transfer coefficient. The channel under this study was a two-pass ribbed triangular channel. They used two orientation respect to the axis of rotation. Murata et al.[64] excluded the turning effect by reversing the flow direction to obtain inward and outward flow in a one-pass square duct with the roughened wall. From their results, the 60-deg rib has better heat transfer improvement than a 90-deg rib. They also concluded, there were no significant changes in the average Nusselt number by counting the effect of radial flow direction. There was another liquid crystal technique measurement performed by Liou et al. [65]. They used a rotating two-pass square duct with standard in-line ribs. Their results have a good agreement with the outcome of Parson et al. [48] study.

Many studies were carried out on the effect of different rib arrangements on the heat transfer enhancement. Al-Hadharmi and Han[66] did a study for five different rib configurations for a rotating two-pass square channel. Their result showed the parallel rib orientation provides

a higher Nusselt number ratio compare with crossed rib orientation. This enhancement is more significant in the higher rotation number than lower rotation numbers.

Cho et al. [67] studied the effect of rotation in the two-pass rectangular duct by using a mass transfer method. The channel aspect ratio was 1:2, and the angle of the ribs was 70-deg. Their results show, due to the 180-deg turn, the rotational effect in the second channel decreased.

Agarwal et al. [68] did an experimental study on a channel with an aspect ratio of 1:4 by using the same method as Cho et al.[67] used. Their result showed, in the smooth channel, the rate of heat and mass transfer is lower than the ribbed wall channel. However, in the channel with normal rib walls, increasing the Reynolds number has a downward effect on the Sherwood number ratio.

Dutta et al.[6] did a numerical study and discussed the combined effects of Coriolis and Buoyancy forces near the leading wall. Pascotto et al.[69] studied the effects of rotation on the flow field inside a radial triangular channel. They measured turbulence intensity under rotation and stabilizing and destabilizing effects of rotation on the boundary layer. Deng et al. [51] did an experimental study on heat transfer in a rotating smooth square U-duct at high Reynolds number. Their results show at high rotation numbers, heat transfer on the trailing wall is higher than the leading wall. In another study, Deng et al.[70] performed an experimental study on the two-pass ribbed square channel to observe the effect of pressure drop on heat transfer. They showed friction factor decrease with rotation number for both heated and unheated channels.

Wagner et al.[40] studied the effects of rotation and density ratio on heat transfer in turbine blade internal cooling passages. They showed increasing the rotation rates causes significant increases in heat transfer on trailing surfaces.

Kim et al. [71] performed an experimental study on heat transfers, and pressure drop characteristics in a rectangular passage used different rib angles. They showed the highest friction coefficient observed for the 45-degree parallel rib pattern, and the highest average Nusselt number on the ribbed walls obtained for the 60-deg model. Singh and Ekkad [72] were done an experimental study on rib turbulated two-pass channel under stationary and rotating conditions with different channel orientations.

Huh et al. [61] did an experimental study on the effect of channel orientation on the heat transfer in a two-pass smooth and ribbed rectangular channel. They developed a correlation for buoyancy parameter useful for predicting heat transfer under rotating conditions. Also, they compared the heat transfer in enhancement for both smooth and ribbed wall channels. Results showed channel orientation in the smooth wall doesn't have any significant effect on the heat transfer; however, changing the channel orientation from 90-deg to 135-deg on the ribbed channel increases the heat transfer dramatically. Li et al.[60] investigate the buoyancy effect on heat transfer in a rotating channel. Their experimental result showed in the same rotation number, increasing the density ratio induces more buoyancy effects, which leads to enhancement in heat transfer in both passages. Johnson et al.[46] done an experimental study to determine the effects of buoyancy and Coriolis forces on heat transfer. Their result showed the effects of rotation are significantly different depending on the flow direction.

Many other parameters affect the heat transfer coefficient in stationary and rotating cases. One of these effects is the entrance effect. In many studies, a fully developed inlet boundary condition was considered. However, in a real gas turbine blade, the flow may be developing ,

which is dependent on the aspect ratio of the channel. The heat transfer behavior is different for fully developed flow compared with the flow at the inlet.

Kays and Crawford [73] repeated the study done by Boelter et al.[74]. They concluded there is a dependency between the entrance length and entrance geometry. They also found the Nusselt Number for a sudden contraction inlet was higher than a fully developed entrance. In another line of study Han,[75] -Park[76] and Park et al.[77] considered different aspect ratio channels. Their studies showed, at the entrance, the Nusselt number starts decreasing in the streamwise direction and reaches a constant value. In the ribbed channels, this constant value happened after approximately three hydraulic diameters from the channel inlet. In another study Wright et al.[78] did experimental research on the different channel entrance geometries. They found that the entrance condition has a significant effect on heat transfer. These effects can decrease by increasing the rotation number. Wright et al.[79] showed that an entrance contraction would enhance heat transfer near the entry region of the channel.

3 Computational Fluid Dynamics of Cooling Channel

Emergence and evolution of computer science have developed fluid flow modeling eminently. Thom[80], solved the two-dimensional linearized Navier-Stokes equations (Euler equations) for flow around a cylinder for the first time in 1930. The Computational Fluid Dynamics (CFD) numerical codes can model three-dimensional Navier Stokes equation for more complex flow conditions.

There are three primary methods available to compute complex turbulent industrial flows. These methods are Reynolds-Averaged-Navier–Stokes (RANS), Large Eddy Simulation(LES), and Direct Numerical Simulation(DNS) [81]. In this chapter, first, a review of these methods and computational set up used in this study are going to be presented.

3.1 Fluid Motion and Heat Transfer

For the fluid motion, the Navier-Stokes equations are going to be discussed. Also, an overview of turbulence and heat transfer models are given.

3.1.1 Continuity

The continuity equation states the conservation of mass, which for all the environment expects nuclear- reaction is valid. The conservative form is:

$$\frac{\partial \rho}{\partial t} + \frac{\partial \rho U_i}{\partial x_i} = 0 \quad \text{Equation 3-1}$$

3.1.2 Momentum

Momentum equation shows a force balance by using Newton's second law. Forces in the momentum equation can be categorized as the body force F_i , gravitational force and surface

forces which can be seen as T_{ij} . The surface forces usually are written as a combination of pressure and viscous stresses (a.k.a as normal stress and shear stress, respectively) as :

$$T_{ij} = -p\delta_{ij} + \tau_{ij} \quad \text{Equation 3-2}$$

For Newtonian incompressible flow, the momentum equation will be:

$$\frac{\partial \rho U_i}{\partial t} + \frac{\partial \rho U_i U_j}{\partial x_j} = \rho g_i + F_i - \frac{\partial P}{\partial x_i} + \frac{\partial}{\partial x_i} (2\mu S_{ij}) \quad \text{Equation 3-3}$$

Where F_i denotes any additional body-forces that can affect the fluid motion, such as rotation, a magnetic or electric field, etc.

3.1.3 Energy

The first law of thermodynamics states that the exchange of energy for a system is the result of applied work and heat transfer through that region. In its most complete formulation, the energy equation is:

$$\frac{\partial \rho E_0}{\partial t} + \frac{\partial \rho U_i E_0}{\partial x_i} = \rho U_i F_i - \frac{\partial q_i}{\partial x_i} + \frac{\partial}{\partial x_j} (U_i T_{ij}) \quad \text{Equation 3-4}$$

Where T_{ij} describes the surface forces similar to the viscous and pressure terms in Equation 3-2. E_0 is the total internal energy, including kinetic energy. The energy equation, as displayed above, is however seldom used and instead, the simplified temperature equation is applied:

$$\frac{\partial \rho C_p T}{\partial t} + \frac{\partial \rho C_p U_i T}{\partial x_i} = \frac{\partial}{\partial x_i} \left(\frac{\mu C_p}{Pr} \frac{\partial T}{\partial x_i} \right) \quad \text{Equation 3-5}$$

3.1.4 Rotational Modification

The Navier-Stokes equation is derived and valid for a Newtonian inertial coordinate system, i.e., System without any forces acceleration. A coordinate system fixed in a rotating structure,

however, involves both Coriolis and centrifugal acceleration, then the commonly applied equations are invalid.

By assuming that the coordinate system is fixed or translate with constant velocity, and the rotation velocity is set, all the acceleration terms in the left-hand side of the momentum equation can be neglected. Thus, the momentum equations can be rewritten as:

$$a_i^{ce} = \epsilon_{ijk} \epsilon_{klm} \Omega_j \Omega_l x_m \quad \text{Equation 3-6}$$

$$a_i^{co} = 2\epsilon_{ij} \Omega_j U_k \quad \text{Equation 3-7}$$

These terms are often considering as a body force modification to the Navier-Stokes equation and hence included, with a change in sign, on the right-hand side of the momentum equation. There is no rotational modification to either the continuity or temperature/energy equation.

3.2 Flow Model

The Navier-Stokes equation is a non-linear partial differential equation. As it is known, most of the partial differential equations cannot be solved by known mathematical tools. Navier-Stokes equations due to the complexity and its nature impose a severe obstacle to the physical world.

To simplify this equation, a few flow models make it possible to obtain an analytical solution. The most accurate models are Direct Numerical Simulations (DNS) and Large Eddy Simulation (LES). Numerical Simulation using Reynolds Averaged Navier-Stokes (RANS) solvers are apart from numerical approximations also affected by physical similarities in the models for the turbulence field. For the current study, both SST K-Omega model and Large Eddy Simulation used. In this part, a brief introduction of both models is going to present.

3.2.1 SST K-Omega Model

K-Omega turbulence model is a two-equation model that solves transport equations for turbulent kinetic energy k and specific dissipation rate ω . This method first proposed by Kolmogorov[82]. However, there were many improvements in this model and the most crucial development in this model presented by Wilcox[83].

The two equations are as below:

$$\frac{\partial(\rho k)}{\partial t} + \frac{\partial(\rho u_j k)}{\partial x_j} = P - \beta^* \rho \omega k + \frac{\partial}{\partial x_j} \left[\left(\mu + \sigma_k \frac{\rho k}{\omega} \right) \frac{\partial k}{\partial x_j} \right] \quad \text{Equation 3-8}$$

$$\frac{\partial(\rho \omega)}{\partial t} + \frac{\partial(\rho u_j \omega)}{\partial x_j} \quad \text{Equation 3-9}$$

$$= \frac{\gamma \omega}{k} P - \beta^* \rho \omega^2 + \frac{\partial}{\partial x_j} \left[\left(\mu + \sigma_k \frac{\rho k}{\omega} \right) \frac{\partial \omega}{\partial x_j} \right] + \frac{\rho \sigma_d}{\omega} \frac{\partial k}{\partial x_j} \frac{\partial \omega}{\partial x_j}$$

Where

$$P = \tau_{ij} \frac{\partial u_i}{\partial x_j} \quad \text{Equation 3-10}$$

$$\tau_{ij} = \mu_t \left(2S_{ij} - \frac{2}{3} \frac{\partial u_k}{\partial x_k} \delta_{ij} \right) - \frac{2}{3} \rho k \delta_{ij} \quad \text{Equation 3-11}$$

$$S_{ij} = \frac{1}{2} \left(\frac{\partial u_i}{\partial x_j} + \frac{\partial u_j}{\partial x_i} \right) \quad \text{Equation 3-12}$$

Also, the turbulent eddy viscosity is computed from:

$$\mu_t = \frac{\rho k}{\hat{\omega}} \quad \text{Equation 3-13}$$

Where

$$\hat{\omega} = \max \left[\omega, C_{lim} \sqrt{\frac{2S_{ij}S_{ij}}{\beta^*}} \right] \quad \text{Equation 3-14}$$

$$\bar{S}_j = S_{ij} - \frac{1}{3} \frac{\partial u_k}{\partial x_k} \delta_{ij} \quad \text{Equation 3-15}$$

However, this version on of the K-Omega model is more accurate than the previous one for the free shear flow, and separated flow, according to the study by Menter [84] there are still some weaknesses when there is free streamflow.

3.2.2 LES Model

LES is a time-dependent approach to solve Large scales of turbulence by using the Navier-Stokes (N-S) equations. Also, to model small-scale motions by implementing one of the subgrid-scale models (SGS). The LES approach is beneficial for the turbulence problem with high Reynolds numbers. Also, this model usually used for assessing other developing turbulence models.

For the LES model instead of time-averaging, to separate the large eddy field from a small eddy field, spatial filtering has been used. This filter described in the Leonard work [85]:

$$\bar{\phi}(x) = \int \phi(\acute{x}) G(x, \acute{x}, \bar{\Delta}) d\acute{x}$$

Where G is the specified filter function, and $\bar{\Delta}$ is the filter width.

LES employs models such as Smagorinsky or Wall-Adapting Local-Eddy (WALE) as an SGS to solve for the turbulent viscosity. By using the LES model, most of the SGS dissipation generates due to resolved turbulence fluctuations. We usually assume that the SGS dissipation takes place at the highest resolved wavenumbers.

To compare Smagorinsky and WALE SGS, one should note that the Smagorinsky SGS assumption is based on the mixing length, which makes this method simple and computationally less expensive, regardless of its limitation due to the damping effects near the wall. Thus, it is required to use a damping function near the wall to have an accurate result. While, based on Nicoud and Ducros study[86], WALE is the simplest and the most precise method to capture the flow behavior near the wall without using damping effects. Now, assuming the filtering operation used now governing equations can be expressed as below.

The continuity equation:

$$\frac{\partial \bar{u}_i}{\partial x_i} = 0 \quad \text{Equation 3-16}$$

Navier- Stokes equations:

$$\frac{\partial \bar{u}_i}{\partial t} + \frac{\partial \bar{u}_i \bar{u}_j}{\partial x_j} = -\frac{1}{\rho} \frac{\partial \bar{p}}{\partial x_i} - \frac{\partial \tau_{ij}}{\partial x_j} + \nu \frac{\partial^2 \bar{u}_i}{\partial x_i \partial x_j} \quad \text{Equation 3-17}$$

Where $\partial \tau_{ij}$ denotes to the Sub-Grid Scale (SGS) stress tensor, defined as:

$$\tau_{ij} = \overline{u_i u_j} - \bar{u}_i \bar{u}_j \quad \text{Equation 3-18}$$

3.3 CFD Set Up

For this thesis application, a U-bend configuration with smooth walls and a 180-degree turn has been used. The channel has a square cross-section with a hydraulic diameter of 5.08 cm (2 inches). The length of the first and second passes is 514 mm and 460 mm, respectively. Figure 3-1, shows the geometry, inlet/outlet planes, and the rotation axis of the system in more detail. The channel is allowed to rotate at the speed range of 0 to 1500 rpm, resulting in the maximum rotation number of 1.5, which is a substantial value as compared to previous studies.

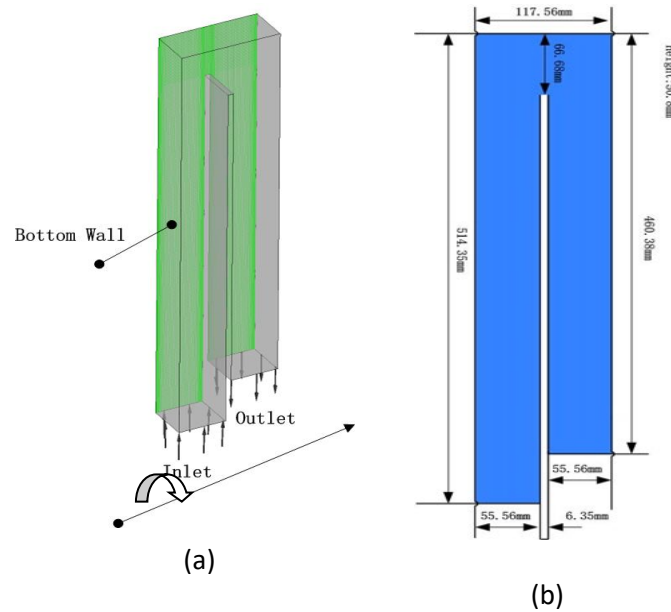
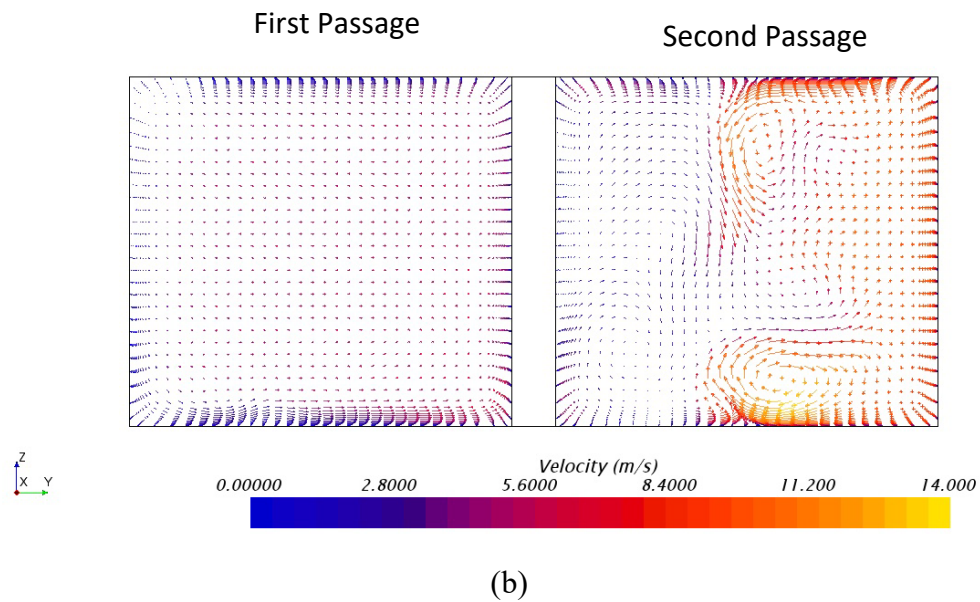
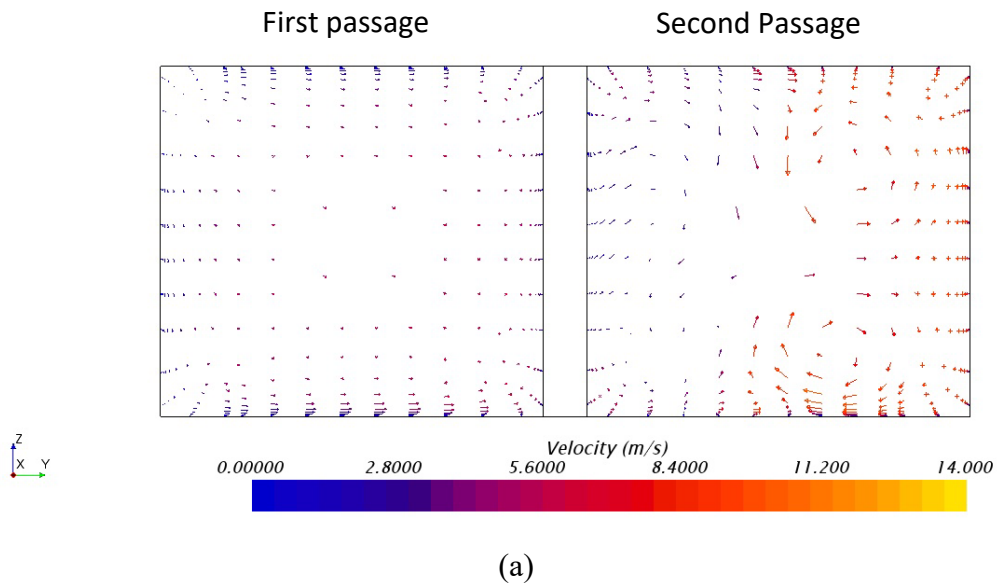


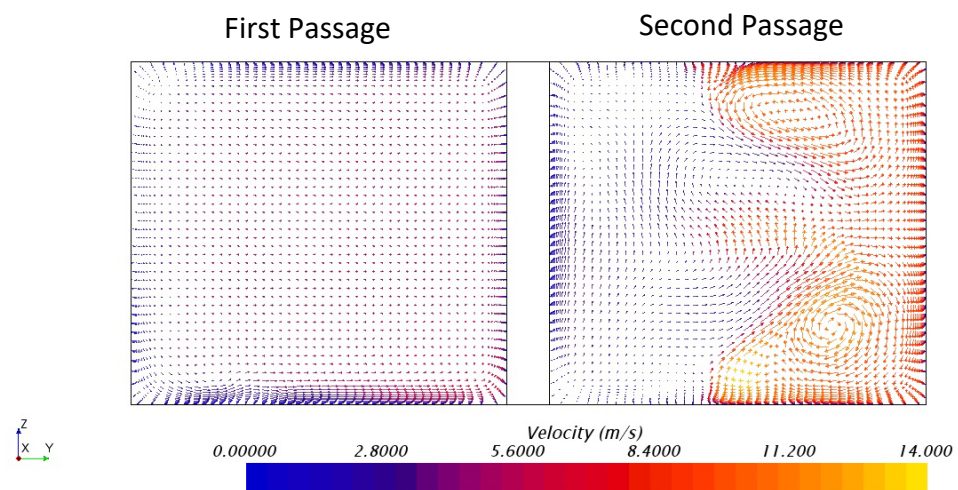
Figure 3-1: U-bend Configuration (a) Inlet/Outlet and rotation axis, (b) Dimensions of the duct

3.3.1 Mesh Independent Study Methodology

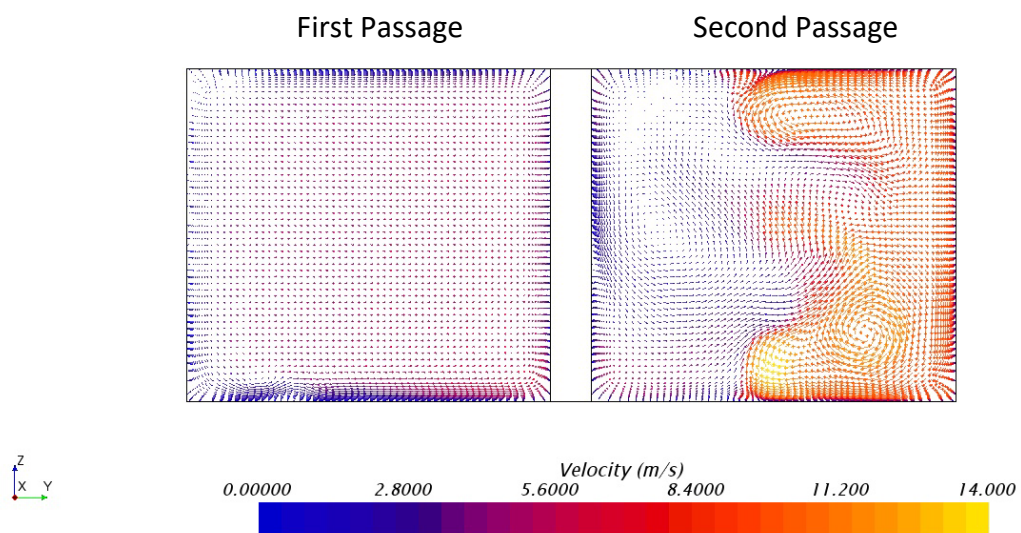
The reliability of resolving a simulation is related to the number of mesh. The finer mesh usually provides more accurate results; however, it increases the computational time. Thus, it is vital to consider a mesh that gives reasonably acceptable results with lower computational time. Figure 3-2 describes the velocity counter on the vertical cross-section for the first and second passage of a smooth wall channel for the same Reynolds number and different mesh sizes. As can be seen, finer mesh resolution captured better flow behavior in these cross-sections. For the 1.8 million mesh size, streamlines were not consistent. Thus, the accuracy of the results on flow behavior from this mesh size could not be acceptable. For 2.6 million mesh,

the streamlines were more consistent. However, there was a significant difference between 2.6 million and 10.5 million stream counters. Furthermore, the velocity streamlines contour for 4.8 million, and 10.5 million mesh were similar.





(c)



(d)

Figure 3-2: Contours of streamline on the normal planes for different mesh size (a) 1.8M (b) 2.6M (c) 4.8M (d)10.5M

There are many consideration criteria to select the right mesh resolution. In industry, choosing the mesh resolution usually is based on the expected outcome and what one can afford computationally. One of the critical criteria is the wall boundary flow, which needs to be captured accurately. The computational package used for this study is Star CCM+, which can model the no-slip walls boundary condition. The Law of the wall, known as Y^+ , is another parameter that needs to be considered. In fluid dynamics, it describes the average velocity of turbulent flow at a certain point is proportional to the logarithm of the distance from a selected point to the wall or the boundary of the fluid region. This concept published by Von Karman [87]. This non-dimensional value can be defined in Equation 3-19

$$y^+ \equiv \frac{yu_\tau}{\vartheta} \quad \text{Equation 3-19}$$

In the heat transfer CFD application, it is suggested to keep the wall Y^+ less than one. Figure 3-3 shows the wall Y^+ value for the smooth U-Bend channel used in this work. Using Y^+ less than one required to use the Prism layer near the walls. Prism layers allow the solver to resolve the near-wall flow accurately without using a fine mesh near the walls. Furthermore, flow feature changes such as velocity and temperature gradients are steeper in the viscous sublayer of the turbulent boundary layer than capturing them from the mesh. Also, using the prism layers and keep the Y^+ less than one allows the turbulent model to resolve the viscous sublayer directly. Which results in having a reasonably good convergence near the wall. For this study, it was concluded to use 15 prism Figure 3-4 shows a closer look at the prism layer on the wall of the channel for this study.

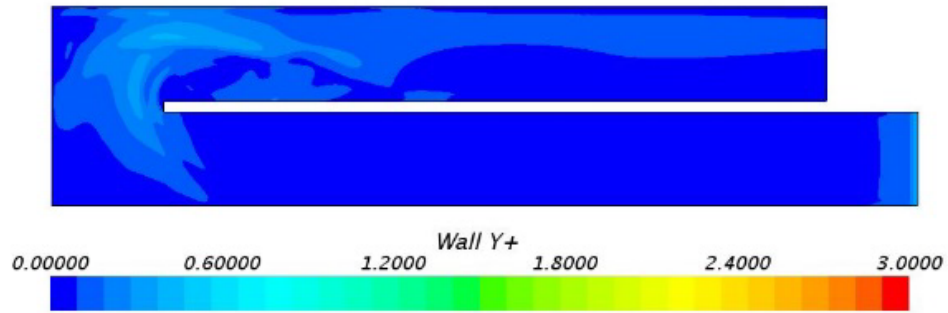


Figure 3-3: Wall y^+ values for the U-Bend Channel

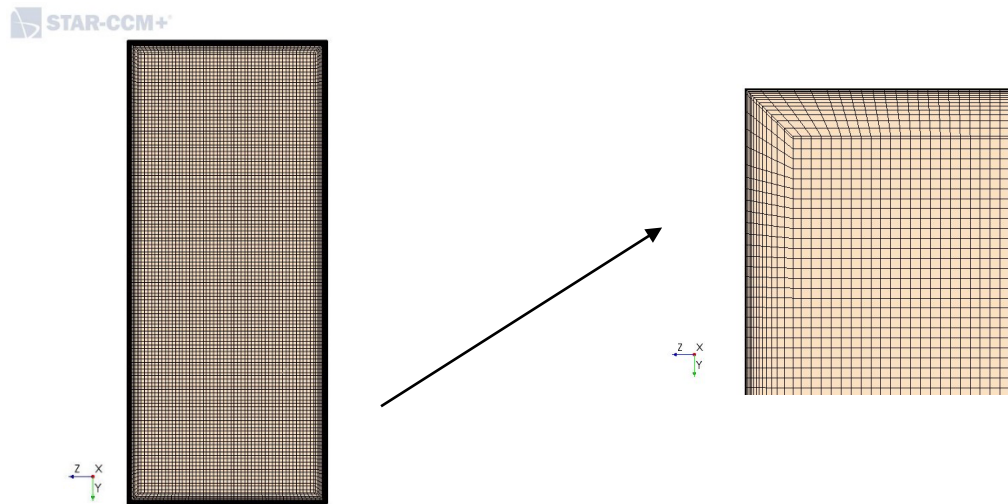
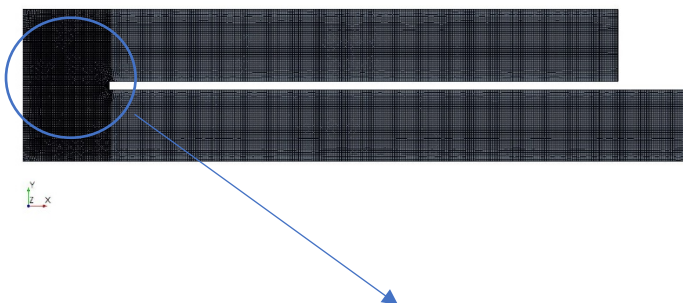


Figure 3-4: A closer look at the prism layer

The turning effect is one of the phenomena in the study of flow behavior along the channel. Flow behavior in the turning region is very unpredictable. Hence, to capture all the changes and the turning effect, customize mesh volume defined for this region. Figure 3-5, shows a closer look at this region.



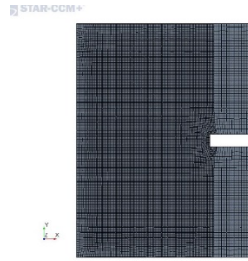


Figure 3-5: Mesh construction in the bending region

As mentioned earlier, Large Eddy Simulation (LES) was mainly used to solve the turbulent flow equations. There are many approaches to mesh sensitivity analysis for the LES method. Thus, for the independent mesh study, first, a preliminary K-Omega simulation for a stationary case with a turbulence intensity of 0.01 was run for various mesh resolutions. The comparison between the Nusselt number on the bottom wall indicated the correct mesh size. Using this method helped to find an accurate number of mesh for the RANS models, while to find the right mesh size for the LES, Kolmogorov length and Taylor Microscale needed to be investigated.

Kolmogorov length η [88], denotes the smallest scales in the turbulent spectrum. LES results are close to DNS results. Additionally, Taylor Microscale λ [89], defines it as a dissipative intermediate length scale. Lengths smaller than the Taylor Microscale are affected by viscosity. Based on a study by Addad et al. [90], Taylor Microscale can be used to determine the maximum mesh size to obtain acceptable results for LES. For this work, it was assumed that if the local cell size length Δ [91] is between the Kolmogorov and Taylor microscale, the results for CFD were acceptable. These two lengths were calculated for selected mesh size from K-Omega mesh independent study if the local cell size length was between the Kolmogorov and Taylor microscale, the mesh size was accepted for the LES simulation.

$$\dot{\eta} = \left(\frac{\vartheta^3}{\omega k \beta^*} \right)^{1/4} \quad \text{Equation 3-20}$$

$$\lambda = \sqrt{10 \vartheta \frac{1}{\omega \beta^*}} \quad \text{Equation 3-21}$$

$$\Delta = (\Delta_x \Delta_y \Delta_z)^{1/3} \quad \text{Equation 3-22}$$

Furthermore, in LES calculation, choosing the right time step is very vital. Stability and accuracy are important factors to have a reliable result. The Courant–Friedrichs–Lewy or CFL condition is a fundamental definition which needs to be considered.

CFL is a condition for the stability of unstable numerical methods that model convection or wave phenomena. According to the computational gas-dynamics book [92], for each dependency in a numerical domain, a physical field of relationship should be considered. Thus, we can say the CFL condition states that the information carries in each time step must be less than the distance between the mesh element.

It must be mentioned CFL condition cannot be used as an only factor for stability condition, and there are other stability conditions with a more restrictive requirement than the CFL condition.

The CFL condition can be derived only and intuitively. Assume a simple linear convection problem of a quantity u :

$$\frac{\partial u_i^{n+1}}{\partial t} + \alpha \frac{\partial u}{\partial x} = 0 \quad \text{Equation 3-23}$$

Equation 3-23 can be written as an explicit forward scheme shown below:

$$\frac{u_i^{n+1} - u_i^n}{\Delta t} + \frac{\alpha}{\Delta x} (u_i^n - u_{i-1}^n) = 0 \quad \text{Equation 3-24}$$

Where a is the velocity magnitude, Δt is the time step, and Δx is the length between mesh elements. Applying Taylor Series Expansion (TSE) to Equation 3-24, diffusion term can be introduced, which can be written as:

$$\mu_{num} = \alpha \frac{\Delta x}{\Delta t} \left(1 - \alpha \frac{\Delta t}{\Delta x}\right) \quad \text{Equation 3-25}$$

From the physics of the diffusion problem, it is clear that the numerical diffusion coefficient must be positive; otherwise, the numerical result is going to be unstable. Also, the $\alpha \frac{\Delta t}{\Delta x}$ term in Equation 3-25, referred to as the Courant number, which is a dimensionless number. From the numerical diffusion coefficient, it can Courant number must be equal or smaller than one since any other value larger than one leads to a negative value for numerical viscosity. It can be said since using a more substantial time step, brings unitability, it is recommended for the explicit method to use a smaller time step. In this study, as mentioned before, the implicit unsteady method is going to be used. Although the implicit technique is unconditionally stable, for more complicated and representative problems, including the current problem, it is recommended to use the CFL condition as a reference for setting the time step. For the present study, the time step size was 6.9E-5 seconds along the entire solution time with a 2nd order solution accuracy considered.

4 Experimental apparatus and test procedures

4.1 Experimental Set up Introduction

An experimental apparatus designed, built, and assembled at the University of Wisconsin-Milwaukee. Previously, another similar test rig was developed for investigation of the heat transfer in a stationary two-pass channel augmented with various types of turbulators [93]. However, due to the rotation of the current setup, an entirely different channel with different size, material, and additional accessories had to be designed.

Figure 4-1 depicts the rotating platform. It includes two main modules; the primary support module, which contains the shaft, the motor, and the blower, and the measurement module, which includes thermocouples and slipring. The slipring supplies power to heaters. Omega® miniature portable wireless thermocouple connectors and data loggers (MWTC-D-K-915) and a wireless receiver (MWTC-REC1-915) are installed to measure and collect temperature values at various points along the channel. 1.5V lithium or alkaline batteries power both thermocouples and the receiver. Thermocouple probes mounted in the test section with the transmitters mounted and adhered to the exterior wall of the test section. The receiver is placed further away from the setup and wirelessly receives the data from the thermocouples and transmits it to a nearby computer with a USB cable. This arrangement will allow for real-time data collection and monitoring.

In the main supporting module, air enters the hollow shaft which can rotate with the rotational speed of up to 1200 RPM. This rotation is enabled by a 7.5 hp, three-phase induction motor via a pulley. A variable frequency drive (VFD) system will be installed on the motor to adjust the rotation speed. A cross-shaped component (A-36 steel alloy) is designed, machined

and then welded in the middle of the main shaft to direct the cold air to the test section (i.e., the two-pass square channel) by making a 90-degree turn. The test section is prepared from A-36 steel to withstand the high rotational velocities; however, it is augmented with a thin layer of packing foam and a 0.125mm-thick layer of a resin-based phenolic sheet from inside to minimize the heat loss from the side walls. Moreover, to balance the test section and to avoid excessive vibrations under rotating conditions, a counter-weight piece composed of a weight-lifting bar and a weight plate with the adjustable position was designed and welded to the opposite side of the four-way connector. For future reference, a detailed stress analysis of the counterweight is discussed on 4.2.

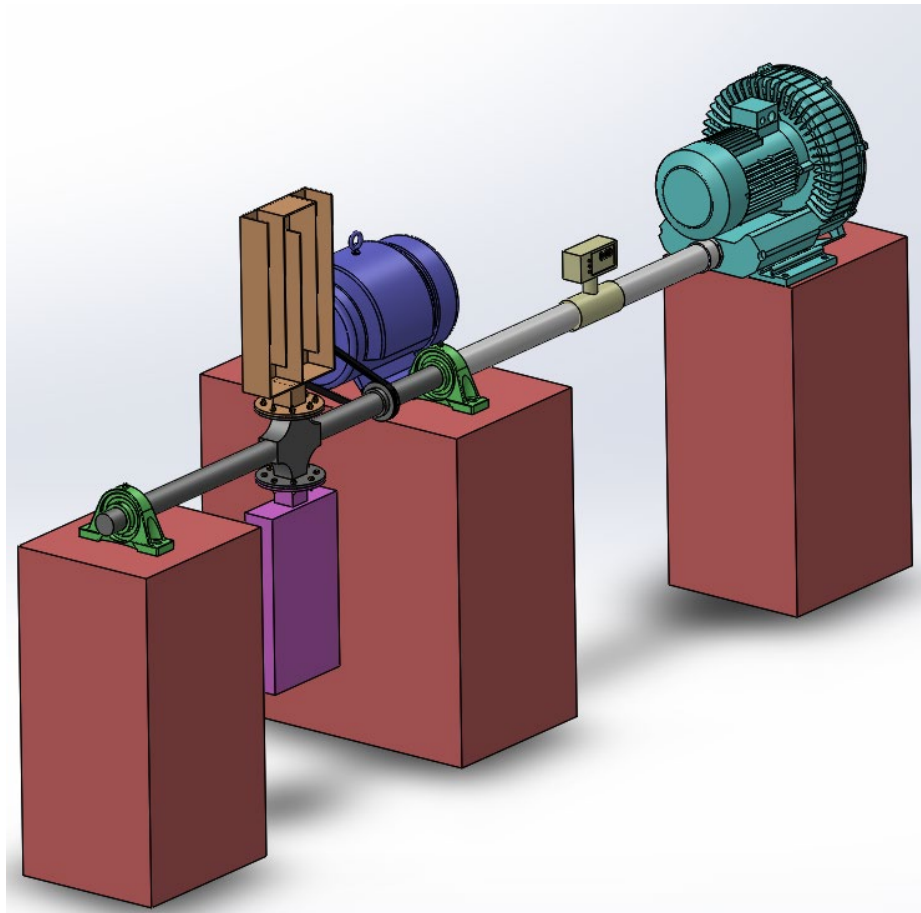


Figure 4-1: The experimental test set up

Figure 4-2 shows the complete test section. The right figure demonstrates a magnified view of the test section, along with the heaters and thermocouples installed on the bottom surface of the channel.

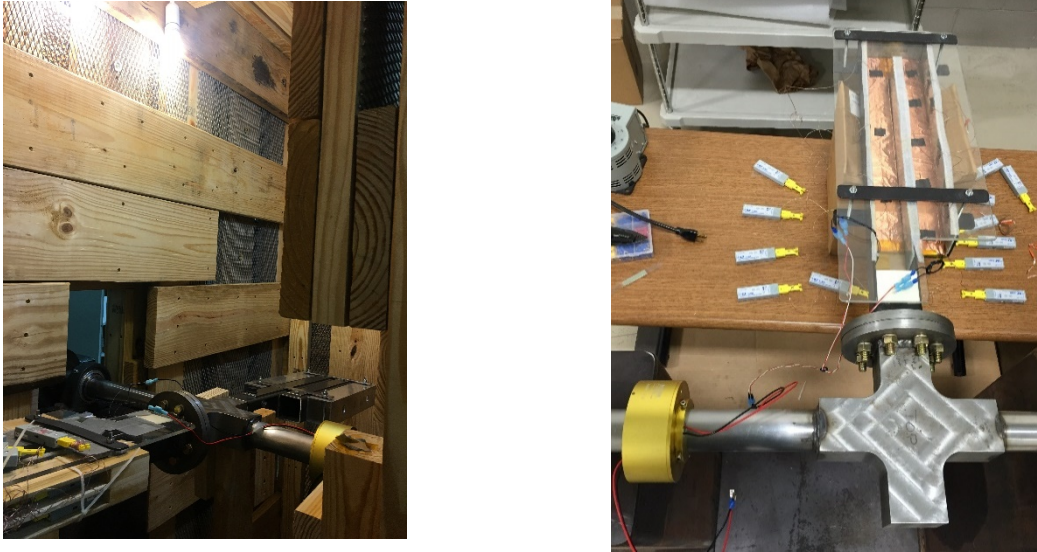


Figure 4-2: (left) The entire experimental setup, and (right) a closer look at the test section, the heater, the thermocouples, and Slip ring

An electric motor drives a belt and pulley system used to rotate the shaft that holds the test blade and counterweight. The electric motor provides a maximum frequency of 1425 rpm. The motor wired with a variable frequency drive, which allows an adjustment to the rate of the motor, but meager rates can cause overheating. Small drive pulley used in the system to enable the motor to run at a higher frequency. The rpm and diameter are inversely proportional, which can be explained in Equation 4-1.

$$RPM_{output} = RPM_{input} \left(\frac{Diameter_{input}}{Diameter_{output}} \right) \quad \text{Equation 4-1}$$

The driven pulley has a diameter of 6 inches. And the smallest available drive pulley with a 1-3/8 inches bore diameter is a 3-3/4 inches diameter pulley. From these values, the output of

the driven shaft would be 890 rpm. This speed allows the variable frequency drive to reduce the speed of the motor to give the desired lowest speed without harming it, while still allowing for the motor to produce a high enough speed for later studies if desired. Also, for the belt, the drive pulley and driven pulley were both able to use an “A” style v-belt, meaning that the top width is ½ inches while the height is 5/16 inches. Once the pulley sizes were decided, the belt length could be determined by using the following equation where L is length, D is the diameter of the driven pulley, d is the diameter of the drive pulley, and C is the distance between the two centers.

$$L = 2C + 1.57(D + d) + \frac{(D - d)^2}{4C}$$

Equation 4-2

With a distance between the two pulleys of around 14 inches and diameters of the drive and driven pulleys is 3-3/4 inches and 6 inches, respectively, a length of 44 inches attained. A “Gripnotch” belt chosen because it slips less than a regular v-belt. Figure 4-3 describes the connecting shaft with the pulley and the motor.



(a)



(b)

Figure 4-3: Experimental setup overview: (a) Connecting Shaft to the motor through the pulley (b) Motor

4.2 Counterweight Stress Analysis

There are many challenges to run the test safely and accurately. Installing the counterweight, stress analysis of the bearings, and also providing a cage around the test rig to avoid any damage in case of shaft failure in the rotational motion, are the most critical challenges in the test set up. Here a detailed discussion for each of the mentioned challenges is going to be presented.

Due to the rotation motion, it is necessary to characterize the stress and strain induced by rotating a shaft and test channel system at a specific rpm. Here data to determine if the shaft and test channel can rotate safely without the risk of a catastrophic failure provided. The shaft made of ST37 steel. The tensile yield strength for ST37 steel is about 36,250 psi, and the ultimate tensile yield strength is 66,700 psi. The stress needs to be lower than the tensile yield strength for reliable functionality during testing

Figure 4-4 shows the 3-D model, which uploaded into ANSYS. The shaft and union were designed and assembled in CREO parametric. The bearings were obtained from the McMaster-Carr website and assembled on the shaft in CREO parametric.

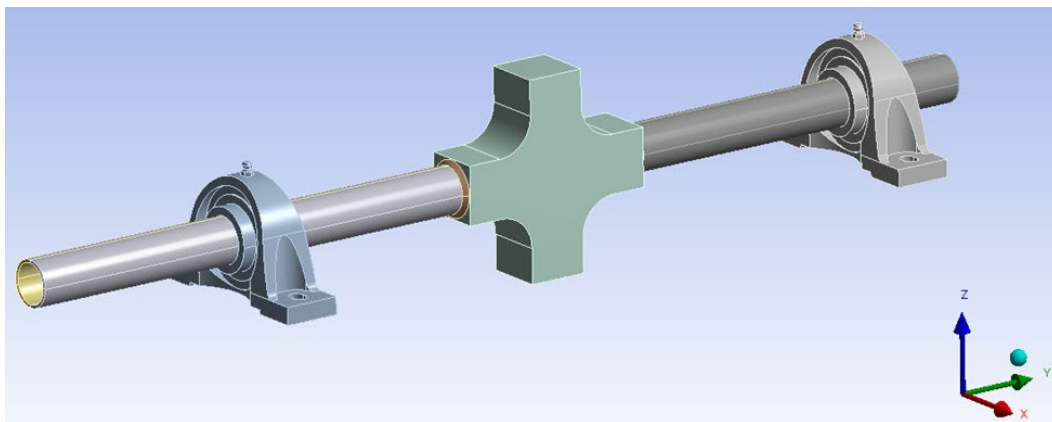


Figure 4-4: ANSYS 3-D Geometry for the Stress Analysis

The model runs for a static structural model for computational simplicity. Stress analysis was done by providing various supports and forces on the model to accurately measure the stress and strain gradients seen by the rotating test section. The model showed the highest stress concentrations near the bearings, which was to be expected because the two bearings support the entire rotating system. Figure 4-5 shows the stress concentrations throughout the entire shaft. The maximum stress seen by the model was 7193.8 psi. This stress is well below the tensile yield strength of the ST37 steel. Table 4-1 shows the stress and strain concentrations in the model. However, the maximum stress was likely caused by the remote displacement in ANSYS. The actual stress concentrations in the bearing discussed below.

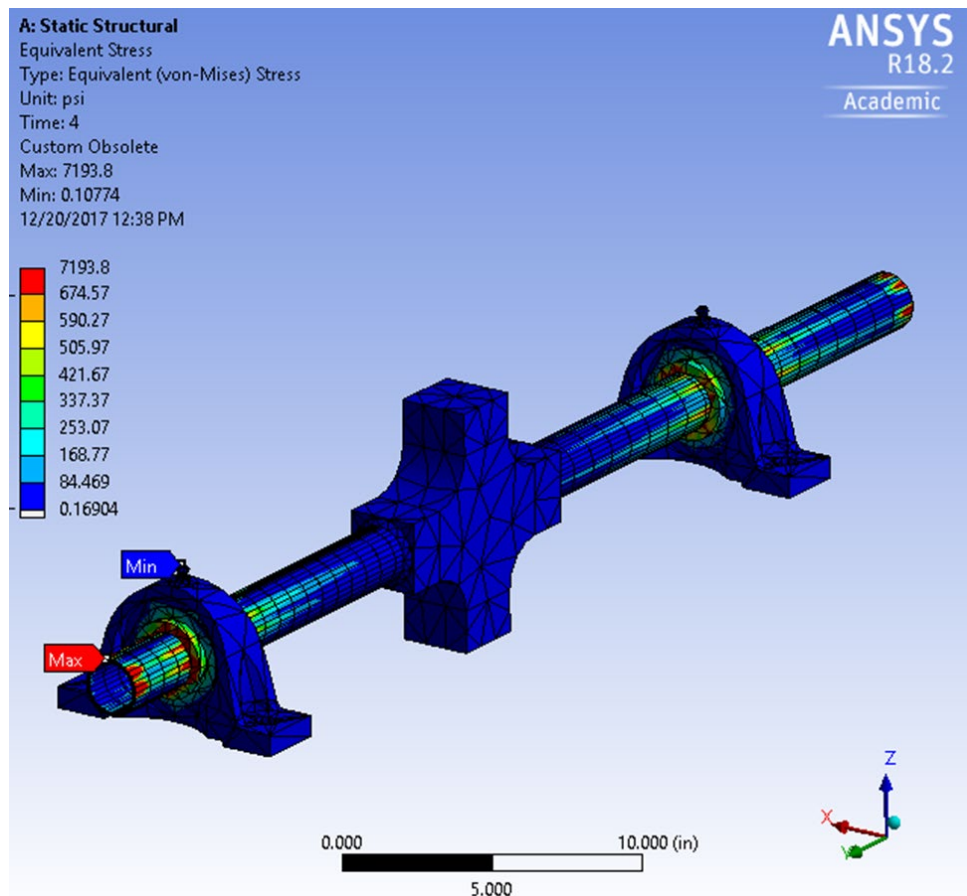


Figure 4-5: Stress contour for the entire shaft and bearing system

Table 4-1: stress and strain concentrations in the model

	Maximum Stress from ANSYS (PSI)	Maximum Yield Stress of ST37 (PSI)
Entire Model	7,193	36,300
Bearing and Shaft	3,133	36,300

The total deformation was also negligible within the model. Furthermore, the maximum deformation occurred where forces applied to the union. At this point, the opposite forces applied to the model, mainly the test section weight and the counterweight. The deformation of the entire model can be seen in Figure 4-6.

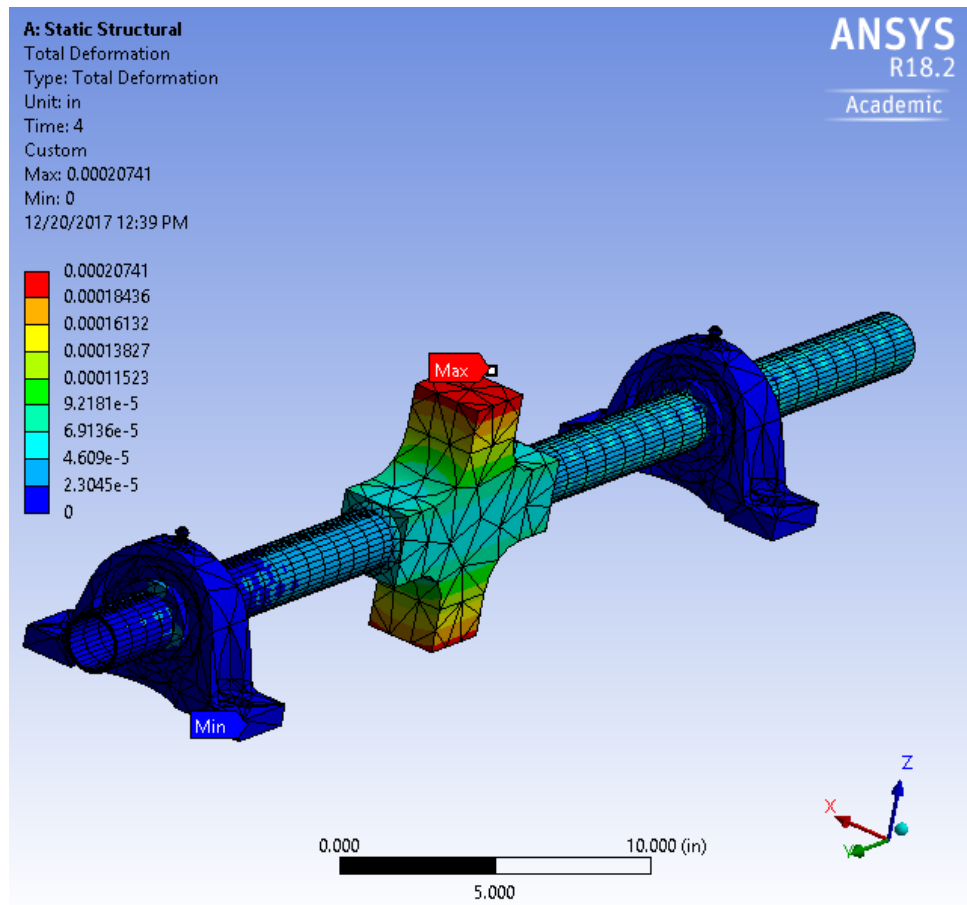


Figure 4-6: Total deformation of the entire shaft and bearing system

The result from the stress analysis gives confidence in running the test safely. However, still for safety proposes to design and to build a cage around the test area is essential. The cage designed and constructed is shown in Figure 4-7.



Figure 4-7: Cage structure set up

4.3 Data Reduction

The goal of this experiment is to compare the local Nusselt number in the smooth and rib roughened channel with the numerical results. In the experimental study, various mass flows were provided by using the blower. These mass flow rates can be calculated from Equation 4-2. Also, the Reynolds number can be estimated by the following Equation 4-3. Air at 300K used as the coolant in this study. Many boundary conditions are going to be discussed in this study; however, for the experimental research, the flux constant boundary condition is going to be used. The amount of heat that goes to the system is equal to the electrical power input; Equation 4-4 describes how to calculate this value. This value will be converted to the heat flux

over the area of the plate in Equation 4-5. To provide a uniform heat flux to the system, copper plates utilized at the bottom wall of the channel.

$$\dot{m} = \rho \times V \times A \quad \text{Equation 4-3}$$

$$Re = \frac{(\rho \times V \times D_h)}{\mu} \quad \text{Equation 4-4}$$

$$Q = R \times I^2 \quad \text{Equation 4-5}$$

$$Q'' = \frac{R \times I^2}{A} \quad \text{Equation 4-6}$$

By having the heat flux, convective heat transfer coefficient (h) can be calculated, which leads to obtaining the Nusselt number. Equation 4-6 and Equation 4-7 describe the equation that h and the Nusselt number can be derived, respectively. As mentioned before, all the properties are computed for air at 300K. The Prandtl number for this study is going to be assumed at 0.7. By using calculated values and the hydraulic diameter and conductive heat transfer coefficient and using air as the working fluid, the Nusselt number can be calculated from the experiment. Also, the theoretical Nusselt number for turbulent flow, for now, will be derived from Dittus Boelter Equation 4-9.

$$h = \frac{Q''}{(T_s - T_m)} \quad \text{Equation 4-7}$$

$$Nu = \frac{(h \times D_h)}{k} \quad \text{Equation 4-8}$$

$$Nu_0 = 0.023 \times Re^{0.8} \times Pr^{0.4} \quad \text{Equation 4-9}$$

4.4 Experimental Results

An experimental study was applied for both stationary and rotational motion for all the cases. For each case, the test was run for 30 - 45 minutes to obtain steady temperature, and different thermocouples were utilized at the different channel's cross-section locations.

The bulk temperature at each point was calculated based on the average temperature in each cross-section. By knowing these temperatures and the heat flux, the convective heat transfer coefficient and Nusselt number can be calculated.

4.4.1 Smooth Wall Validation

Figure 4-8 and Table 4-2 show the location of thermocouples that were installed on the bottom wall of the rig for the smooth wall channel.

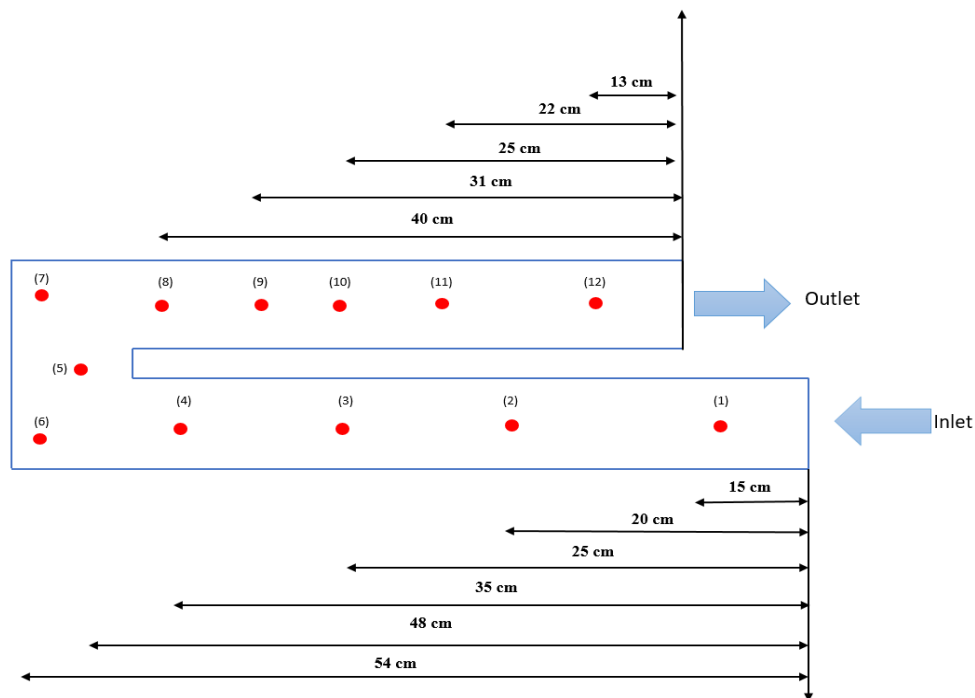


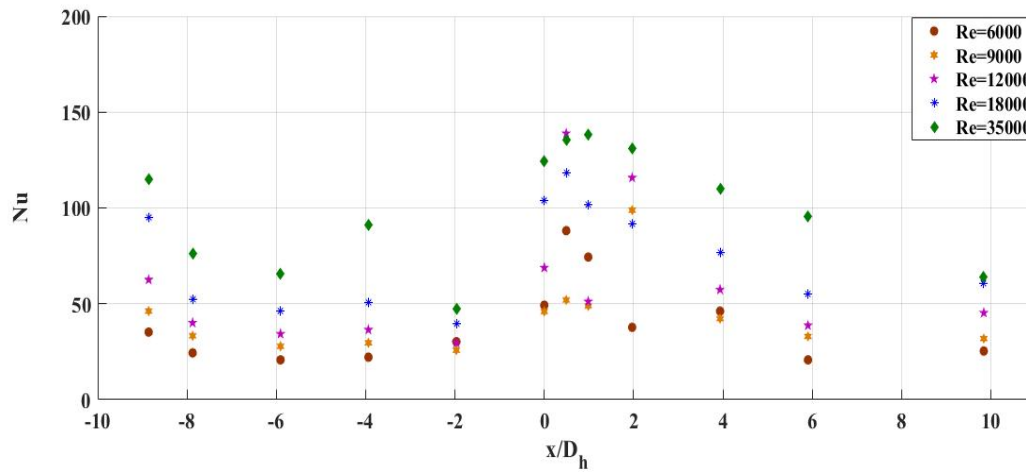
Figure 4-8: The approximate locations of the thermocouples along the channels

Table 4-2: Location of thermocouples on the bottom of the channel

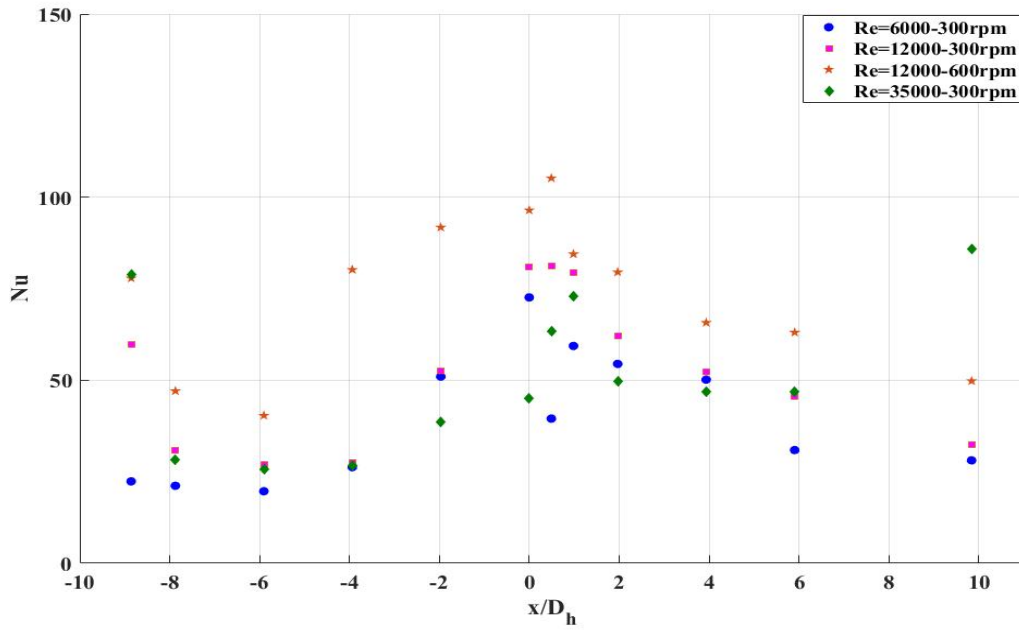
Thermocouple number	Thermocouple Location
1	15 cm from the inlet plane
2	20 cm from the inlet plane
3	25 cm from the inlet plane
4	35 cm from the inlet plane
5	48 cm from the inlet plane
6	54 cm from the exit plane
7	54 cm from the exit plane

8	40 cm from the exit plane
9	31 cm from the exit plane
10	25 cm from the exit plane
11	22cm from the exit plane
12	13cm from the exit plane

Figure 4-9 describes the channel average Nusselt number for various Reynolds numbers and rotation speed in stationary and rotational cases, respectively. As can be seen, increasing the Reynolds number increased the heat transfer ratio. This trend had a good agreement with the numerical results.



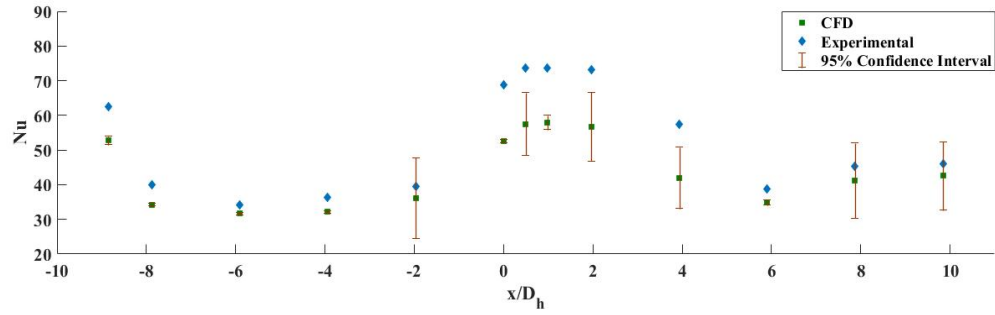
(a)



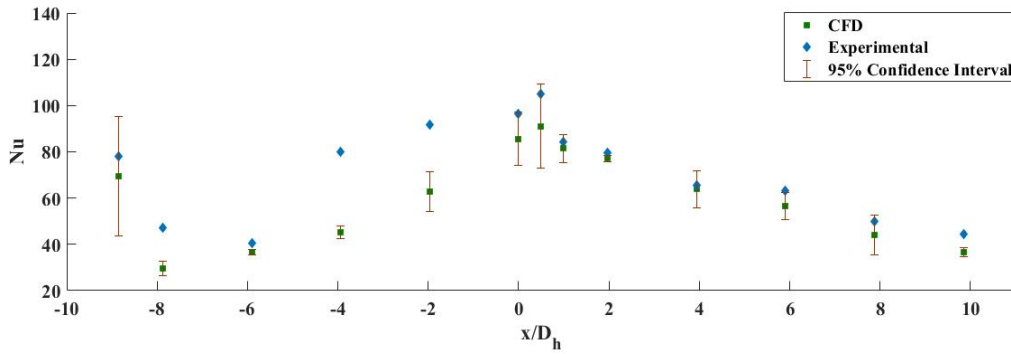
(b)

Figure 4-9: Experimental Nusselt Number Distribution along the channel for Various Reynolds number and Rotation Speed (a) stationery, (b) Rotation

Figure 4-10 shows the numerical and experimental Nusselt number distribution along the channel for a stationary and rotational motion for Reynolds number of 12,000 and a rotational speed of 600 rpm. For the rotational case, increasing the rotation speed increases the buoyancy effects, which results in increasing the Nusselt number. In all results, as flow reached the turning region, a significant increase in the Nusselt number was observed. The experimental results showed a good agreement with the numerical results. For the error analysis, the 95% confidence level method was used [94]. The scatter bar was calculated based on the standard deviations. The disparity between the two sets of data can be counted as the inaccuracy of the experimental data. Due to the current fluctuation in the power supplier, the amount of heat flux and airflow might slightly change.



(a)



(b)

Figure 4-10: Experimental Nusselt number distribution along the channel for a U-Bend Channel (a) Stationary $Re=12000$ (b) Rotational cases $Re=12000$, and $\omega=600$ rpm

4.4.2 Ribbed Wall Validation

Various rib geometries were cut to investigate rib turbulators effects on the temperature distribution and Nusselt number. Figure 4-11 describes the ribs designs that were used in the experimental study. These turbulators are made from plexiglass. They were wrapped in the copper foil and installed on the channel bottom wall. The added rib area was considered in the Nusselt calculations. The thermocouple probes were utilized between each rib. The experimental study implemented for the Rib-Pitch-to-Rib-Height (P/e) ratio of 10 for all the configurations.



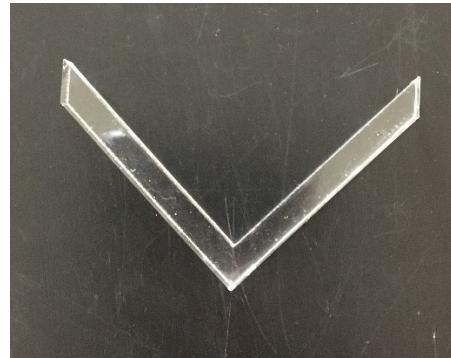
(a)



(b)



(c)



(d)

Figure 4-11: Experimental Rib Configuration (a) 45-deg rib,(b) 60-deg rib,(c) 90-deg rib, (d) V-shape rib

4.4.2.1 90-degree Ribbed Wall Validation

Figure 4-12 illustrates the comparison of the experimental results for stationary and rotational cases for Reynolds number 35000 and rotational speed between 300 and 600 rpm. Similar to the smooth wall results, rotation increases the heat transfer coefficient due to the existence of buoyancy forces. Furthermore, from the figure, it can be observed, in a constant Reynolds number, increasing the rotational speed increased the Nusselt number coefficient.

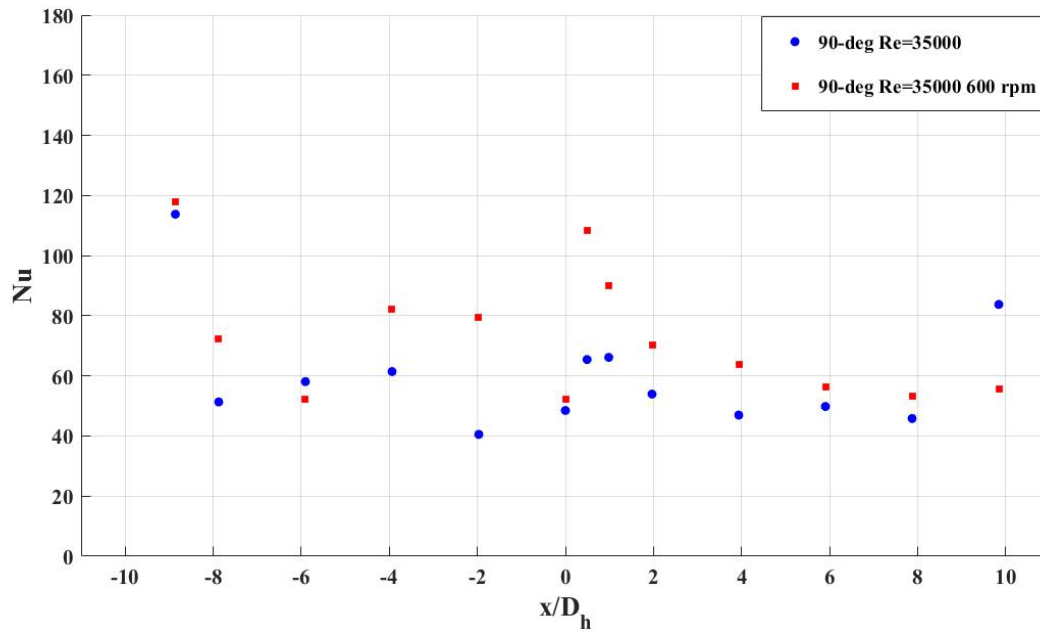
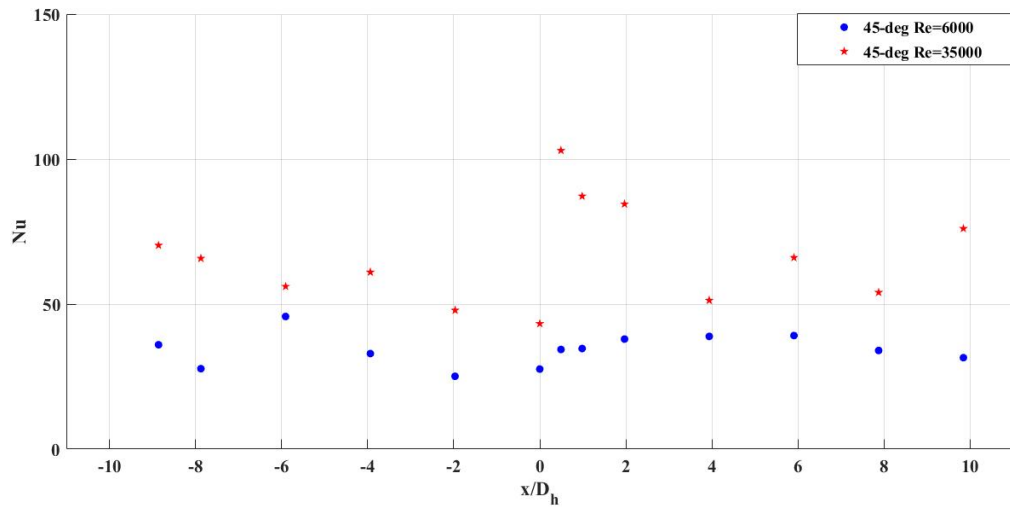


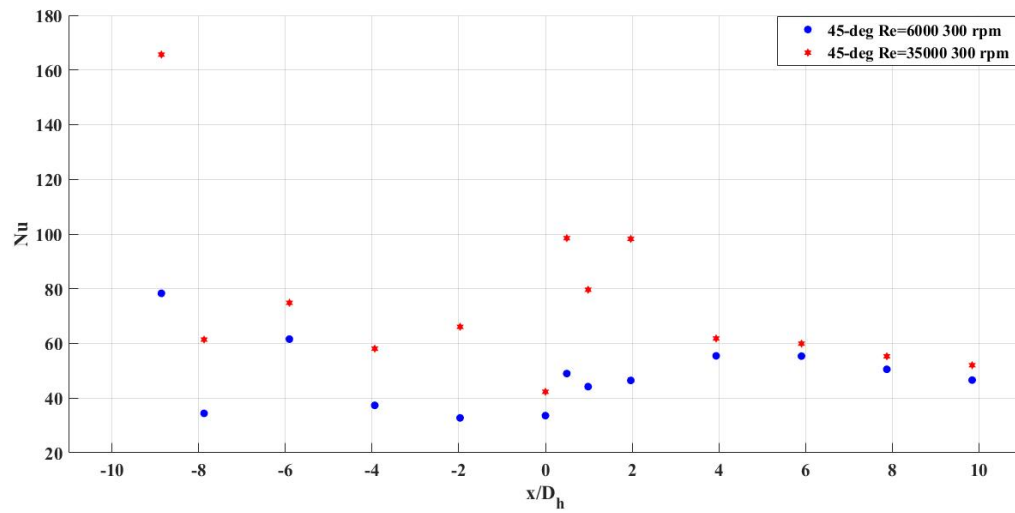
Figure 4-12: Experimental Nusselt Number Distribution comparison along the channel with 90 deg parallel ribs stationary and rotational cases

4.4.2.2 45-degree Ribbed Wall Validation

Figure 4-13 describes the channel average Nusselt number for Reynolds numbers 6000 and 35000 and a rotation speed of 300 rpm in stationary and rotational cases, respectively. As can be seen, increasing the Reynolds number increased the heat transfer ratio. Also, in rotational instances similar to the numerical results, in the same rotational speed, increasing the inlet velocity (Reynolds number) enhanced the heat transfer coefficient.



(a)



(b)

Figure 4-13: Experimental Nusselt Number Distribution along the channel with 45 deg parallel ribs for Various Reynolds number and Rotation Speed (a) stationery, (b) Rotation

Figure 4-14 shows the error analysis for rotational and stationary cases. Similar to the smooth wall channel, for the error analysis, the 95% confidence level method was used. Both stationary and rotational results showed a good agreement with the numerical results. The

inaccuracy of the experimental data can be due fluctuation in the power supplier; the amount of heat flux and airflow might slightly change.

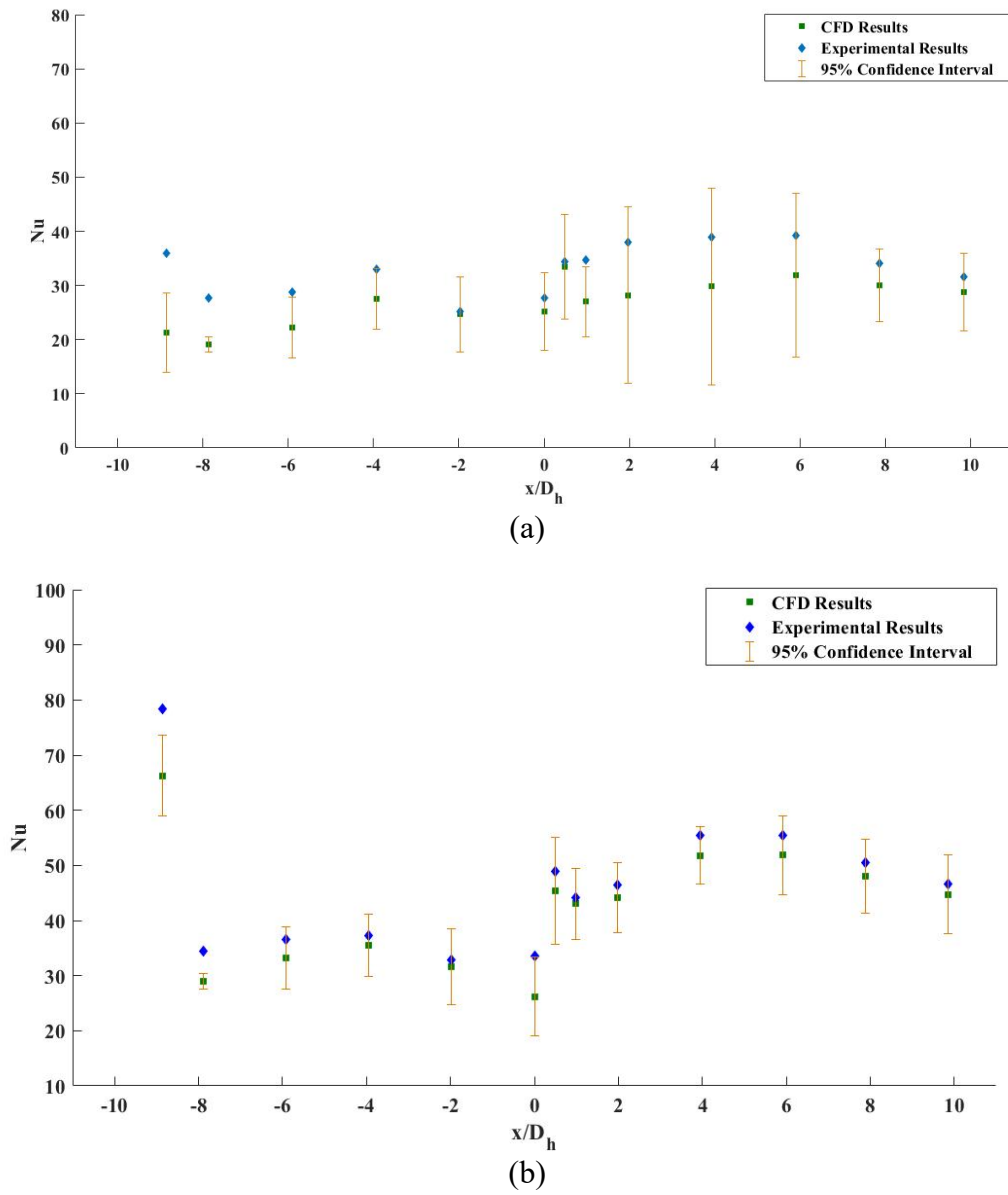
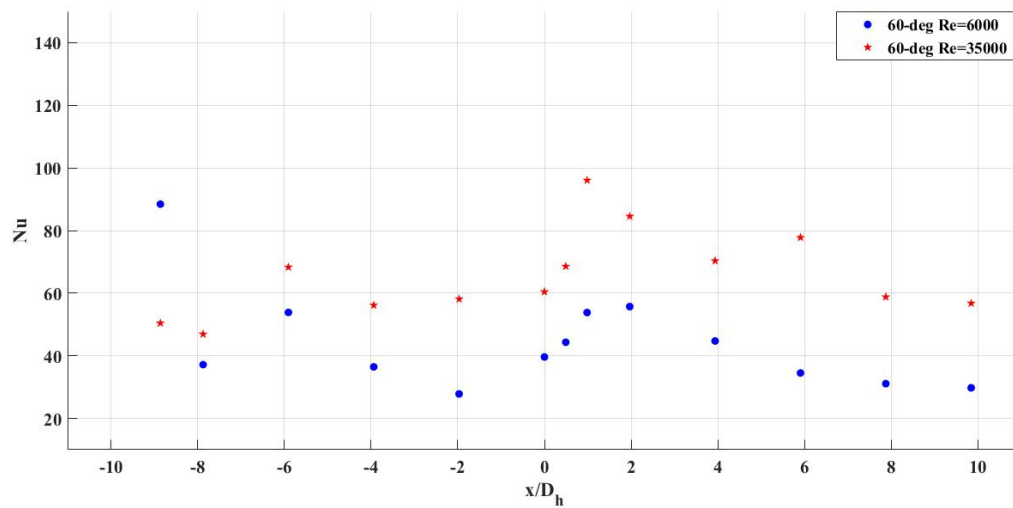


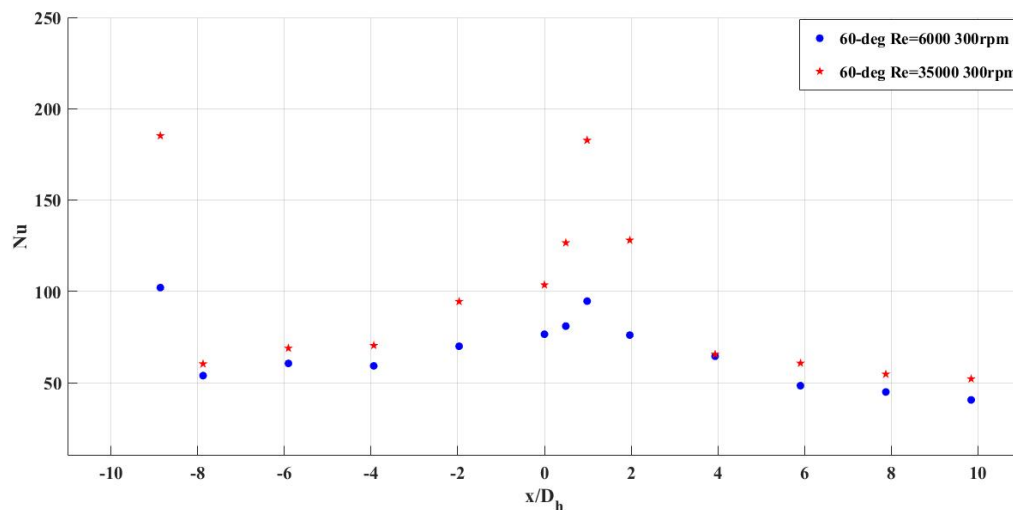
Figure 4-14: Experimental Nusselt number distribution along the channel for a U-Bend Channel (a) Stationary $Re=6000$ (b) Rotational cases $Re=6000$, and $\omega=300$ rpm

4.4.2.3 60-degree ribbed wall Validation

Figure 4-15 shows the Nusselt number distribution along the channel with 60-degree parallel ribs installed on the bottom wall. Both Reynolds number 6000 and 35000 results were presented for stationary cases. Similar to the previous results, increasing the Reynolds number increased the Nusselt number, especially near the bending region. Rotational results at 300 rpm with different Reynolds numbers were presented. For the rotational cases, it can be concluded in constant rotation speed, increasing the Reynolds number increased the Nusselt number.



(a)



(b)

Figure 4-15: Experimental Nusselt Number Distribution along the channel with 60 deg parallel ribs for Various Reynolds number and Rotation Speed (a) stationery, (b) Rotation

4.4.2.4 High-Performance V-rib wall Validation

Figure 4-16 describes the Nusselt number distribution for the stationary and rotational channel with V-Shaped ribs. Reynolds number 35000 and rotation speed 300 and 600 employed for this study. Similar to previous results, the Nusselt number increased near the turning region. Furthermore, in a constant inlet condition, increasing the rotational speed increased the Nusselt number. Despite the differences between experimental and numerical results, a similar trend can be observed.

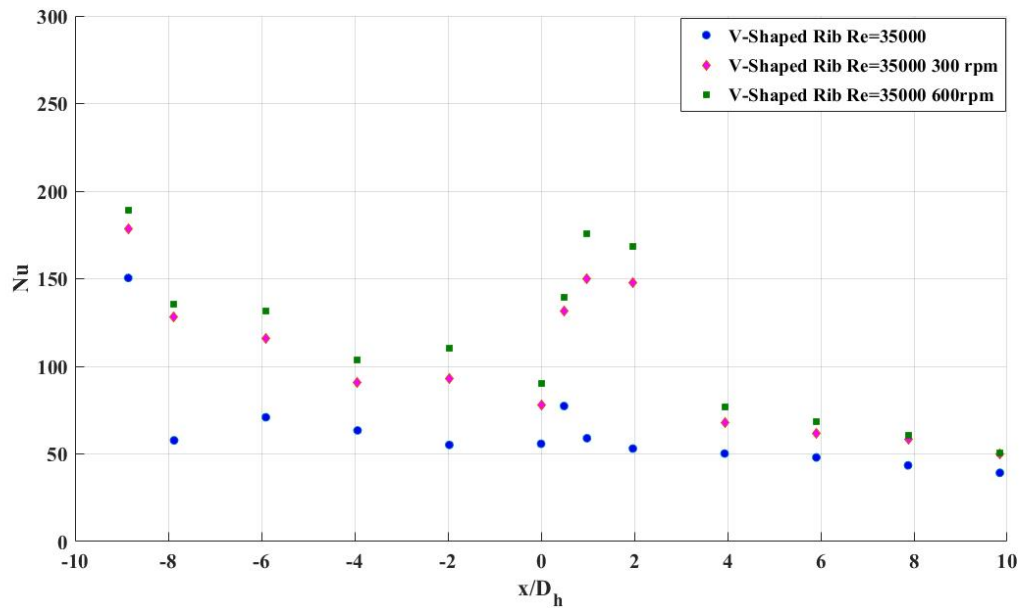
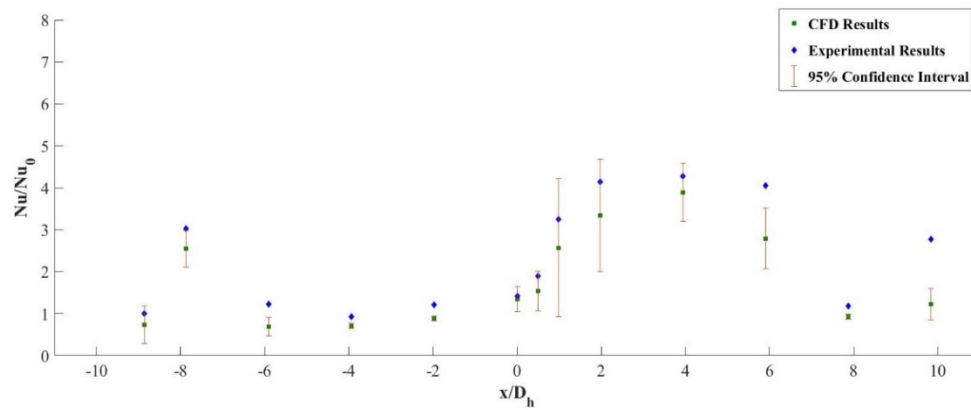


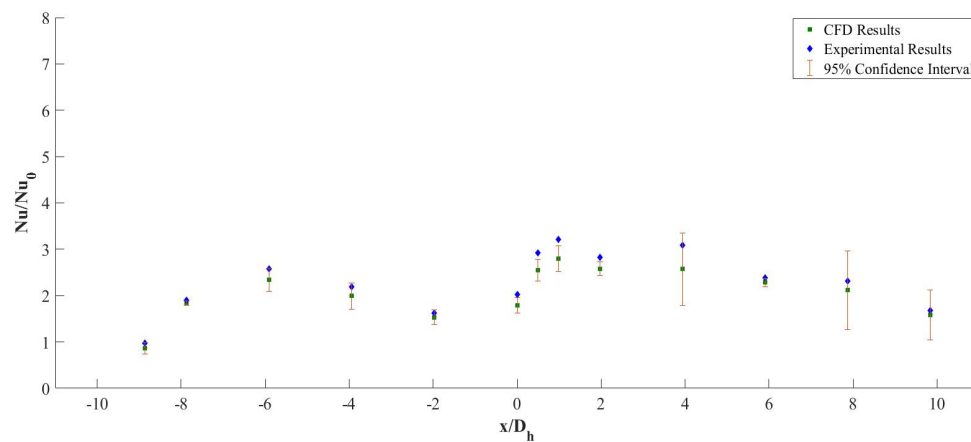
Figure 4-16: Experimental Nusselt Number Distribution along the channel with V-Shaped ribs for Various Reynolds number and Rotation Speed

4.4.2.5 Guide Vane with Parallel 45-deg rib Validation

Figure 4-17 presents the Nusselt ratio (Nu/Nu_0) on the bottom wall at various locations for both experimental and CFD analysis for one guide vane after the bend design. The test was run for the Reynolds of 6000 and a rotation number of 0.75. It can be seen both rotational and stationary results are in good agreement with the numerical results. Similar to previous cases, the sensitivity analysis was obtained built on a 95% confidence level, and the standard deviations are used to determine the scatter bars.



(a)



(b)

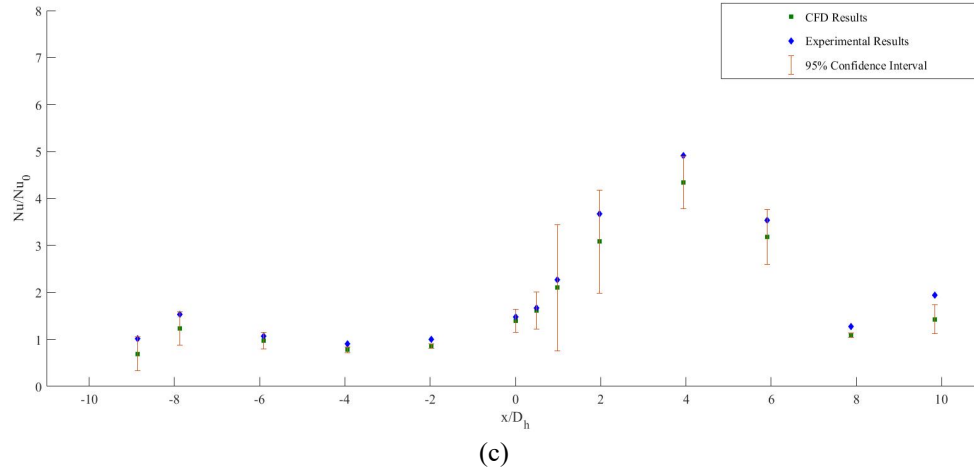


Figure 4-17: Comparison of Nusselt number ratio results for the experimental and CFD for case V1 (a) Stationary $Re=6000$ (b) Stationary $Re=35000$, (c) Rotational $RO=0.75$

As it showed, the Nusselt number had a slight increase in the first passage. After reaching the turning region, the guide vane creates more turbulence and circulations in the turning region, which causes an increase in the Nusselt number ratio in this area. After the bending zone, the Nusselt number starts to decrease smoothly.

4.5 Conclusions

The experimental results were used to validate the numerical findings. A 95% confidence level was used for the error analysis. Despite the variance between the numerical and experimental data, the overall trend was similar for all cases. It has also been observed for the rotational cases that there is more improvement in the Nusselt number ratio compare with the stationary cases. This improvement may be the result of buoyancy and centrifugal forces induced due to the rotation.

Differences between provided airflow rate in experiment and CFD can be the main factor for the inconsistency between the two sets of data. Furthermore, for the CFD analysis, these Nusselt numbers corresponded to the center-point of each cross-section, while for the experimental study, the exact location of the thermocouple probes may have been slightly

different. This effect can be pronounced, especially near the bend region, where higher gradients of temperature are expected. The Nusselt number ratio trend along the channel for stationary cases was similar to the previous study performed by Kumar[93]. However, the operating conditions were different, thus comparing the actual results might not give an accurate comparison.

5 Heat Transfer Investigation for a Two-Passage Smooth Wall Channel

Two-Passage (Smooth and Ribbed wall) channel physical model and numerical set up were presented in chapter 3. In this chapter, a detailed investigation on the effect of Reynolds number, rotation number, and wall heating condition (density ratio) in a smooth wall channel is presented.

5.1 Effect of Reynolds number in Smooth Wall Channel

As mentioned in the literature survey, the Reynolds number has a significant impact on the Nusselt number. Reynolds number can be calculated from Equation 5-1.

$$Re = \frac{\rho U D_h}{\mu} \quad \text{Equation 5-1}$$

In this study, first, the effect of Reynolds number on a stationary and rotational smooth channel investigated. Table 5-1 and Table 5-2 show the cases that have been run in CFD simulations for stationary and rotation motion, respectively.

Table 5-1: Stationary Cases Parameter Used for Computation and Experiments

Case#	1	2	3	4	5
Rotation speed (RPM)	0	0	0	0	0
Rotation number Ro	0	0	0	0	0
Inlet velocity Vin (m/s)	2.12	3.12	4.15	6.25	12.5
Reynolds Number	6,000	9,000	12,000	18,000	35,000

Table 5-2: Rotational Cases Parameter Used for Computations and Experiments

Case#	6	7	8	9	10	11	12
Rotation speed (RPM)	300	600	300	600	600	600	1500
Rotation number Ro	0.75	1.5	0.38	0.77	0.51	0.25	0.64
Inlet velocity Vin (m/s)	2.12	2.12	4.15	4.15	6.25	12.5	12.5
Reynolds Number	6,000	6,000	36,000	12,000	18,000	35,000	35,000

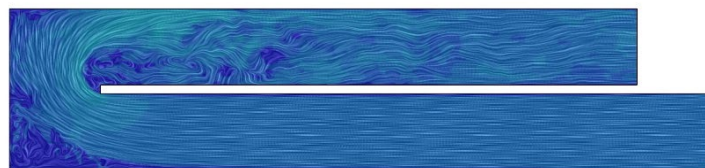
5.1.1 Numerical Results

5.1.1.1 Stationary Cases

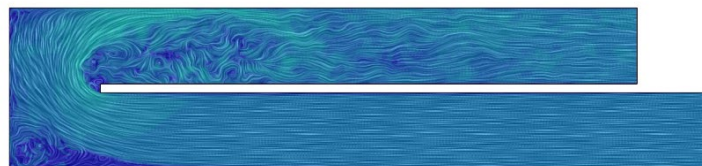
The velocity contours at the horizontal mid-plane for all the stationary cases are presented in Figure 5-1.

All the stationary cases had the same general velocity pattern; it started with a rather uniform velocity distribution in the first leg, followed by similar fluctuations in the bend section. The flow became more irregular in the second leg due to the continuous generation and decay of the vortices. Turbulent vortices generated in the second leg can be detected by investigating the contours of velocity magnitude.

For the stationary case with the highest inlet velocity (case e), there was a significant increase of velocity magnitude in the bend region and the second leg. A large recirculation zone is also identified immediately after the bend. However, as the inlet velocity decreases (cases a and b), the size and the form of the recirculation zone changes.



(a)



(b)

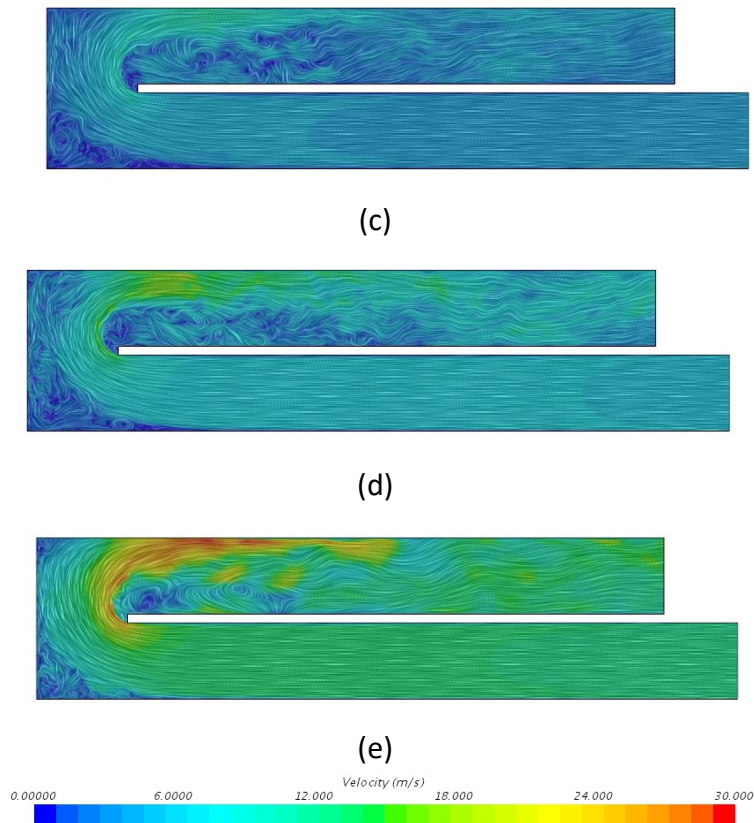


Figure 5-1: Velocity magnitude contours (U_{in}) at the horizontal mid-plane for stationary cases (a) $Re=6000$, (b) $Re=9000$, (c) $Re=12000$, (d) $Re=18000$, and (e) $Re=35000$

To better visualize the mixing effect, the contours of normalized velocity magnitude, along with some in-plane streamlines, are presented below.

Figure 5-2 to Figure 5-6 show eight different normal planes that are defined along the channel for this purpose. For the stationary case, the velocity is quite uniform in the first pass, and there is no evidence of recirculation. On the contrary, the presence of the vortical structures and secondary flow patterns is evident in the second pass. The highest velocities are observed near the walls immediately after the completion of the bend (plane 6). However, the secondary flow continues to appear to the end of the second pass.

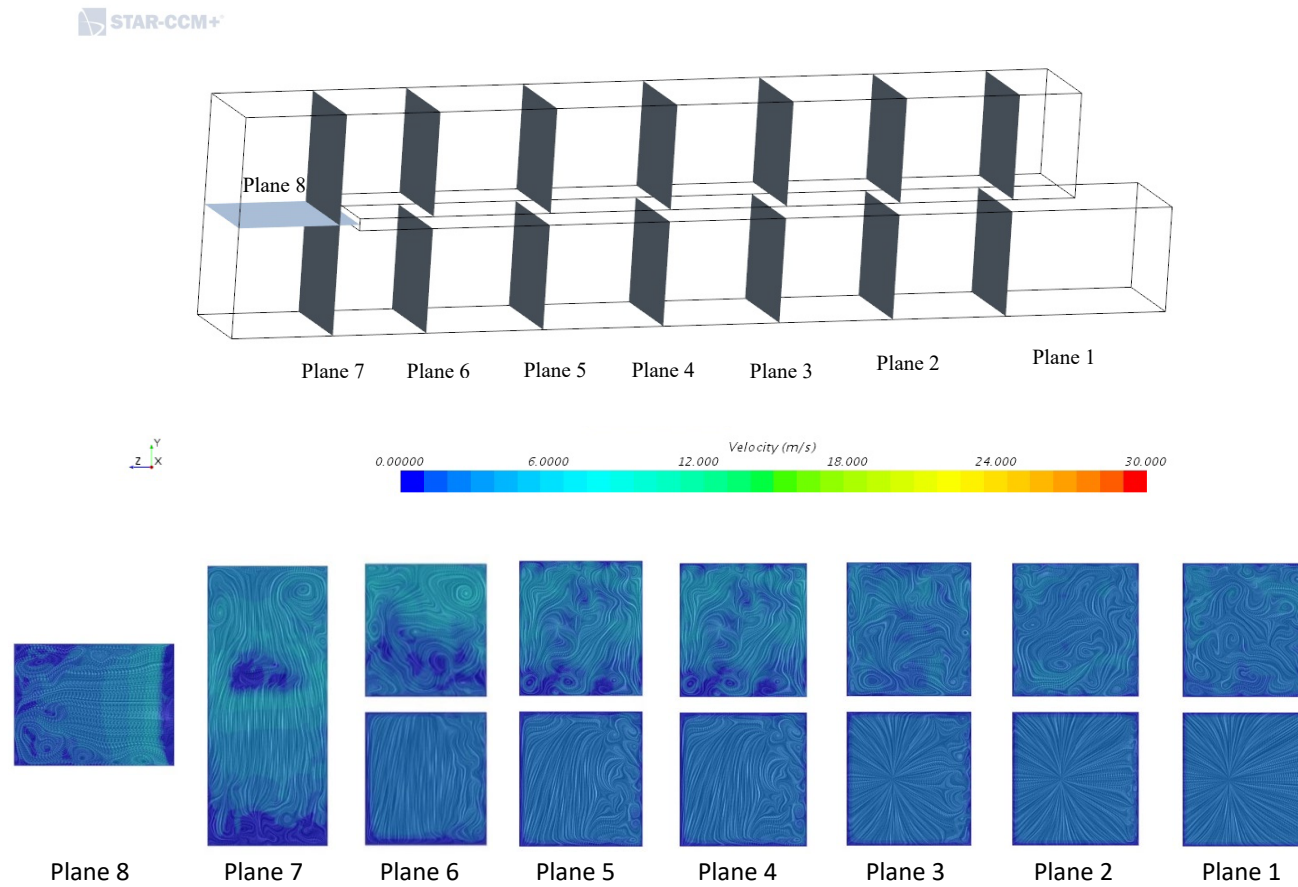


Figure 5-2: Velocity contours on the normal planes $Re=6000$

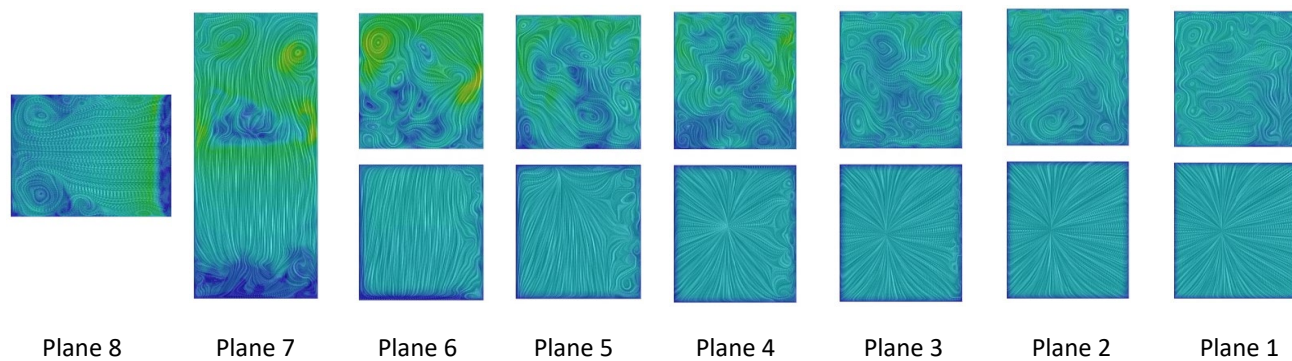


Figure 5-3: Velocity contours the normal planes, $Re=9000$

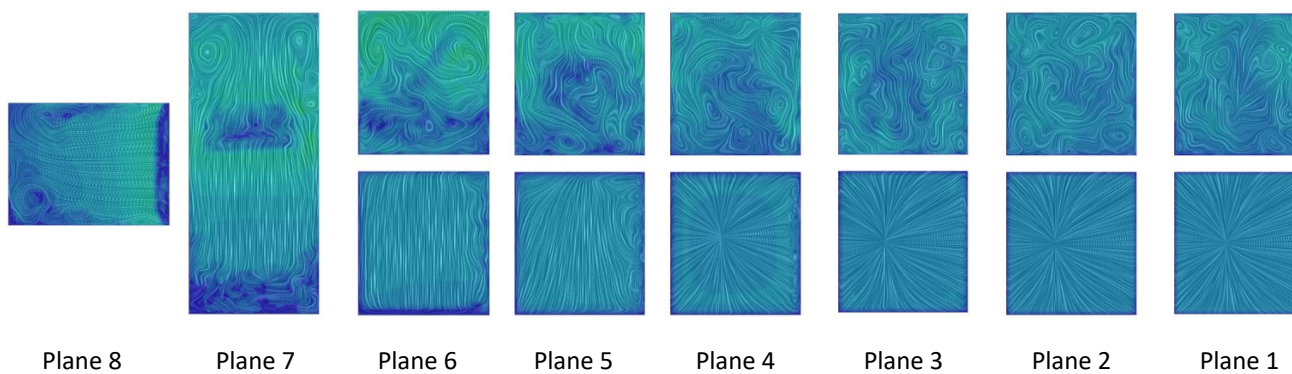


Figure 5-4: Velocity contours on the normal planes, $Re=12000$

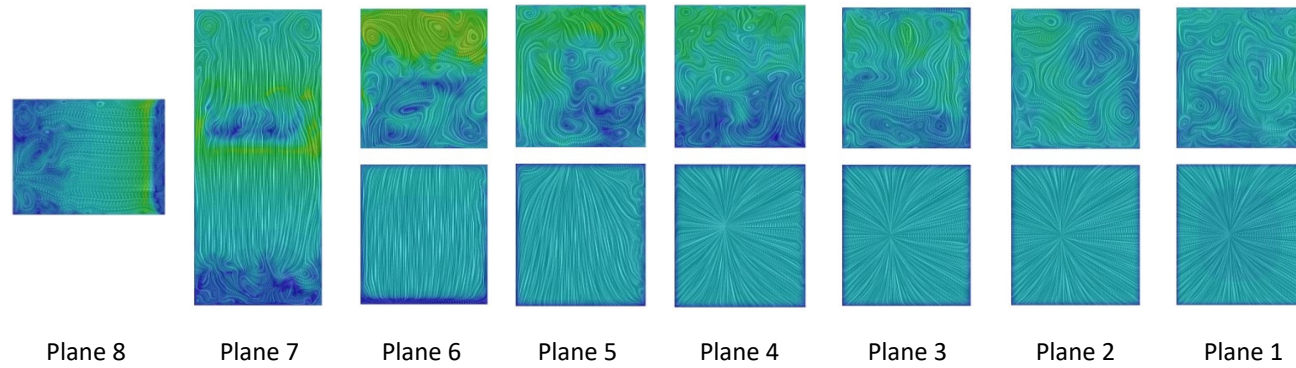


Figure 5-5: Velocity contours on the normal planes, $Re=18000$

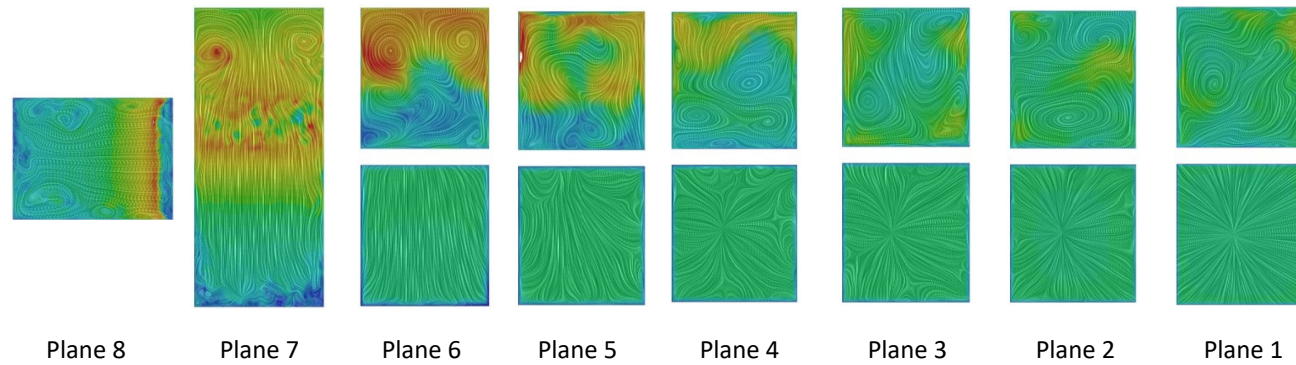


Figure 5-6: Velocity contours on the normal planes, $Re=35000$

In stationary cases, the heat transfer coefficient is mainly dependent on the Reynolds number. Figure 5-7 describes the local time-averaged Nusselt number along the channel in different Reynolds numbers for stationary channels. In the smooth wall channel, by increasing the Reynolds number, in the first leg, the Nusselt number slightly increased. Then in the bend region, because of increasing the turbulence and recirculation, the Nusselt number increased significantly. After the bending area, the Nusselt number started decreasing. However, it is still more than the Nusselt number in the first channel.

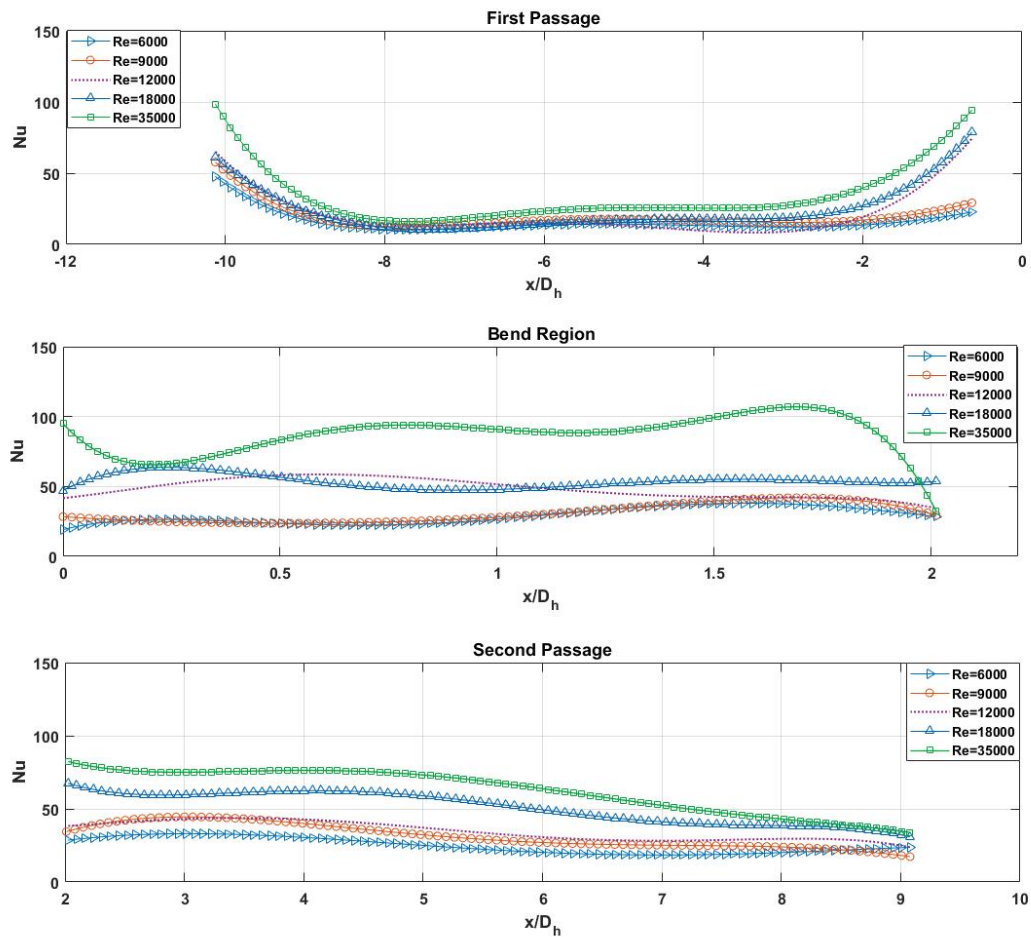


Figure 5-7: Nusselt number augmentation along U-shape channel for different Reynolds number (a) First Passage, (b) U-bend Region, (c) Second Passage

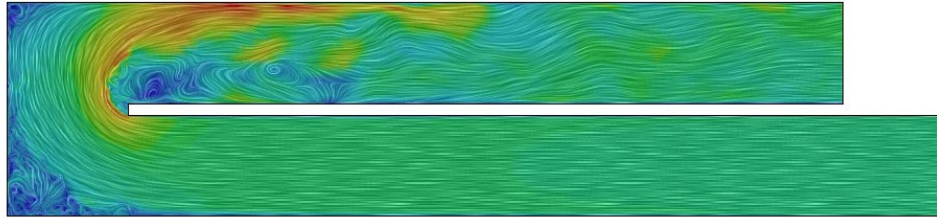
As can be seen, as flow passed through the first passage, the Nusselt number decreased, and by reaching the turning region, the turbulence increased, which resulted in a significant increase in the Nusselt number. As flow entered the second passage, the velocity of the flow decreased, which decreased the turbulence and the Nusselt number; however, the Nusselt number in the second passage is still higher than the Nusselt number in the first passage. It can be observed that an increase in the Reynolds number has a direct effect on the Nusselt number enhancement. Due to the absence of the Coriolis and centrifugal forces in stationary cases, the symmetrical flow field was observed in all the stationary cases.

One of the objectives of this study is to develop a correlation for calculating the Nusselt number for a fully developing flow in a stationary channel. Numbers of numerical and experimental investigations were performed for a square inlet cross-section. Various heat flux was applied at the bottom wall. At each constant heat flux flow, flow behavior for different velocity inlet was investigated. Based on the CFD and experimental results, the correlation of $Nu = 0.086 Re^{0.68}$ was developed for this channel.

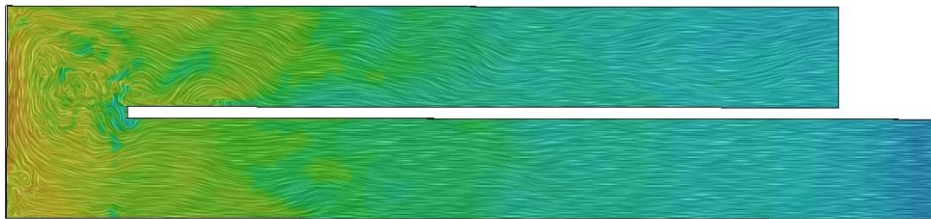
5.1.1.2 Rotation Cases

The rotation has a significant effect on the Nusselt number along the channel due to centrifugal and buoyancy forces induced in this motion. Coriolis forces generate cross-stream flow patterns. In the first passage, this flow patterns leans the cooling flow to the trailing surface, while in the second passage, it moves the coolant to the leading surface. Figure 5-8 shows the vector velocity contour at the middle plane for both stationary and rotational cases for the same Reynolds number. The flow behavior in the rotational cases was significantly different. In the rotational motion, the higher rate of mixing caused a more uniform velocity

distribution along the channel, especially in the bending region compared with the stationary cases.



(a)



(b)

Figure 5-8: Vector velocity contours comparison at horizontal mid-plane for (a) stationary case with $U_{in} = 4.15$ m/s and (b) rotating case with $U_{in} = 4.15$ m/s and $\omega = 300$ rpm

In rotational motion, combined effects of physical parameters such as Reynolds number, heating condition, and rotational speeds brings complexity to the heat transfer study in internal channels. Thus, to have a better understanding of the rotational effects, the heating condition was assumed to be identical in all the cases, and constant heat flux of 2700 W/m^2 was only applied to the bottom wall. Three different test conditions were organized as follows. First, for the same rotational speed, flow with different Reynolds numbers entered the channel. Then in

a constant Reynolds number, various rotational speeds were applied to the channel. For the last part of the study, the combined effect of rotation and Reynolds number was investigated.

Figure 5-9 shows the local time-averaged Nusselt number distribution along the smooth wall channel at the constant rotational speed of 600 rpm. In the first passage, due to the thermal entrance effects, the Nusselt number was higher near the inlet, while it decreased along the channel. In the bending region, the U-turn induced the additional secondary flow vortices. This increased the Nusselt number regardless of the Reynolds numbers and started decreasing in the second channel. It can be concluded that in the same rotational speed, Nusselt number behavior is independent of the rotation number changes.

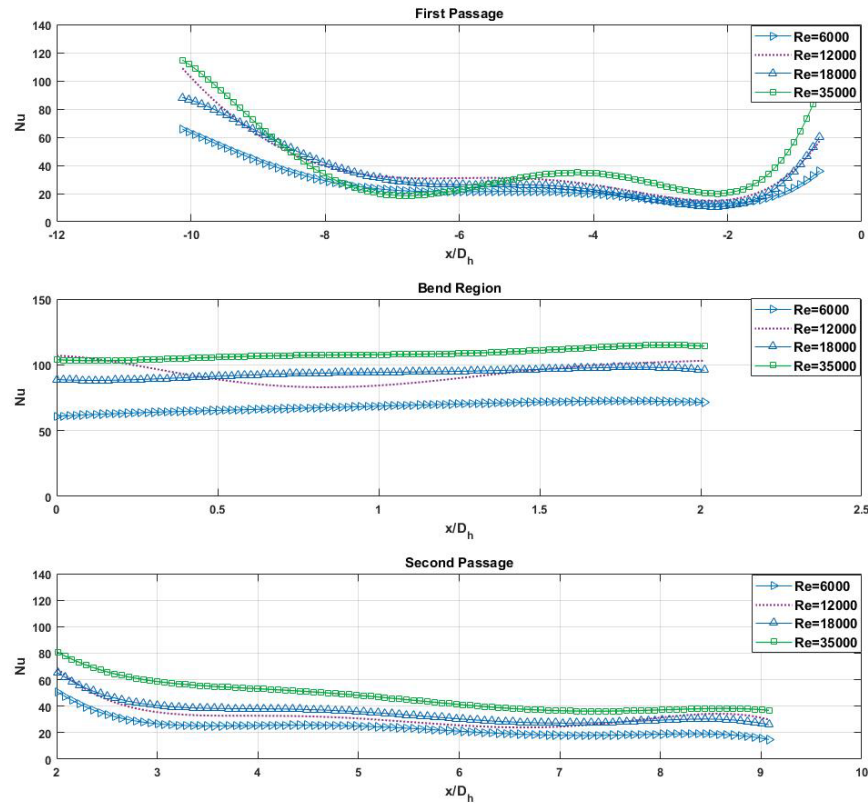


Figure 5-9: Effect of Reynolds number on the Nusselt number in the same rotational speed $\omega = 600$ rpm
(a) First Passage, (b) U-Turn Region, (c) Second Passage

Same as the stationary cases, in a constant rotational speed, increasing the Reynolds number increased the local time-averaged Nusselt number. However, in the same Reynolds number and different rotational speeds, the local time-averaged Nusselt number is much dependent on the Rotation number. Figure 5-10 shows the local time-averaged Nusselt number along the rotational smooth wall channel for the Reynolds number of 35,000.

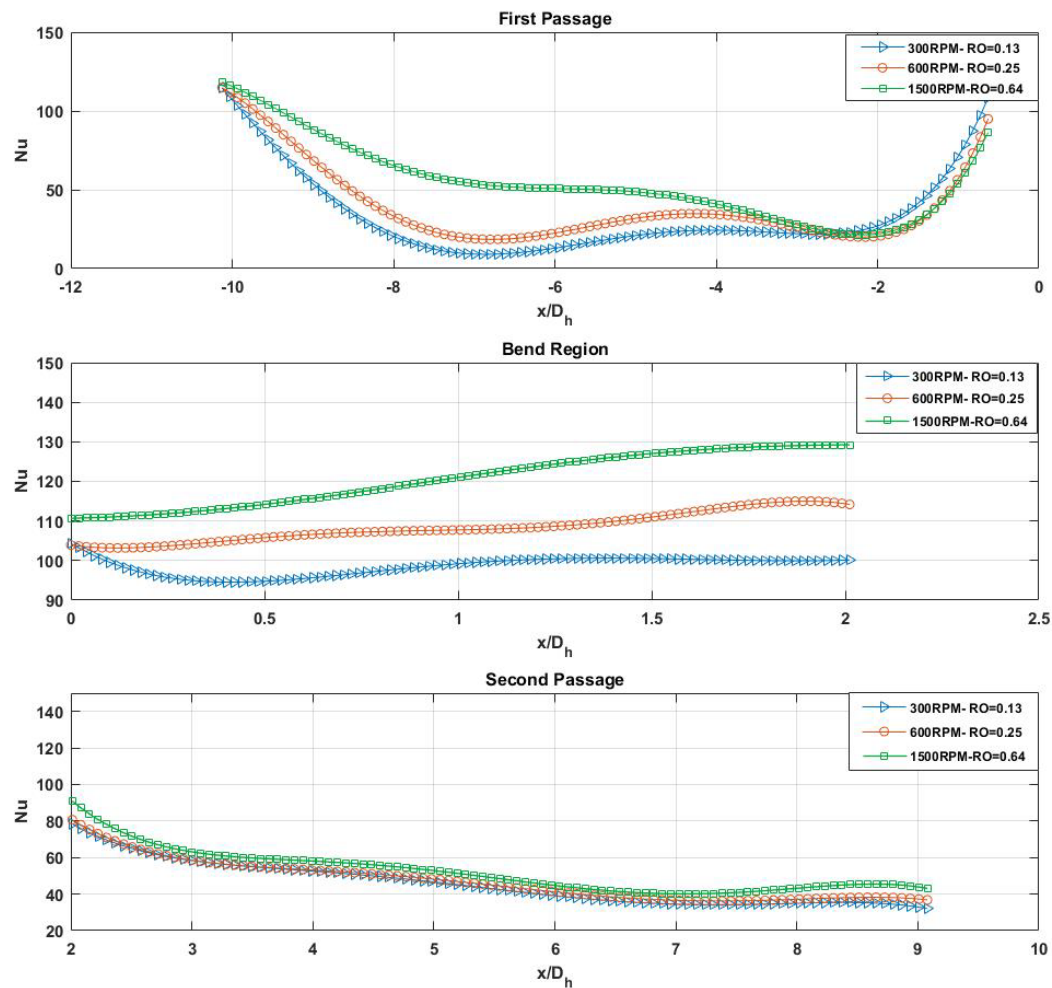


Figure 5-10: Effect of rotational speed on the Nusselt number with the same Reynolds number $Re = 35000$ (a) First Passage, (b) U-Turn Region, (c) Second Passage

Figure 5-11 describes the combined effect of Reynolds number and rotational speed. From the results, it can be concluded that the increase in both parameters was in favor of increasing the heat transfer coefficient. Increasing the rotational speed increased the rotation number, which resulted in an increase in the heat transfer coefficient in both passages.

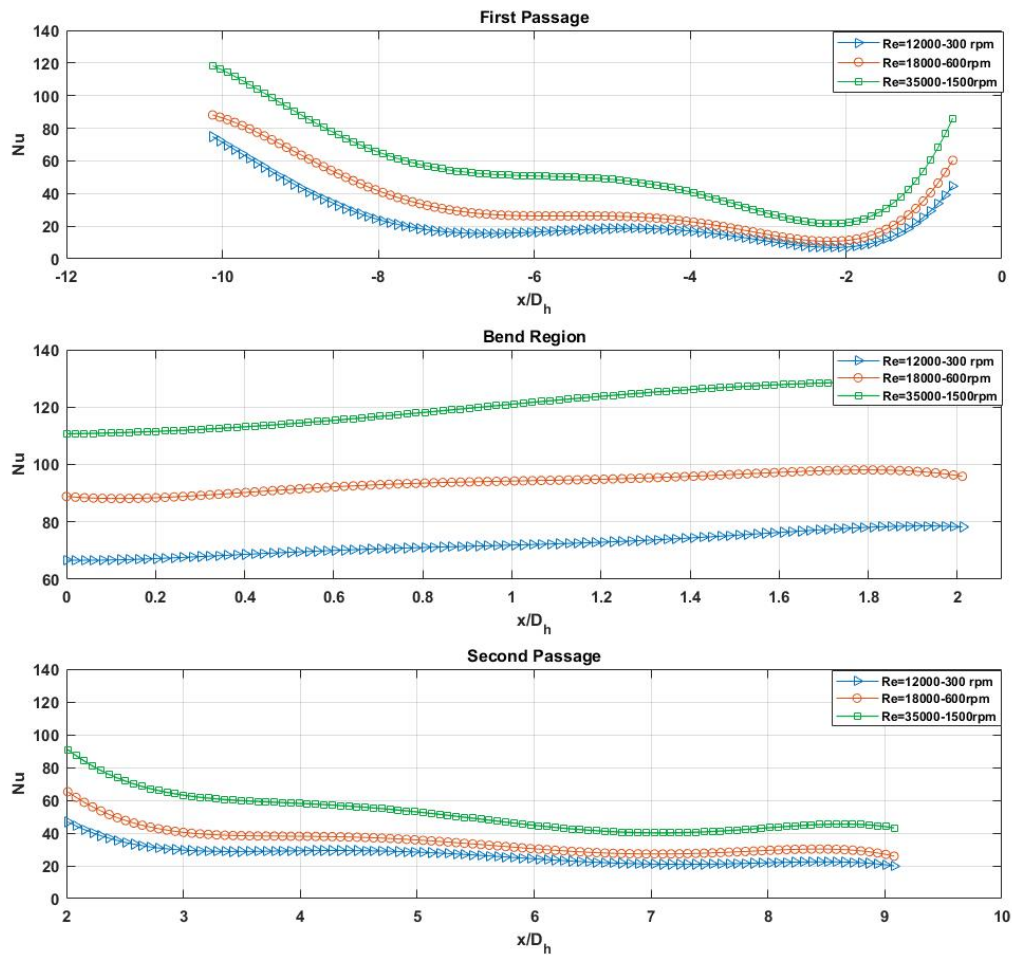


Figure 5-11: Combined effects of rotational speed and Reynolds number on the Nusselt number (a) First Passage, (b) U-Turn Region, (c) Second Passage

5.1.1.3 Pressure Drop Comparison

Another critical factor that needs to be considered in investigating the flow behavior in the cooling channel is the pressure losses. The pressure drop effects can be presented by calculating the friction factor. The friction factor, f , can be represented by the fanning factor in Equation 5-2 [31].

$$f = \left(\frac{D_h}{2L} \right) \left(\frac{\Delta p}{\rho U_m^2} \right) \quad \text{Equation 5-2}$$

In order to present the normalized friction factor, in this study, the correlation which was proposed by Blasius [24] for the friction factor in a smooth circular tube was used, Equation 5-3.

$$f_0 = 0.079 \text{Re}^{-0.25} \quad \text{Equation 5-3}$$

Where L is the channel length, ρ is the cooling air density. Figure 5-12 presents the numerical results for the friction factor ratio for the rotational and stationary motion for different Reynolds numbers. It can be seen the secondary flow induced due to the rotation and existence of buoyancy forces reduces the friction factor compared with the stationary motion. Furthermore, at the constant rotational speed, increasing the Reynolds number is in favor of reducing the pressure drop.

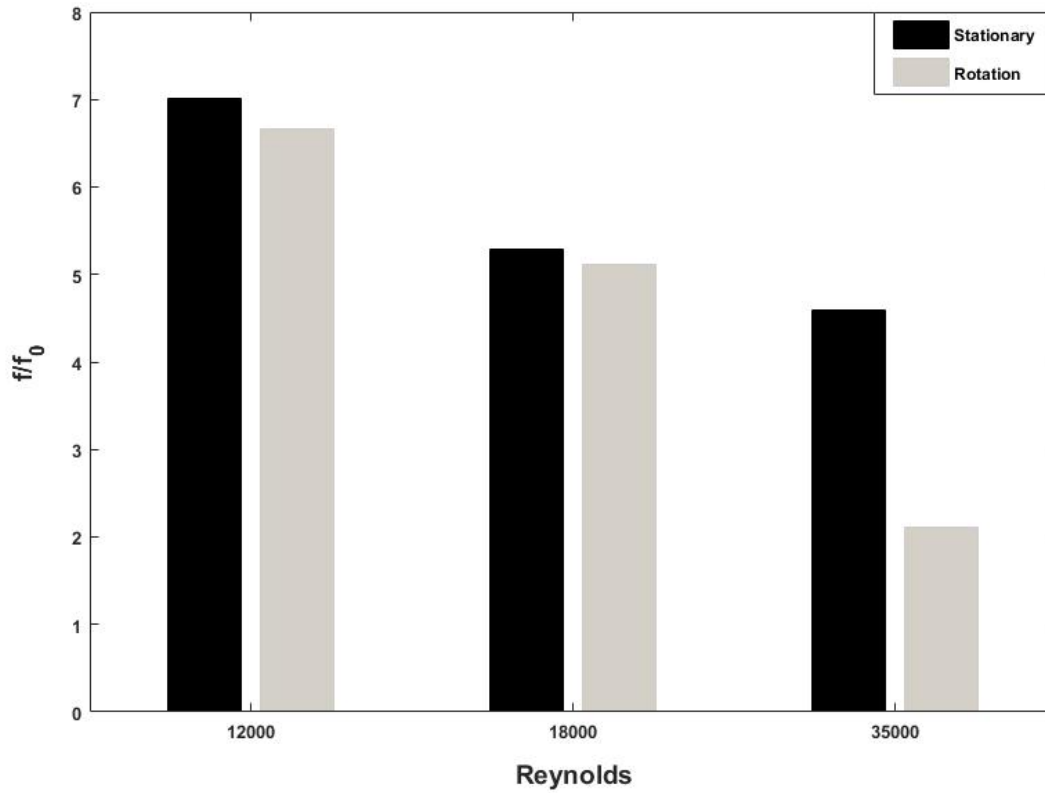


Figure 5-12: Friction factor ratio comparison in stationery and rotation cases

5.2 Effect Wall Heating in constant Reynolds number

The Wall heating condition is one of the critical parameters in the study of heat transfer in a U-bend duct. Different heat flux applied to the bottom surface while all the other walls assumed to be adiabatic. By using this boundary condition, the wall heating effect on the heat transfer coefficient studied. For this part of the study, the Reynolds number was constant at 12000. To present the results average density ratio definition used. Local fluid density ratio can be defined by Equation 5-4.

$$\frac{\Delta\rho}{\rho} = \frac{T_w - T_i}{T_w} \quad \text{Equation 5-4}$$

Summary of all the stationary cases and the results are presented in Table 5-3.

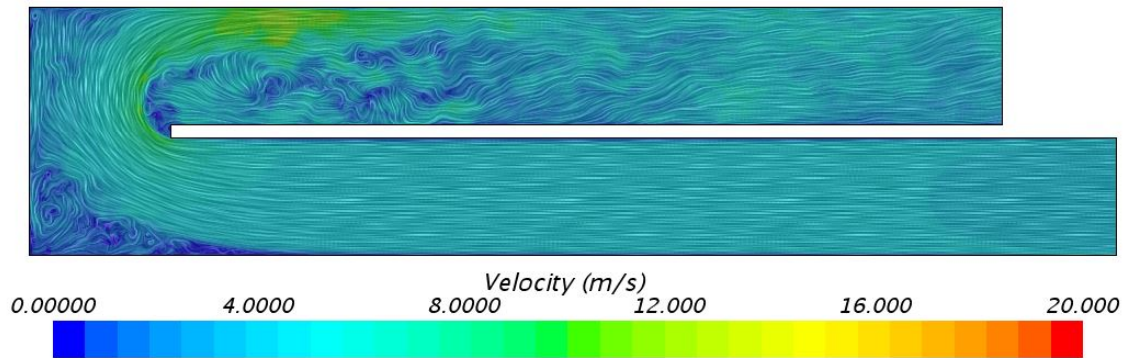
Table 5-3: Summary of Stationary Cases with variable heat flux

Case	Heat	Inlet Velocity	Mean Density
Number	Flux(W/m^2)		Ratio($\frac{\Delta\rho}{\rho}$)
1	2,700	4.15m/s	0.13
2	12,500	4.15m/s	0.49
3	16,200	4.15m/s	1.09
4	25,150	4.15m/s	1.89

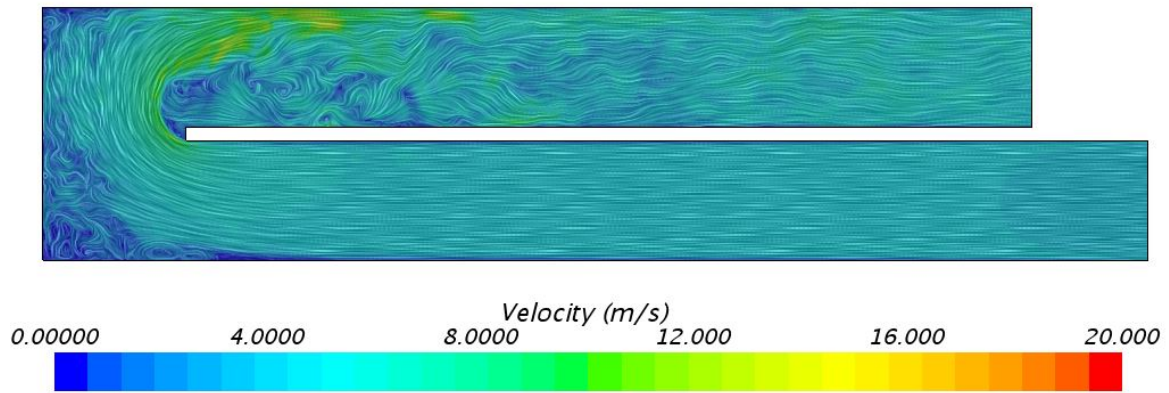
5.2.1 Numerical Results

5.2.1.1 Stationary Results

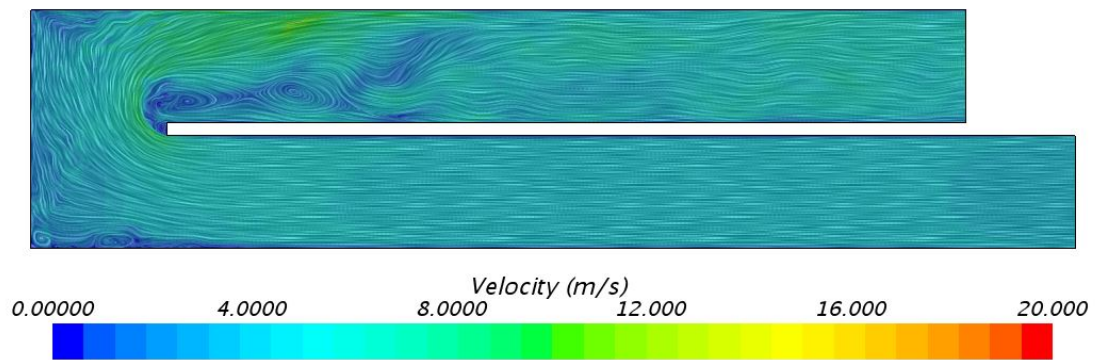
Velocity vectors for all the cases are presented in Figure 5-13. Velocity profile for all cases follow a similar trend. In the first passage, the velocity profile for all the cases showed a uniform pattern. However, in the bending region, as the density ratio increases, more recirculation zone observed. More turbulent vorticities are generated as the flow passes the bending area and enters the second leg.



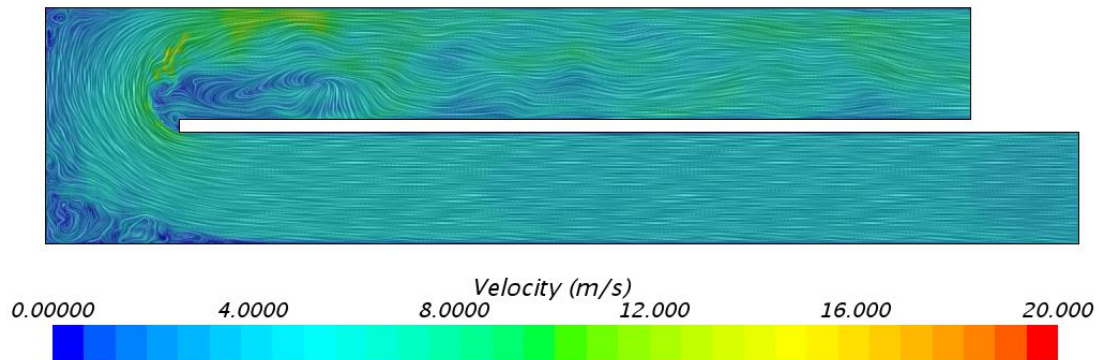
(a)



(b)



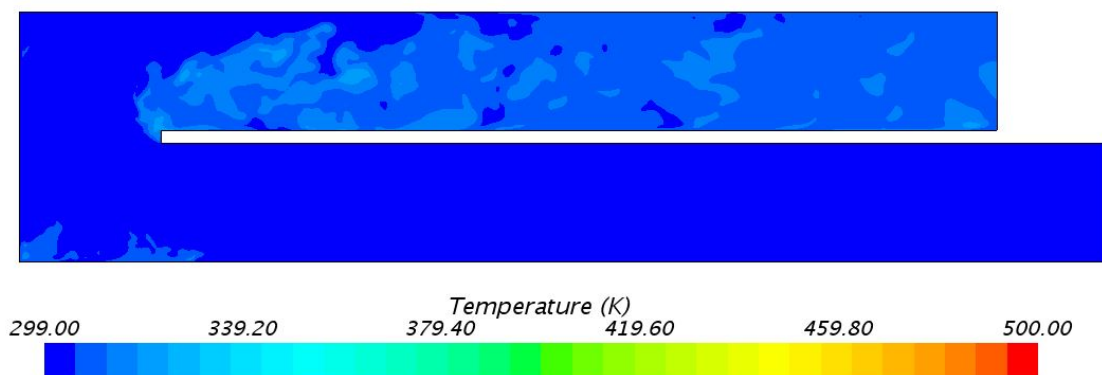
(c)



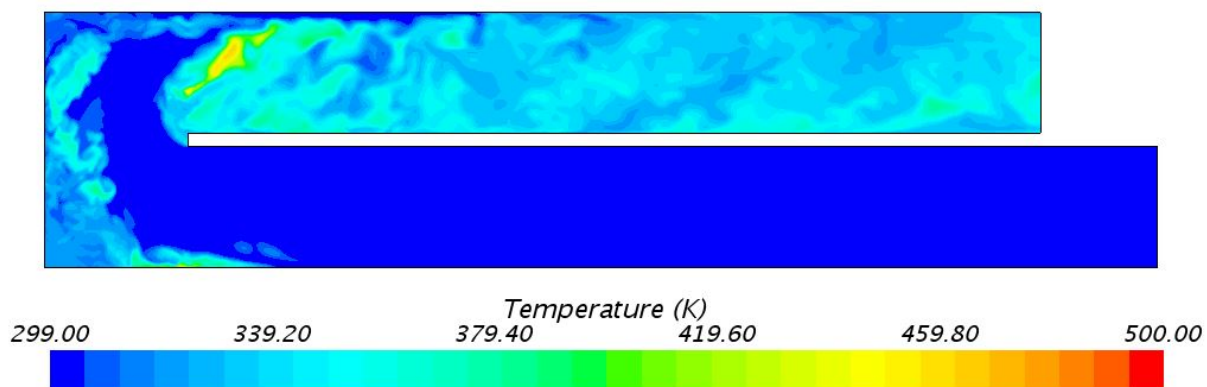
(d)

Figure 5-13: Velocity vectors for (a) $q=2700 \text{ W/m}^2$ (b) $q=12500 \text{ W/m}^2$ (c) $q=16200 \text{ W/m}^2$ (d) $q=25000 \text{ W/m}^2$

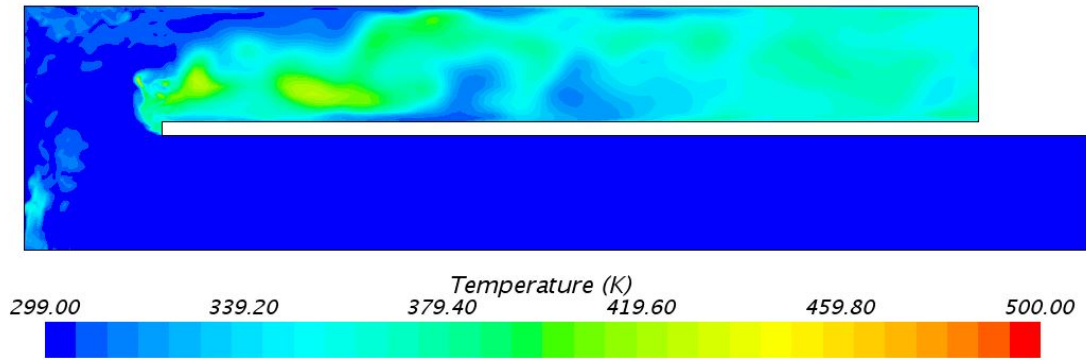
Temperature distribution at the horizontal mid-plane is shown in Figure 5-14, the mid-plane temperature increases along the channel. The increase in the temperature can be the result attributed to the higher local velocities. Also, by increasing the density ratio in the same inlet velocity, increasing the temperature beyond the bending area and second leg, is more significant.



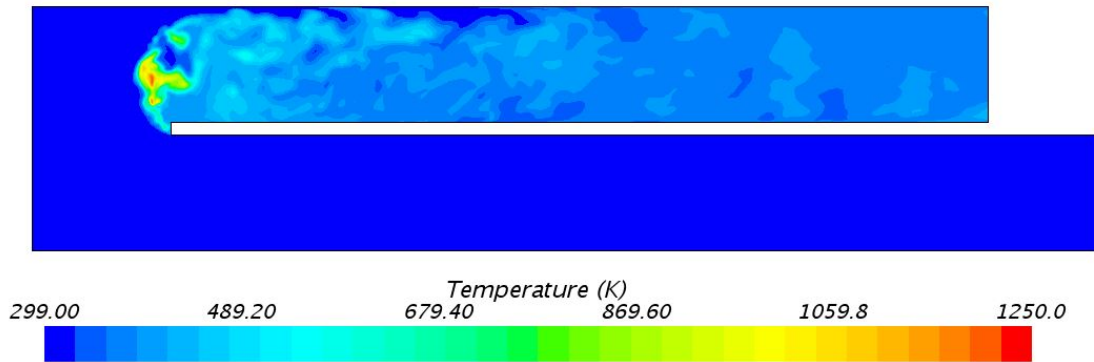
(a)



(b)



(c)



(d)

Figure 5-14: Temperature distribution (a) $q=2700 \text{ W/m}^2$ (b) $q=12500 \text{ W/m}^2$ (c) $q=16200 \text{ W/m}^2$ (d) $q=25000 \text{ W/m}^2$

Figure 5-15 shows the heat transfer augmentation in different density ratios. By changing the wall heating condition and increasing the density ratio, an enhancement in the heat transfer coefficient was observed in the channel, especially in the bend area.

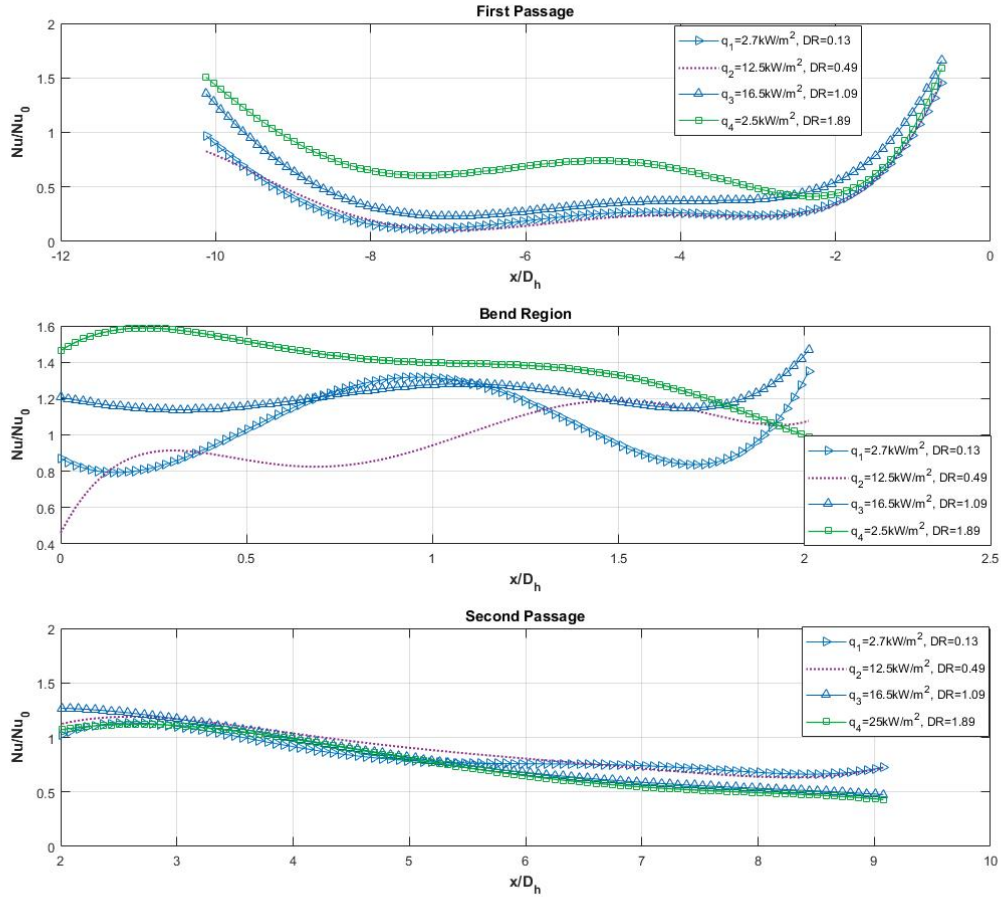


Figure 5-15: Heat transfer augmentation along a smooth wall U-shape channel in different heat flux- Stationary case

5.2.1.2 Rotational Results

Besides the geometry challenges in the turbine cooling technologies in a rotating channel, effects such as Buoyancy forces play a significant role in the heat transfer trend in the cooling channel. In order to investigate the impact of rotation on the heat transfer coefficient, it is essential to know the relationship between Nusselt number, Buoyancy number, and rotation number [53], [55], and [95].

$$Nu_i = f\left(\frac{x_i}{D_h}, Re, Ro, Bo\right) \quad \text{Equation 5-5}$$

$$Re = \frac{\rho U D_h}{\mu} \quad \text{Equation 5-6}$$

$$Ro = \frac{\Omega D_h}{U} \quad \text{Equation 5-7}$$

$$Bo_x = \left(\frac{\Delta\rho}{\rho}\right) \cdot Ro^2 \cdot \frac{x_i}{D_h} \quad \text{Equation 5-8}$$

$$Nu_0 = 0.023 \cdot Re^{0.8} \cdot Pr^{0.4} \quad \text{Equation 5-9}$$

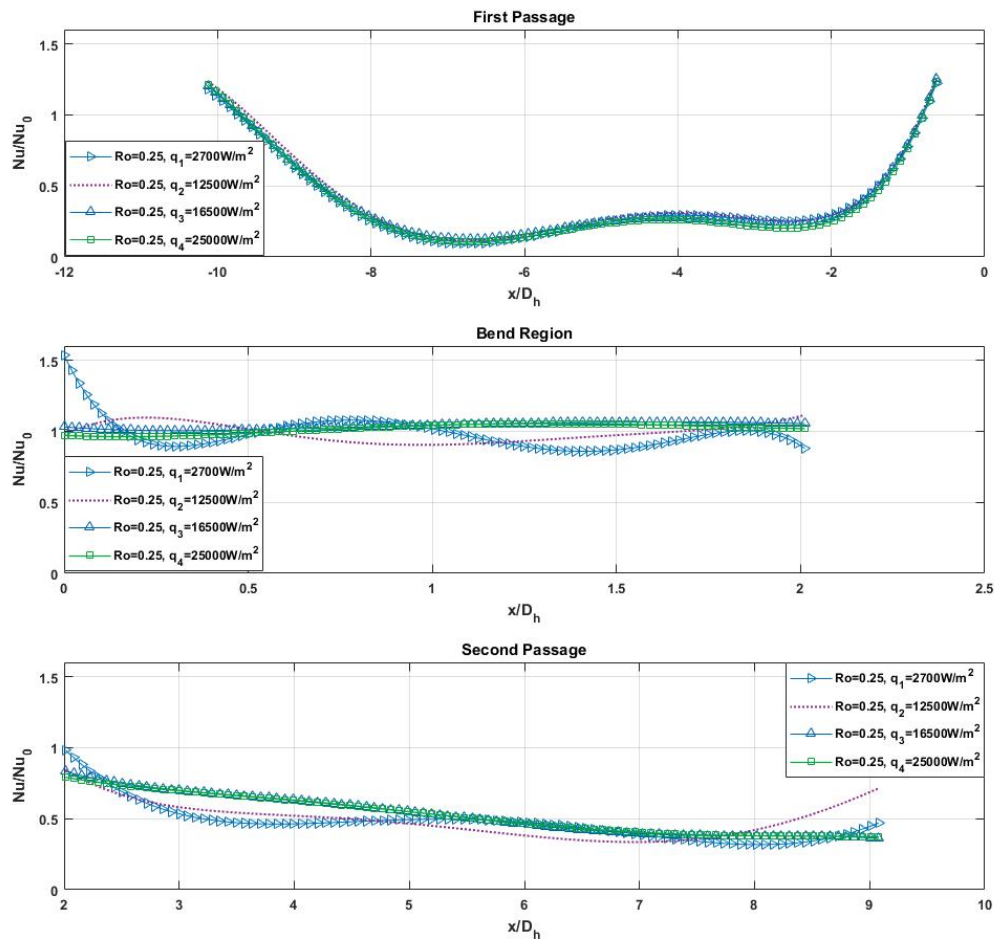
Typically, heat transfer in a two-Passage Channel was studied at different rotational numbers. Table 5-4 describes the rotation cases for this study. As shown in Equation 5-8, Buoyancy is a function of wall heating condition (density ratio) and rotation number. Thus, in this study for each rotation number, different constant heat fluxes were applied to the bottom wall, and the Nusselt number distribution was investigated.

Table 5-4: Summary of rotation cases

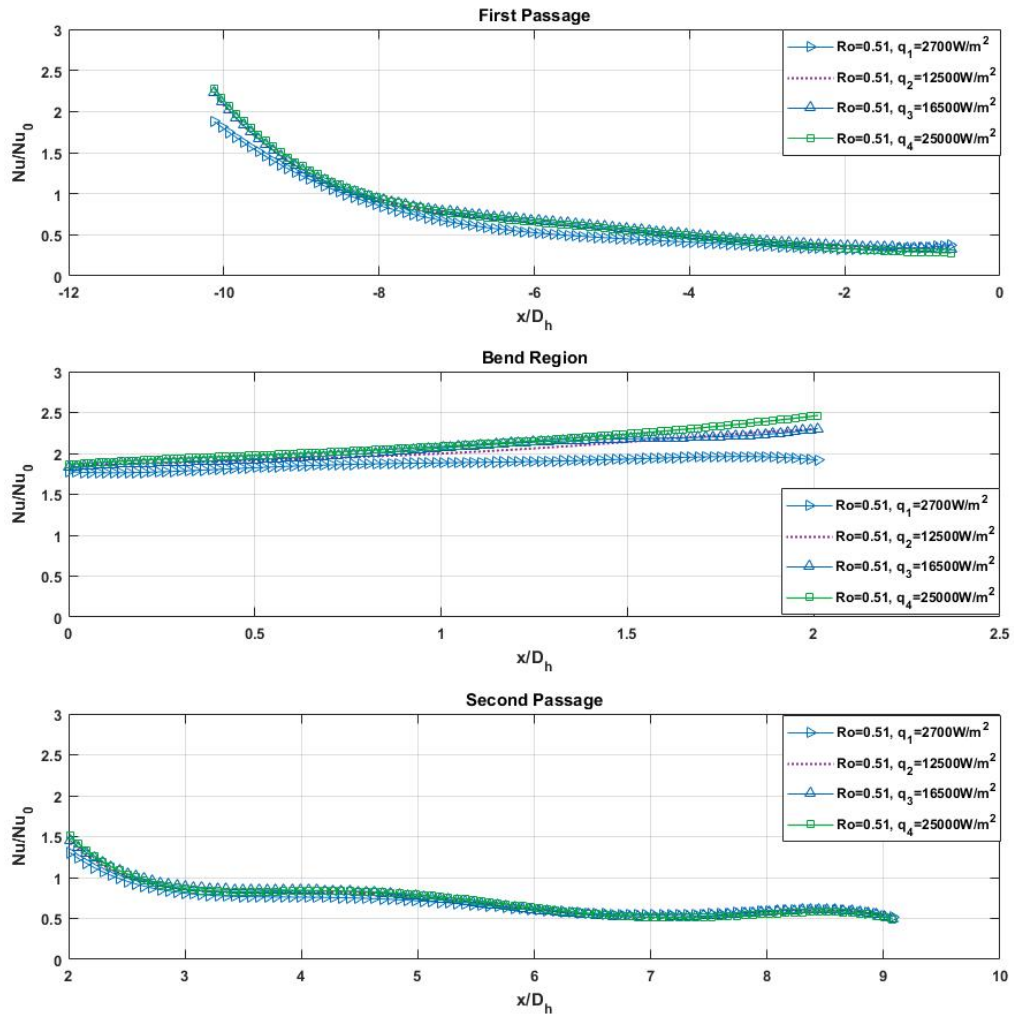
Case#	1	2	3
Rotation speed (RPM)	600	600	600
Angular velocity Ω (rad/s)	62.8	62.8	62.8
Rotation number Ro	0.25	0.51	0.75
Inlet velocity U_{in} (m/s)	12.5	6.25	4.15
Reynolds number	35000	18000	12000

Figure 5-16 describes the average heat transfer augmentation along the heated wall for different rotation numbers and density ratios. As it can be seen in Figure 5-16, by increasing the rotation number in a constant density ratio along the channel, the Buoyancy number increased

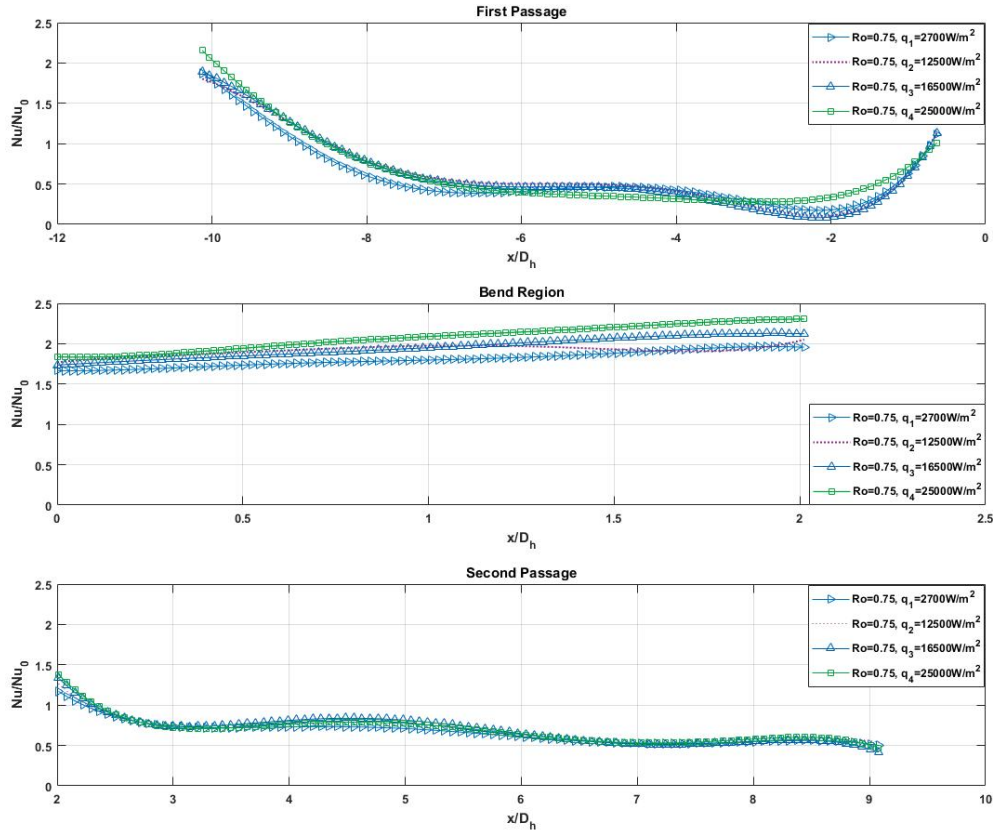
proportionally. Also, in the same rotation number increasing the density ratio increased the Nusselt number. This effect was interpreted that by increasing the buoyancy number, it increased the Buoyancy forces along the channel, which increased the Nusselt number. Considering the fixed rotation ratio and density ratio means the variation in buoyancy number only depended on rotation number. Increasing the rotation number increased the buoyancy number, which increased the Nusselt number ratio. Furthermore, in the bending region, the buoyancy number increased significantly, which followed by increasing the Nusselt number ratio.



(a)



(b)



(c)

Figure 5-16: Heat transfer augmentation along a smooth wall U-shape channel in different rotation number and density Ratio

In rotational motion, many parameters, such as rotational effects, turn effect, Buoyancy, and Coriolis forces, are involved. These effects make the heat transfer analysis difficult. Figure 5-15 and Figure 5-16 show the heat transfer ratio for various rotation speeds. From the figures, it can be seen the heat transfer ratio in a rotating setup increased in comparison with stationary cases. It can be observed in the bending region, because of the more turbulence and vorticities, the Nusselt number is increasing. Moreover, the Nusselt number has a higher ratio in the bend section in comparison with the legs, which means there is more heat transfer taking place in the bend region.

5.3 Conclusion

In this chapter, the effect of several parameters on flow behavior and heat transfer distribution for a two-passage smooth wall internal cooling channel was investigated. A 3-D CFD model using LES was used to obtain the heat transfer trend along the channel. The effect of Reynolds number, wall heating condition was carried out in both stationary and rotational cases. In the rotational cases, a wide range of rotation numbers between 0.25-1.5 was implemented. The conclusions that emerged from this part of the study are

- Based on the simulation and the experimental results for the stationary cases, the correlation of $Nu = 0.086 Re^{0.68}$ was found to be applied for this channel.
- In the stationary cases, the time-averaged Nusselt number enhancement varied from 22 to 53 as Reynolds number increased from 6000 to 35,000.
- Under the constant rotational speed, the variation of the Nusselt number is independent of the rotation number changes. Increasing the Reynolds number enhanced the local time-averaged Nusselt number, which is a similar trend, which was observed in stationary cases.
- In the constant Reynolds number and different rotational speed cases, the local time-averaged Nusselt number is dependent on the rotation number. As rotational speed increased, heat transfer enhancement in both passages was observed.
- The combined effect of the Reynolds number and rotational speed enhanced the buoyancy and centrifugal forces, which results in an improvement in the Nusselt number in both passages. Furthermore, in the bending region, maximum buoyancy force can be

observed, which is one of the main reasons for the significant Nusselt number increase in this region.

- In the rotational motion, buoyancy forces induced the secondary flow, which reduced the friction factor significantly.
- In the stationary cases, as Reynolds number increased, the friction factor ratio decreased from 7 to 5.
- Increasing the wall heating condition (density ratio) in a constant Reynolds number in stationary cases increased the heat transfer ratio along the channel.
- The experimental results showed a good agreement with the CFD result.

6 Heat Transfer Investigation for a Two-Passage Ribbed Wall Channel

In this study, the main objective is to investigate the geometrical factors such as rib geometry and spacing, which usually discussed by rib-pitch-to-rib-ratio (P/e). In this chapter, the geometrical effect for different rib configurations, 90-deg, parallel 45-deg, parallel 60-deg, and high-performance rib, V-shaped rib on heat transfer performance will be discussed. Rib spacing is one of the most critical challenges in designing the rib roughened channels for each rib configuration; the effect of rib spacing using the rib-pitch-to-rib-height ratio of 7, 10, 12, was investigated. Both rotation and stationary motion were investigated. Airflow at 300K with Reynolds number 35000 was entered to the channel. Furthermore, a rotation speed of 300 rpm was used for this part of the study.

6.1 Heat Transfer Distribution Study for 90-deg Rib with Different P/e ratio

One of the first rib turbulator concepts used in cooling channels was utilizing 90-deg ribs. In this study, first, a 90-deg rib turbulator considered as the baseline of the roughened wall. Various rib-pitch-to rib height ratio for both stationary and rotational cases was used. Flow with Reynolds number 35000 and uniform velocity profile entered the channel. Figure 6-1 and Figure 6-2 describe the channel geometry in different views. A constant heat flux boundary condition was applied to the channel bottom wall and ribs placed on this wall.

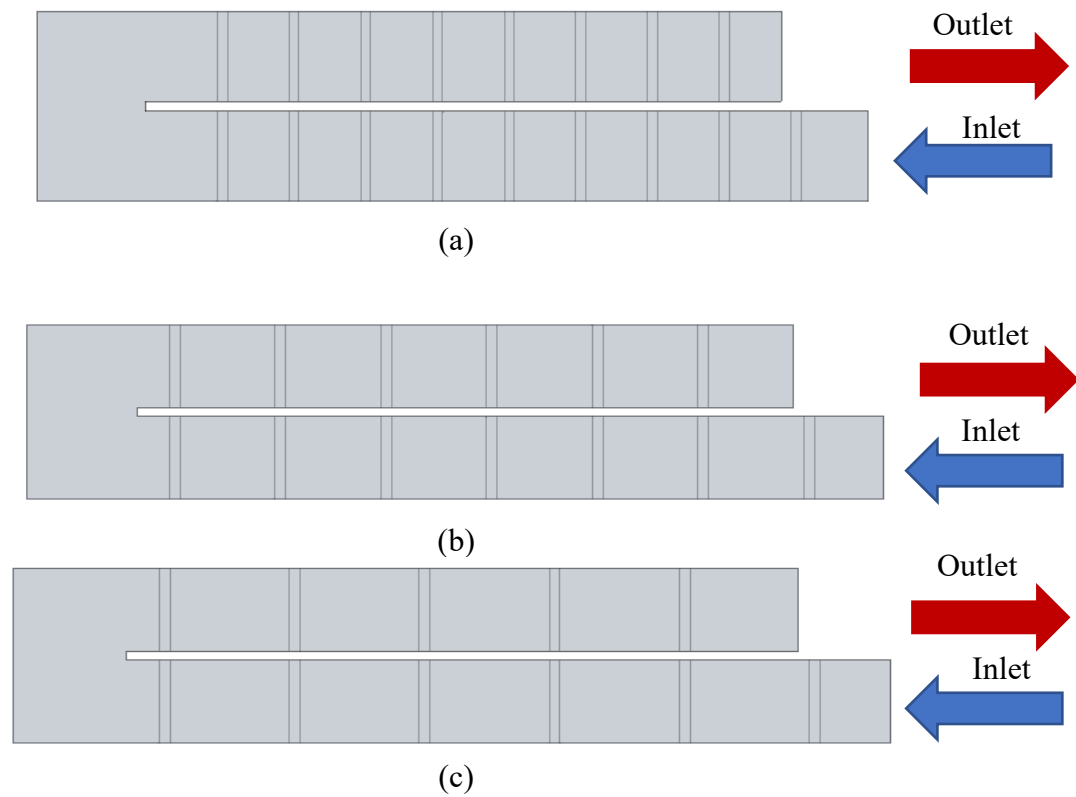
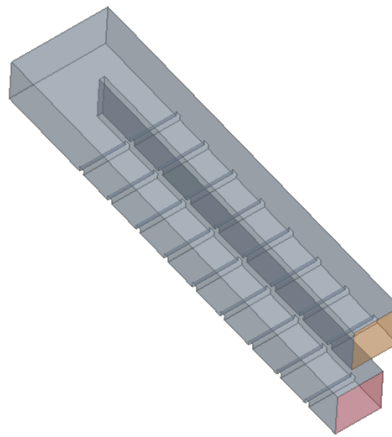


Figure 6-1: : inlet/outlet for Channel with 90-deg rib configuration (a) $p/e=7$, (b) $p/e=10$, (c) $p/e=12$



(a)

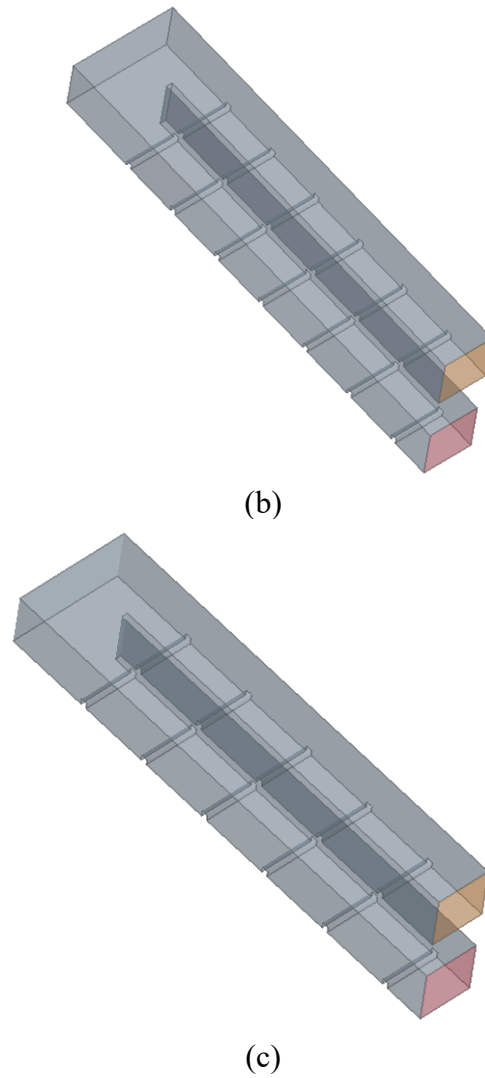


Figure 6-2: Isometric view for Channel with 90-deg rib configuration (a) $p/e=7$, (b) $p/e=10$, (c) $p/e=12$

6.1.1 Stationary Cases

As it was mentioned in the literature review, installing the ribs on the internal surface of the channel generates more turbulent. It increases the rate of mixing hot gases with the cooling air. Figure 6-3, Figure 6-4, and Figure 6-5 show the velocity counter on different channel cross-sections in the stationary channel. Normal plane sections after each rib were utilized to capture the effect of ribs on the flow distribution. For all P/e ratios, as the flow enters the first passage,

symmetrical flow distribution was found in the first passage. As flow reached the turning region, more irregular behavior was observed. This change in mainstream flow behavior increased the flow turbulent. As flow entered the second passage, it lost the symmetrical distribution after turning region; however, as flow distanced from the bending region, the distribution trend became more symmetrical. Despite the similar flow distribution behavior for all P/e ratios, the velocity distribution after each rib is slightly different. For the P/e ratio 10 and 12, the rib blockage affected the velocity near the bottom wall and generated more recirculation zones. While for P/e 7, velocity transformation along the cross-section is more uniform.

This observation can be counted as an excellent example of the importance of the rib spacing in the cooling channels. For P/e 10 and 12, the distance is more than what is needed for flow separation and reattachment in the flow. Therefore, more recirculation zones behind the ribs were observed. While for P/e 7, the flow had enough time to fully separated from the mainstream and re-attached to it again before passing through the next rib.

Figure 6-6 presents the bottom wall temperature distribution along the channel. For the design with P/e 7, due to symmetrical velocity distribution, a better temperature distribution is observed. As a result of higher turbulence in the turning region and the second passage, the temperature is lower in these areas. The lower temperature at the turning region resulted in higher heat removal from these surfaces. For the P/e 10 and 12 ratios, an uneven temperature distribution is observed in two passages. Due to the existence of recirculation zones after each rib in the first passage, less heat was removed from this section resulted in higher surface

temperature. The high temperature at the entrance of the first passage is due to the entrance effect and solver limitation to consider these effects.

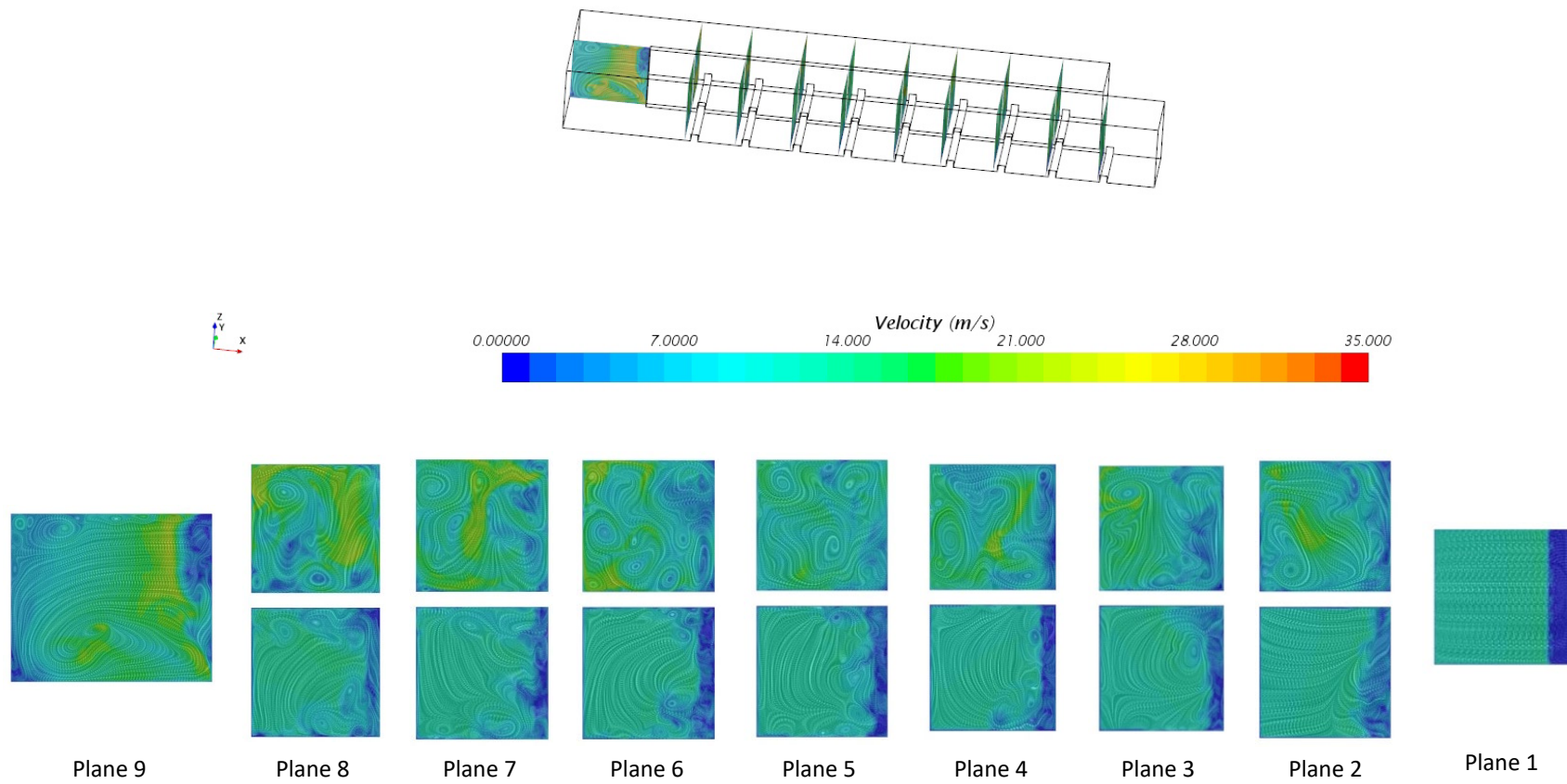


Figure 6-3: Contours of velocity and streamline on the normal planes for 90-deg rib configuration, $P/e=7$ $U_{in}=12.5\text{m/s}$

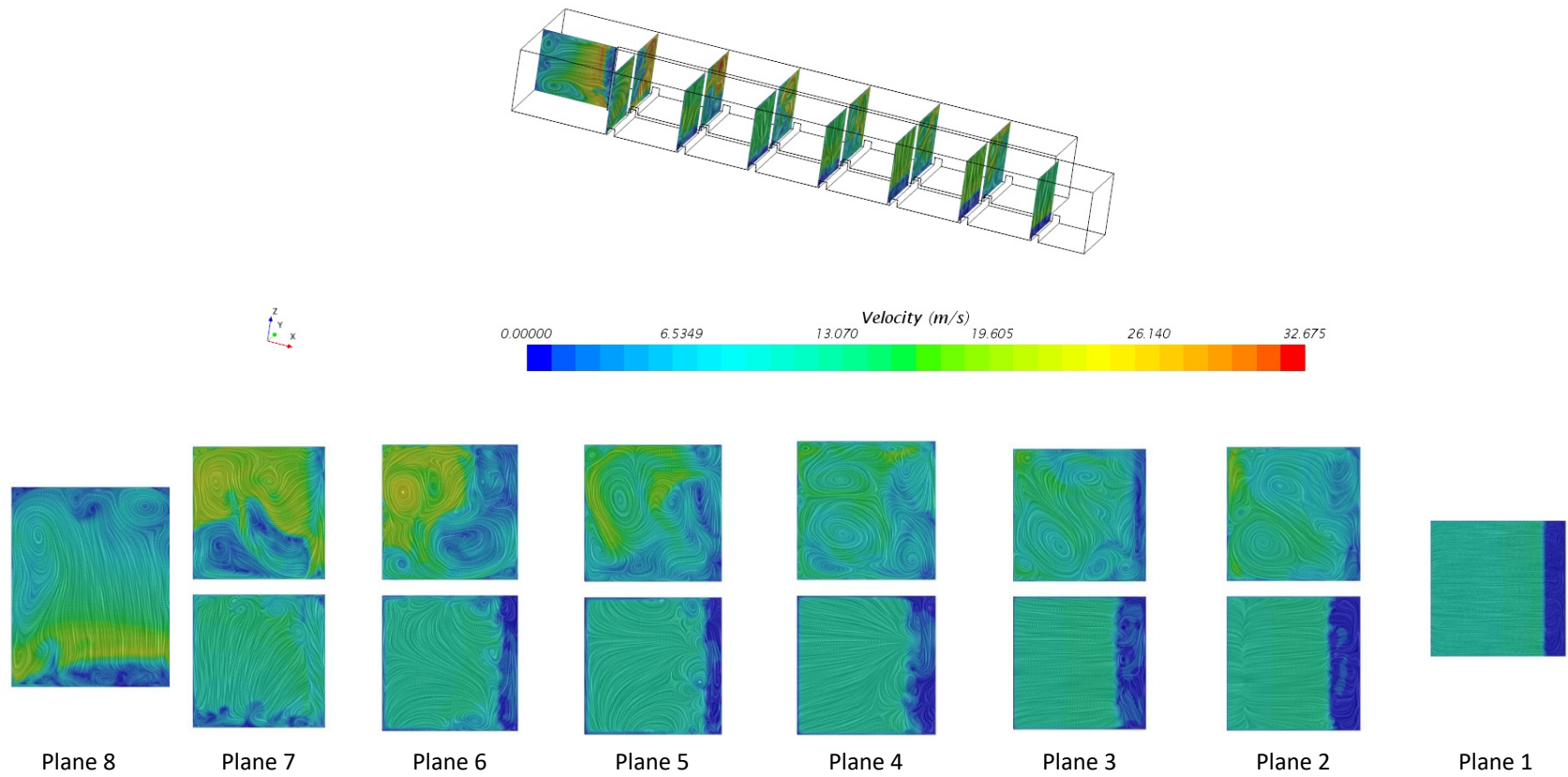


Figure 6-4: Contours of velocity and streamline on the normal planes for 90-deg rib configuration, $P/e=10$ $U_{in}=12.5\text{m/s}$

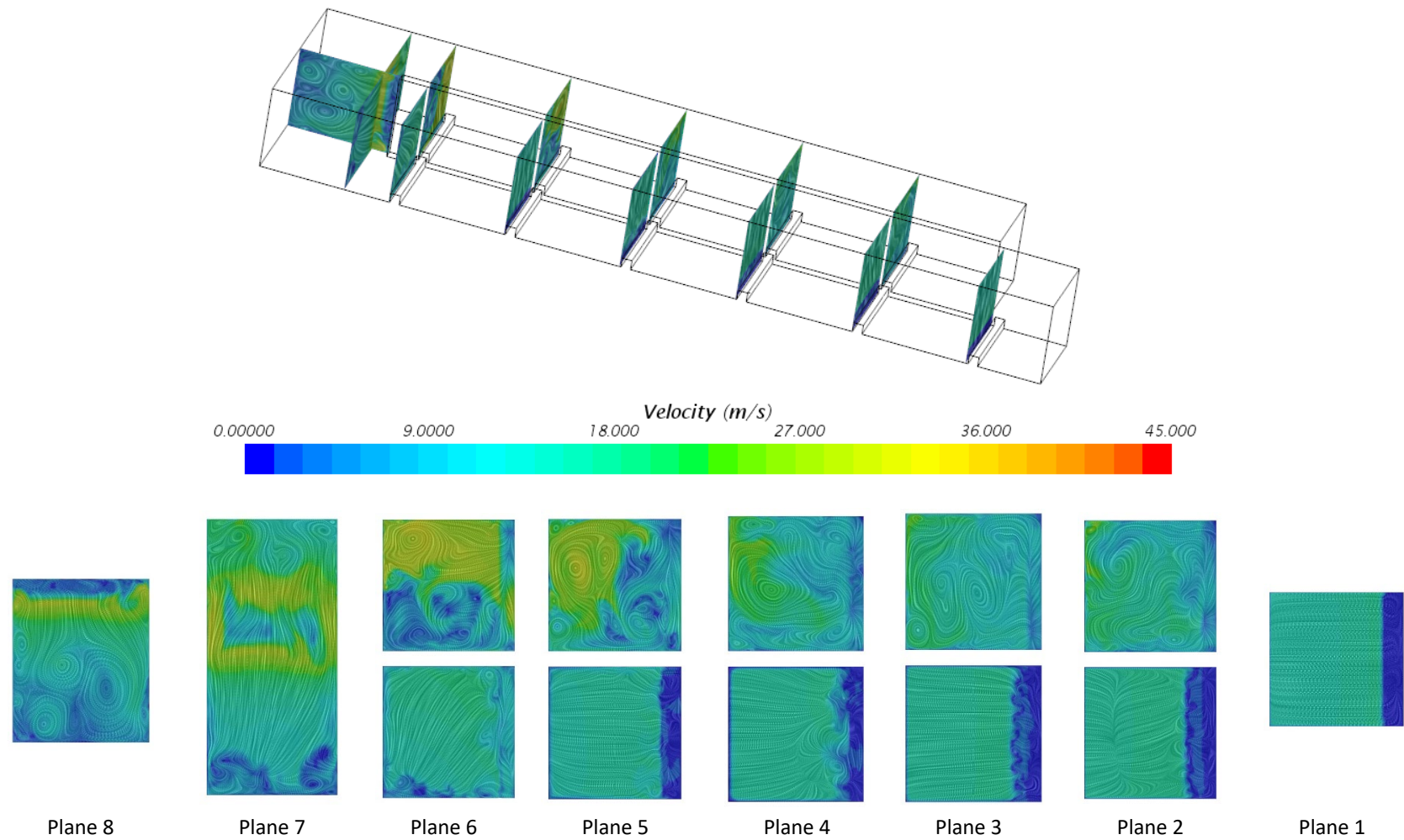
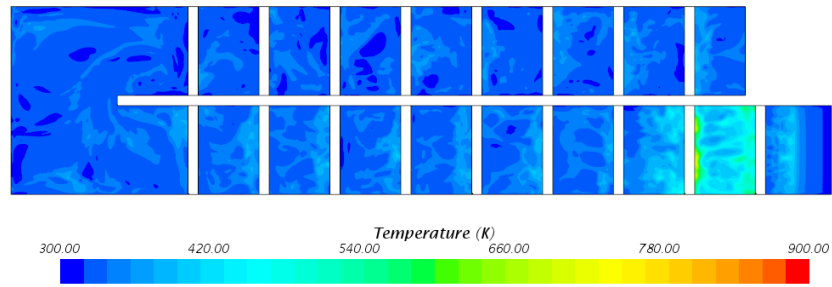
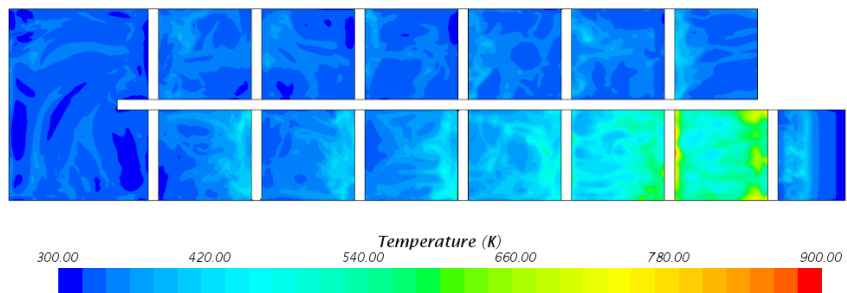


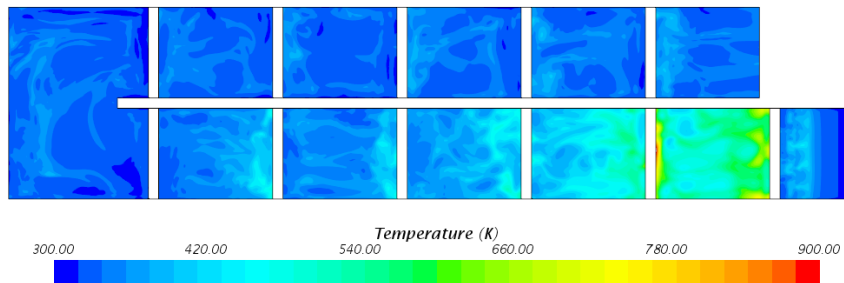
Figure 6-5: Contours of velocity and streamline on the normal planes for 90-deg rib configuration, $P/e=12$ $U_{in}=12.5\text{m/s}$



(a)

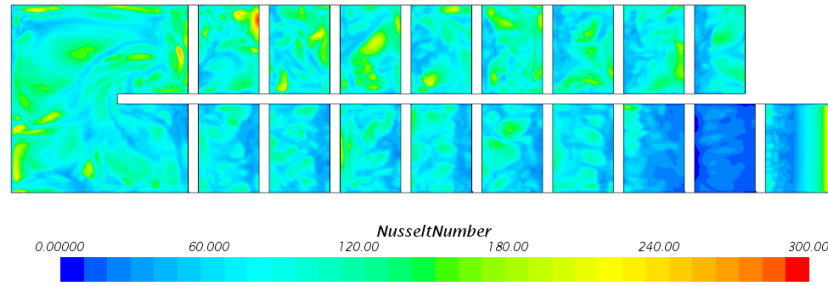


(b)

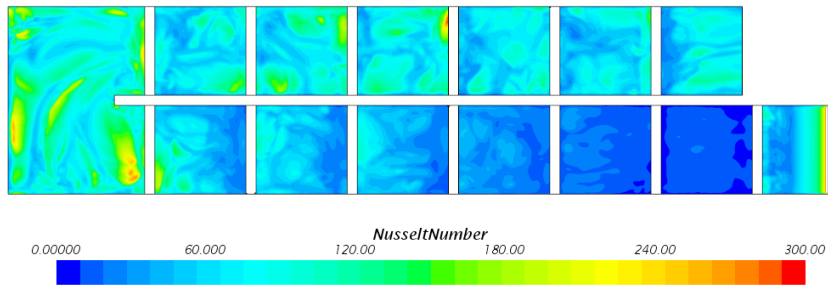


(c)

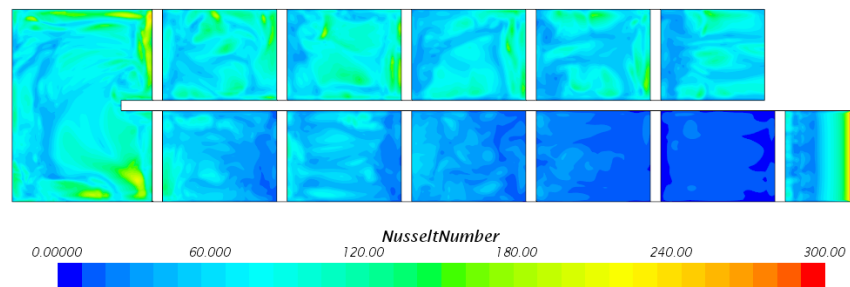
Figure 6-6: Temperature distribution at the bottom wall of the channel for stationary case 90-deg rib configuration $U_{in} = 12.5 \text{ m/s}$ (a) $p/e=7$, (b) $p/e=10$, (c) $p/e=12$



(a)



(b)



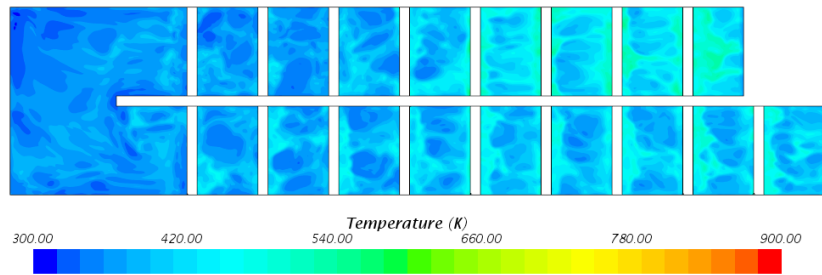
(c)

Figure 6-7: Nusselt distribution at the bottom wall of the channel for stationary case 90-deg rib configuration $U_{in} = 12.5 \text{ m/s}$ (a) $p/e=7$, (b) $p/e=10$, (c) $p/e=12$

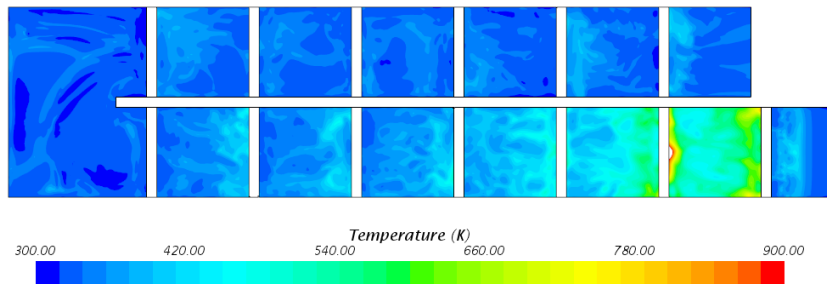
6.1.2 Rotational Cases

Rotation effect on heat transfer coefficient and velocity distribution was extensively discussed in the previous chapters. Due to rotation, the number of recirculation zones after each rib decreased, and more flow re-attached to the mainstream. Rib spacing effects can change this trend. Figure 6-8 illustrates the temperature distribution at the bottom wall of the two-pass channel. For smaller P/e 7, the ribs blockage effect mainly observed when the flow

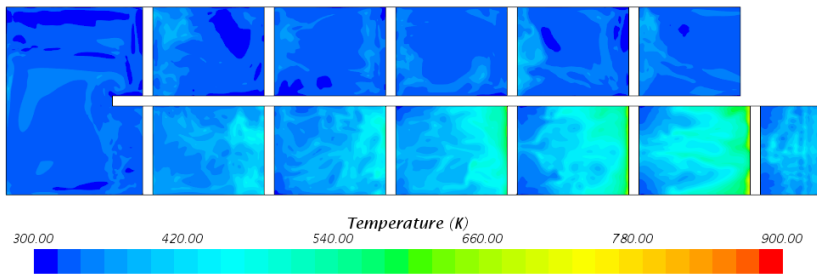
was passing the ribs; this can be due to the buoyancy and centrifugal forces. As flow entered the second passage, due to the turning effect and higher buoyancy effect, more turbulence generated resulted in removing more heat. For the P/e ten ratio, it can be seen temperature at the second passage is lower than the first passage. Also, in the turning region, lower temperature distribution can be observed compared with the other two P/e ratios. The lower temperature on the turning area resulted in a higher rate of heat removal from the bottom wall and higher Nusselt number, which is shown in Figure 6-9.



(a)



(b)



(c)

Figure 6-8: Temperature distribution at the bottom wall of the channel for rotational case 90-deg rib configuration $U_{in}= 12.5\text{m/s}$ (a) $p/e=7$, (b) $p/e=10$, (c) $p/e=12$

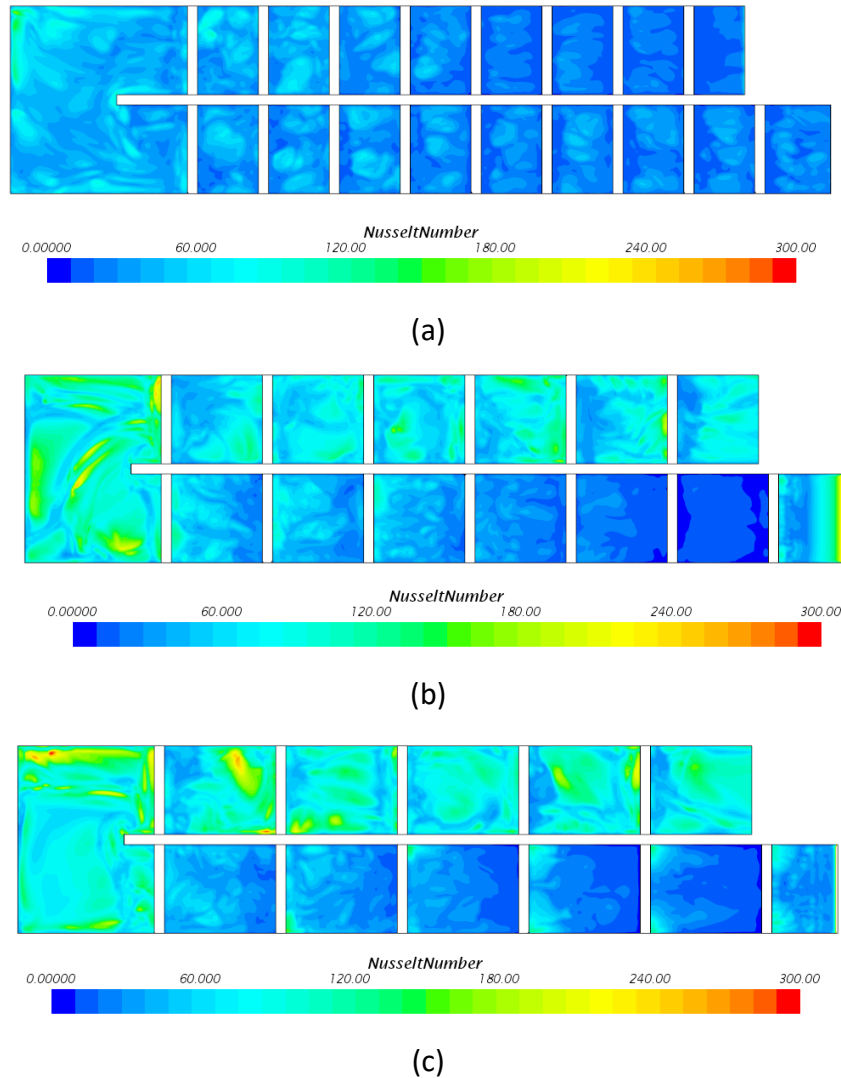
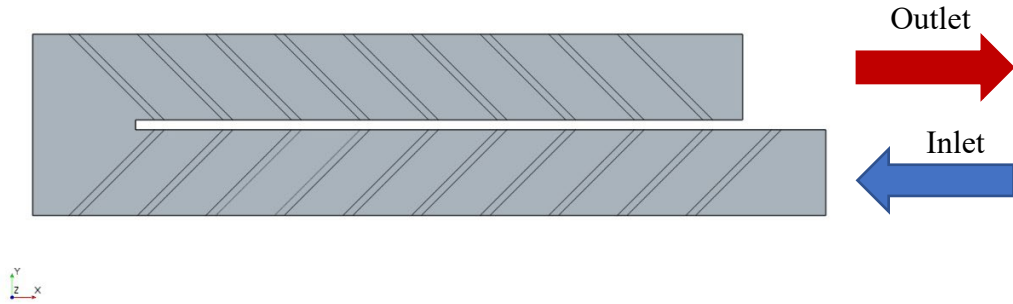


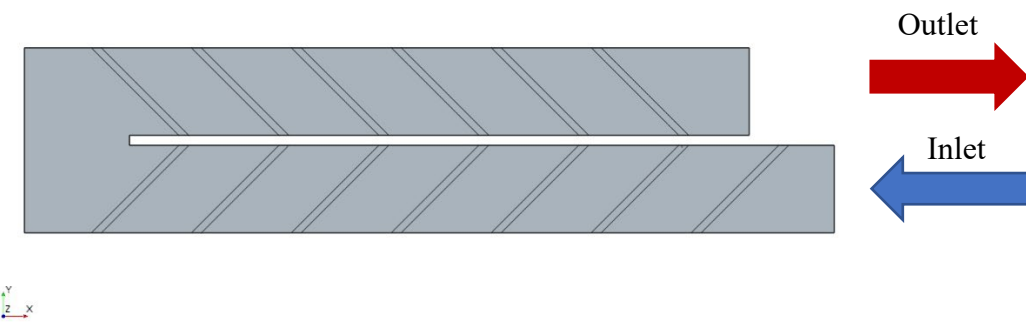
Figure 6-9: Nusselt distribution at the bottom wall of the channel for rotational case 90-deg rib configuration $U_{in}= 12.5\text{m/s}$ (a) $p/e=7$, (b) $p/e=10$, (c) $p/e=12$

6.2 Heat Transfer Distribution Study for 45-deg Rib with Different P/e ratio

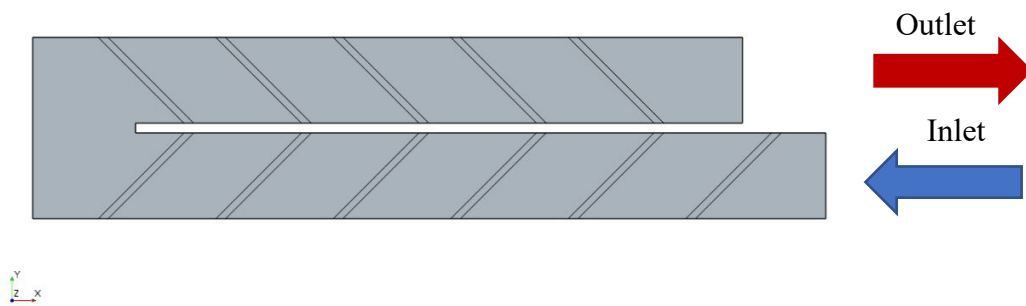
As mentioned earlier, the objective of this part of the study is to compare the heat transfer distribution and pressure loss in different P/e ratios. Figure 6-10 and Figure 6-11 describe channel top view and isometric view for the 45-deg parallel ribs for different rib spacing. The ribs were installed on the bottom wall of the channel, where the constant heat flux boundary condition was applied to both the bottom wall and the ribs.



(a)



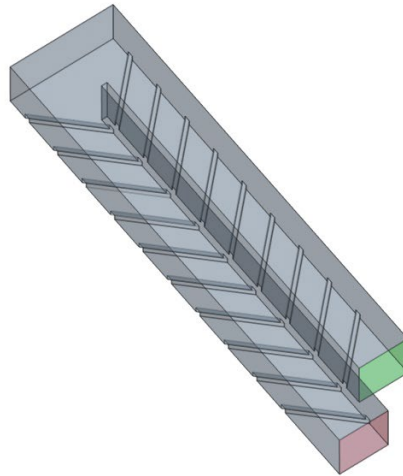
(b)



(c)

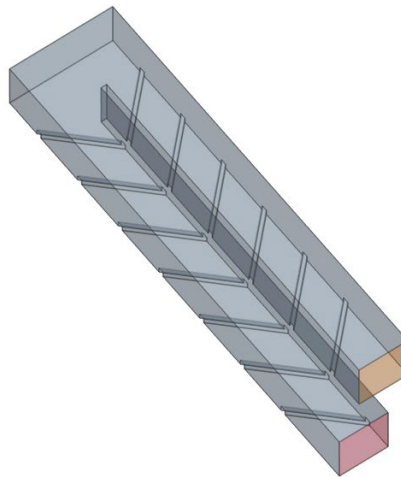
Figure 6-10: inlet/outlet for Channel with 45-deg rib configuration (a) $p/e=7$, (b) $p/e=10$, (c) $p/e=12$

STAR-CCM+



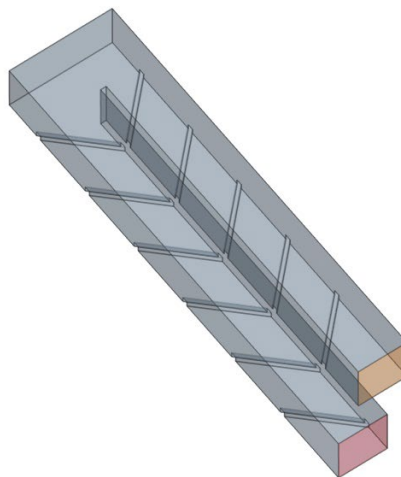
(a)

STAR-CCM+



(b)

STAR-CCM+



(c)

Figure 6-11: isometric view for Channel with 45-deg rib configuration (a) $p/e=7$, (b) $p/e=10$, (c) $p/e=12$

6.2.1 Stationary Cases

For the stationary cases, Reynolds number as 35000 was considered for the call cases.

Figure 6-12, Figure 6-13, and Figure 6-14 describe the contours of normalized vector velocity magnitude along with in-plane streamlines. As can be seen, as flow passed each rib, the velocity increases significantly after each rib, which can be explained as the effect of flow separation. In the space between the ribs, separated flow re-attaches to the mainstream flow, and the same phenomena are repeated for each rib. In the bending region, more irregular flow behavior can be observed due to the turn. In the bending region, a significant increase in the velocity can be observed. This increase helps the flow to remove more heat from the bend region. The flow trend is relatively similar for all the ratios. However, for the rib-pitch-to-rib height ratio 7, due to less space between the ribs, flow cannot have complete separation and re-attachment; thus, an asymmetrical pattern can be seen on the vector velocity profile.

The figure for P/e ratio 12 shows that due to the increase in the rib spacing, after flow re-attached to the mainstream, it still is passing the distance between the ribs; thus, more recirculation zones can be observed.

For the P/e ratio 10, it can be seen flow has enough time to separate and re-attach the mainstream flow, which results in reducing the recirculation zone and increasing the overall turbulence between each rib.

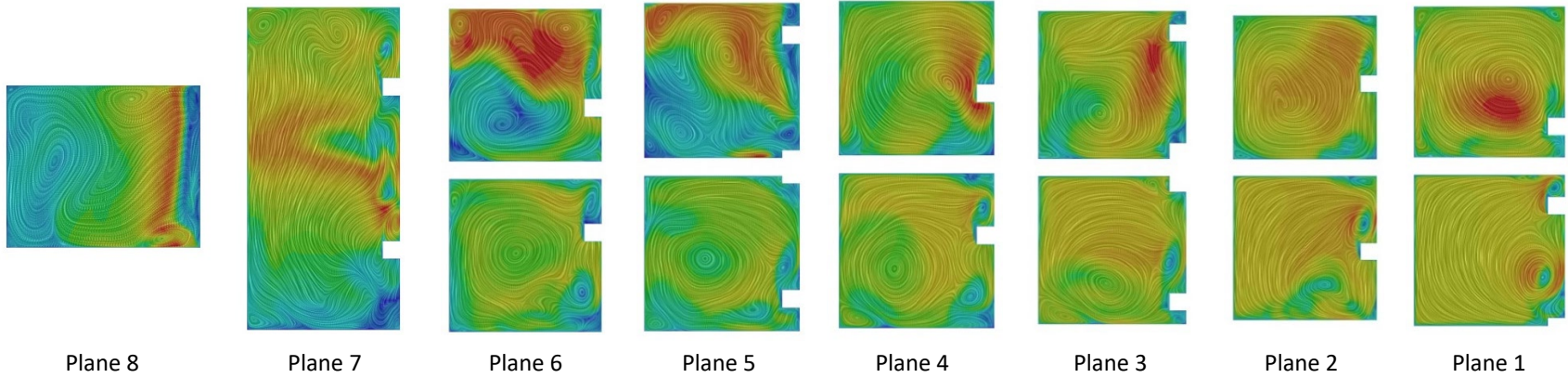
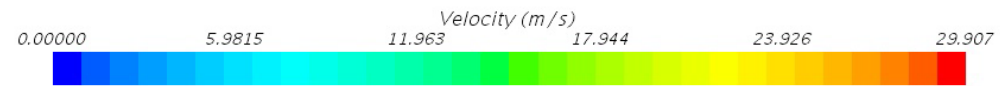
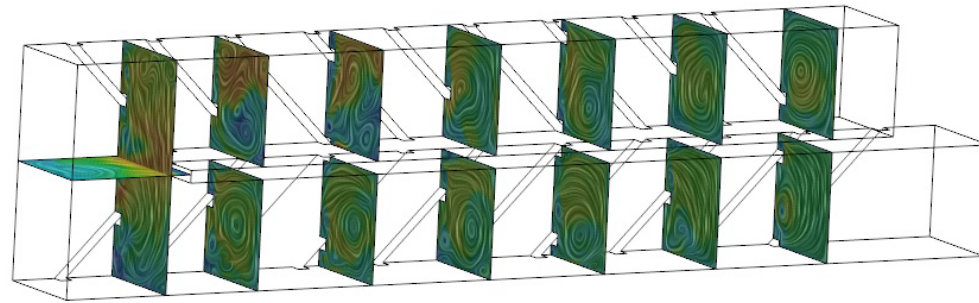


Figure 6-12: Contours of velocity and streamline on the normal planes 45-deg rib configuration, $P/e=7$ $U_{in}=12.5\text{m/s}$

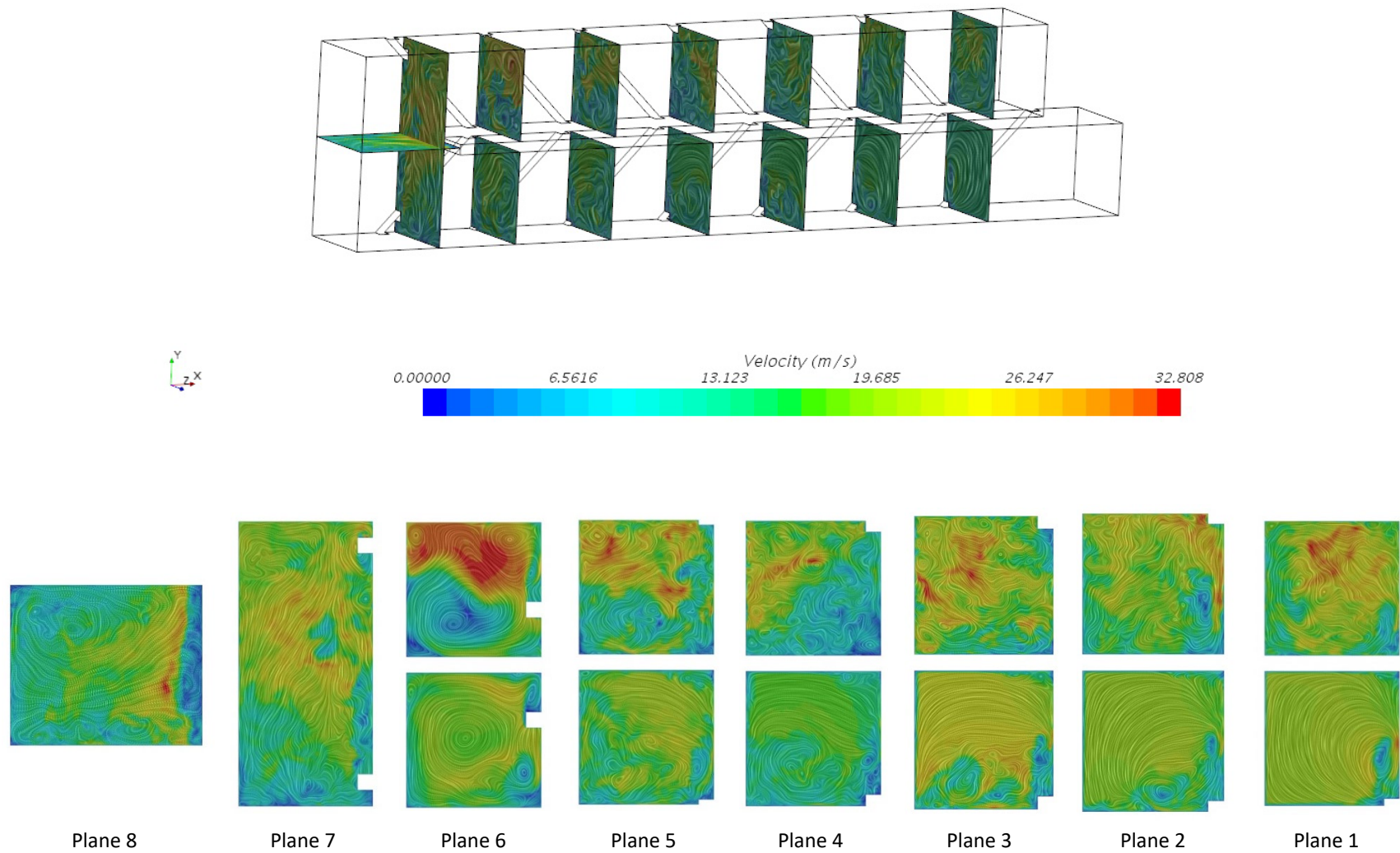


Figure 6-13: Contours of velocity and streamline on the normal planes, 45-deg rib configuration $P/e=10$ $U_{in}=12.5\text{m/s}$

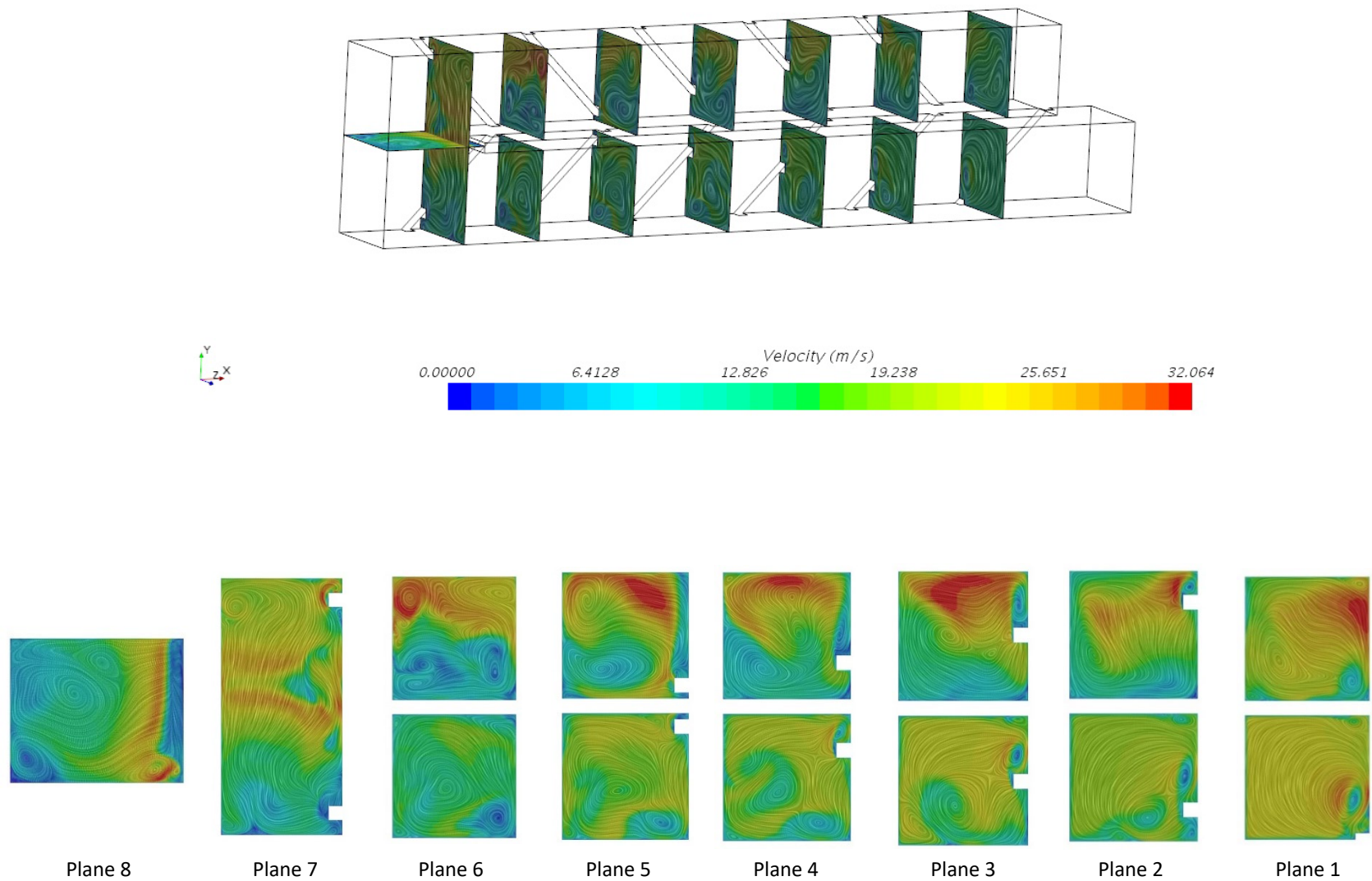


Figure 6-14: Contours of velocity and streamline on the normal planes, 45-deg rib configuration, $P/e=12$ $U_{in}=12.5\text{m/s}$

The bottom wall temperature distribution for different P/e ratio is presented in Figure 6-15. Similar to velocity distribution figures. The trend is the same for all the cases. However, for the P/e 10, the temperature distribution is more uniform, which resulted in more uniform heat transfer. For the P/e 7 and 12, lower temperatures happens in some spots. This temperature distribution can increase the overall heat transfer coefficient; however, it is not in favor of uniform heat removal from the bottom wall of the channel.

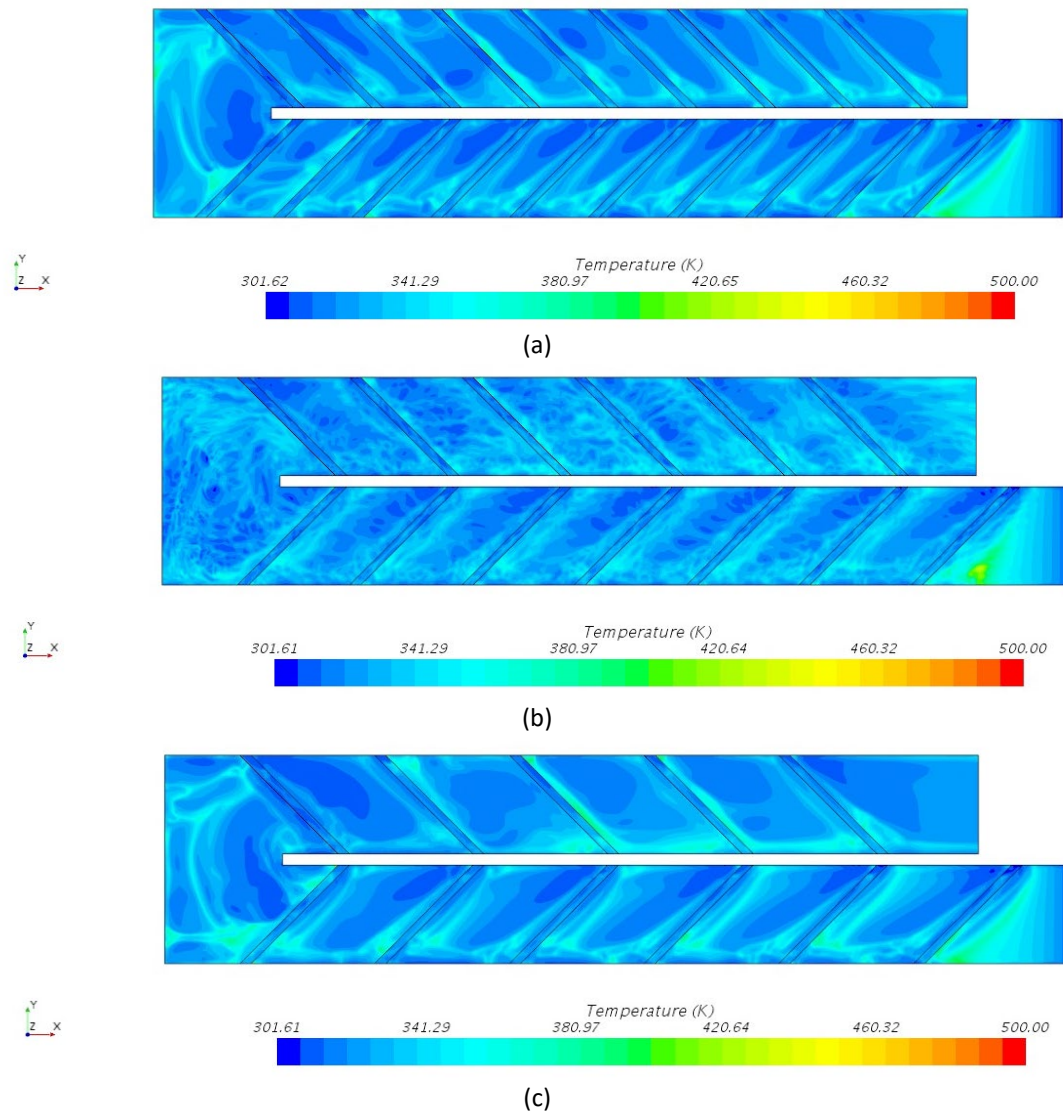


Figure 6-15: Temperature distribution at the bottom wall of the channel for stationary case $U_{in} = 12.5 \text{ m/s}$, 45-deg rib configuration (a) $p/e=7$, (b) $p/e=10$, (c) $p/e=12$

Figure 6-16 describes the Nusselt number distribution on the channel bottom wall. It can be seen as the flow passes the ribs immediately after the ribs, there is a significant increase in the Nusselt number. This change can be explained as flow separation and re-attachment. Similar to temperature distribution scenes for the P/e ratio of 10, the Nusselt number distribution is more uniform, which results in higher heat removal from the distance between the ribs.

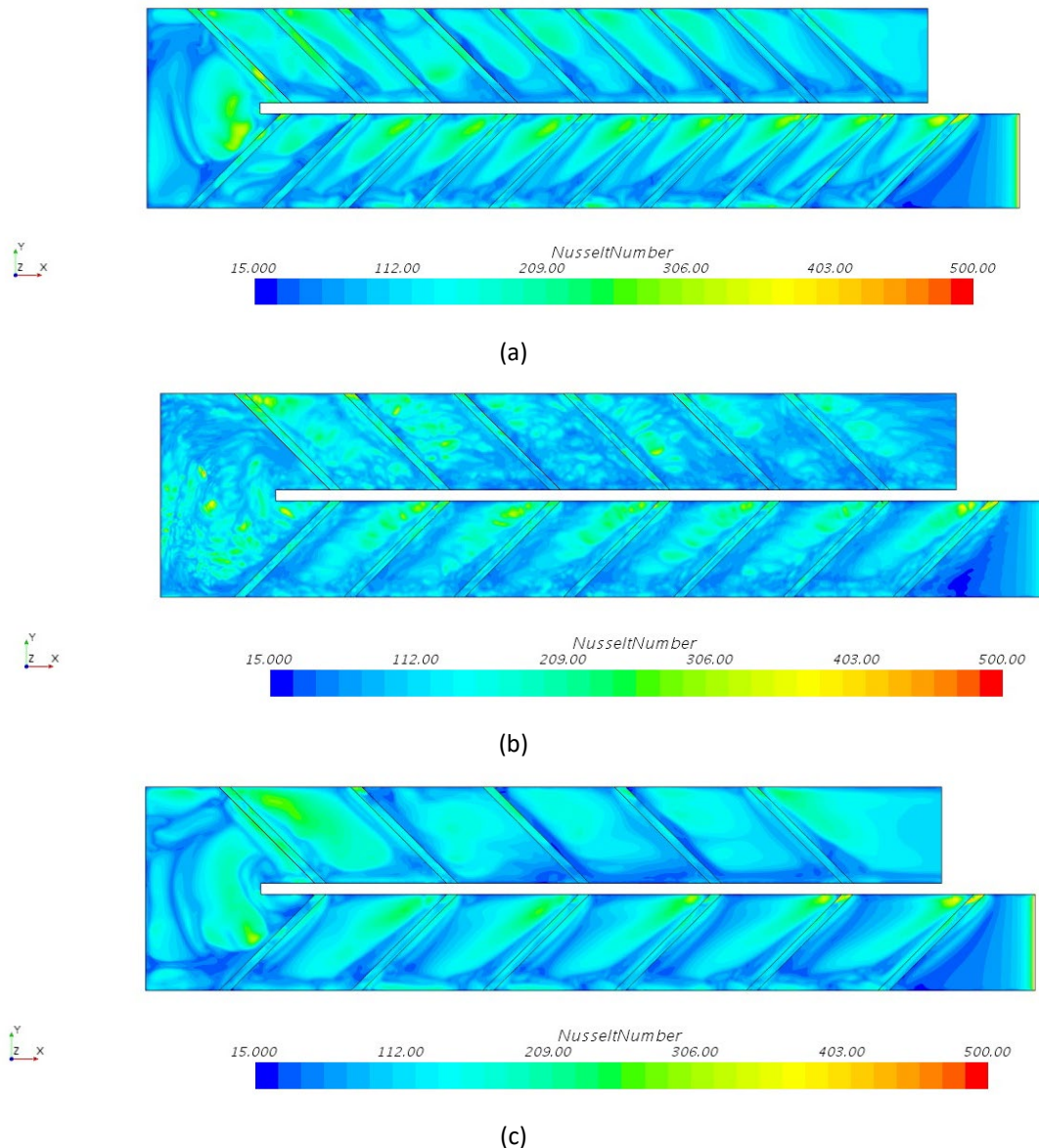
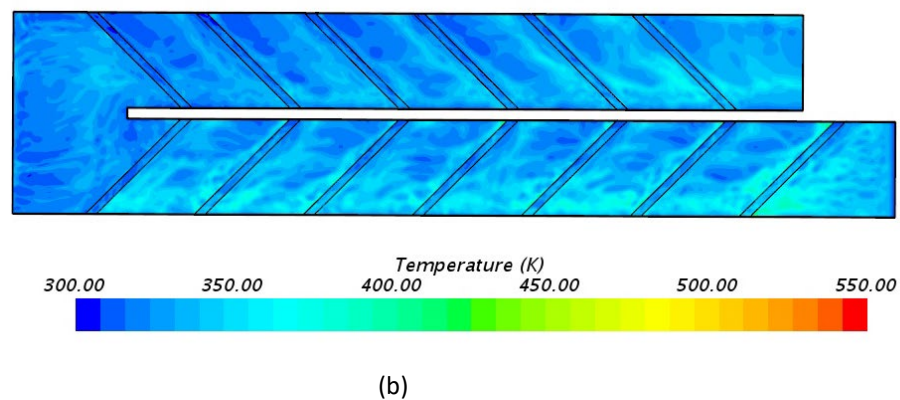
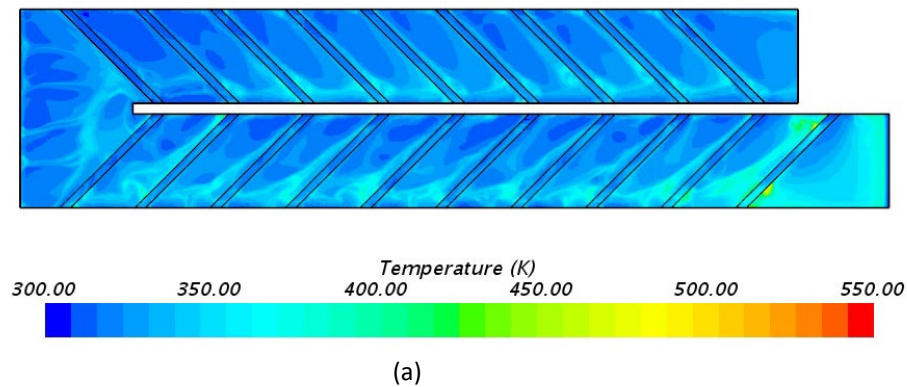
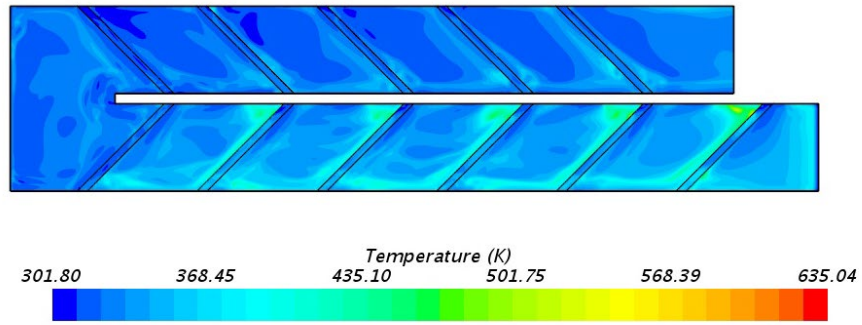


Figure 6-16: Nusselt distribution at the bottom wall of the channel for stationary case $U_{in}= 12.5\text{m/s}$, 45-deg rib configuration (a) $p/e=7$, (b) $p/e=10$, (c) $p/e=12$

6.2.2 Rotational Cases

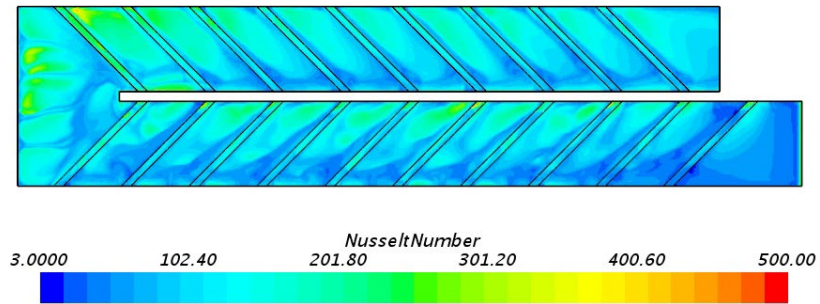
Rotation induces the Centrifugal forces and Buoyancy forces. The effect of these forces significantly can be seen in the second passages. Figure 6-17 shows the bottom wall temperature profile for the rotational speed of 300rpm. It can be observed as flow passing through the channel, due to the increase in buoyancy forces, recirculation zones decrease, and turbulence increases. As a result of these changes, more heat is removed from the walls, especially more on the second passage. Figure 6-18 shows the Nusselt number distribution on the bottom wall. It can be seen due to the increase in flow turbulence, more heat removed from the bottom wall. P/e ten configuration shows better performance as the Nusselt number increases more uniformly in the bending region.



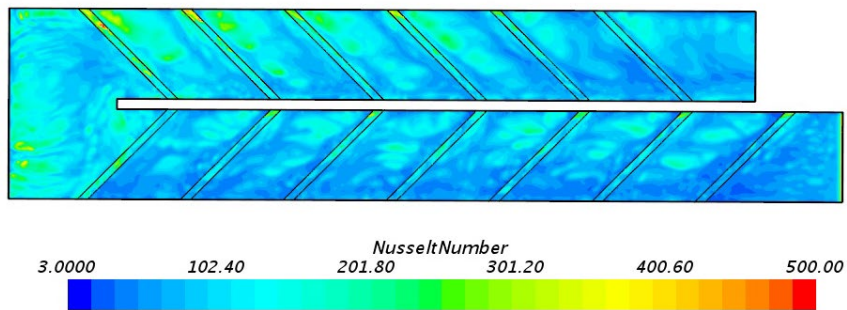


(c)

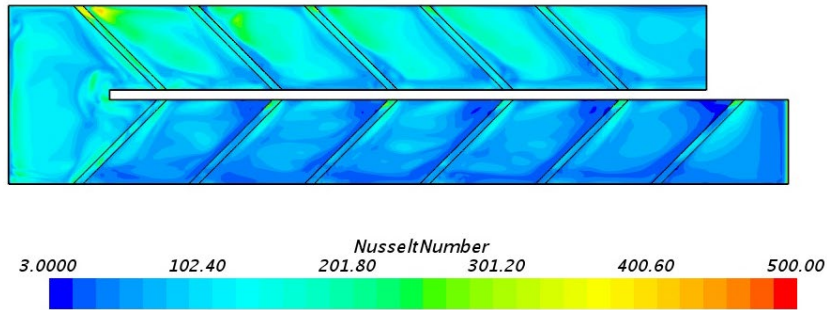
Figure 6-17: Temperature distribution at the bottom wall of the channel for stationary case $U_{in}=12.5\text{m/s}$, 45-deg rib configuration (a) $p/e=7$, (b) $p/e=10$, (c) $p/e=12$



(a)



(b)

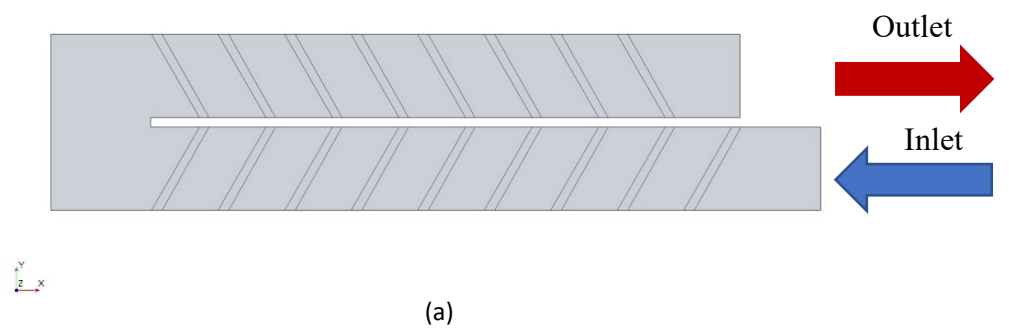


(c)

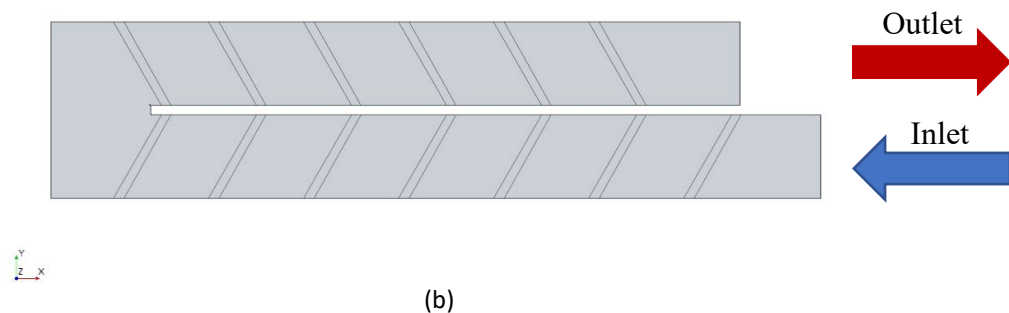
Figure 6-18: Nusselt distribution at the bottom wall of the channel for stationary case $U_{in} = 12.5 \text{ m/s}$, 45-deg rib configuration (a) $p/e=7$, (b) $p/e=10$, (c) $p/e=12$

6.3 Heat Transfer Distribution Study for 60-deg Parallel Rib with Different P/e ratio

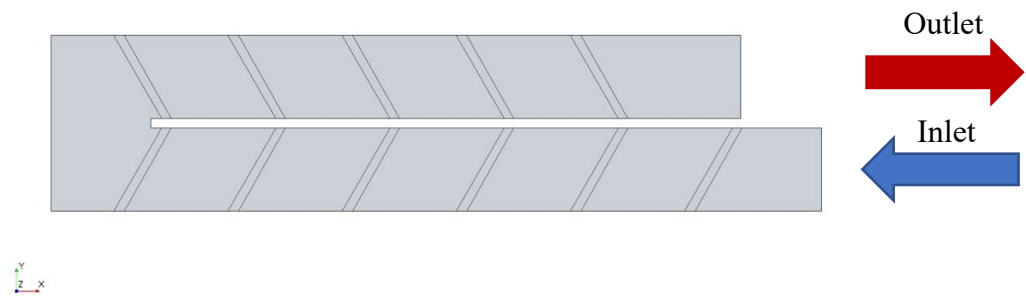
Similar to the previous sections, 60-deg parallel ribs were installed on the bottom wall of the channel. Figure 6-19 and Figure 6-20 show the top view and isometric view for three different P/e ratios.



(a)



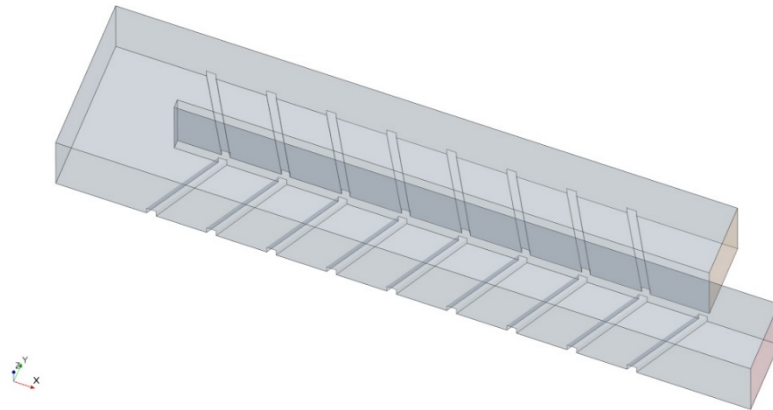
(b)



(c)

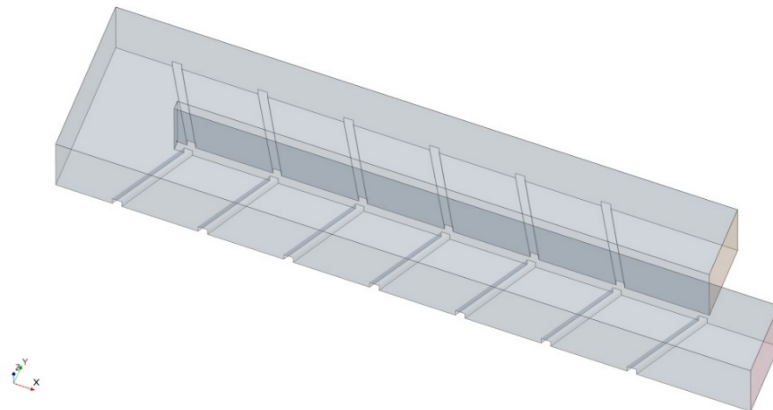
Figure 6-19: inlet/outlet for Channel with 60-deg rib configuration (a) $p/e=7$, (b) $p/e=10$, (c) $p/e=12$

STAR-CCM+

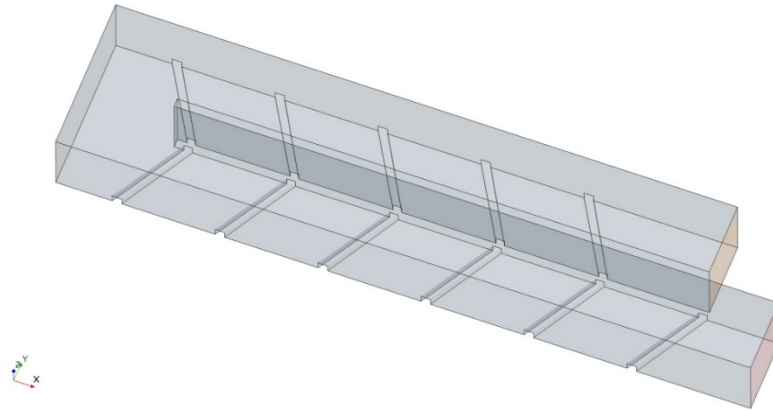


(a)

STAR-CCM+



(b)



(c)

Figure 6-20: Isometric view for Channel with 60-deg rib configuration (a) $p/e=7$, (b) $p/e=10$, (c) $p/e=12$

6.3.1 Stationary Cases

Figure 6-21, Figure 6-22, and Figure 6-23 describe contours of normalized vector velocity magnitude along with some in-plane streamlines. As flow passes ribs due to the flow separation, a significant velocity increase is observed after each rib. Similar to 45-deg, the velocity distribution profile for the P/e ratio 10 has a more symmetrical trend, especially in the U-turn region. However, the flow velocity does not have a significant increase compared with the 45-deg ribs. In the bending region, more irregular flow behavior can be observed due to the turning regions. Also, in this region, a significant increase in velocity can be found. This increase helps the flow to remove more heat from the bend region. The flow trend is relatively similar for all the ratios. However, for the rib-pith-to-rib height ratio 7, due to less space between the ribs, flow cannot have complete separation and re-attachment. Thus, an asymmetrical pattern can be seen on the vector velocity profile.

The figure for P/e ratio 12 shows that due to the increase in the rib spacing, after the flow re-attached to the mainstream, it still is passing the distance between the ribs; thus, more

recirculation zones can be observed. For the P/e ratio 10, it can be seen flow has enough time to separate and re-attach the main streamflow. This results in reducing the recirculation zone and increasing the overall turbulence between each rib. In the turning region, a significant increase in the turbulence can be observed for all three ratios. However, the recirculation zone for P/e ten is reduced, and a more uniform pattern can be observed. This uniform increase in velocity at the bending region helps to remove more heat from the turning region.

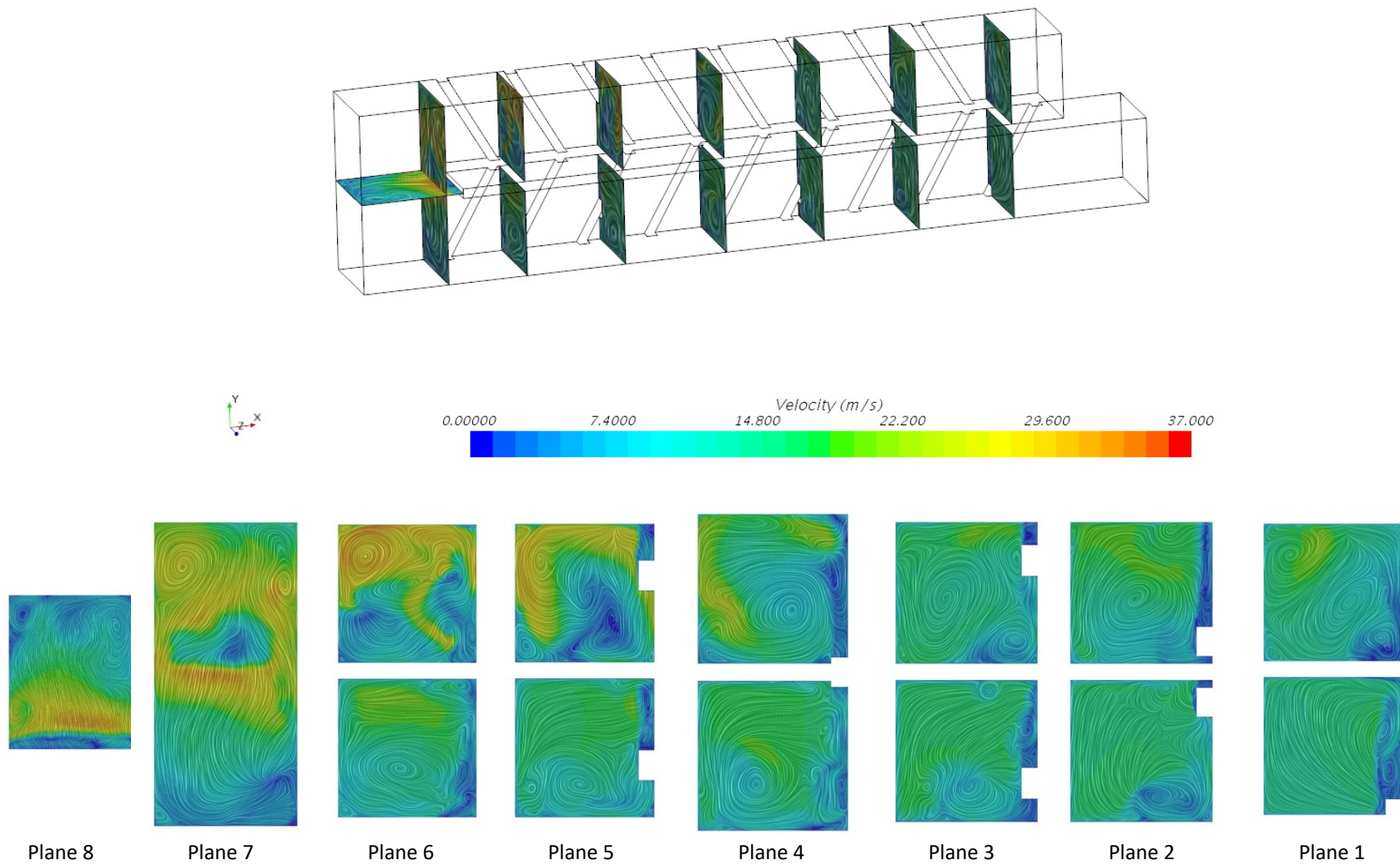


Figure 6-21: contours of velocity and streamline on the normal planes, 60-deg rib configuration, $P/e=7$ $U_{in}=12.5\text{m/s}$

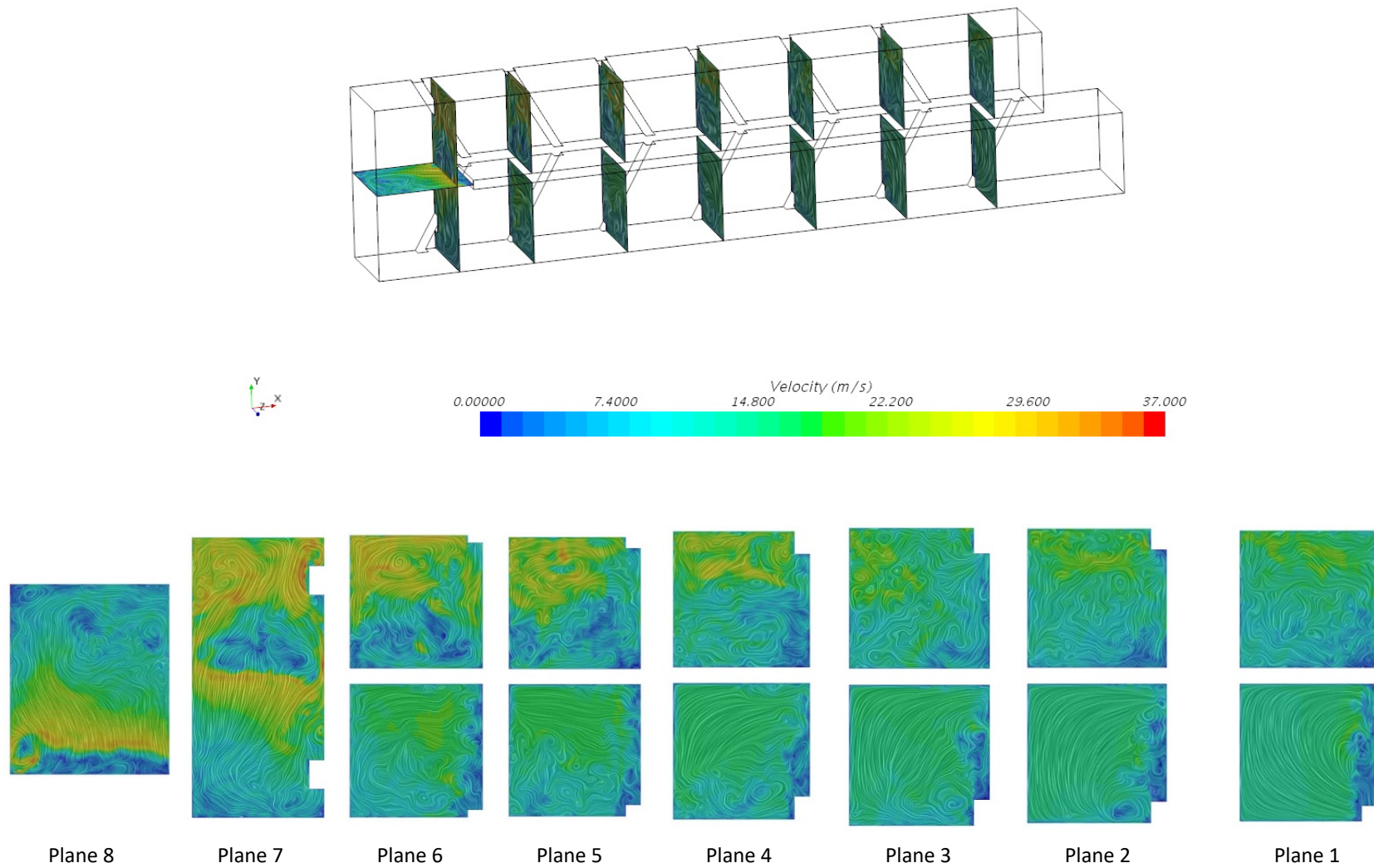


Figure 6-22: contours of velocity and streamline on the normal planes, 60-deg rib configuration $P/e=10$ $U_{in}=12.5\text{m/s}$

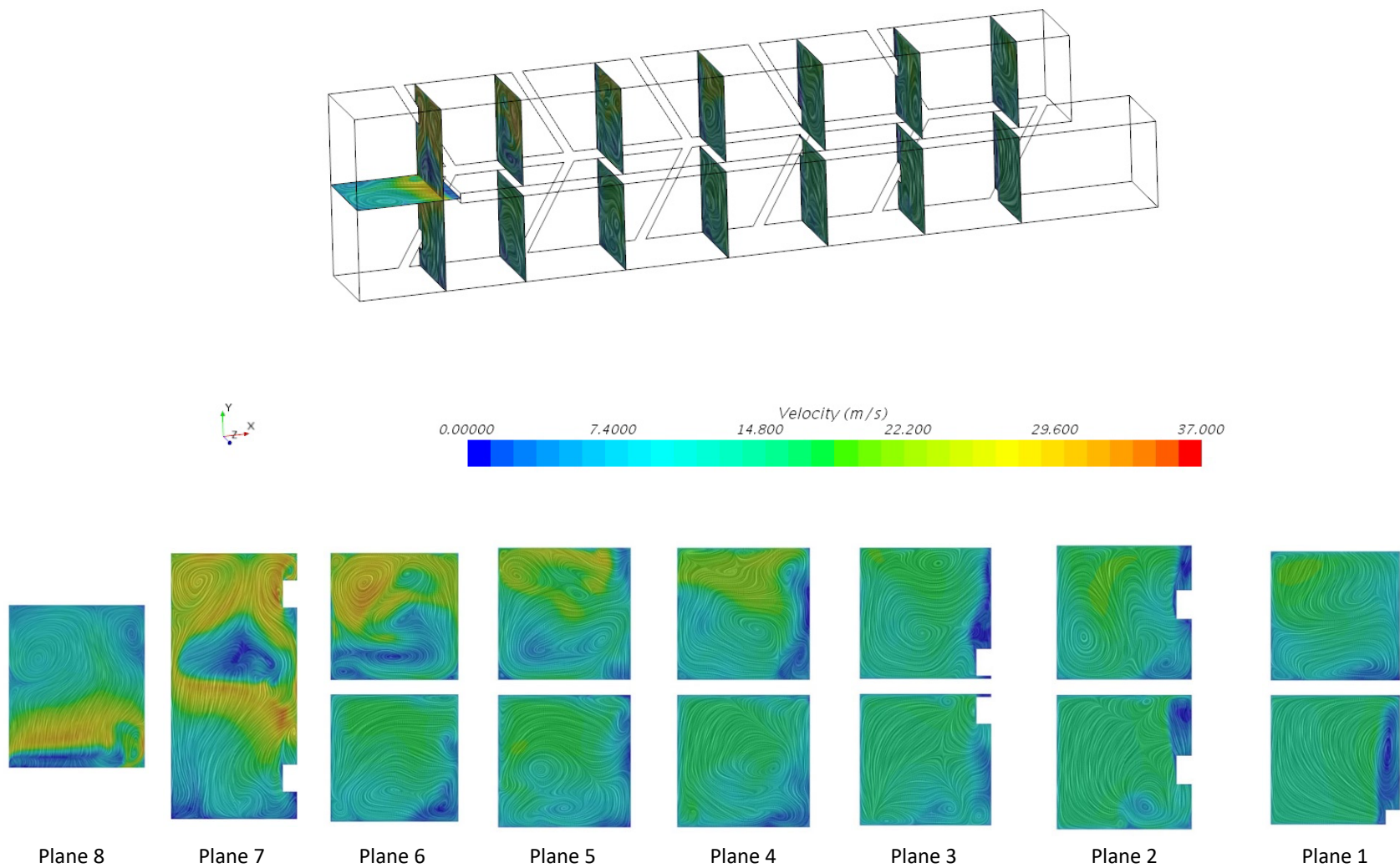


Figure 6-23: contours of velocity and streamline on the normal planes, 60-deg rib configuration $P/e=12$ $U_{in}=12.5\text{m/s}$

Figure 6-24 shows the temperature distribution on the bottom wall. As discussed earlier, due to the turbulence increase, more heat will be removed, especially after each rib, which increased the Nusselt number. Figure 5-16 shows the Nusselt number distribution on the bottom wall. Similar to 45-deg ribs, a significant increase in the Nusselt number can be observed between each rib in all the ratios. However, for P/e seven, the trend is more uniform, especially in the bending region.

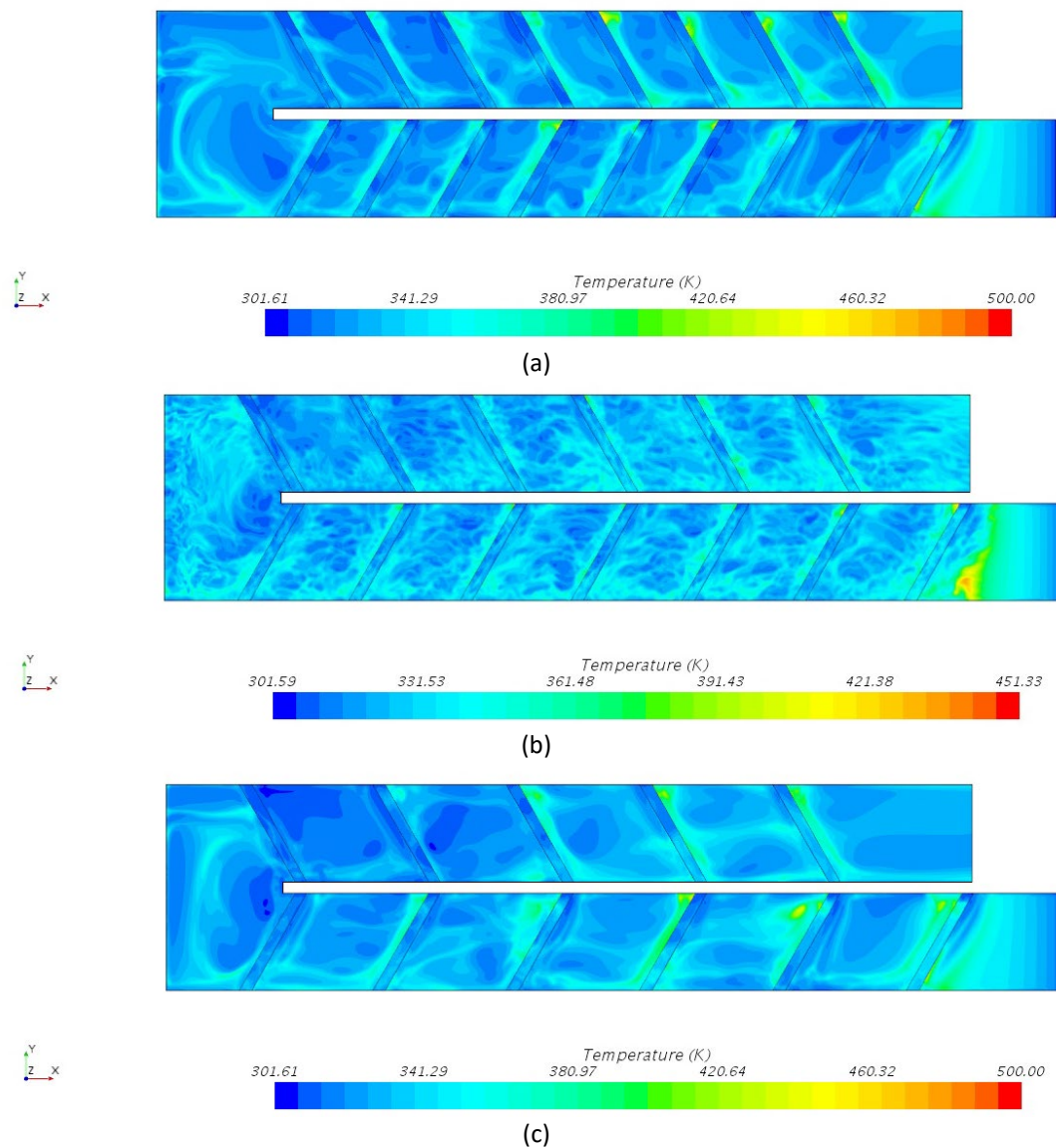


Figure 6-24: Temperature distribution at the bottom wall of the channel for stationary case $U_{in}=12.5\text{m/s}$, 60-deg rib configuration (a) $p/e=7$, (b) $p/e=10$, (c) $p/e=12$

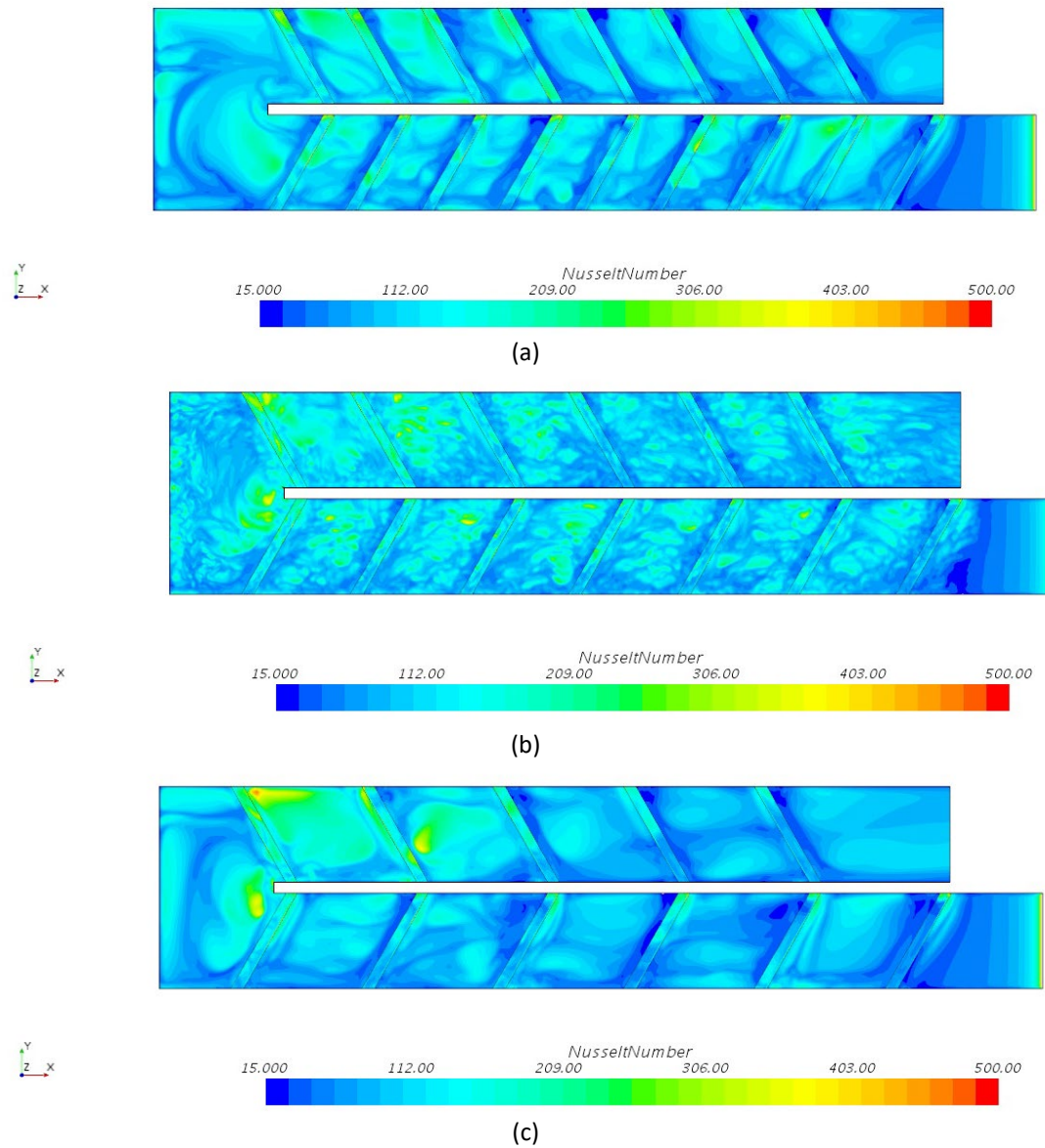
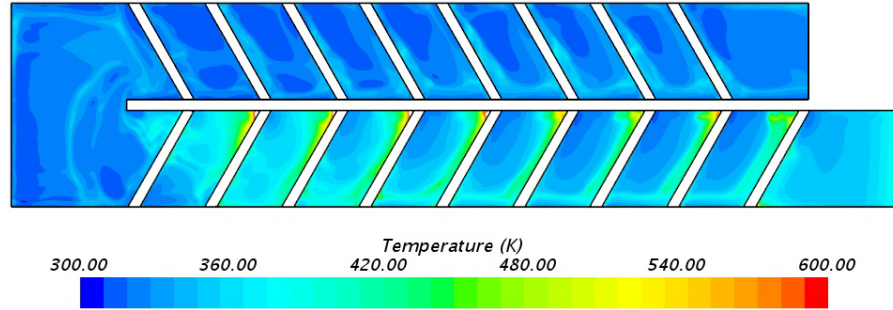


Figure 6-25: Nusselt distribution at the bottom wall of the channel for stationary case 60-deg rib $U_{in}=12.5\text{m/s}$ (a) $p/e=7$, (b) $p/e=10$, (c) $p/e=12$

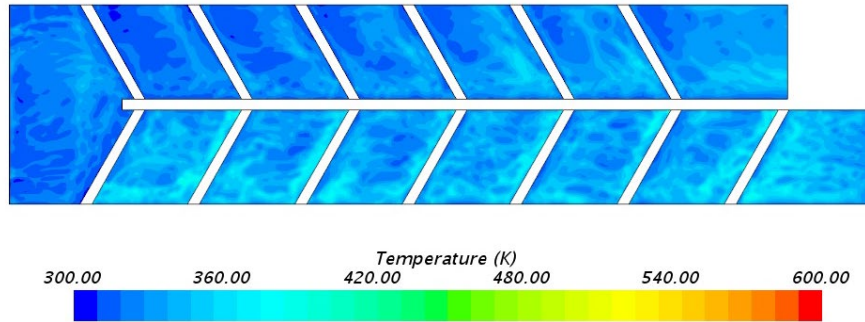
6.3.2 Rotational Cases

Due to the rotation, buoyancy and centrifugal forces are induced in the channel. As a result of these forces, secondary flow increases, which leads to an increase in the heat transfer coefficient. Figure 6-26 and Figure 6-27 describe the temperature and Nusselt number distribution on the bottom wall. It can be seen in rotational cases more heat is removed in the second passage. Despite stationary cases, P/e 7 and 12 have a higher Nusselt number increase

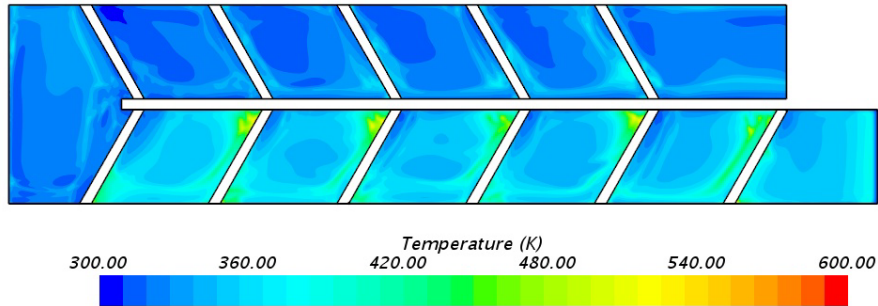
compare with P/e 10. This might be due to the decreasing the recirculation zones in the presence of rotation effects.



(a)

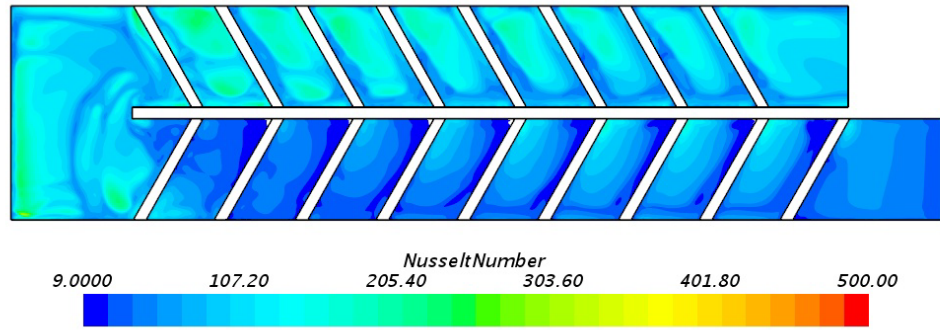


(b)

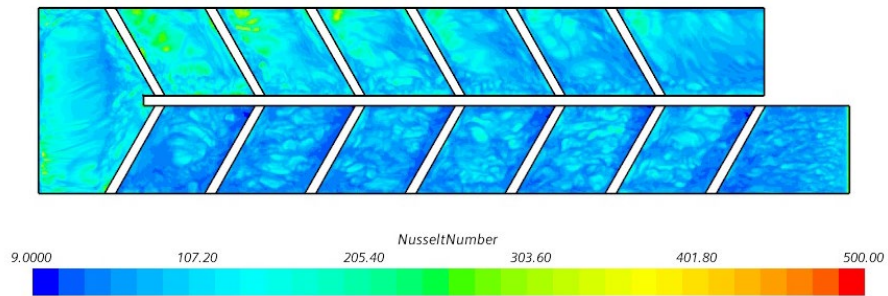


(c)

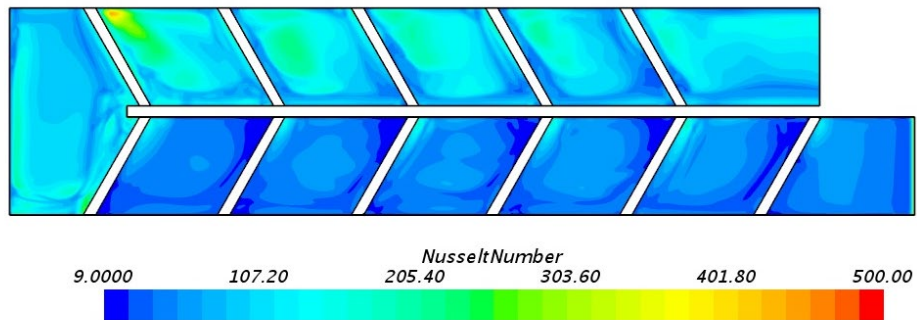
Figure 6-26: Temperature distribution at the bottom wall of the channel for stationary case, 60-deg rib configuration $U_{in}=12.5\text{m/s}$ (a) $p/e=7$, (b) $p/e=10$, (c) $p/e=12$



(a)



(b)



(c)

Figure 6-27: Nusselt distribution at the bottom wall of the channel for rotational case 60-deg rib configuration $U_{in}=12.5\text{m/s}$ (a) $p/e=7$, (b) $p/e=10$, (c) $p/e=12$

6.4 Heat Transfer Distribution Study for V-Shape Rib with Different P/e ratio

Figure 6-28 and Figure 6-29 show the rib configuration in channels that the angle of attack is in the first passages is against the flow stream, and in the second passage, while in the second passage, it is in the same direction of the flow.

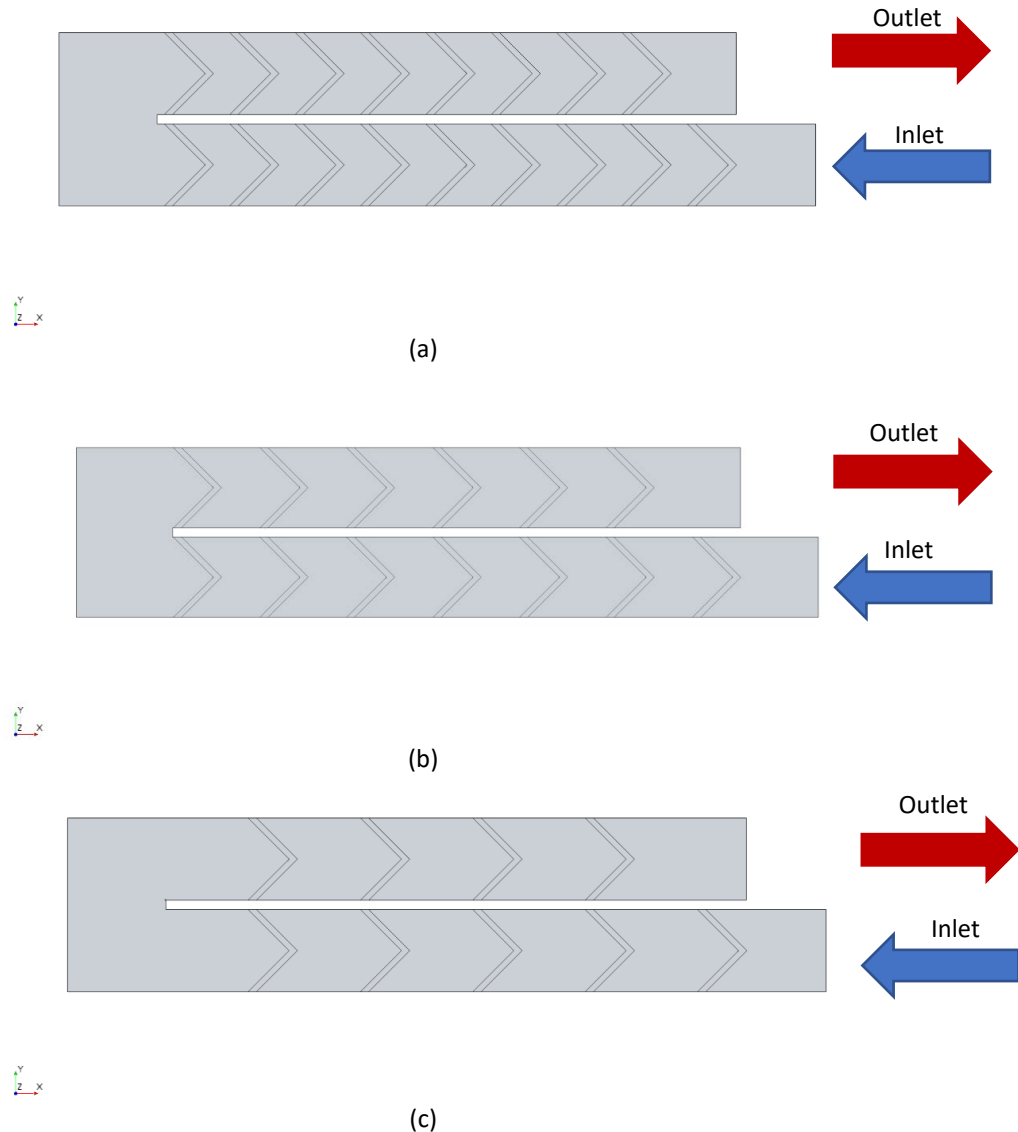
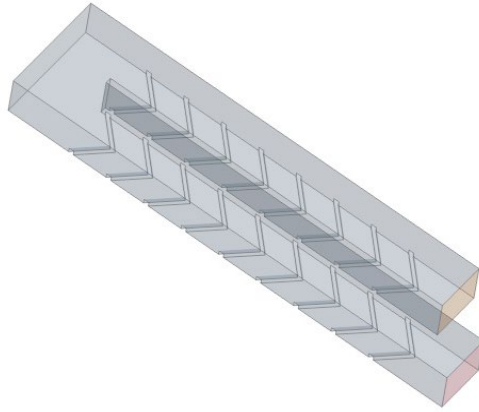
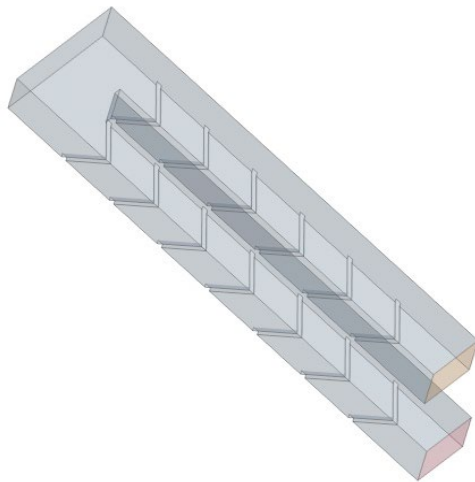


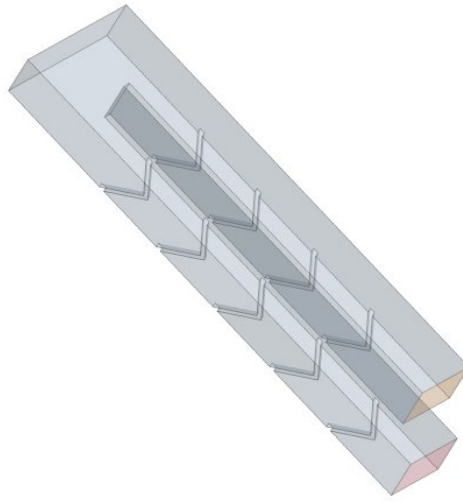
Figure 6-28: inlet/outlet for Channel with V-shape rib configuration (a) $p/e=7$, (b) $p/e=10$, (c) $p/e=12$



(a)



(b)



(c)

Figure 6-29: Isometric view for Channel with V-Shape rib configuration (a) $p/e=7$, (b) $p/e=10$, (c) $p/e=12$

6.4.1 Stationary Cases

Figure 6-30, Figure 6-31, and Figure 6-32 describe the velocity counter for each P/e ratios.

For all ratios at the first passage, while the mainstream passed through, the sharp edge of V ribs velocity contour is more symmetrical compared with the second passage. The symmetrical distribution can be due to the rib orientation in each pass. In the first passage, first flow separation happens at the sharp edge of the rib, and it develops more while it is passing the entire ribs. While in the second passage, flow separation occurred first on the arms of the rib and then the sharp edge of the rib. This type of separation on the second passage causes asymmetrical turbulence distribution in each cross-section.

As mentioned earlier, the distance between each rib plays a crucial role in generating more turbulence. This distance should be engineered in a way that flow has enough time to entirely separate and re-attached to the mainstream. Similar to previous rib configurations, it can be

seen P/e ratio 10 has a better performance than the P/e ratio of 7 and 12. From the vector velocity contour, it can be observed for the P/e ten ratio, after each separation flow has enough time to re-attach to the mainstream. This causes more symmetrical turbulence distribution after each rib and higher heat removal from the surface of the blade.

Rib-Pitch-to-rib-height ratio effects on temperature distribution can be seen in Figure 6-33. Temperature distribution for the P/e 10 is more uniform, especially in the bending region compare with the other ratios. This can be due to the more symmetrical velocity distribution after each rib in the P/e ratio 10.

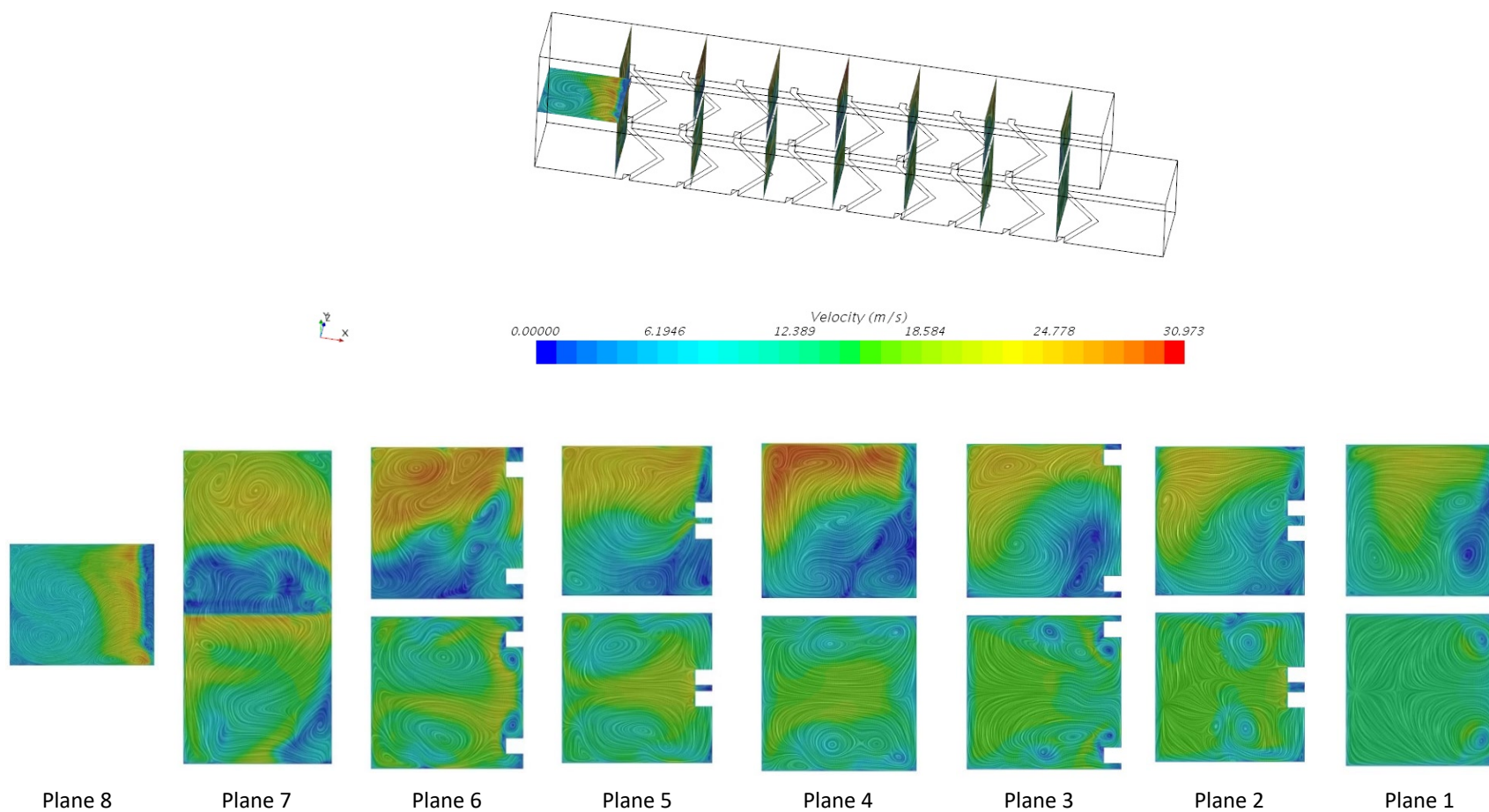


Figure 6-30: contours of velocity and streamline on the normal planes, V-Shape configuration $P/e=7$ $U_{in}=12.5\text{m/s}$

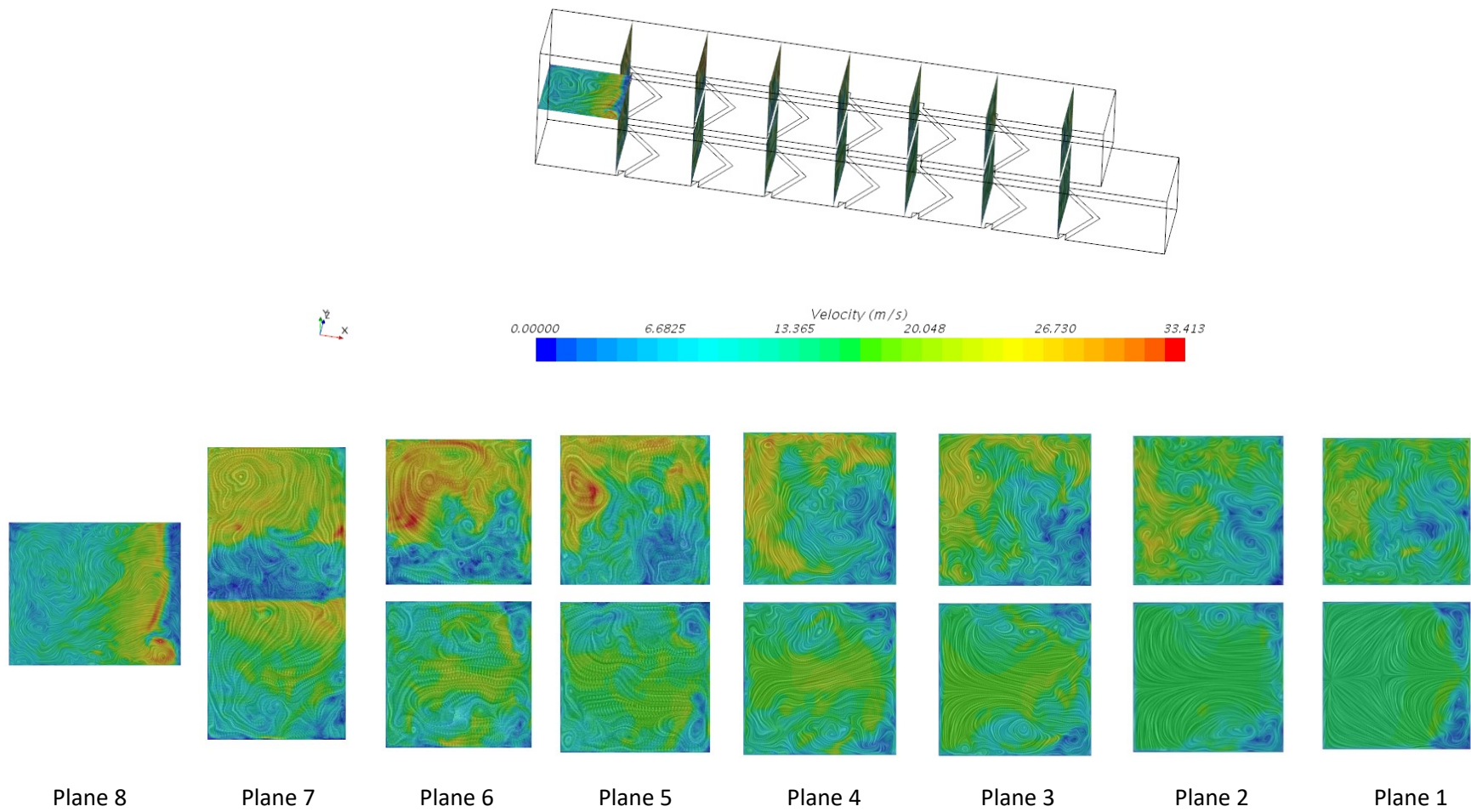


Figure 6-31: contours of velocity and streamline on the normal planes, V-Shape configuration $P/e=10$ $U_{in}=12.5\text{m/s}$

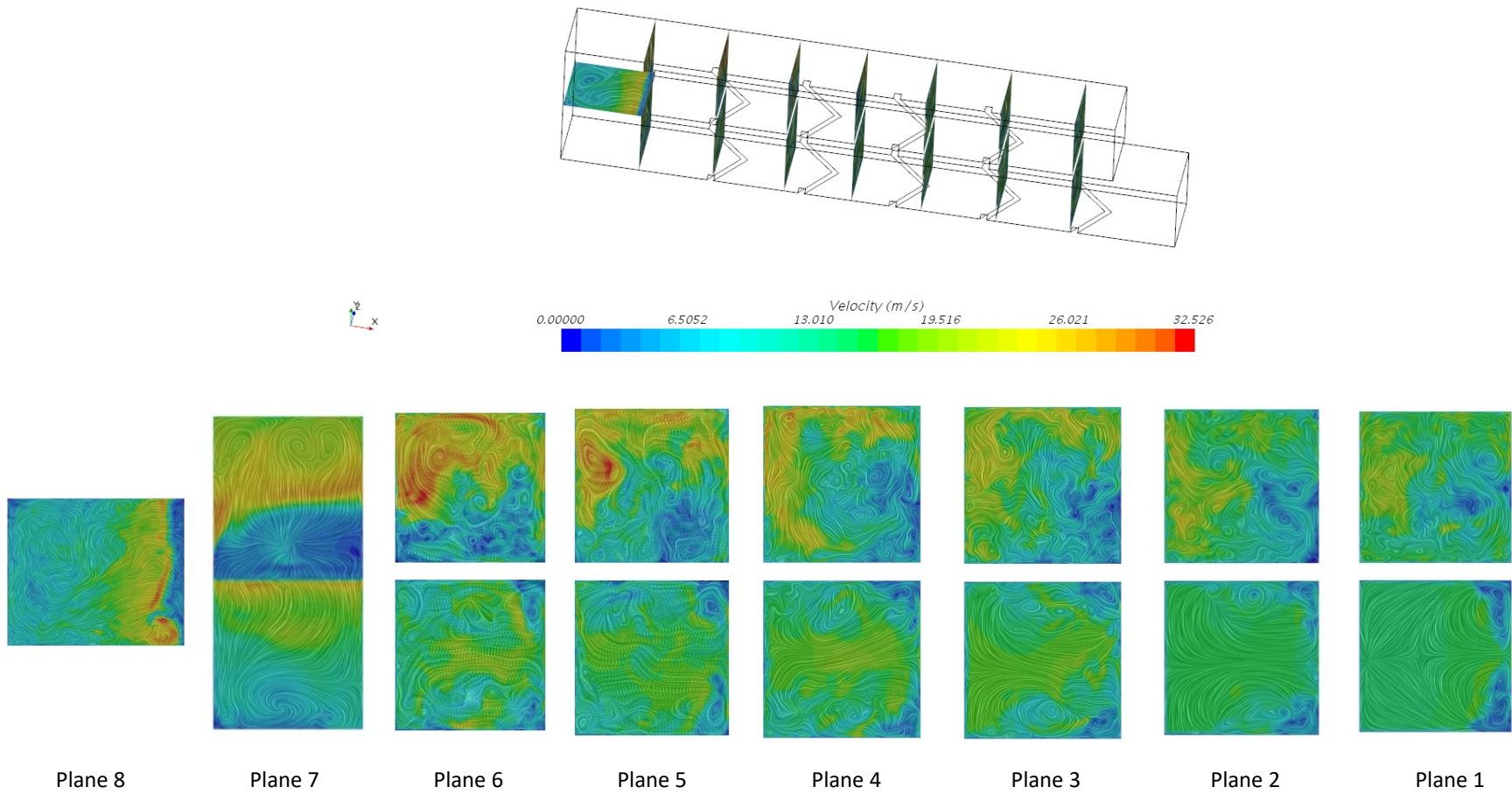


Figure 6-32: contours of velocity and streamline on the normal planes, V-Shape configuration $P/e=12$ $U_{in}=12.5\text{m/s}$

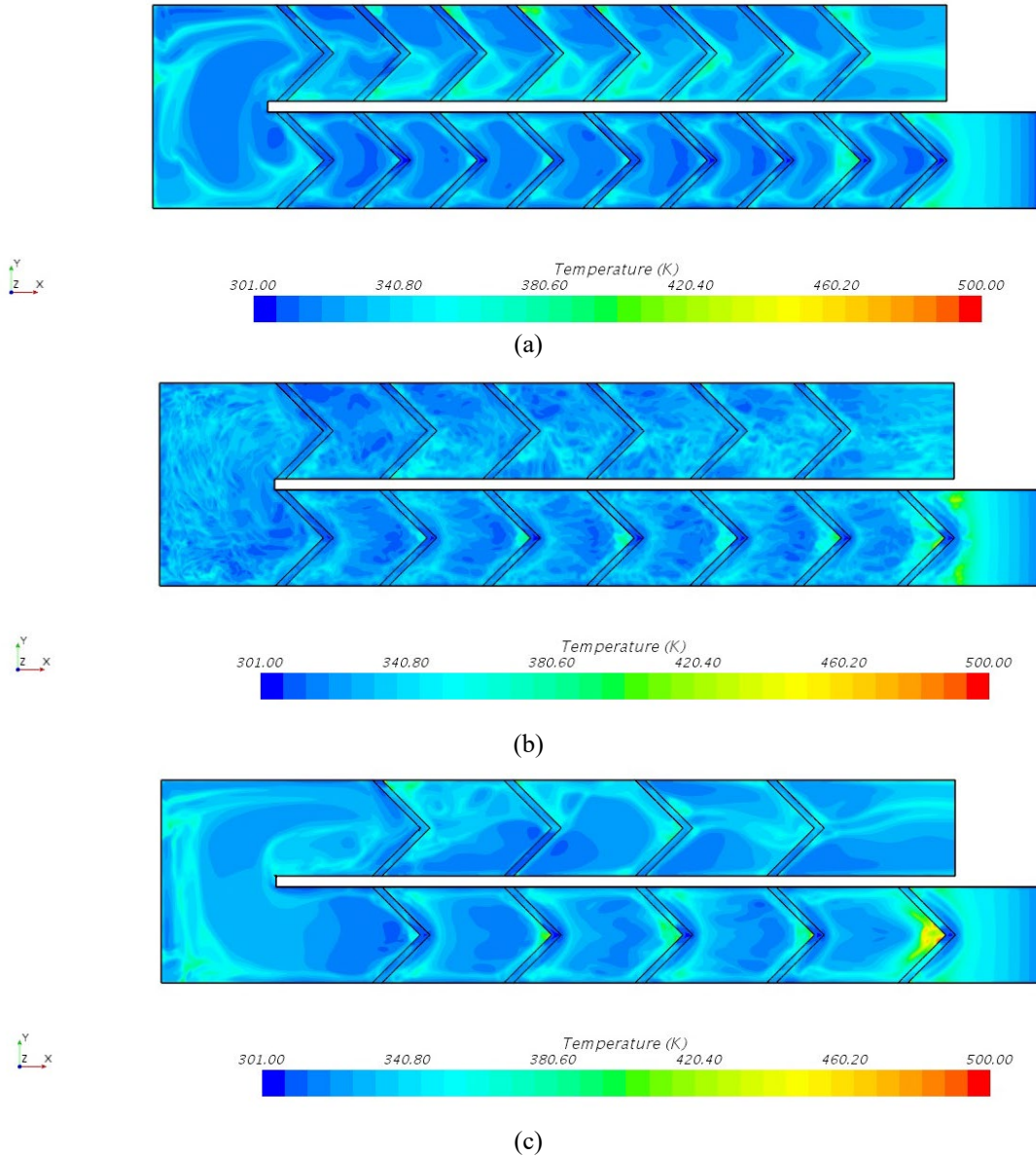


Figure 6-33: Temperature distribution at the bottom wall of the channel for stationary case – V-Shape rib $U_{in}= 12.5\text{m/s}$ (a) $p/e=7$, (b) $p/e=10$, (c) $p/e=12$

Figure 6-34 presents the Nusselt number distribution on the bottom wall. Due to the rib configuration on the first passage, it can be seen the heat transfer coefficient increase between each rib is higher in the second passage. In the second passage, heat transfer increase is mainly closer to the outside walls. This trend is similar in all the P/e ratios; however, for the P/e ratios

due to the reduction in the recirculation zones, more uniform Nusselt number distribution can be observed in the second passage.

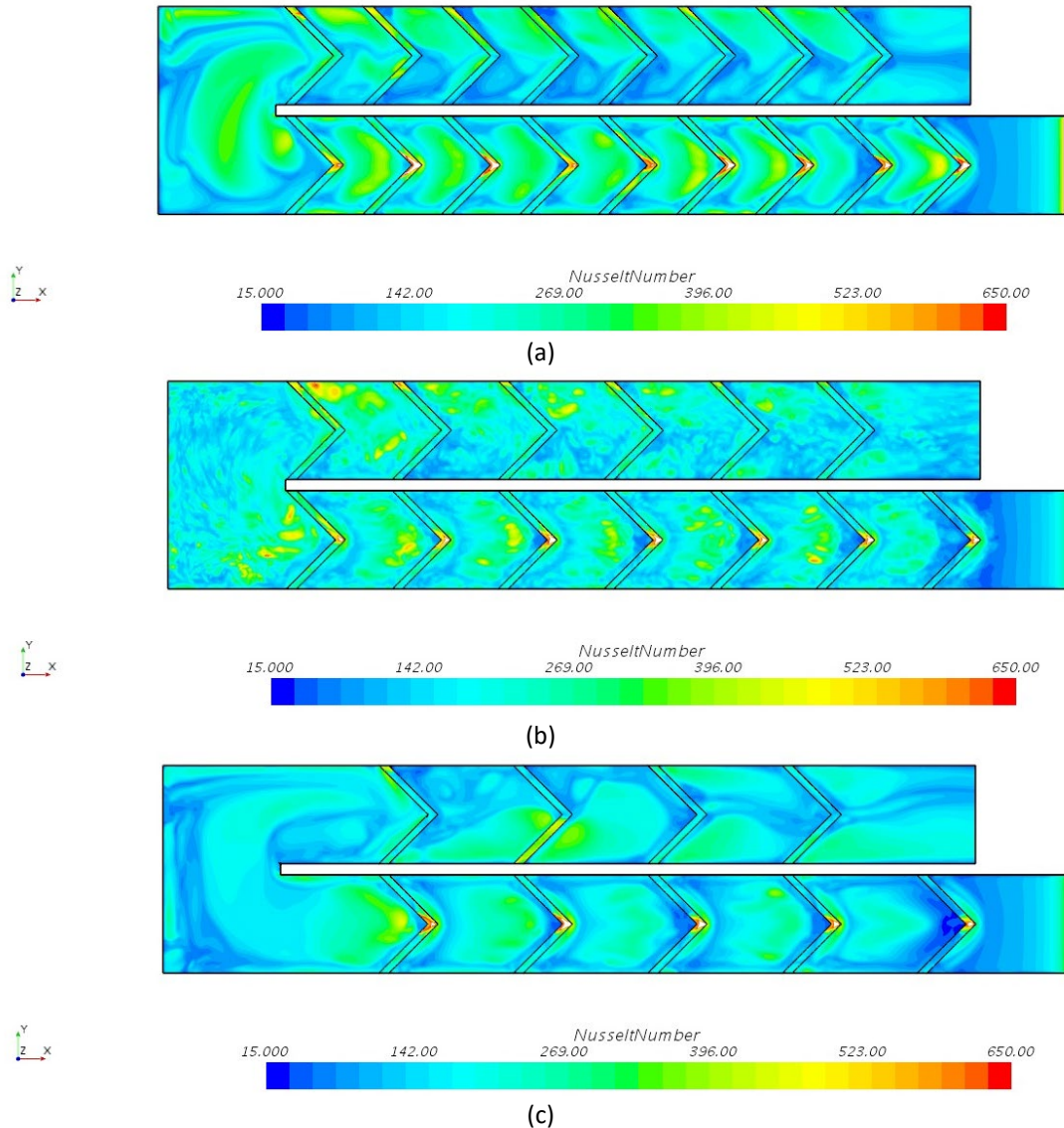
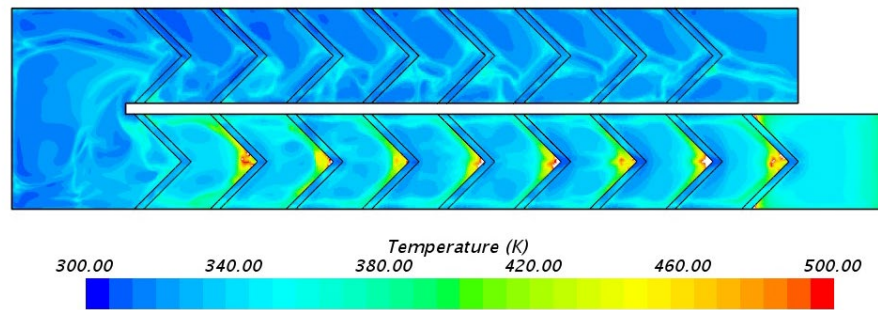


Figure 6-34: Nusselt distribution at the bottom wall of the channel for stationary channel with V-Shape rib case $U_{in} = 12.5 \text{ m/s}$ (a) $p/e=7$, (b) $p/e=10$, (c) $p/e=12$

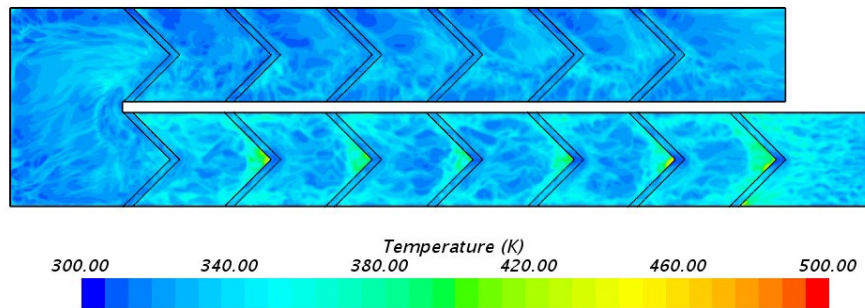
6.4.2 Rotational Cases

As discussed earlier, rotation induces buoyancy and centrifugal forces. These forces reduce the number of recirculation zones and create a uniform flow distribution. Figure 6-35 shows the

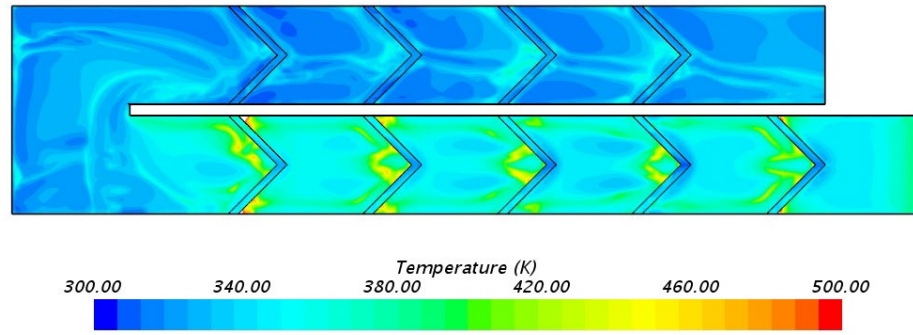
temperature distribution on the bottom wall. As can be seen for P/e 7, due to small distance between the ribs, pressure drop increases, and small recirculation zones generate after the sharp edge of the ribs in the first passage. At the same time, for the other ratios, the temperature distribution is more uniform. Furthermore, Figure 6-36 presents the Nusselt number distribution on the bottom wall. There is a significant increase in Nusselt number distribution on the second passage due to the turning effects and inducing secondary flow. For the first passage, the heat transfer increase in the P/e ratio 10, is higher than the other ratios, and it can be concluded the Pitch-to-rib height ratio 10 has the best performance for both stationary and rotational cases.



(a)

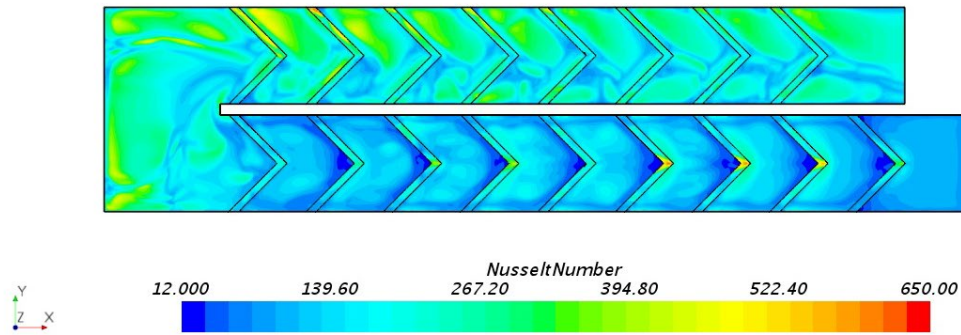


(b)

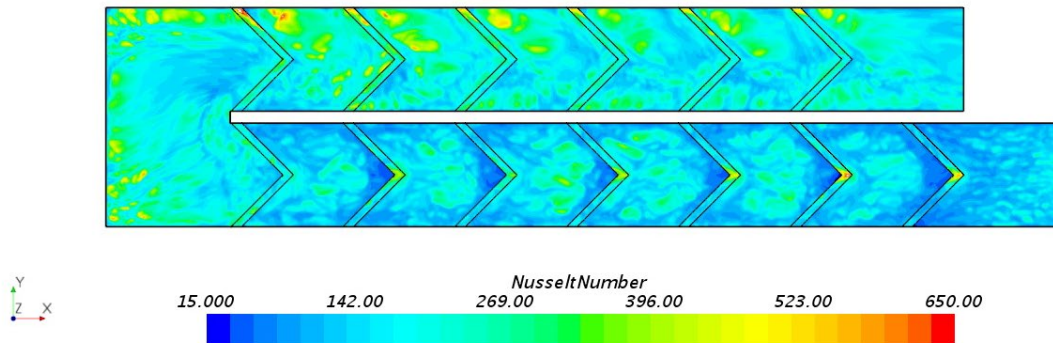


(c)

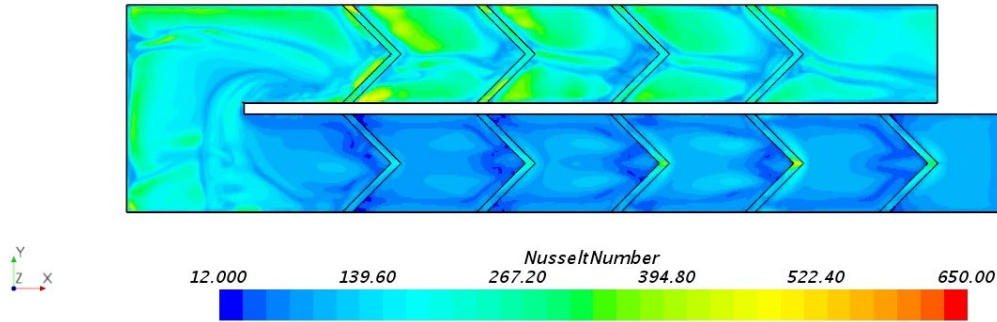
Figure 6-35: Temperature distribution at the bottom wall of the channel with V-Shape rib for rotational case $U_{in}= 12.5\text{m/s}$, V-Shape (a) $p/e=7$, (b) $p/e=10$, (c) $p/e=12$



(a)



(b)



(c)

Figure 6-36: Nusselt distribution at the bottom wall of the channel with V-Shape rib for Rotational case $U_{in}=12.5\text{m/s}$ (a) $p/e=7$, (b) $p/e=10$, (c) $p/e=12$

6.4.3 V-Rib different installation configuration

Another installation for V-rib configuration can be considered where at the second passage, flow first passes the angles of the rib the arms. It was decided to denote this configuration as V-shape design 2. Figure 6-37 illustrates the new rib configuration. From the results presented in the previous section, it was decided to investigate the flow distribution only for P/e 10.

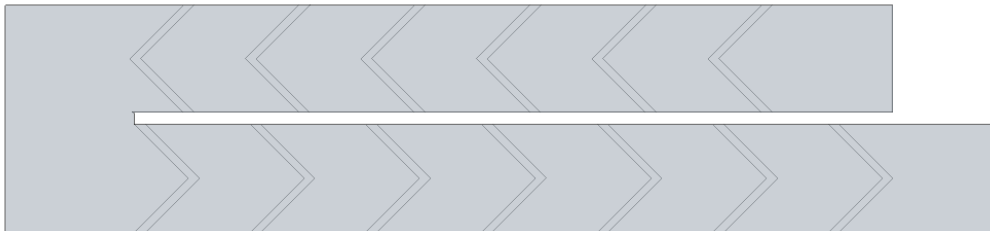
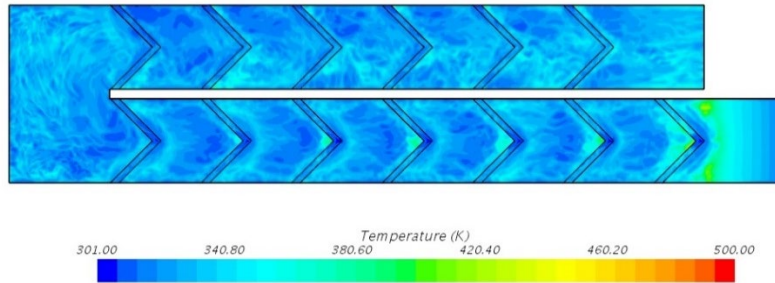


Figure 6-37: inlet/outlet for Channel with V-shape rib design two configuration $P/e=10$

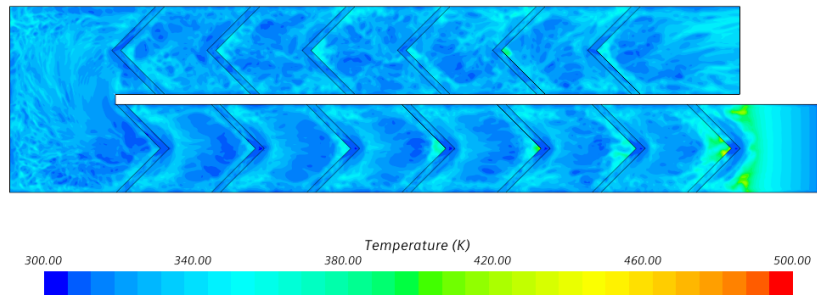
6.4.3.1 Stationary results comparison

The temperature distribution comparison between two V-rib configurations is shown in Figure 6-38. As can be seen, the overall temperature distribution remained the same in the first passage. While in the second passage, the temperature distribution for ribs in the second

configuration had better uniformity, which can be due to better velocity distribution after each rib.



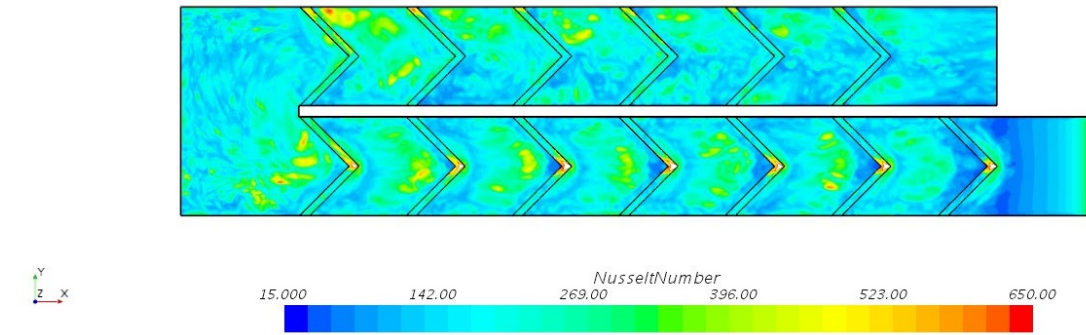
(a)



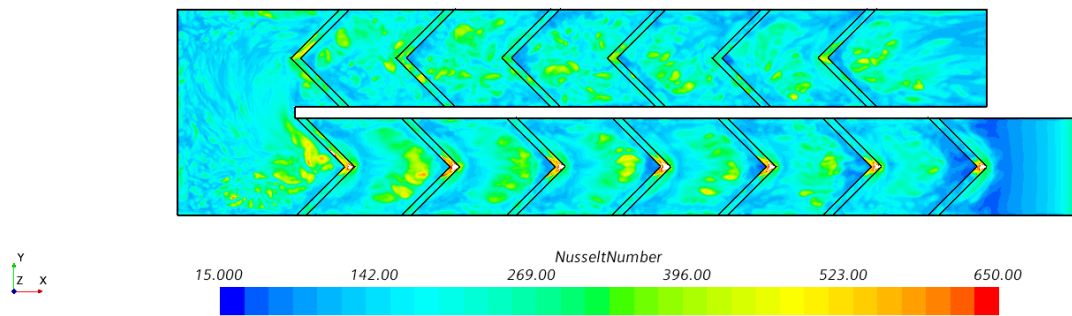
(b)

Figure 6-38: Temperature distribution comparison for various V-rib configuration, Stationary case with $Re=35000$, (a) Initial Design, (b) V-Shape Design 2

Figure 6-39 describes the Nusselt number distribution on the bottom wall of the two-pass channel. Similar to temperature distribution, both configurations had slightly similar Nusselt number distribution in the first passage. While in the second for the second rib installation configuration, the higher Nusselt number value distribution is more uniform between each rib while for the setting, one higher Nusselt number was identified closer to the out walls.



(a)

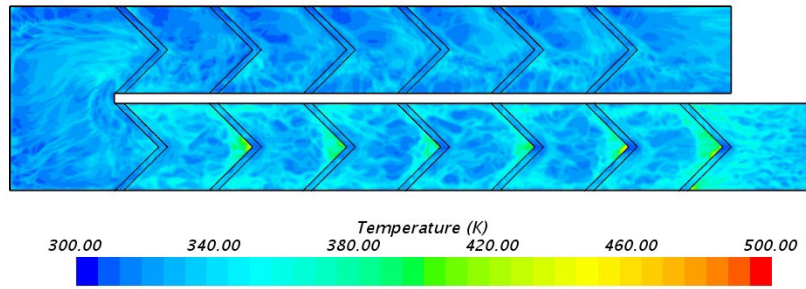


(b)

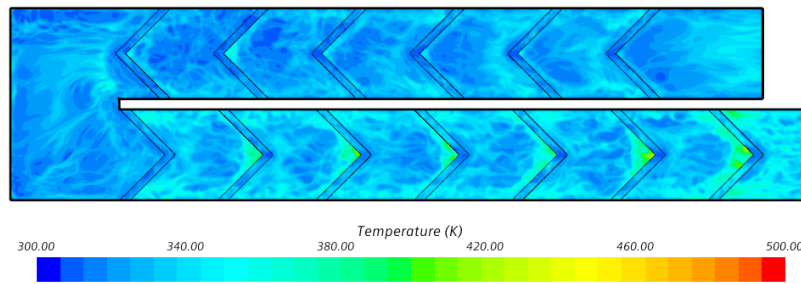
Figure 6-39: Nusselt distribution comparison for various V-rib configuration, Stationary case with $Re=35000$, (a) Initial Design, (b) V-Shape Design 2

6.4.3.2 Rotational results comparison

Figure 6-40 and Figure 6-41 show the temperature and Nusselt number distribution on the channel bottom wall in the rotation. As can be seen for the second configuration, lower temperature distribution can be seen mainly in the center of space between the ribs. While for the design 2 setting, the lower distribution mostly observed near the other wall.

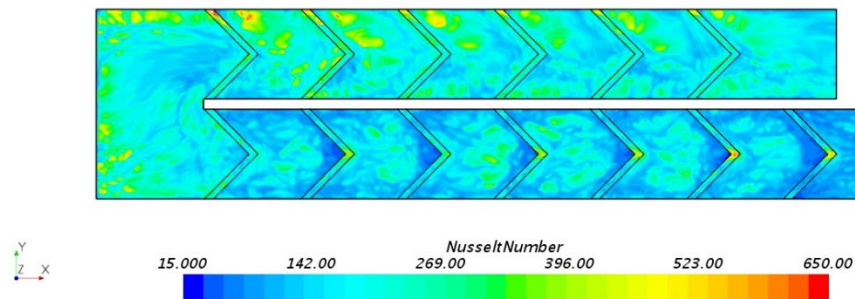


(a)

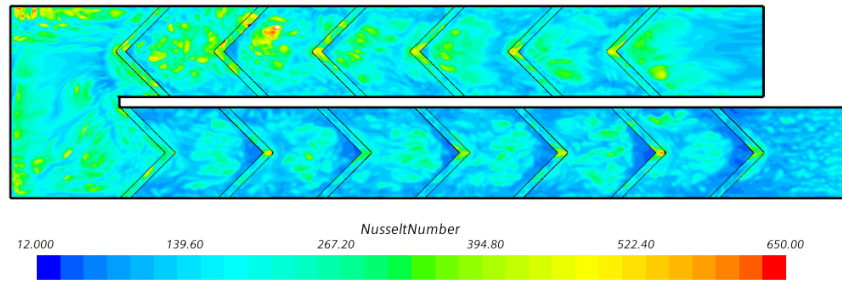


(b)

Figure 6-40: Temperature distribution comparison for various V-rib configuration, the rotational case with $Re=35000$, (a) Initial Design, (b) V-Shape Design 2



(a)



(b)

Figure 6-41: Nusselt distribution comparison for various V-rib configuration, the rotational case with $Re=35000$, (a) Initial Design, (b) V-Shape Design 2

From stationary and rotational results, it can be concluded the overall Nusselt number for both settings are similar. However, for the initial V-shape configuration, the Nusselt distribution is more uniform. Thus, it was decided to use the initial V-shape setup results for the rest of this thesis.

6.5 Summary of P/e Ratio and rib Geometry Comparison

In the previous sections, three different rib turbulator configuration with various rib spacing (mentioned as P/e ratio) were studied. For each rib configuration, a detailed investigation of the effect of the P/e ratio was implemented. In this part, results from all these configurations are compared.

As mentioned earlier, the objective of optimizing the internal cooling channels is to increase the heat transfer between the coolant and the channel walls and reduce the pressure drop. Installing turbulators enhances the Nusselt number coefficient while it increases the pressure drop. Thus, in the rib configuration study, it is necessary to capture the amount of pressure

drop. For calculating the friction factor and thermal performance for each configuration, Equation 5-2, Equation 5-3, and Equation 5-4 were used.

In the following sections, results for the Nusselt number, friction factor, and rib thermal performance for stationary and rotational motion is going to be presented.

6.5.1 stationary

Figure 6-42 and Figure 6-43 describe the total Nusselt number and friction factor for three rib geometries with different Rib Pitch-to-Rib height (P/e) ratios, respectively. For 45-deg ribs, P/e ratios of 7 and 12 had a higher Nusselt number while both had a higher pressure drop. For the 60-deg ribs ratio, ten had a higher Nusselt number compare with the same ribs with various rib spacing ratios. While the Nusselt number for 45-deg ribs is still higher. V-rib configuration had a significantly higher Nusselt number compare with the other rib geometry, while its pressure drop also is slightly higher for all the rib spacing ratios.

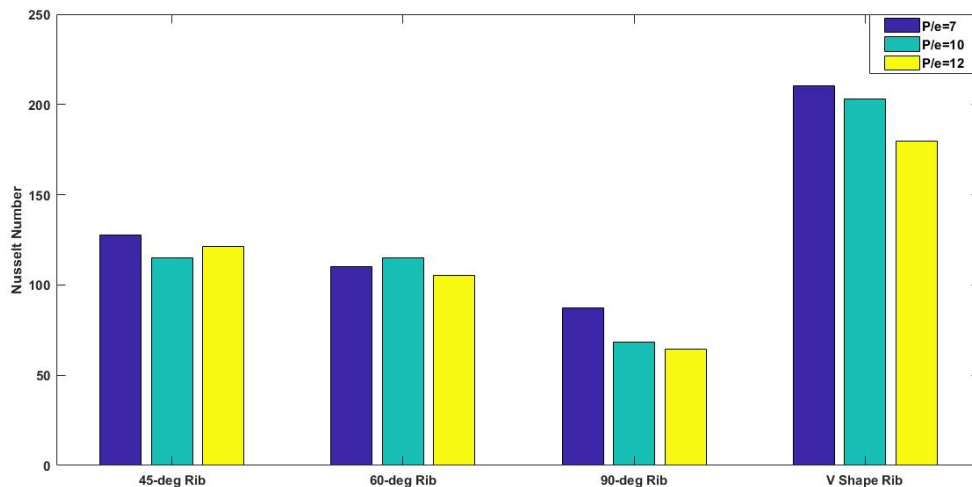


Figure 6-42: Nusselt Comparison of Stationary Cases for various rib configurations and P/e ratios

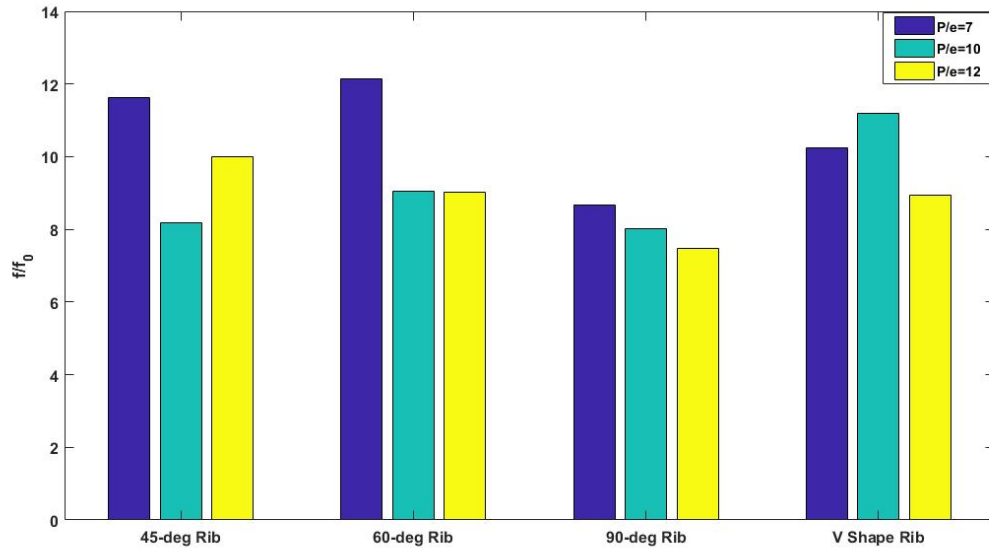


Figure 6-43: Pressure Drop Comparison for various rib configuration and P/e ratios

As mentioned earlier, due to the effects of rib turbulators on Nusselt number and pressure drop, selecting the right rib geometry and rib spacing is usually based on the trade-off between the amount of increasing the Nusselt number and pressure drop.

The thermal performance, η , can be calculated based on the Nusselt number improvement and normalized friction factor [24].

$$\eta = \frac{(Nu/N_0)}{(f/f_0)^{1/3}} \quad \text{Equation 6-1}$$

Figure 6-44 shows the rib thermal performance for different rib geometry and rib spacing. From this figure, it can be concluded despite the high-pressure drop V-ribs still have a higher thermal performance compared with the other rib geometry. 45-deg rib with different rib

spacing slightly has similar thermal performance; however, due to the less pressure drop for P/e ratio 10, it has better thermal performance between the angled ribs.

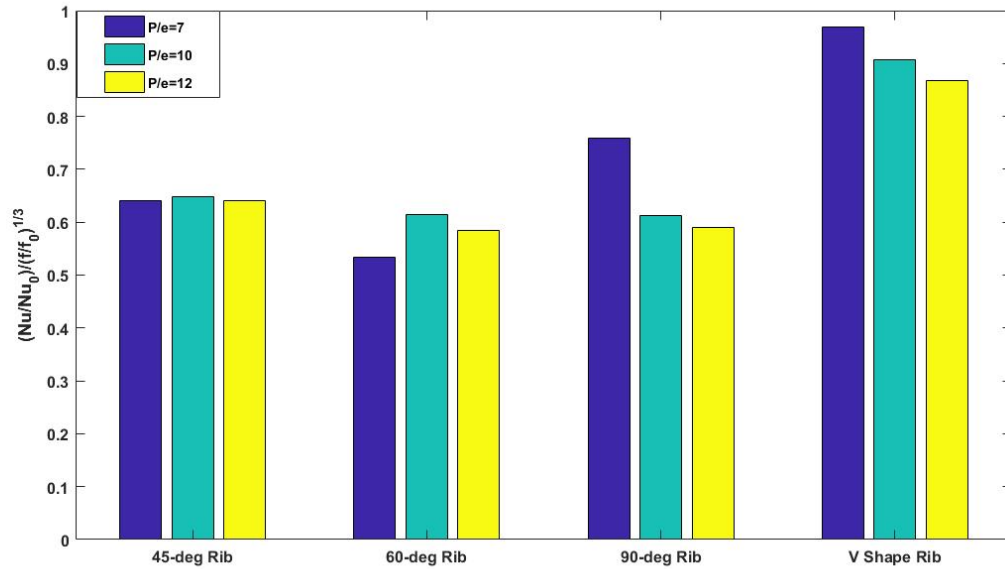


Figure 6-44: Performance Comparison for various rib configurations and P/e ratios

6.5.2 Rotation

Similar to the stationary cases, Nusselt number, friction factor, and rib thermal performance have been compared for the rotational motion. Figure 6-45 and Figure 6-46 show the Nusselt number and friction factor for various rib geometry. Like the stationary cases, the V-shape rib has a higher Nusselt number values for all the P/e ratios compare with the other ribs. Between the angled ribs, 45-deg rib has a higher Nusselt number. Furthermore, 45-deg rib has a lower pressure drop compared with the other rib configurations.

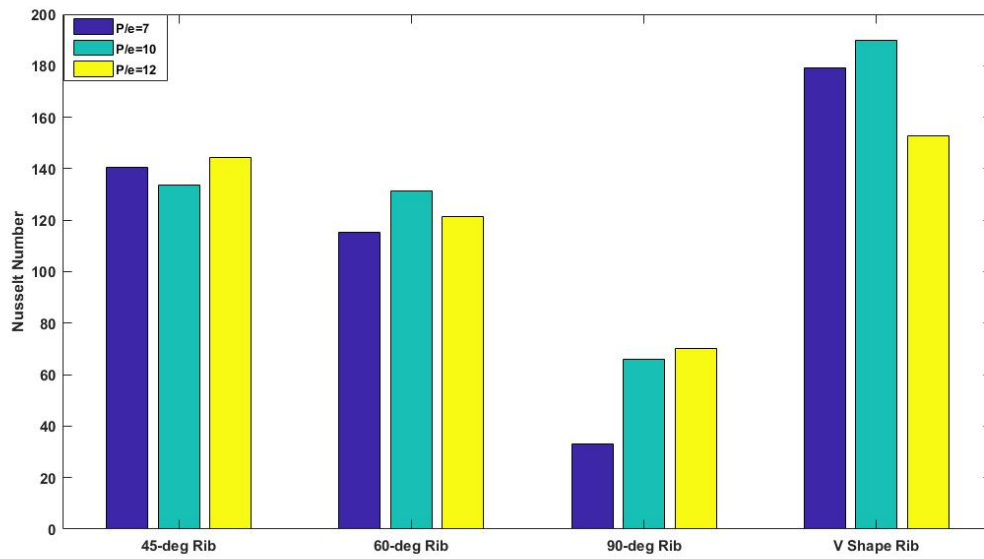


Figure 6-45: Nusselt Comparison Rotational Cases for various rib configurations and P/e ratios

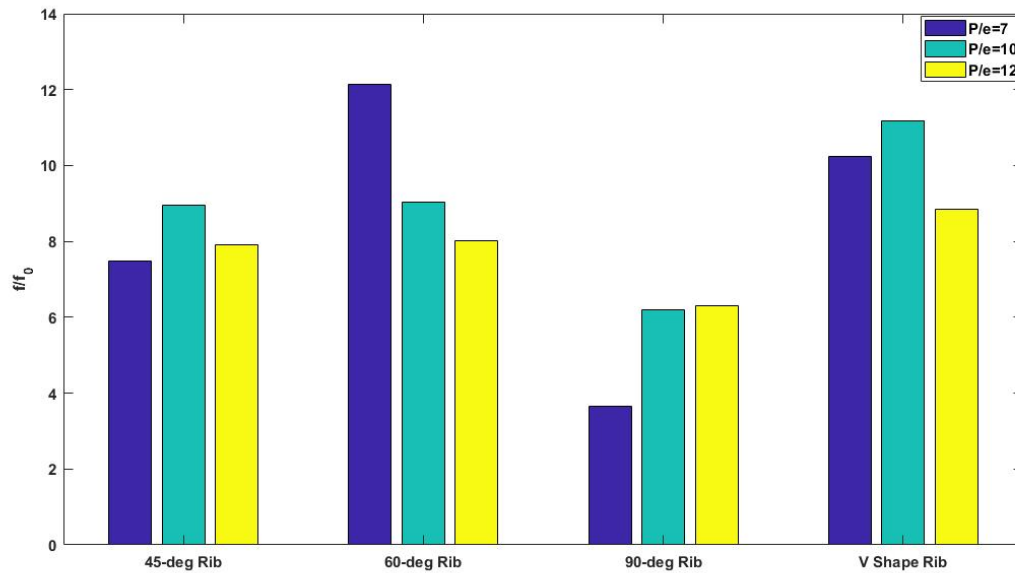


Figure 6-46: Pressure Drop Comparison for various rib configurations and P/e ratios

Figure 6-47 indicates the rib thermal performance. For the V-shape rib P/e ratio, 10 had the highest thermal performance. For the 60-deg ribs, P/e ratio 7 had a better performance than other ratios, while for the 45-deg ribs P/e 10 has the better performance.

Results from stationary and rotational cases show that for the current channel, V-shape Ribs in any P/e ratio have a higher thermal performance than parallel angled ribs. However, it should be noted this type of rib configuration has a higher pressure drop among the other ribs. In Parallel angled ribs, 45-deg rib shows a better thermal efficiency, especially for P/e ratio 10. Due to the less pressure drop and higher thermal efficiency, 45-deg rib with P/e ratio ten was considered to be the best rib configuration for the channel under this study.

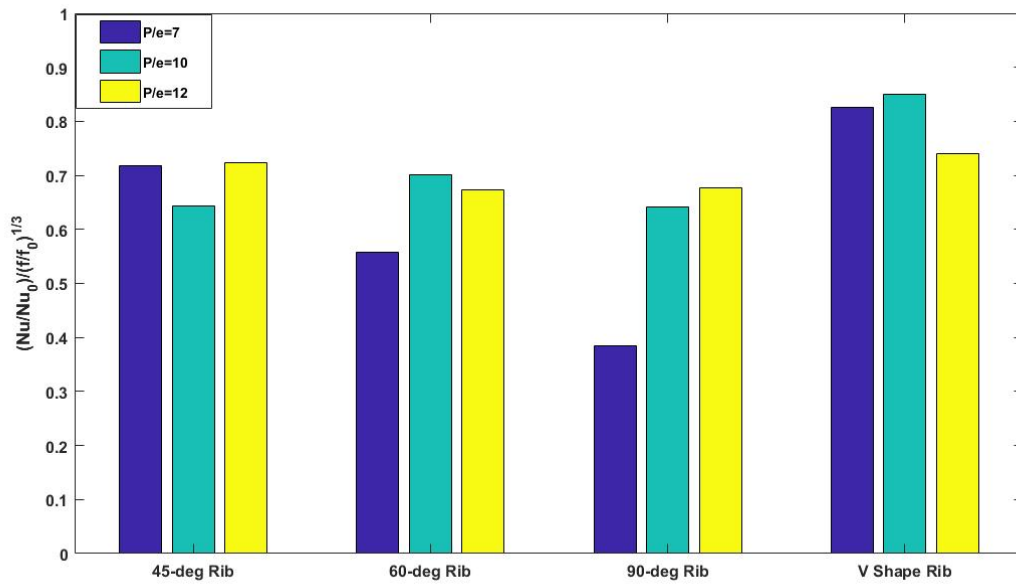


Figure 6-47: Performance Comparison for various rib configuration sand P/e ratios

6.6 Conclusions

In this chapter, computational results for different rib configurations were presented. For the rotational cases in the first passage, heat transfer increases further on the trailing wall under centrifugal buoyancy effects. Nusselt number increases along the channel for all rib configurations. Furthermore, the impact of rib spacing was discussed in this chapter. For the parallel rib configuration, 45-deg ribs with P/e ratio 10, has higher thermal efficiency and lower pressure drop.

For the high-performance V-shaped rib, the P/e ratio ten has a better performance than ratio seven and 12. Two installation configurations have been investigated. Here these two configurations denoted as design one and design 2. Results showed that various installation configuration does not have a significant effect on the heat transfer coefficient. However, Design 2 configuration increases the pressure drop compared with the design one.

In general, installing ribs increases the pressure drop from inlet to outlet of the channel, while the Nusselt number significantly increased. Thus deciding on the installing ribs usually is based on the trade-off between increasing the heat transfer capability and increasing the pressure drop.

7 Turning Guide Vane Effect on Internal cooling of Two-Passage channel

7.1 Introduction

As mentioned in the Literature survey, flow behavior in the turning regions is unpredictable. While flow passes through these turning regions, there are considerable changes in heat transfer and pressure distribution. Thus, the turning effect can be considered as one of the most critical phenomena in the flow behavior and overall heat transfer performance of the cooling channels. As flow passes through the turning regions, several recirculation regions are generated, and a significant pressure drop is observed. These changes in the turning area result in a decrease in the overall heat transfer rate.

While many researchers emphasized the turning region effects, a limited number of studies performed on the flow behavior and heat transfer ratio in this region. Zehnder et al. [96] added guide vanes on a two-passage channel and investigated heat transfer and pressure drop. Their results implied that using guide vanes in this region significantly affected the heat transfer ratio in cooling channels. Bunker [97] investigated the effect of adding various tip shaped surfaces into the channels. His results indicated that implementing these changes had significant enhancement on the heat transfer coefficient compared with the smooth channels.

In this chapter, the main focus is to have a better understanding of flow behavior in the turning region. New turning guide vane designs and orientations to evaluate maximum heat transfer coefficient enhancement was proposed. A detailed heat transfer and pressure measurement were performed both experimentally and numerically for all guide vane configurations. This study was inspired by the work of Park et al. [98], who used different guide

vanes to investigate the thermal performance enhancement. The results suggested that adding a turning guide vane to the cooling channel enhances the heat transfer coefficient ratio.

For this study first, the effect of installing turning guide vanes on Nusselt number in a smooth wall was investigated. Once an initial evaluation of the impact of turning guide vanes on the pressure drop and heat transfer coefficient performed, the effect of turning guide vane for the roughened wall was investigated.

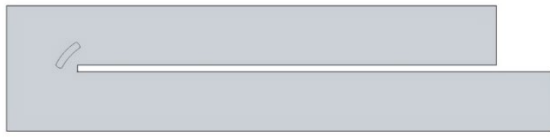
For the roughened wall study, 45-deg angle ribs were installed on the bottom wall of the channel. Rib turbulators had a parallelogram cross-section of 6.35mm×6.35mm. The rib pitch-to-rib height (P/e) was 10, and the rib height-to-hydraulic diameter ratio (e/D_h) was 0.125. Table 7-1 indicates the detailed dimensions of the geometrical model used in this study.

Table 7-1: Dimensions of the channel with 45-deg parallel rib

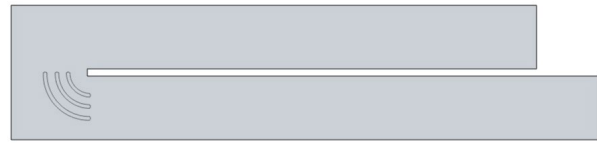
Description	Size
Hydraulic Diameter (D_h)	50.8mm
First Passage Length (L_1)	514mm
Second Passage Length (L_2)	460mm
Rib Height to Channel Hydraulic Diameter Ratio (e/D_h)	0.125
Rib Pitch to Rib height Ratio(p/e)	10

7.2 Effect of Turning Guide Vanes on the Smooth Wall Channel

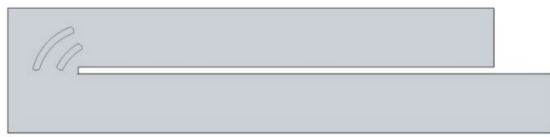
Figure 7-1 shows the eight proposed guide vane schemes for the smooth wall channel. The inner and outer radius of these guide vanes are $1D_h$ and in some designs were $2D_h$. The guide vane thickness was 6.35mm.



(a)



(e)



(b)



(f)



(c)



(g)



(d)



(h)

Figure 7-1: Various guide vane designs: (a) V1 (one guide vane after the turn);(b) V2 (two guide vanes after the turn) (c)V3 (Semi circle guide vane),(d) V4(three guide vanes after the turn) (e) V5(three guide vanes before the bend, (f)V6 one guide vane before the bend(g) V7(two guide vanes before the bend, (h) V8 one guide vane with longer length before the turn

From heat transfer results in chapter five, it was observed higher heat removal rate happens at the turning region and second passage. While flow passes through the first passage, the

Nusselt number slightly decreased up to the turning region. In the turning region, due to the increase in the turbulence Nusselt number significantly increased. As flow passed through the second passage, the Nusselt number decreased; however, due to the higher turbulence, the Nusselt number was higher than the first passage. Furthermore, from the previous chapters, it can be concluded increasing flow turbulence increases the mixing of hot and cold gases and boost the heat transfer coefficient. Thus, it is necessary to use a turbulator design in the turning region to prevent lower velocity areas near the edges.

7.2.1 Smooth Wall channel with Turning Guide Vanes-Stationary results

Figure 7-2 Shows the Nusselt number comparison in stationary cases between Reynolds number 6000 and 35000. Similar to the results from chapters five and six, in the stationary cases increasing the Reynolds number increased the Nusselt number coefficient. From the figure, it can be observed installing the guide vane improved the Nusselt number coefficient compare with the smooth wall with no guide vane. This enhancement could be due to increasing the turbulence and reducing the recirculation zones in the turning region.

From the figure, it can be observed installing one guide vane after the turning region (denoted as V1) and installing three guide vane (denoted as V4), and one guide vane before the turning region (indicated as V6) showed a better performance in increasing the Nusselt number.

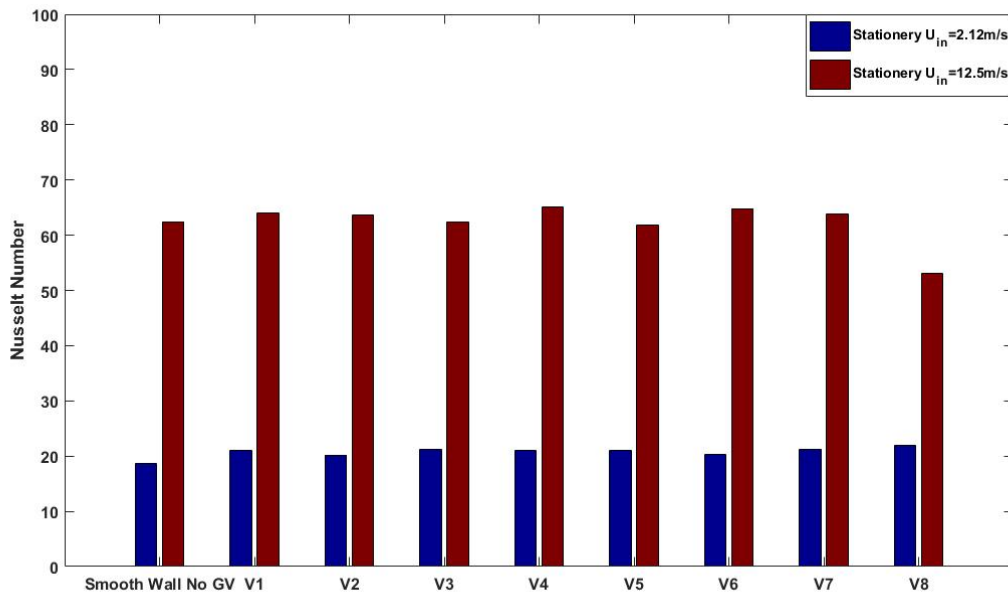


Figure 7-2: Nusselt number comparison in the stationary case for $Re=6000$ and $Re=35000$

The objective of the optimization of the cooling channels is to reduce the pressure drop and enhanced the heat transfer coefficient. The pressure drop was evaluated by calculating the fanning friction factor from Equation 5-2.

Figure 7-3 compares the friction factors for different Reynolds numbers. As it was predicted, installing the turning guide vanes increases the pressure drop in most cases. However, guide vane design V1 creates less pressure drop in the higher Reynolds number.

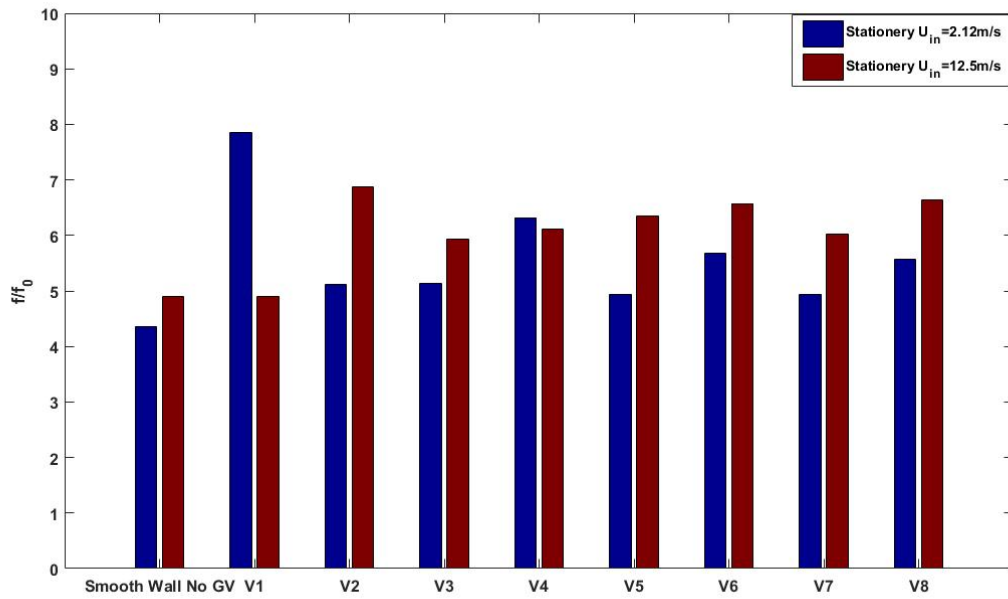


Figure 7-3: Normalized friction factor comparison for stationary cases with Reynolds 6000 and 35000

From the presented results, it can be observed installing turning guide vane increases both heat transfer coefficient and pressure drop. While in the designing cooling channels, the objective is to increase the heat transfer ratio and decrease the pressure drop. Thus, to have a better design evaluation, it is necessary to investigate the thermal performance of each design. Thermal performance was discussed extensively in earlier chapters. Figure 7-4 describes the thermal performance comparison for Reynolds number 6000 and 35000. For the Reynolds number 6000, in the stationary cases installing the turning guide vane reduces the thermal performance of the cooling channel. While for the higher Reynolds number, 35000, installing turning guide vanes enhanced the thermal performance. Among the turning guide vanes design V2, V4 and V8 showed a better performance.

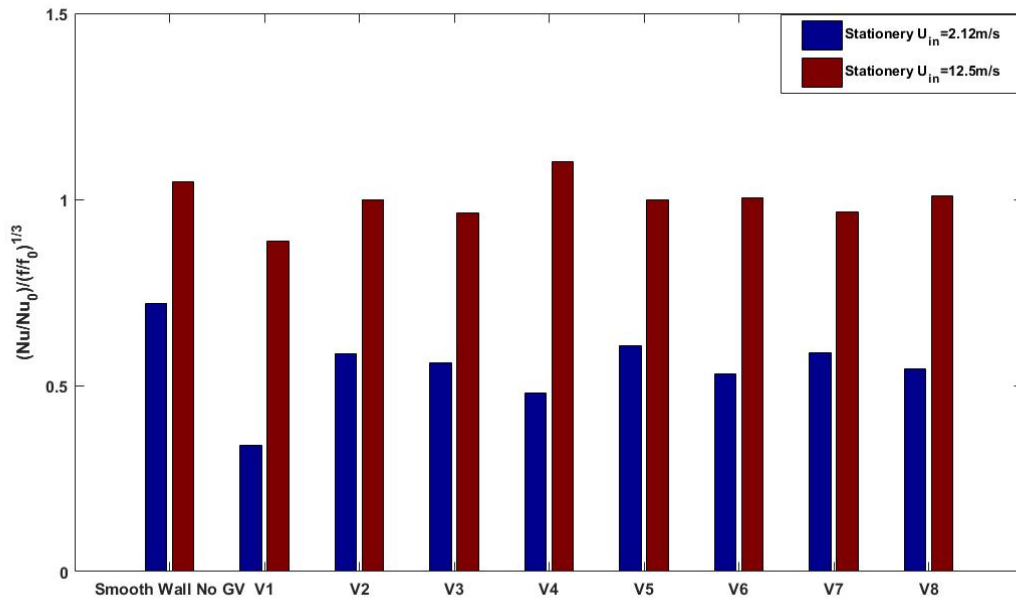


Figure 7-4: Thermal performance comparison for stationary cases for Re=6000 and Re=35000

7.2.2 Rotational Results

Figure 7-5 describes the Nusselt number comparison between stationary and rotational cases with Reynolds number 6000 and Rotation number of 0.75. Similar to previous chapters' results, the Nusselt number in rotational cases was higher than the stationary cases. Unlike the stationary results, installing the turning guide vanes in the smooth wall increases the Nusselt number significantly, especially in guide vane design V5. While from Figure 7-6, it can be seen installing V5 turning guide vane design generated a higher pressure drop. Also, guide vane design V8, and V3 had a lower pressure drop compared with the other designs.

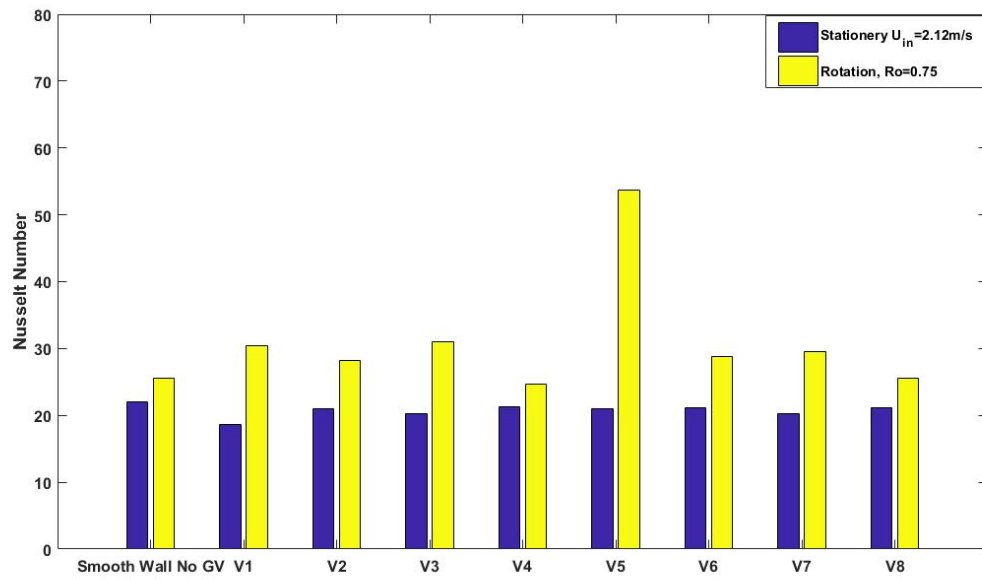


Figure 7-5:Nusselt Number comparison for various guide vane in stationary and rotational condition

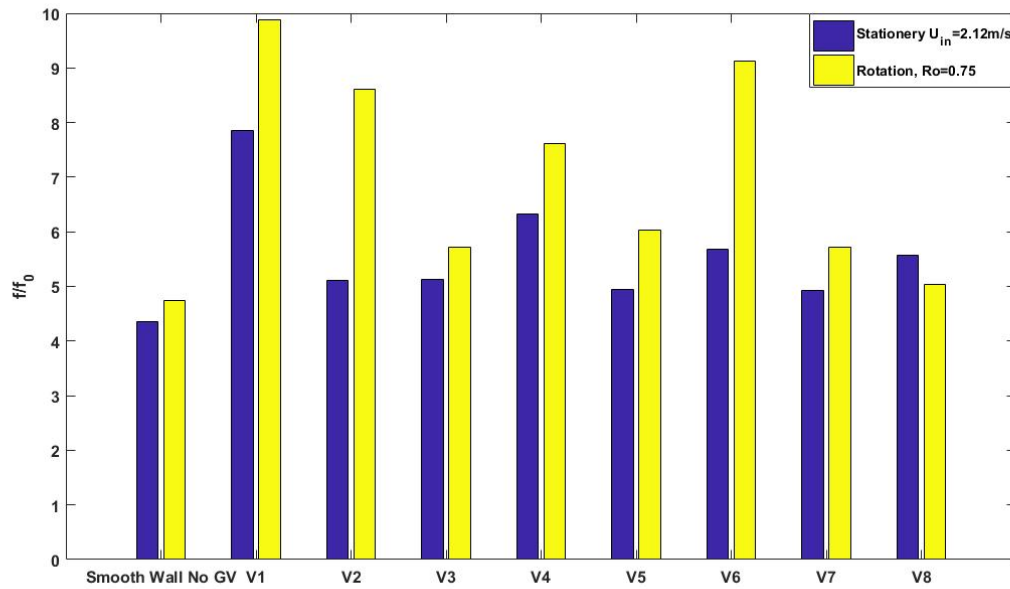


Figure 7-6: Friction factor comparison for smooth wall channel and turning guide vane, stationary and rotational cases

Channel thermal performance is presented in Figure 7-7. In the rotational cases, the channel thermal performance for most of guide vane designs was higher than the smooth wall channel. Among the guide vane designs, V6 and V8 show a better performance.

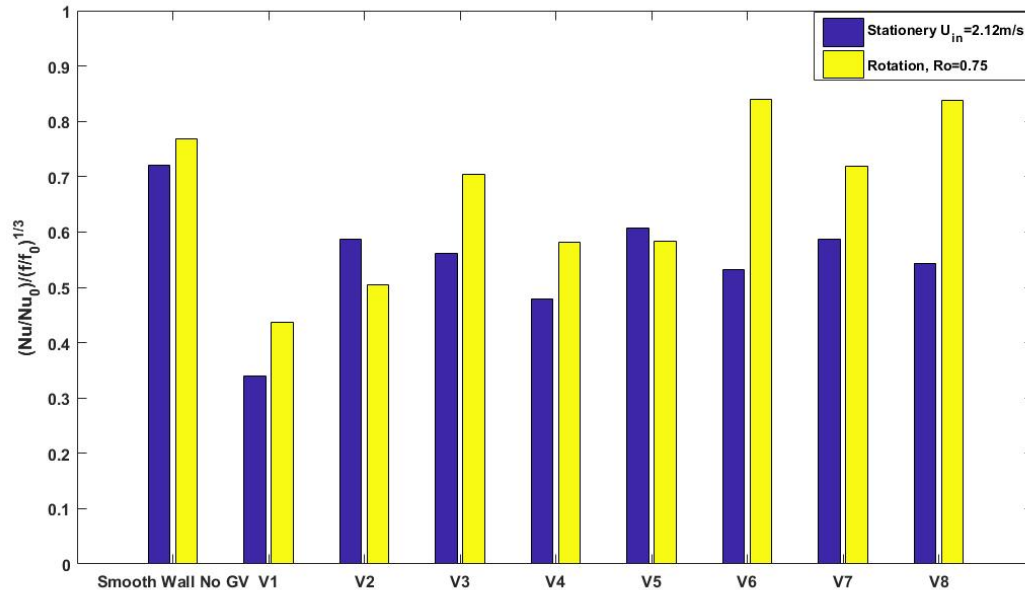


Figure 7-7: Thermal performance comparison for the smooth wall channel and turning guide vane, stationary and rotational cases

From the presented results, it can be concluded despite the higher pressure drop, the turning guide vane installed on channels created more turbulence and increased the heat transfer coefficient. Furthermore, roughened wall channels had higher thermal performance compare with the smooth wall channels. Therefore, to find an optimum rib roughened configuration for the current channel, a combination of rib roughened wall and turning guide vane effect on the overall heat transfer was studied.

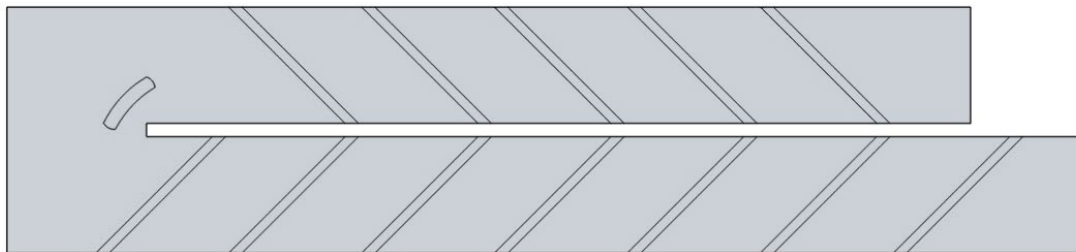
7.3 The effect of turning guide vane on the channel with parallel 45-deg rib channel

45-deg parallel Rib turbulators with a parallelogram cross-section of 6.35mm×6.35mm was installed on the channel bottom wall. The rib pitch-to-rib height (P/e) was 10, and the rib height-to-hydraulic diameter ratio (e/D_h) was 0.125. Table 7-2 indicates the detailed dimensions of the geometrical model used.

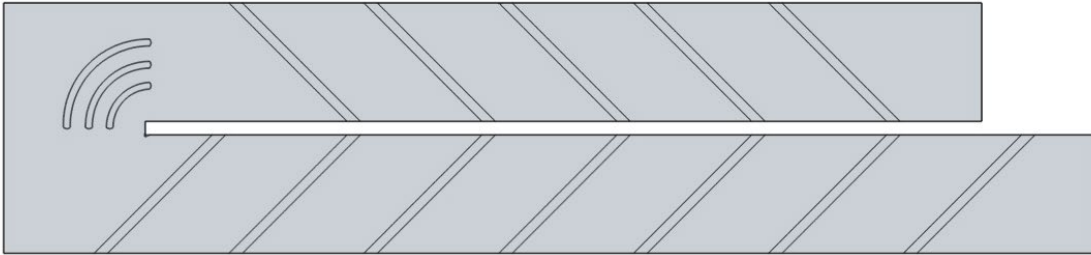
Table 7-2: Dimensions of the channel with 45-deg parallel rib

Description	Size
Hydraulic Diameter (D_h)	50.8mm
First Passage Length (L_1)	514mm
Second Passage Length (L_2)	460mm
Rib Height to Channel Hydraulic Diameter Ratio (e/D_h)	0.125
Rib Pitch to Rib height Ratio (p/e)	10

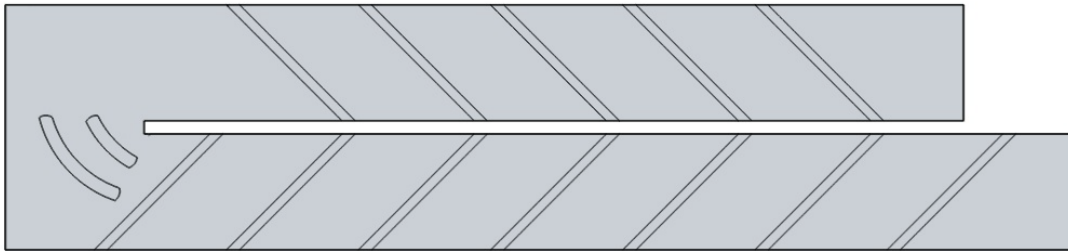
Furthermore, four turning guide vane orientations (VR1, VR2, VR4, and VR8) were selected from section 7.2 for this study. Figure 7-8 shows the four guide vane scheme used in this study. For all the proposed designs, the total surface of the ribs stayed constant. However, because of the geometry of the last design, VR8, the number of ribs decreased. The current study mainly focuses on the design of the guide vane and its effect on the heat transfer coefficient on the turning region.



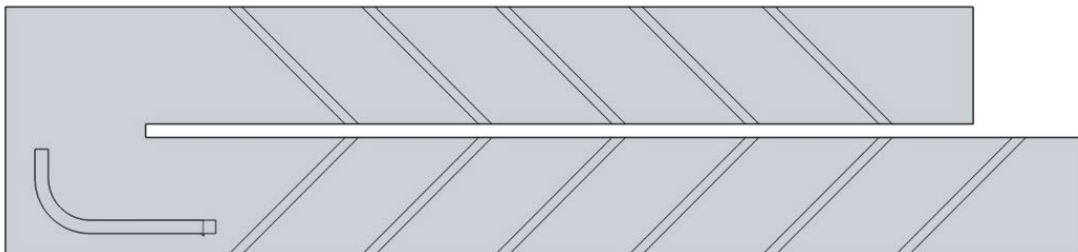
(a)



(b)



(c)



(d)

Figure 7-8: Various guide vane designs: (a) VR1 (one guide vane after the turn);(b) VR2 (two guide vanes before the turn);(c) VR4 (three guide vanes after the turn)(d) VR8 (one guide vane with longer length before the turn)

7.3.1 Results for Stationary Cases

Figure 7-9 shows the time-averaged Nusselt number distribution along the channel. As can be seen, after flow passed through each rib, the Nusselt number increased in both passages. In the turning region, when flow passed the guide vane, more turbulence was generated, which

results in an increase in the Nusselt number in this region. For the cases VR1 and VR2, this enhancement is more significant.

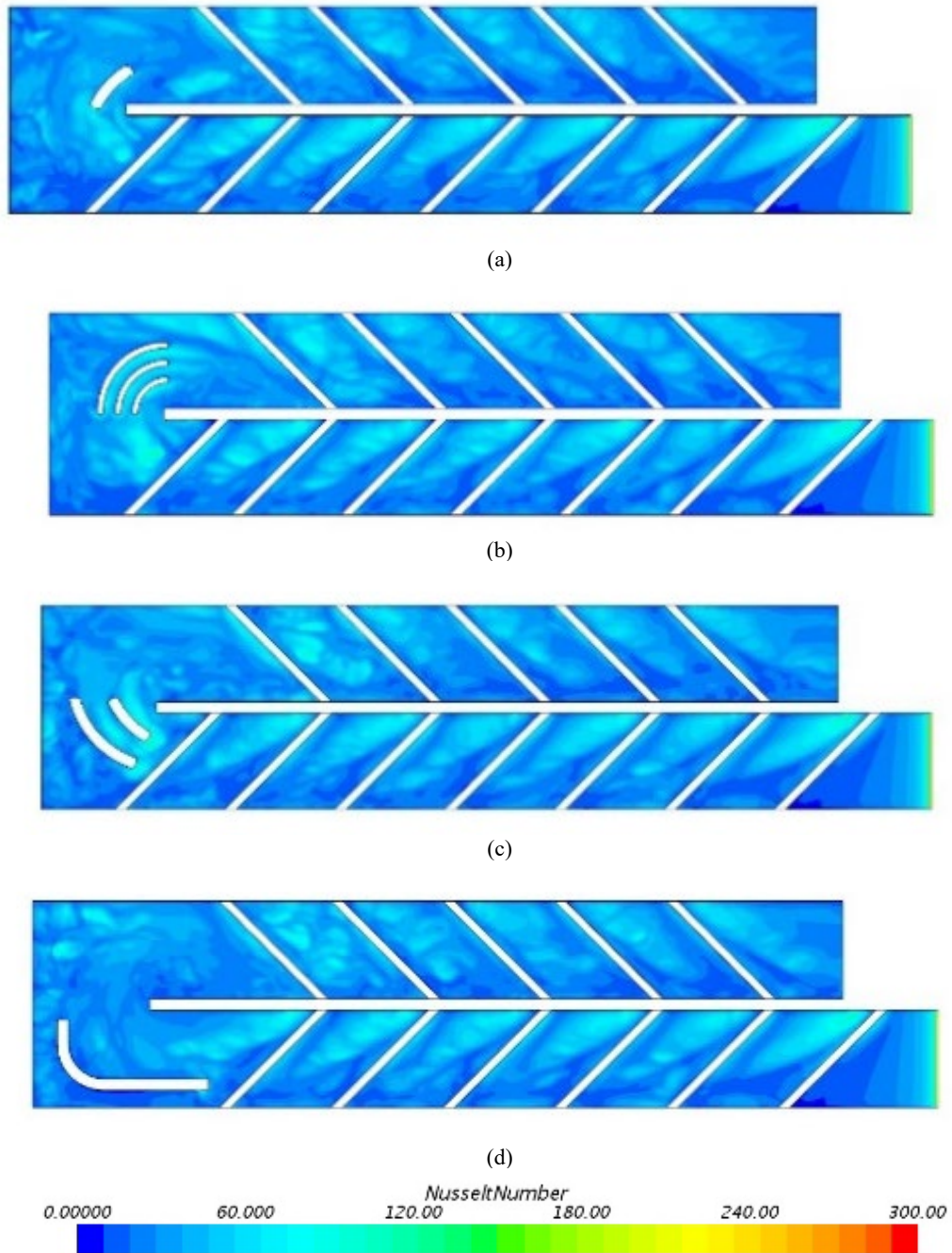


Figure 7-9: Nusselt number distribution for the stationary cases for Re=6000 (a) VR1(b) VR2 (c) VR4 (d) VR8

Figure 7-10 displays the time average of the Nusselt number ratio distribution along the channel for the 45-deg rib configuration with and without designed guide vanes. From the stationary data. Figure 7-10 shows the heat transfer augmentation along the channel for stationary cases. As flow passed through the first passage, flow started to develop, which caused a slight decrease in the Nusselt number ratio. In the bending region, a significant increase in velocity was observed, which resulted in inducing more irregular behavior to the flow in this region. These velocity changes increased the Nusselt number ratio. However, when flow passed the bending area, flow separation was induced by the divider wall, which decreased the heat transfer ratio in the second passage.

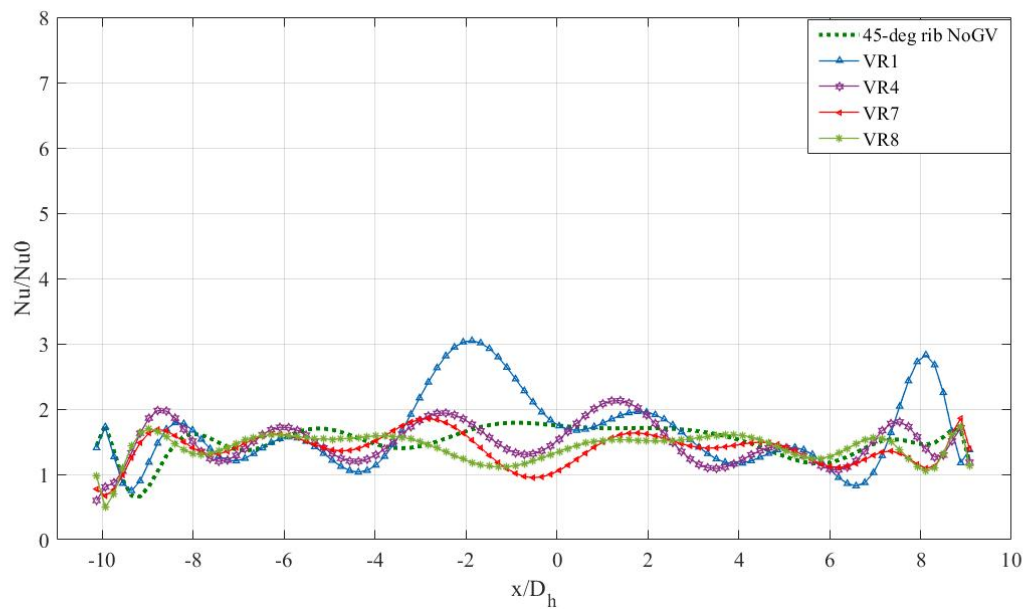


Figure 7-10: Heat Transfer augmentation along the channel, with different guide vane designs for $Re=6000$

From Figure 7-10, it can be observed that guide vanes improved the heat transfer ratio in the bending region. It was noted that between the different guide vane design, one guide vane before the bend and three guide vanes after the bend had the best performance. Figure 7-11

describes the total average of Nusselt numbers for different Reynolds numbers in stationary cases. As can be seen, by increasing the Reynolds number, the Nusselt number enhancement increased significantly.

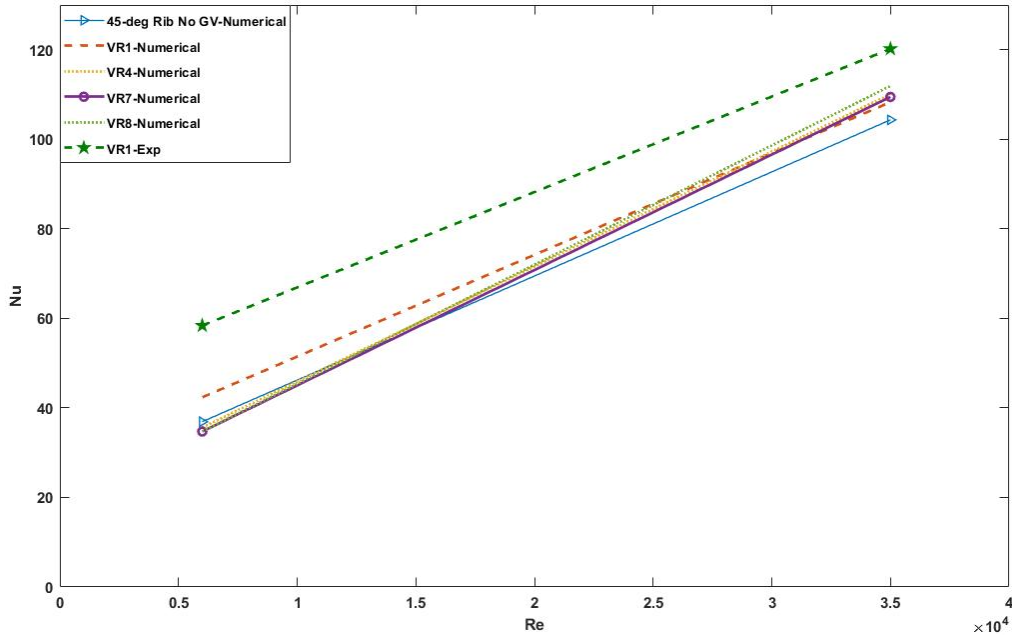


Figure 7-11: Channel Nusselt number for stationary case in various Reynolds number

7.3.2 Heat transfer for rotational Cases

Figure 7-12 shows the time-averaged Nusselt number ratio along the channel for the 45-deg rib configuration with and without the guide vanes. A similar trend for the Nusselt number ratio can be observed for all cases. Rotation induced the buoyancy forces, which influenced the recirculation zones at the channel corners in both passages. The rotation effect decreased the recirculation zones, which resulted in less fluctuation in the Nusselt number trend in the first passage. As flow passed the bending region, the buoyancy forces reached its highest value. Thus, the flow characteristics in this region changed.

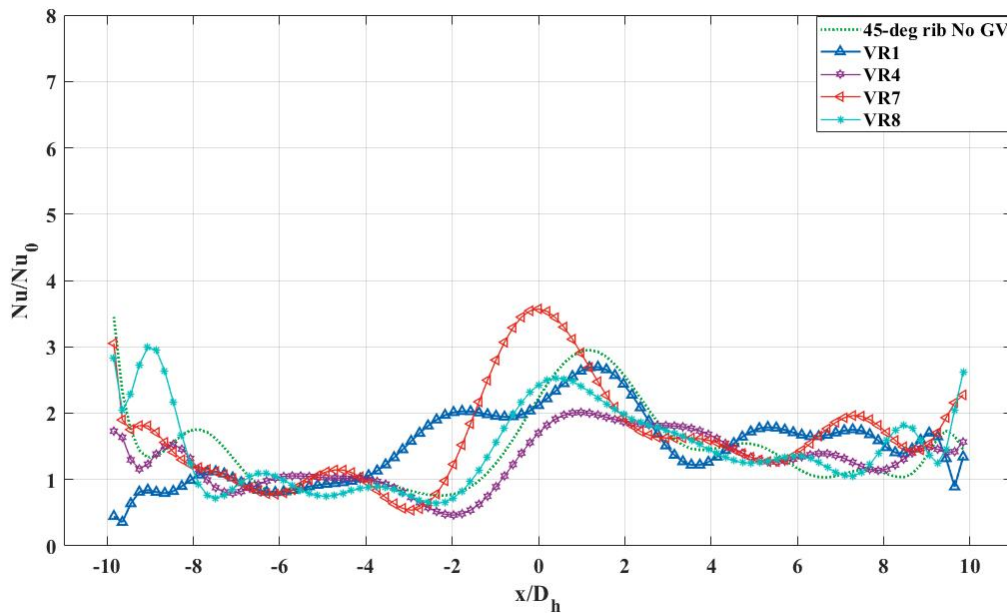


Figure 7-12: Heat Transfer augmentation along the channel, with different guide vane designs for $RO=0.75$

It can be observed that the Nusselt number ratio was highest in this area. The Nusselt number ratio reduced while passing the second passage of the channel. Installing the guide vane improves the overall Nusselt number ratio along the channel, especially in the turning region.

Figure 7-13 shows the friction factor ratio for rotational and stationary cases with and without the guide vanes. The friction factor was higher for stationary cases. However, installing the guide vanes decreased the friction factor for all the cases. This enhancement can be observed mostly in rotational cases due to existence of the buoyancy forces the recirculation zones generated near end walls started to expand and attached to the main streamflow.

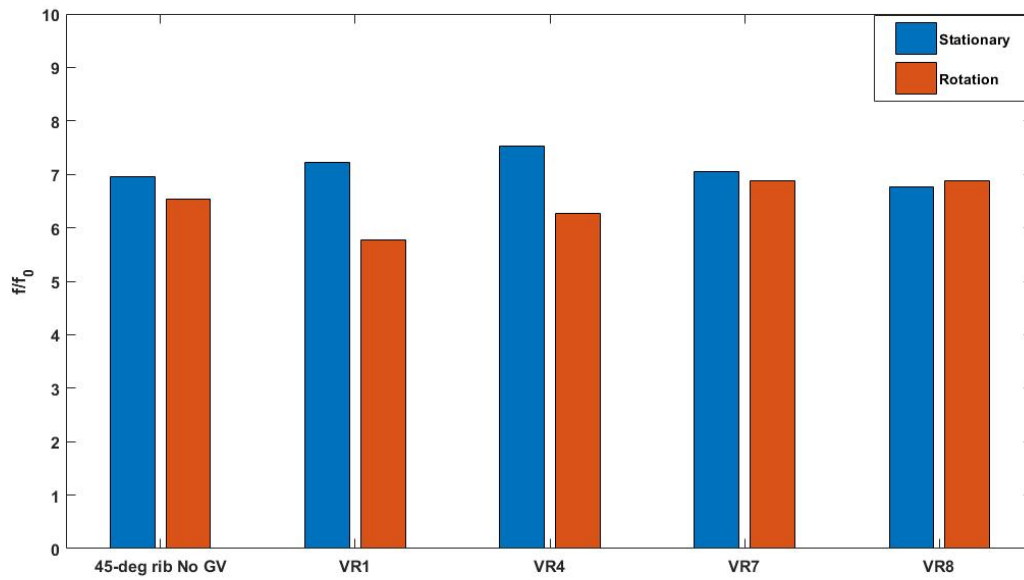


Figure 7-13: Friction factor ratio comparison in stationary and rotation cases for different guide vane designs

The overall thermal performance for all the stationary and rotational cases is presented in Figure 14. Some of the guide vane designs improved the thermal performance, while the other designs did not have any effect on the thermal performance. These changes are mainly dependent on the guide vane location and its impact on the flow separation on the turning region. Furthermore, it needs to be considered that installing the turning the guide vanes increase the pressure drop, which decreased the thermal performance of the guide vanes.

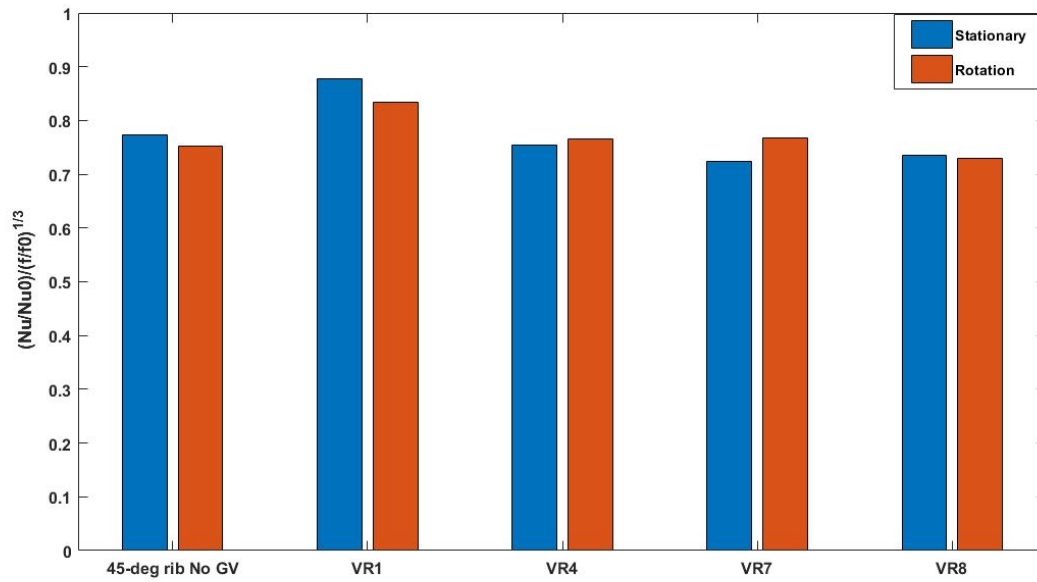


Figure 7-14: Thermal Performance comparison in stationery and rotation cases for different guide vane designs

7.4 Conclusion

In this chapter, several guide vanes, designed and installed on the turning region of a two-pass internal cooling channel with smooth and 45-deg ribs on the bottom wall, were investigated. For the CFD analysis, LES was implemented to investigate the flow behavior in the cooling channel. The effect of the guide vanes on heat transfer enhancement and pressure drop were studied for both stationary and rotational cases. The following is the summary of the findings in this study:

- In the stationary cases, thermal efficiency increased when the guide vane after the bend (denoted by VR1) was used, while the rest of the designs had the same rate of thermal performance.
- Installing the guide vane, in general, enhanced the heat transfer coefficient.
- In the stationary cases, installing the guide vanes reduced the pressure drop, which plays a vital role in the study of the cooling channel.

- In the rotational cases, the installation of the guide vanes enhanced the local heat transfer coefficient in the turning region.
- Increasing the Reynolds number increased the Nusselt number. Additionally, for the higher Reynolds number, the effect of the guide vanes for enhancing the heat transfer coefficient is more significant.
- All proposed designs for the guide vanes improved the overall Nusselt number ratio. However, for the lower Reynolds number, the VR1 case might be the best design.

8 Conjugate Heat Transfer

8.1 Introduction

An accurate heat transfer prediction in the turbine blade cooling channels attracts designers' interests to estimate the blade lifetime. Thus, besides the fundamental knowledge of the convective heat transfer in fluid flow, it is necessary to perform a coupled computations between the fluid flow and the solid body, which is also known as Conjugate Heat Transfer (CHT). This method has been intensively used in industries for the 1D models to obtain the actual durability of the system. In this chapter, a 3-D CHT analysis on the channel cooling system is presented.

8.2 Numerical Set Up

The conjugate heat transfer model solves the heat transfer problem across a contact interface, which is between different materials. In the current study, the contact interface is between fluid and solid. Figure 8-1 shows this interface.

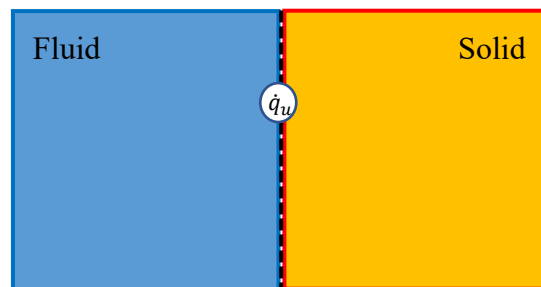


Figure 8-1: Fluid and solid interface schematic

Conjugate heat transfer problem can be solved by considering the conservation of energy, which is the total heat flux is conserved across the interface. Thus, first, it is needed to define boundaries for the fluid and solid region.

Assuming A, B, and C as linearized heat flux coefficient. Also, the temperature at the cells near the fluid and solid boundaries is shown as T_c , and the interface temperature is demonstrated by T_w . For each boundary the heat flux can be calculated from below equations

$$\dot{q}_F = A_F + B_F T_{cF} + C_F T_{wF} + D_F T_{wF}^4 \quad \text{Equation 8-1}$$

$$\dot{q}_S = A_S + B_S T_{cS} + C_S T_{wS} + D_S T_{wS}^4 \quad \text{Equation 8-2}$$

Where F and S denote the fluid and solid properties, respectively. From Equation 8-1 and Equation 8-2, energy conservation can be obtained from the below equation

$$\dot{q}_S + \dot{q}_F = -\dot{q}_u \quad \text{Equation 8-3}$$

Where \dot{q}_u is an optional user-specified heat flux that applied within the interface.

Due to the different heat transfer properties for the regions, the temperature in fluid and solid side of the interface would be different thus, heat flux in each side can be rewritten as below

$$\dot{q}_F = -\frac{\dot{q}_u}{2} + \frac{T_{wS} - T_{wF}}{R} \quad \text{Equation 8-4}$$

Where R is the thermal resistance, solving these equations for the heat flux and temperature resulted in an accurate heat transfer behavior in the cooling channel.

For this study, similar to the previous simulations, the Star CCM+ package was utilized. Both fluid and solid regions were defined. For the fluid region steady-state K-Omega model, with segregated flow temperature and energy was selected. Wall Y+ treatment also was considered. Furthermore, for the solid region, similar material as the test rig, stainless steel (ST37), with constant density and segregated solid energy, was considered. An implicit unsteady condition was solved for the solid region physics.

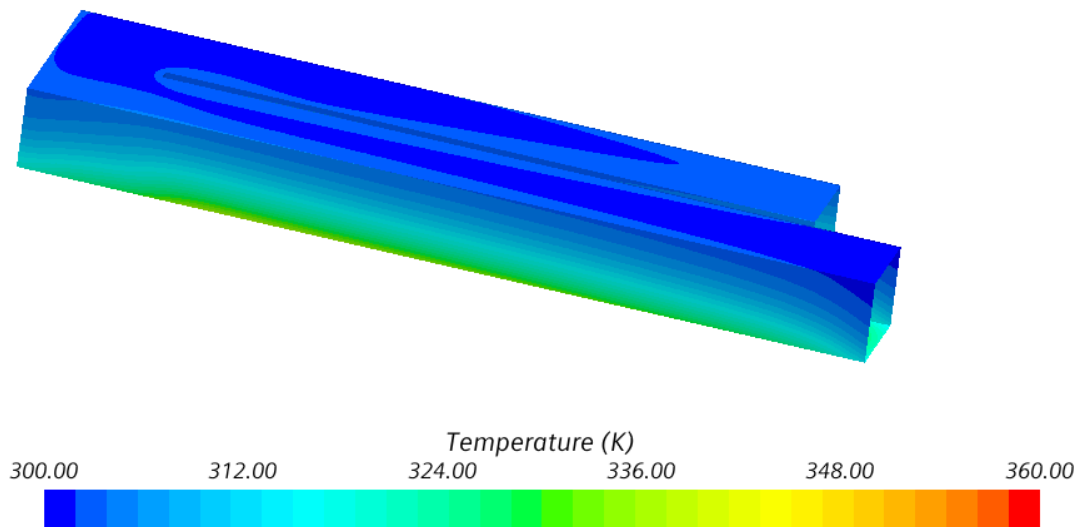
8.3 Results

In the application for this thesis, the conjugate heat transfer study was utilized for a smooth wall channel and a 45-deg parallel rib wall channel. Both stationary and rotational cases were studied.

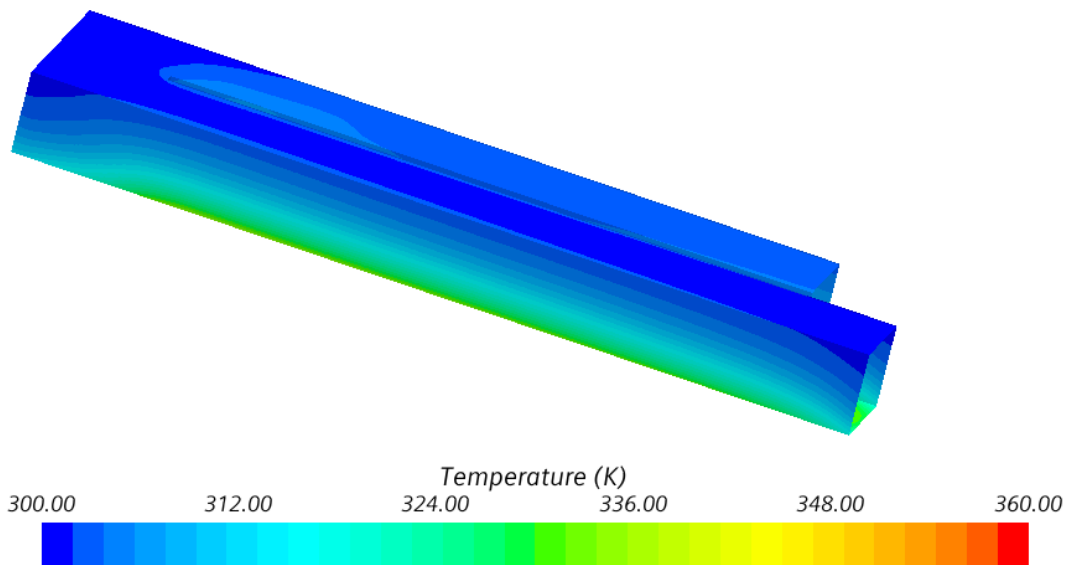
Similar to the previous numerical study, air as coolant with a uniform velocity profile entered the channel. Reynolds number 35000 and rotation speed of 300 rpm was used as the operation point in both channels. For the wall boundary conditions, in the solid region, a constant heat flux 2700 W/m^2 was applied to the bottom wall while the rest of the walls considered to be adiabatic in the fluid region, all the walls considered to have conjugate heat transfer interface condition. In the conjugate heat transfer studies, the main focus is to investigate the temperature distribution at the solid and fluid interface.

8.3.1 Smooth wall Results

Figure 8-2 and Figure 8-3 illustrates the wall temperature distribution for a smooth wall channel in stationary and rotation cases. From the figures, it can be observed for both cases, the temperature at the bottom wall of the first passage is slightly higher than the second passage. This higher temperature can be due to flow turbulence reduction before reaching the turning region. As flow entered, the second passage more due to the turning effect flow became more turbulent, and more heat was removed from the wall, which caused lower temperatures on the second passage. Furthermore, due to the rotation, and existence of buoyancy and centrifugal forces, recirculation, heat transfer between the coolant and the channel walls increased. Figure 8-3 describes the lower temperature at the rotational motion.



(a)



(b)

Figure 8-2: Temperature distribution on the solid wall of a smooth wall Channel (a) Stationary with $Re=35000$, (b) Rotation with $Re=35000$ and 300 rpm

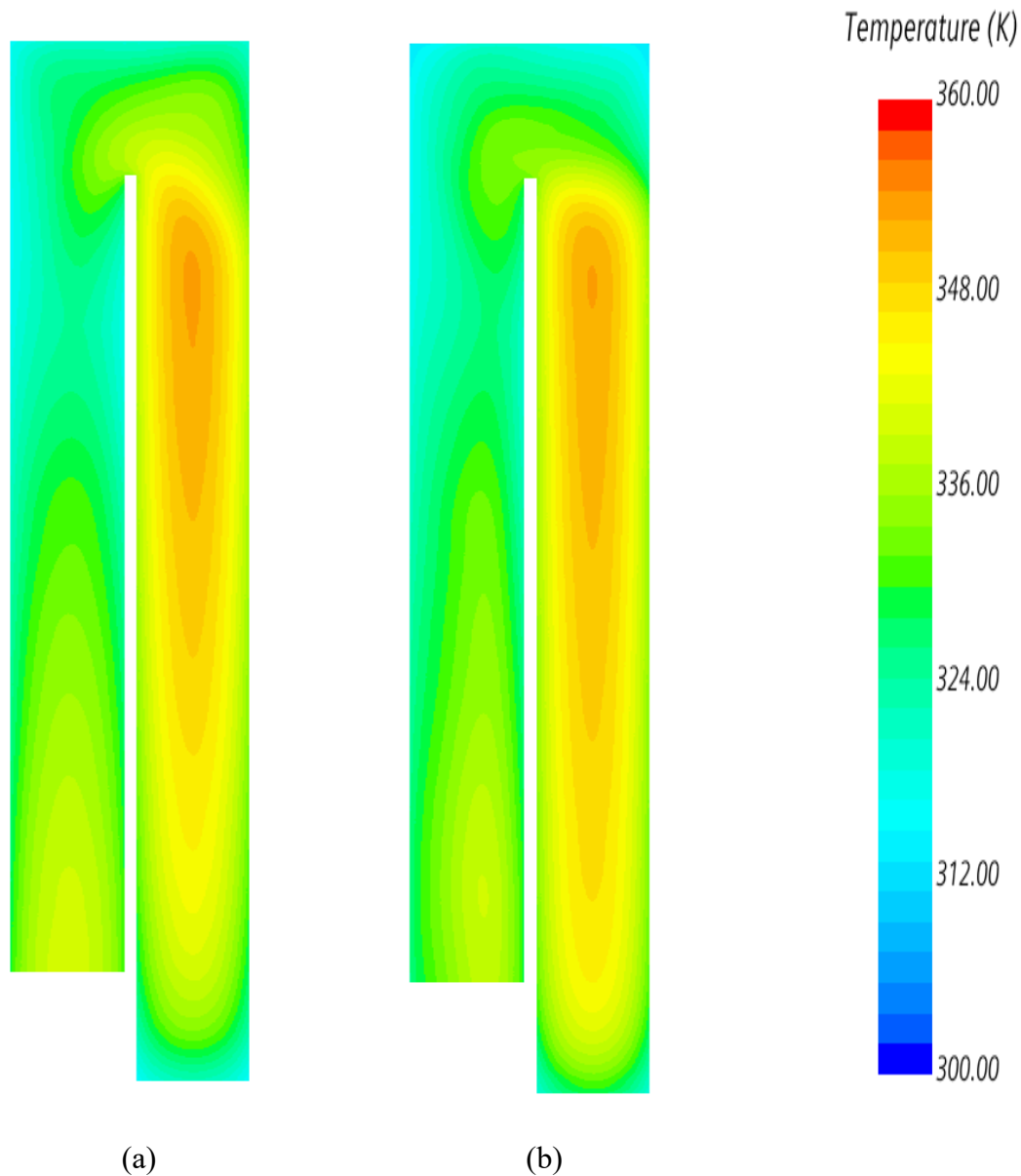


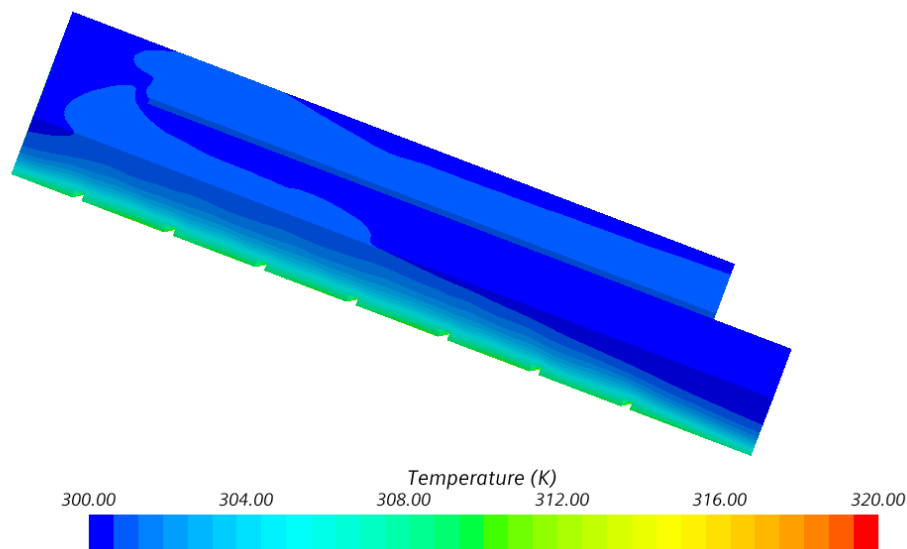
Figure 8-3: Bottom wall temperature distribution for the smooth wall channel (a) Stationary (b) Rotation

In the CHT study, it should be noted the objective is to investigate the temperature distribution on the metal. CHT results are aligned with the presented results in chapter 5. The temperature distribution in the LES model is slightly higher. This difference is mainly due to considering the heat transfer between solid and fluid in the CHT model.

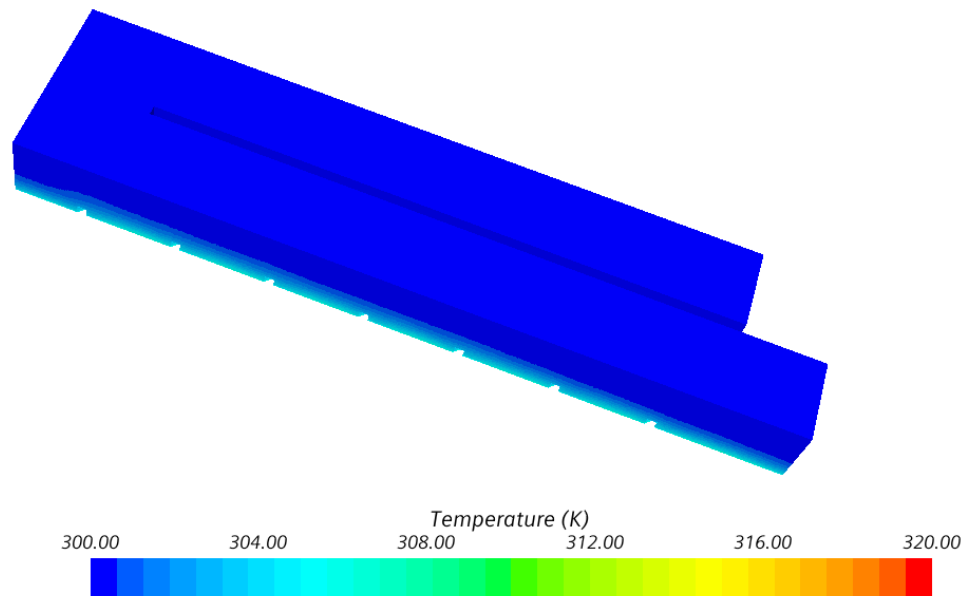
8.3.2 Ribbed Wall Results

Figure 8-4 and Figure 8-5 illustrate the wall temperature distribution for the 45-deg ribbed wall channel in stationary and rotation cases. From the figures, it can be found for both cases, installing the ribs enhanced the heat transfer between coolant and channel wall, especially between each rib. This enhancement results in lower wall temperature.

In stationary cases, due to the absence of buoyancy and centrifugal forces, the wall temperature is slightly higher than the rotational case. Due to the rotation, and existence of buoyancy and centrifugal forces, recirculation, heat transfer between the coolant and the channel walls increased. This observation is aligned with the results presented in chapter 6 for the 45-deg ribbed wall, where it was observed the Nusselt number in rotational cases is higher than stationary cases.



(a)



(b)

Figure 8-4: Temperature distribution on the solid wall of a 45-deg ribbed wall Channel (a) Stationary with $Re=35000$, (b) Rotation with $Re=35000$ and 300 rpm

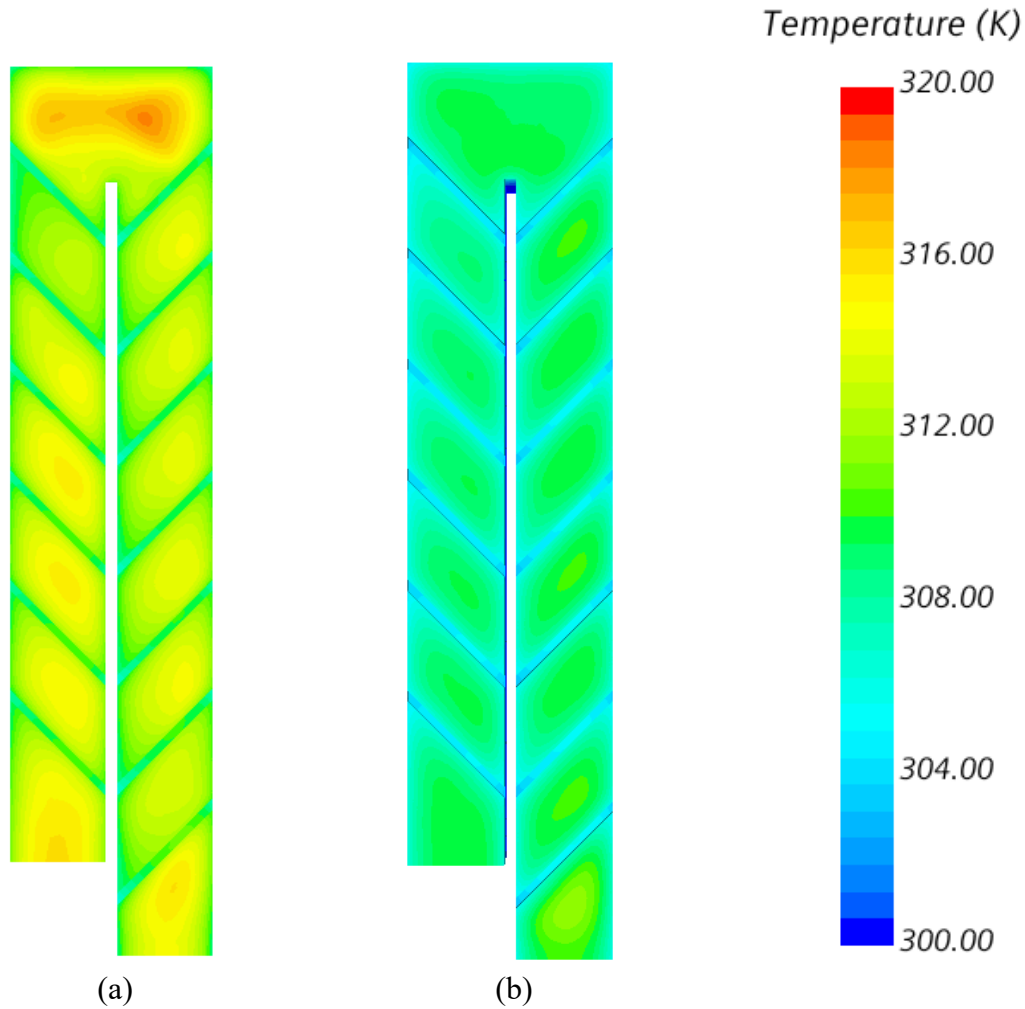


Figure 8-5: Temperature distribution for top and the bottom wall of the 45-deg ribbed wall channel (a) Stationary (b) Rotation

8.4 Conclusions

In this chapter, a brief introduction of the advantage of the conjugate heat transfer model is presented. A fully developed coupled conjugate heat transfer simulation is performed on a smooth and ribbed wall channel. The simulations set up based on fully developed flow and heat transfer boundary conditions. An unsteady state solver and steady-state solver are coupled to solve the heat transfer problem in the solid and fluid regions, respectively.

The current results were compared with the results from previous chapters, where only the fluid domain was considered. Numerical results comparison showed that the temperature distribution trend is the same in both LES and CHT calculations.

In cooling systems, one of the most important objectives is to obtain a uniform surface temperature distribution. The presented coupled CHT model is capturing the more accurate temperature distribution along the channel. Thus, proposing an optimum cooling system would be more specific.

9 Overall Conclusions and Recommendations

The gas turbine design mainly involves finding a balance between maximizing power generation and engine lifetime capability. Gas turbine power generation is directly related to the inlet mass flow and temperature. Thermal stresses are one of the main factors that reduce gas turbine performance and life. Besides the thermal stresses, the rotational motion brings a significant amount of mechanical stress to the rotor and the blade parts. The combined effect of rotational and high operating temperatures dramatically reduces the gas turbine components, especially the blades. Thus, optimizing the cooling system for the gas turbine components becomes a priority to increase the reliability of the application.

In the presented work, the focus is on investigating the physical phenomenon in blade cooling channels and using a suitable numerical method, which provides a realistic result for industrial turbine blades. Here are the main findings of this research.

Numerical setup for heat transfer investigation

Due to the complex flow behavior in the cooling channels, utilizing the best numerical approach to solve the heat transfer equation is crucial. Between the various methods, RANS models mainly rely on isentropic flow assumption, which allows mostly to capture the small unsteady scale. However, the LES model is more adaptive to solve any scale turbulent configurations. In the blade cooling systems, the main phenomena are large separated flows. Hence, the LES model is more suitable for investigating the complex flows in the cooling system.

The reliability of resolving a simulation is related to the number of mesh, especially for the LES model. In this research, a novel approach for finding a correct mesh size has been introduced. This approach is coupling the RANS model with Kolmogorov length and Taylor

Microscale concepts to find the right cell size for the LES model that can assure the smallest scales in the turbulent spectrum can be solved. Besides the LES model, a coupled conjugate heat transfer model is implemented for a smooth and ribbed wall channel. While various CHT combinations can be used to solve the heat transfer, here a steady state fluid and unsteady state solid solver are employed. This coupling approach is close to the CHT approach that is used in the industry.

The calculated Nusselt number and temperatures from the CFD were compared with the experimental data from the same size channel geometry. A good agreement between the two data sets is observed, which confirms the validity of both CFD models and results.

Heat transfer investigation for a smooth wall with high rotation

Several physical parameters are investigated for both stationary and rotational cases. Results from this part identify the importance of rotation, inlet velocity, on the heat transfer coefficient. In the stationary cases, the time-averaged Nusselt number enhancement varies from 22 to 53 as Reynolds number increased from 6000 to 35,000. Also, it is shown under the constant rotational speed, the variation of the Nusselt number is independent of the rotation number changes. Increasing the Reynolds number enhanced the local time-averaged Nusselt number, which is a similar trend, which was observed in stationary cases.

Furthermore, the combined effect of the Reynolds number and rotational speed enhances the buoyancy and centrifugal forces, which results in an enhancement in the Nusselt number in both passages. In the bending region, maximum buoyancy force can be observed, which is one of the main reasons for the significant Nusselt number increase in this region.

From the smooth wall results in a heat transfer correlation for calculating local Nusselt number for a developing flow passing the channel was proposed. This correlation is used to calculate the reference Nusselt number.

Effect of Rib turbulator on the heat transfer coefficient in a channel with 1:1 aspect ratio

For this part, the objective is to investigate the geometrical factors such as rib geometry, installation configurations, and rib spacing effects on the heat transfer coefficient. Thermal performance, which is the ratio between the Nusselt number and pressure drop, is used as the factor in identifying the optimum rib configuration for the channel in this study. From the results, it can be concluded in the parallel rib configurations, 45-deg rib with Rib-Pitch-to-Rib-height ten has the best performance compared with the other 90-deg and 60-deg ribs. Additionally, the V-shape rib, regardless of the installation configurations, has the highest thermal performance.

Turning guide vane effect on the heat transfer and pressure drop in square U-bend channel

A novel turning guide vane concept is introduced, and various designs have been implemented. From the results, it is concluded, having a turbulator at the turning region where the flow behavior is unpredictable, helps to reduce the recirculation zones near the channel edges. Reducing these zones increases the flow turbulence and mixing, resulted in an increase in the Nusselt number coefficient at the turning region and second passages.

10 References

- [1] Z. S. Spakovszky, E. M. Greitzer, I. a Waitz, and D. Quattrochi, "Thermodynamics and propulsion," *MIT*, 2006. [Online]. Available: <https://web.mit.edu/16.unified/www/FALL/thermodynamics/notes/notes.html>
- [2] J. H. Perepezko, "The hotter the engine, the better," *Science (80-.)*, vol. 326, no. 5956, pp. 1068–1069, 2009.
- [3] P. Ireland and D. G., "Aerothermal performance of internal cooling systems in turbomachines," *Von Karman Inst. Lect. Ser. Intern. Cool. Turbomach.*, vol. 2010, no. May, p. 2010, 2010.
- [4] D. E. Metzger, W. B. Shepard, and S. W. Haley, "Row resolved heat transfer variations in pin-fin arrays including effects of non-uniform arrays and flow convergence," in *ASME International Gas Turbine Conference and Exhibit*, 1986, pp. 1–9.
- [5] F. J. Cunha, "Heat Transfer Analysis - Introduction," in *The Gas Turbine Handbook*, no. 860, 2006.
- [6] J. C. Han, S. Dutta, and S. Ekkad, *Gas Turbine Heat Transfer and Cooling Technology*. New York: Taylor and Francis, NewYork, 2001.
- [7] R. J. Goldstein, "Film Cooling," in *Advances in Heat transfer*, vol. 7, 1971, pp. 321–379.
- [8] B. Lakshminarayana, *Fluid Dynamics and heat transfer for turbomachinery*, First. New York: A Wiley-Interscience Publication, 1996.
- [9] L. M., S. M. Shaahid, and A. A., "Jet Impingement Cooling in Gas Turbines for Improving Thermal Efficiency and Power Density," in *Advances in Gas Turbine Technology*, no. state 3, InTech, 2011.
- [10] J. Han and L. M. Wright, "Enhanced Internal Cooling of Turbine Blades and Van," 2000.
- [11] L. W. Florschuetz, R. A. Berry, and D. E. Metzger, "Periodic Streamwise Variations of Heat Transfer Coefficients for Inline and Staggered Arrays of Circular Jets with Crossflow of Spent Air," *J. Heat Transfer*, vol. 102, no. 1, pp. 132–137, Feb. 1980.
- [12] D. E. Metzger, L. W. Florschuetz, D. I. Takeuchi, R. D. Behee, and R. A. Berry, "Periodic

- Streamwise Variations of Heat Transfer Coefficients for Inline and Staggered Arrays of Circular Jets with Crossflow of Spent Air," *J. Heat Transfer*, vol. 101, no. August 1979, pp. 526–531, 1979.
- [13] R. N. Koopman and E. . Sparrow, "Local and Average Transfer Coefficients Due to Impinging of Jets," *Int. J. Heat Mass Transf.*, vol. 19, pp. 673–683, 1976.
- [14] D. M. Kercher and W. Tabakoff, "Heat Transfer by a Square Array of Round Air Jets Impinging Perpendicular to a Flat Surface Including the Effect of Spent Air," *J. Eng. Power*, vol. 92, no. 1, pp. 73–82, 1970.
- [15] L. W. Florschuetz, C. R. Truman, and D. E. Metzger, "Streamwise Flow and Heat Transfer Distributions for Jet Array Impingement with Crossflow," *J. Heat Transfer*, vol. 103, no. 2, pp. 337–342, May 1981.
- [16] R. E. CHUPP, H. E. HELMS, P. W. MCFADDEN, and T. R. BROWN, "Evaluation of internal heat-transfer coefficients for impingement-cooled turbine airfoils," *J. Aircr.*, vol. 6, no. 3, pp. 203–208, May 1969.
- [17] R. S. Bunker and D. E. Metzger, "Local Heat Transfer in Internally Cooled Turbine Airfoil Leading Edge Regions: Part I—Impingement Cooling Without Film Coolant Extraction," *J. Turbomach.*, vol. 112, no. 3, pp. 451–458, 1990.
- [18] D. E. Metzger, R. A. Berry, and J. P. Bronson, "Developing Heat Transfer in Rectangular Ducts With Staggered Arrays of Short Pin Fins," *J. Heat Transfer*, vol. 104, no. 4, pp. 700–706, 1982.
- [19] M. K. Chyu, Y. C. Hsing, T. I.-P. Shih, and V. Natarajan, "Heat Transfer Contributions of Pins and Endwall in Pin-Fin Arrays: Effects of Thermal Boundary Condition Modeling," *J. Turbomach.*, vol. 121, no. 2, pp. 257–263, 1999.
- [20] G. J. VanFossen, "Heat-Transfer Coefficients for Staggered Arrays of Short Pin Fins," *J. Eng. Power*, vol. 104, no. 2, pp. 268–274, 1982.
- [21] M. K. Chyu, Y. Yu, H. Ding, J. P. Downs, and F. O. Soechting, "Concavity Enhanced Heat Transfer in an Internal Cooling Passage," in *Volume 3: Heat Transfer; Electric Power; Industrial and Cogeneration*, 1997, pp. 1–7.
- [22] H. K. Moon, T. O'Connell, and B. Glezer, "Channel Height Effect on Heat Transfer and

- Friction in a Dimpled Passage," *Vol. 3 Heat Transf. Electr. Power; Ind. Cogener.*, vol. 122, no. April 2000, p. V003T01A043, 1999.
- [23] G. I. Mahmood, M. L. Hill, D. L. Nelson, P. M. Ligrani, H.-K. Moon, and B. Glezer, "Local Heat Transfer and Flow Structure on and Above a Dimpled Surface in a Channel," *J. Turbomach.*, vol. 123, no. 1, pp. 115–123, 2001.
- [24] S. W. Moon and S. C. Lau, "Turbulent Heat Transfer Measurements on a Wall With Concave and Cylindrical Dimples in a Square Channel," in *Volume 3: Turbo Expo 2002, Parts A and B*, 2002, pp. 459–467.
- [25] R. S. Bunker and K. F. Donnellan, "Heat Transfer and Friction Factors for Flows Inside Circular Tubes With Concavity Surfaces," *J. Turbomach.*, vol. 125, no. 4, pp. 665–672, 2003.
- [26] J. C. Han, L. R. Glicksman, and W. M. Rohsenow, "An Investigation of Heat Transfer and Friction for Rib-Roughened Surfaces," *Int. J. Heat Mass Transf.*, vol. 21, no. 8, pp. 321–328, 1978.
- [27] J. Sundberg, "Heat Transfer Correlations for Gas Turbine Cooling," 2006.
- [28] J. C. Han, "Heat Transfer and Friction in Channels With Two Opposite Rib-Roughened Walls," *J. Heat Transfer*, vol. 106, no. 4, p. 774, 1984.
- [29] J. C. Han, "Heat Transfer and Friction Characteristics in Rectangular Channels With Rib Turbulators," *J. Heat Transfer*, vol. 110, no. 2, pp. 321–328, May 1988.
- [30] M. E. Taslim and C. M. Wadsworth, "An Experimental Investigation of the Rib Surface-Averaged Heat Transfer Coefficient in a Rib-Roughened Square Passage," *J. Turbomach.*, vol. 119, no. 2, pp. 381–389, 1997.
- [31] Y.-H. Liu, L. M. Wright, W.-L. Fu, and J.-C. Han, "Rib Spacing Effect on Heat Transfer and Pressure Loss in a Rotating Two-Pass Rectangular Channel (AR=1:2) With 45-Degree Angled Ribs," in *Volume 3: Heat Transfer, Parts A and B*, 2006, no. 4238X, pp. 363–373.
- [32] J. . Han, "Heat transfer and friction characteristics in rectangular channels with rib turbulators," *ASME Journal heat Transf.*, vol. 110, no. 2, pp. 321–328, 1988.
- [33] M. E. Taslim and S. D. Spring, "Effect of Turbulator Profile and Spacing on Heat Transfer and Friction in a Channel," *J. Thermophys. Heat Transf.*, vol. 8, no. 3, pp. 555–562, 1994.

- [34] D. E. Metzger and M. K. Sahm, "Heat Transfer Around Sharp 180-deg Turns in Smooth Rectangular Channels," *J. Heat Transfer*, vol. 108, no. 3, pp. 500–506, Aug. 1986.
- [35] C. S. Fan and D. E. Metzger, "Effects of Channel Aspect Ratio on Heat Transfer in Rectangular Passage Sharp 180° Turn," in *ASME, International Gas Turbine Conference and Exhibition*, 1987.
- [36] J. C. Han, P. R. Chandra, and S. C. Lau, "Local Heat/Mass Transfer Distributions Around Sharp 180 deg Turns in Two-Pass Smooth and Rib-Roughened Channels," *J. Heat Transfer*, vol. 110, no. 1, pp. 91–98, 1988.
- [37] P. Han J. C., Zhang, "Effect of Rib-Angle orientation on local mass transfer distribution in a three-pass rib-roughened channel," *J. Turbomach.*, vol. 113, no. 1, p. 113/123, 1991.
- [38] Park, J. S., Han, J. C., Huang, Y., and S. Ou, "Heat Transfer Performance Comparisons of Five Different Rectangular Channel with Parallel Angled Ribs," *Int. J. Heat Mass Transf.*, vol. 35, no. 11, pp. 2891–2903, 1992.
- [39] Ekkad, S. V. and J. C. Han, "Detailed Heat Transfer Distributions in Two-Pass Square Channels with Rib Turbulators," *Int. J. Heat Mass Transf.*, vol. 40, no. 11, pp. 2525–2537, 1997.
- [40] J. H. Wagner, B. V. Johnson, and T. J. Hajek, "Heat Transfer in Rotating Passages With Smooth Walls and Radial Outward Flow," *J. Turbomach.*, vol. 113, no. 1, pp. 42–51, 1999.
- [41] J. H. Wagner, B. V. Johnson, and F. C. Kopper, "Heat Transfer in Rotating Serpentine Passages With Smooth Walls," *J. Turbomach.*, vol. 113, no. 3, pp. 321–330, Jul. 1991.
- [42] M. E. Taslim, L. A. Bondi, and D. M. Kercher, "Experimental investigation of heat transfer in an orthogonally rotating channel roughened with 45 deg criss-cross ribs on two opposite walls," *J. Turbomach.*, vol. 113, no. 3, pp. 346–353, 1991.
- [43] M. E. Taslim, A. Rahman, and S. D. Spring, "An Experimental Investigation of Heat transfer Coefficients in a Spanwise Rotating Channel with Two Opposite Rib-Roughened Walls," *J. Turbomachinery*, vol. 113, no. 1, pp. 75–82, 1991.
- [44] J. C. Han, Y. M. Zhang, and K. Kalkuehler, "Uneven Wall Temperature Effect on Local Heat Transfer in a Rotating Two-Pass Square Channel with Smooth Walls," *J. Eng. Power*, vol. 115, no. 4, pp. 912–920, 1993.

- [45] Y. M. Zhang, J. C. Han, and J. A. Parsons, "Surface Heating Effect on Local Heat Transfer in a Rotating Two-Pass Square Channel with 60 deg Angled Rib Turbulators," *J. Turbomachinery*, vol. 117, no. 2, pp. 272–280, 1995.
- [46] B. V. Johnson, J. H. Wagner, G. D. Steuber, and F. C. Yeh, "Heat Transfer in Rotating Serpentine Passages With Trips Skewed to the Flow," *J. Turbomach.*, vol. 116, no. 1, pp. 113–123, Jan. 1994.
- [47] B. V. Johnson, J. H. Wagner, G. D. Steuber, and F. C. Yeh, "Heat Transfer in Rotating Serpentine Passages With Selected Model Orientations for Smooth or Skewed Trip Walls," *J. Turbomach.*, vol. 116, no. 4, pp. 738–744, Oct. 1994.
- [48] J. A. Parsons, H. Je-Chin, and Z. Yuming, "Wall heating effect on local heat transfer in a rotating two-pass square channel with 90° rib turbulators," *Int. J. Heat Mass Transf.*, vol. 37, no. 9, pp. 1411–1420, Jun. 1994.
- [49] Y. Parsons, J. A., Han, J.C.,Zhang, "Effect of Model Orientation and Wall Heating Condition on Local Heat Transfer in a Rotating Two-Pass Square Channel with Rib Turbulators," *Int. J. Heat Mass Transf.*, vol. 38, no. 7, pp. 1151–1159, 1995.
- [50] S. Dutta and J. C. Han, "Local Heat Transfer in Rotating Smooth and Ribbed Two-Pass Square Channels with Three Channel Orientations," *J. Heat Transfer*, vol. 118, no. 3, pp. 578–584, 1996.
- [51] H. Deng, L. Qiu, Z. Tao, and S. Tian, "Heat transfer study in rotating smooth square U-duct at high rotation numbers," *Int. J. Heat Mass Transf.*, vol. 66, pp. 733–744, Nov. 2013.
- [52] R. S. Amano and S. Beyhaghi, "Heat Transfer in a Rotating Two-pass Square Channel Representing Internal Cooling of Gas Turbine Blades," in *54th AIAA Aerospace Sciences Meeting*, 2016, no. January, pp. 1–11.
- [53] Y. Li, H. Deng, G. Xu, and S. Tian, "Heat transfer investigation in rotating smooth square U-duct with different wall-temperature ratios and channel orientations," *Int. J. Heat Mass Transf.*, vol. 89, pp. 10–23, Oct. 2015.
- [54] E. Burberi, D. Massini, L. Cocchi, L. Mazzei, A. Andreini, and B. Facchini, "Effect of Rotation on a Gas Turbine Blade Internal Cooling System: Numerical Investigation," *J. turbomachinery*, vol. 139, no. 3, p. 031005, 2016.

- [55] F. P. Incropera, D. P. Dewitt, and T. L. Bergman, *Fundamental of Heat and Mass Transfer*, 7th ed. New York: John Wiley and Sons. Inc., 2007.
- [56] E. N. Sieder and G. E. Tate, "Heat transfer and Pressure Drop of Liquids in tubes," *Ind. Eng. Chem.*, vol. 28, no. 12, pp. 1429–1435, 1936.
- [57] A. P. Colburn, "A method of correlating forced convection heat transfer data and a comparison with fluid friction," *Int. J. Heat Mass Transf.*, vol. 7, no. 12, pp. 1359–1384, 1964.
- [58] Yongniang, Yang, and L. Fuchs, "Numerical study of viscous flow in a rotating rectangular channel," *Int. J. Eng. Sci.*, vol. 31, no. 6, pp. 873–881, 1993.
- [59] E. A. Sewall and D. K. Tafti, "Large Eddy Simulation of Flow and Heat Transfer in the 180-Deg Bend Region of a Stationary Gas Turbine Blade Ribbed Internal Cooling Duct," *J. Turbomach.*, vol. 128, no. 4, pp. 763–771, Oct. 2006.
- [60] Y. Li, G. Xu, H. Deng, and S. Tian, "Buoyancy effect on heat transfer in rotating smooth square U-duct at high rotation number," *Propuls. Power Res.*, vol. 3, no. 3, pp. 107–120, Sep. 2014.
- [61] M. Huh, J. Lei, and J.-C. Han, "Influence of Channel Orientation on Heat Transfer in a Two-Pass Smooth and Ribbed Rectangular Channel (AR=2:1) Under Large Rotation Numbers," *J. Turbomach.*, vol. 134, no. 1, p. 011022, 2012.
- [62] Huh, Michael, Lei, Jiang, Liu, Yao Hsein, and J.-C. Han, "High Rotation Number Effects on Heat Transfer in a Rectangular (AR=2:1)(AR=2:1) Two-Pass Channel," *J. turbomachinery*, vol. 133, no. 2, p. 021001, 2010.
- [63] S. Dutta, J.-C. Han, and C. P. Lee, "Local heat transfer in a rotating two-pass ribbed triangular duct with two model orientations," *Int. J. Heat Mass Transf.*, vol. 39, no. 4, pp. 707–715, Mar. 1996.
- [64] A. Murata, S. Mochizuki, and T. Takahashi, "Local heat transfer measurements of an orthogonally rotating square duct with angled rib turbulators," *Int. J. Heat Mass Transf.*, vol. 42, no. 16, pp. 3047–3056, 1999.
- [65] T.-M. Liou, M.-Y. Chen, and M.-H. Tsai, "Fluid Flow and Heat Transfer in a Rotating Two-Pass Square Duct With In-Line 90-deg Ribs," *J. Turbomach.*, vol. 124, no. 2, pp. 260–268,

Apr. 2002.

- [66] L. Al-Hadhrami and J.-C. Han, "Effect of rotation on heat transfer in two-pass square channels with five different orientations of 45° angled rib turbulators," *Int. J. Heat Mass Transf.*, vol. 46, no. 4, pp. 653–669, Feb. 2003.
- [67] H. H. Cho, Y. Y. Kim, K. M. Kim, and D. H. Rhee, "Effects of Rib Arrangements and Rotation Speed on Heat Transfer in a Two-Pass Duct," in *Volume 5: Turbo Expo 2003, Parts A and B*, 2003, vol. 5 A, pp. 433–442.
- [68] P. Agarwal, S. Acharya, and D. E. Nikitopoulos, "Heat/Mass Transfer in 1:4 Rectangular Passages With Rotation," *ASME Conf. Proc.*, vol. 125, no. 4, pp. 726–733, 2003.
- [69] M. Pascotto, A. Armellini, C. Mucignat, and L. Casarsa, "Coriolis Effects on the Flow Field Inside a Rotating Triangular Channel for Leading Edge Cooling," *J. Turbomach.*, vol. 136, no. 3, p. 031016, 2013.
- [70] H. Deng, Y. Li, Z. Tao, G. Xu, and S. Tian, "Pressure drop and heat transfer performance in a rotating two-pass channel with staggered 45-deg ribs," *Int. J. Heat Mass Transf.*, vol. 108, pp. 2273–2282, 2017.
- [71] R. Kiml, S. Mochizuki, and A. Murata, "Effects of Rib Arrangements on Heat Transfer and Flow Behavior in a Rectangular Rib-Roughened Passage: Application to Cooling of Gas Turbine Blade Trailing Edge," *J. Heat Transfer*, vol. 123, no. 4, pp. 675–681, Aug. 2001.
- [72] P. Singh and S. V. Ekkad, "Experimental Investigation of Rotating Rib Roughened Two-Pass Square Duct With Two Different Channel Orientations," in *Volume 5A: Heat Transfer*, 2017, pp. 1–16.
- [73] W. Kays and M. Crawford, *Convective Heat and Mass Transfer*, 3rd ed. New York: McGraw-Hill, 1993.
- [74] L. M. K. Boelter, G. Young, and H. W. Iverson, "Distribution of Heat Transfer Rate in the Entrance Section of a Circular Tube," 1948.
- [75] J.C. Han, "Heat Transfer and Friction Characteristics in Rectangular channels with rib turbulators," *ASME Journal heat Transf.*, vol. 110, no. 2, pp. 321–328, 1988.
- [76] J. C. Han and J. S. Park, "Developing heat transfer in rectangular channels with rib turbulators," *Int. J. Heat Mass Transf.*, vol. 31, no. 1, pp. 183–195, 1988.

- [77] J. Park, J. Han, Y. Huang, S. Ou, and R. Boyle, "Heat transfer performance comparisons of five different rectangular channels with parallel angled ribs," ... *Heat Mass Transf.*, vol. 35, no. 11, pp. 2891–2903, 1992.
- [78] L. M. Wright, W.-L. Fu, and J.-C. Han, "Influence of Entrance Geometry on Heat Transfer in Rotating Rectangular Cooling Channels (AR=4:1) With Angled Ribs," *J. Heat Transfer*, vol. 127, no. 4, pp. 378–387, Apr. 2005.
- [79] L. M. Wright, Y.-H. Liu, J.-C. Han, and S. Chopra, "Heat Transfer in Trailing Edge, Wedge-Shaped Cooling Channels Under High Rotation Numbers," *J. Heat Transfer*, vol. 130, no. 7, p. 071701, Jul. 2008.
- [80] A. Thom, "The effect of bubbles attached to an electrode on electrical resistance and dissolved gas concentration," *Proc. R. Soc. London. A. Math. Phys. Sci.*, vol. 387, no. 1792, pp. 133–146, May 1983.
- [81] S. B. Pope, *Turbulent Flows*, 1st ed. Cambridge: Cambridge University Press, 2000.
- [82] V. M. Tikhomirov, "Equations of Turbulent Motion in an Incompressible Fluid," in *Selected Works of AN Kolmogorov*, vol. 6, Springer, Dordrecht., 1942, pp. 328–330.
- [83] D. C. Wilcox, *Turbulence modeling for CFD*, 3rd ed., vol. 93. DCW Industries, Inc., 2006.
- [84] F. R. Menter, "Review of the shear-stress transport turbulence model experience from an industrial perspective," *Int. J. Comput. Fluid Dyn.*, vol. 23, no. 4, pp. 305–316, Apr. 2009.
- [85] A. Leonard, "Energy Cascade in Large-Eddy Simulations of Turbulent Fluid Flows," *Adv. Geophys. A*, vol. 18, pp. 237–248, 1974.
- [86] F. Nicoud and F. Ducros, "Subgrid-Scale Stress Modelling Based on the Square of the Velocity Gradient Tensor", *Flow, Turbulence and Combustion*, *Flow, Turbul. Combust.*, vol. 62, pp. 183–200, 1999.
- [87] V. T. Karman, "Mechanical Similitude and Turbulence," *Tech. Natl. Serv. Inf.*, 1931.
- [88] M. T. Landahl and E. Mollo-Christensen, "Turbulence and Random Processes in Fluid Mechanics," *J. Acoust. Soc. Am.*, vol. 86, p. 2471, 1989.
- [89] D. Albertson, M. B. Parlange, and W. E. Eichinger, "The Average Dissipation Rate of Turbulent Kinetic Energy in the Neutral and Unstable Atmospheric Surface Layer," *J. Geophys. Res.*, vol. 102, no. 96, pp. 13423–13432, 1997.

- [90] Y. Addad, U. Gaitonde, D. Laurence, and S. Rolfo, "Optimal unstructured meshing for large eddy simulations," *Qual. Reliab. Large-Eddy Simulations. Springer*, vol. 12, no. January, pp. 93–103, 2008.
- [91] X. Jiang and C.-H. Lai, *Numerical Techniques for Direct and Large-Eddy Simulations*, 1st ed., no. April. Taylor and Francis Group, 2009.
- [92] Culbert B. Laney, *Computational Gasdynamics*. Cambridge University Press, 1998.
- [93] S. Kumar, "Investigation of heat transfer and flow using ribs within gas turbine blade cooling passage: experimental and hybrid LES/RANS modeling," University of Wisconsin-Milwaukee, 2012.
- [94] A. J. Wheeler and A. R. Ganji, *Introduction to Engineering Experimentation*, 3rd ed. New Jersey: Pearson Higher Education, 2010.
- [95] E. A. Sewall and D. K. Tafti, "Large eddy simulation of flow and heat transfer in the developing flow region of a rotating gas turbine blade internal cooling duct with coriolis and buoyancy forces," *J. Turbomachineryurbomachinary*, vol. 130, no. 1, p. 0011005, 2005.
- [96] M. Schüler, F. Zehnder, B. Weigand, J. von Wolfersdorf, and S. O. Neumann, "The Effect of Turning Vanes on Pressure Loss and Heat Transfer of a Ribbed Rectangular Two-Pass Internal Cooling Channel," *J. Turbomach.*, vol. 133, no. 2, p. 021017, 2010.
- [97] R. S. Bunker, "The Augmentation of Internal Blade Tip-Cap Cooling by Arrays of Shaped Pins," *J. Turbomachineryurbomachinary*, vol. 130, no. October 2008, pp. 041007–1, 2008.
- [98] J. S. Park, D. M. Lee, D. H. Lee, S. Lee, B. S. Kim, and H. H. Cho, "Thermal performance in a rotating two-passage channel with various turning guide vanes," *J. Mech. Sci. Technol.*, vol. 31, no. 7, pp. 3581–3591, 2017.

CURRICULUM VITAE

Mandana Sheikhzad Saravani

Place of Birth: Rasht, Iran

EDUCATION

- **Ph.D. Mechanical Engineering** (August 2015-May 2020)
University of Wisconsin Milwaukee
Dissertation: "Investigation of Heat Transfer in Stationary and Rotating U-Duct Passage Representing Internal Cooling of Gas Turbine Blade Channel"
- **MSc Mechanical Engineering** (December 2014)
University of Wollongong, Wollongong NSW, Australia
- **BSc Mechanical Engineering** (September 2012)
University of Guilan, Rasht, Iran

PROFESSIONAL EXPERIENCES

CFD Engineer (May 2020-Present)

Johns Manville, Littleton, CO

Senior CFD Engineer (Jan 2020-April 2020)

Modine Manufacturing Company, Racine, WI

- Develop novel heat transfer techniques for heat exchanger
- Orchestrating process improvements using CFD methodologies to effectively reduce computation

Research Intern (2019-2020)

University of Wisconsin Milwaukee

- Work at CFD group at Harley-Davidson Product Development Center, Wauwatosa, WI
- Construct Mesh Morphing/ CAD Parametrization models on CFD simulations of OE parts
- Architect automated topological optimization processes integrating multiple CAE software (Mesh/CAD control, CFD, and DOE/ Optimization/ Statistical Analysis Tool)
- Liaison with software technical supports to have their aid and give our feedback for fulfilling the company's needs.
- Create tutorials and training materials for the new proprietary software/tools and train engineers to use them

**Technical Support Engineer
(2011–2013)**

Parshan Tosane Tiva, Iran

- Developed engineering design, cost estimates, and project management for gas transmission lines
 - Provided technical support to gas technical supervisors, distribution design supervisors, and field engineers
 - Supervised pipeline safety tests, leakage and damage detection
-

RESEARCH EXPERIENCES**Research Ph.D. Student
(2015–Present)**

University of Wisconsin Milwaukee -Gas turbine

- Optimized cooling channel design of gas turbine blade (CFD and experiment) resulted in an increase in the thermal efficiency of the gas turbine, at the University Services and Research Building (USRB)
- Optimized the geometrical aspects of some components in gas turbine cooling channel system (e.g., rib aspect ratio, rib angle, guide van design)
- Simulated turbulent flow in a cooling channel with different operating conditions. Built and optimized guide vans to enhance the thermal performance of the gas turbine
- Performed Finite Element Analysis and failure analysis for experimental setup components
- Selected material for internal cooling channel experimental set up based on high rotational speed operation condition
- Developed empirical correlation predicting the heat transfer coefficient for developing flow in microchannels
- Experimental measurements and data analysis for (Hydro turbine performance, Internal cooling of the gas turbine blade) project.

**Member of Industrial Assessment Center (IAC)
(2017–Present)**

UW-Milwaukee industrial assessment center

- Performed ASHRAE level I and II energy audits on industrial facilities across Wisconsin and Illinois
- Conducted 20+ and led 6 ASHRAE level I and II energy audits
- Proposed more than 50 energy-saving recommendations and identified over \$2.8 million worth of energy savings.
- Prepared audit reports delineating the outcomes of the assessment regarding energy savings, cost reduction in utility bills, and the return of investment
- Analyzed and assessed equipment, systems and processes to provide energy savings and improve productivity
- Evaluated utility bills and carried out a comprehensive analysis to trace the energy usage trend
- Analyzed the utility data of various facilities to get the baseline energy consumptions and identified possible energy savings measures by energy modeling

Research Assistant (2010-2012)

University of Gilan, Rasht, Iran

- Optimized the Fuzzy controller design for inverted pendulum by Genetic algorithms
- Designed a fuzzy controller for the system and applied the code in MATLAB and gained the motion diagram.
- Found an efficient coefficient for the controller by using the Genetic algorithm

TEACHING EXPERIENCES

Introduction to Fluid Mechanics Lecturer

(Fall 2018)

Mechanical Engineering Department, CEAS, University of Wisconsin Milwaukee

- Planned and taught theoretical lectures on aerodynamics fluid dynamics concepts

Teaching Assistant

(2015-2016)

Mechanical Engineering Department, CEAS, university of Wisconsin Milwaukee

- Introduction to Control system and Basic engineering thermodynamics instructor
 - Taught theoretical lectures about the dynamic system, analysis and design of feedback control
 - Taught cycle analysis the power plants concepts
 - Instructed students to handle experimental setups (e.g., QuaRC controllers, 1-DOF and 2-DOF Inverted pendulum)
-

MANAGEMENT EXPERIENCE

- President of American Institute of Aeronautics and Astronautics (AIAA) student organization at UWM
 - Raised more than \$20,000 operation budget for AIAA organization within a 3-year period
 - Mentor at Student Mentor ship Program for female students in the Industrial Assessment Center (IAC) program
-

MENTORSHIP EXPERIENCE

- Mentor for female students in the Industrial Assessment Center (IAC) mentorship program since 2019
-

CONFERENCE ORGANIZATION

- Organized “4th Aerospace and Green Energy Symposium” Fall 2017, Milwaukee, WI, USA
 - Organized” Design for Reliability in Aeronautical Engineering seminar” Fall 2018, Milwaukee, WI, USA
 - Organizing “5th Aerospace and Green Energy Symposium” Fall 2019, Milwaukee, WI, USA
-

AWARDS AND CERTIFICATIONS

- 2019 UWM Graduate Student Excellence Fellowship Award
- 2018 UWM Mechanical Department Foreign Student Scholarship Award

- Certificate for the completion of requirements mandated by the U.S. Department of Energy's Industrial Assessment Center program at the University of Wisconsin Milwaukee
- Honorable mention at 2016 UWM student research poster competition
- The Association of energy engineering, certificate of completion, 35th Energy Management Congress West 2017
- The Association of energy engineering, certificate of completion, 40th world energy congress conference- 2017

PUBLICATIONS

JOURNALS

- Mandana S. Saravani, Nicholas DiPasquale, Joseph Halmo, Ryoichi S. Amano," Turning Guide Vane Effect on Internal Cooling of Two-Passage Channel with Parallel Ribs", ASME Journal of Energy Resources (accepted)
- Mandana S. Saravani, Nicholas DiPasquale, Ahmad Abbas, Ryoichi S. Amano," Heat transfer Evaluation for a Two-Pass Smooth Wall Channel: Stationary and Rotational", ASME Journal of Energy Resources , Vol 142,pp 061305, 2020
- Mandana S. Saravani, Nicholas DiPasquale, Saman Beyhaghi, Ryoichi S. Amano," Heat Transfer in Internal Cooling Channels of Gas Turbine Blades: Buoyancy and Density Ratio Effects", ASME Journal of Energy Resources Technology JERT-19-1035, Vol 141,pp112001, 2019
- Ahmad Abbas, Mandana S. Saravani, Mohammad Qandil, Ryoichi S. Amani," Optimization of Kaplan Hydro-Turbine at Very Low Head with Rim-Driven Generator", ASME Journal of Energy Resources Technology, JERT-18-1701, Vol 141, pp 11204, 2019
- Ahmad Abbas, Muhannad Al-Haddad, Mohammad Qandil, Mandana S. Saravani, Ryoichi S. Amano," Utilization of Hydro-turbines in Wastewater Treatment Plants", ASME Journal of Energy Resources Technology, JERT-18-1688,Vol 141,pp062011, 2019
- Sina Modares Ahmadi, M Ghazavi, Mandana S. Saravani " Dynamic Analysis of Rotor Supported on Ball Bearings with Waviness and Centralizing Springs and Squeeze Film Damper" IJE Transactions: Aspects Vol. 28, No.9,pp.1351-1358, 2015

PROCEEDINGS

- Mandana S. Saravani, Ahmad Abbas, Ryoichi S. Amano," The Opportunity for Energy Saving in Foundry-Case study" AIAA Propulsion and Energy 2019
- Mandana S. Saravani, Nicholas DiPasquale, Caleb Rezoma, Ryoichi S. Amano," Numerical Investigation on Internal Cooling of Two-Passage Channels with Parallel Ribs and Guide Vanes" ASME Turbo Expo 2019: Turbomachinery Technical Conference and Exposition
- Mandana S. Saravani, Nicholas DiPasquale, Ryoichi S. Amano," Heat Transfer Enhancement in Stationary and Rotating Internal Cooling Channels using Angled Ribs" ,2019 AIAA Aerospace Sciences Meeting
- Muhannad Al-Haddad, Ahmad Abbas, Mohammad Qandil, Mandana S. Saravani, Ryoichi S. Amano," Energy Value Analysis(EVA) of an office building-case study", 2019 AIAA Aerospace Sciences Meeting
- Mandana S. Saravani, Saman Beyhaghi, Ryoichi S. Amano," Effect of Buoyancy and Density Ratio on Heat Transfer in a Smooth Cooling Channel of a Gas Turbine Blade", ASME Turbo Expo 2018: Turbomachinery Technical Conference and Exposition, Oslo, Norway
- Mandana S. Saravani, Saman Beyhaghi, Ryoichi S. Amano "Experimental Analysis of Heat Transfer in Stationary and Rotating Internal Cooling Channels" 2018 AIAA Aerospace Sciences Meeting
- Ahmad Abbas, Muhannad Al-Haddad, Mohammad Qandil, Mandana S. Saravani, Ryoichi S. Amano,"Utilization of Hydro-Turbines in Wastewater Treatment Plants (WWTPs)", ASME 2018 12th International Conference on Energy Sustainability
- Ahmad Abbas, Mandana S. Saravani, Muhannad Al-Haddad, Mohammad Qandil, Ryoichi S. Amano,"A Comparative Study of Industrial Energy Assessments for Small and Medium-Sized Industrial Facilities"ASME 2018 12th International Conference on Energy Sustainability
- Ahmad Abbas, Mandana S. Saravani, Muhannad Al-Haddad, Ryoichi S. Amano, "Net-Zero-Energy(NZE) Wastewater Treatment Plants (WWTPs),2018 AIAA Aerospace Sciences Meeting
- Muhannad Al-Haddad, Mandana S. Saravani, Ahmad Abbas, Ryoichi S. Amano," An Analytical Study of Energy Efficiency Opportunities in Some Industrial Facilities" 2018 AIAA Aerospace Sciences Meeting

- Ahmad Abbas, Tomoki Sakamoto, Mandana S. Saravani, Ryoichi S. Amano, J. Millevolte, B. Lequesne "Optimization of Kaplan Hydro-Turbine at Very Low Head with Rim-Driven Generator" ASME 2017 Power Conference Joint with ICOPE-17 collocated with ASME2017
- Ryoichi S. Amano, Saman Beyhaghi, Ping Dong, Mandana S. Saravani, Madison Morrison," Computational and Experimental Investigation of Heat Transfer in Stationary and Rotating Internal Cooling Ducts with High Rotation Number" 15th International Energy Conversion Engineering Conference 2017
- Mandana S. Saravani, Ryoichi S. Amano, "Energy Saving Concepts and Opportunities in Foundry"-Sustainability Summit and Exposition 2018- Milwaukee, WI, USA
- Mandana S. Saravani, Ryoichi S. Amano, "Energy Saving Concepts and Opportunities in Foundry (A case Study)" 2018, Sustainable Energy System Panel, AIAA Propulsion and Energy, Cincinnati, OH

POSTERS

- Mandana S. Saravani, Ryoichi S. Amano, "Energy Saving Concepts and Opportunities in Foundry (A case Study)" 2018, AIAA Propulsion and Energy, Cincinnati, OH
- Mandana S. Saravani, Ryoichi S. Amano, "Energy Saving Concepts and Opportunities in Foundry" 2018 UWM student research poster competition
- Mandana S. Saravani, Ryoichi S. Amano "Investigation of Heat Transfer in Stationary and Rotating Internal Cooling Channels with High Rotation Numbers"2017 UWM student research poster competition
- Mandana S. Saravani, Ryoichi S. Amano "Optimal Design of Fuzzy Controller for Inverted Pendulum by Generic Algorithms" 2016 UWM student research poster competition